Development of Hydrodynamic Density Functional Theory for Mixtures and Application to Droplet Coalescence

A thesis accepted by the Faculty of Energy-, Process- and Bio-Engineering of the University of Stuttgart in partial fulfilment of the requirements for the degree of Doctor of Engineering Sciences (Dr.-Ing.)

by

Rolf Stierle

born in Esslingen am Neckar

Committee chair:	Prof. Dr.-Ing. Joachim Groß
Committee member:	Prof. Dr. Andrew J. Archer
Date of defence:	08.10.2021

Institute of Thermodynamics and Thermal Process Engineering
University of Stuttgart

2021

Contents

List of Figures

List of Tables

Abstract

Predicting accurately coalescence phenomena is critical to the accurate description of the hydrodynamics of fluids and their mixtures. A promising framework for the development of models for such phenomena is dynamic density functional theory. Dynamic density functional theory enables the analysis of dynamical processes in inhomogeneous systems of pure fluids and fluid mixtures at the molecular level. In this work, a hydrodynamic density functional theory model for mixtures in conjunction with Helmholtz energy functionals based on the PC-SAFT equation of state is proposed, that obeys the first and second law of thermodynamics and simplifies to the isothermal Navier-Stokes equation for homogeneous systems. The hydrodynamic density functional theory model is derived from a variational principle and accounts for both viscous forces and diffusive molecular transport. A Maxwell-Stefan model is applied for molecular transport. This work identifies a suitable expression for the driving force for molecular diffusion of inhomogeneous systems that captures the effect of interfacial tension. The proposed hydrodynamic density functional theory is a non-local theory that requires the computation of weighted (spatial averaged) densities around each considered spatial coordinate by convolution, which is computationally expensive. This work uses Fourier-type transforms to determine the weighted densities. A pedagogical derivation is presented for the efficient computation of the convolution integrals occurring in the Helmholtz energy functionals in Cartesian, cylindrical, and spherical coordinates on equidistant grids using fast Fourier and similar transforms. The applied off-the-shelf algorithms allow to reduce dimensionality and complexity of many practical problems. Furthermore, an algorithm for a fast first-order Hankel transform is proposed, allowing fast and easy density functional theory calculations in rotationally symmetric systems. Application of the hydrodynamic density functional theory model using a well-balanced finite-volume scheme to one-dimensional droplet and bubble coalescence of pure fluids and binary mixtures is presented. The required transport coefficients, shear viscosity and Maxwell-Stefan diffusion coefficients, are obtained by applying entropy scaling to inhomogeneous fluids. The considered systems show a qualitative difference in the coalescence characteristics of droplets compared to bubbles. This constitutes a first step towards predicting the phase rupture leading to coalescence using dynamic density functional theory.

Kurzfassung

Genaue Vorhersage von Koaleszenzphänomenen ist entscheidend für die genaue hydrodynamische Beschreibung von Flüssigkeiten und ihren Gemischen. Eine vielversprechende Methode für die Entwicklung von Modellen für solche Phänomene ist die dynamische Dichtefunktionaltheorie. Dynamische Dichtefunktionaltheorie ermöglicht die Analyse dynamischer Prozesse inhomogener Systeme aus Reinstoffen oder Fluidgemischen auf molekularer Ebene. In dieser Arbeit wird eine hydrodynamische Dichtefunktionaltheorie für Mischungen mit Helmholtz-Energie-Funktionalen basierend auf der PC-SAFT Zustandsgleichung vorgeschlagen, die den ersten und zweiten Hauptsatz der Thermodynamik erfüllt und sich für homogene Systeme auf die isotherme Navier-Stokes-Gleichung vereinfacht. Die hydrodynamische Dichtefunktionaltheorie wird aus einem Variationsprinzip abgeleitet und berücksichtigt viskose Kräfte und diffusiven Stofftransport; letzterer wird mittels Maxwell-Stefan-Diffusion modelliert. Diese Arbeit identifiziert eine geeignete Triebkraft für diffusiven Stofftransport in inhomogenen Systemen, die den Effekt von Grenzflächenspannung berücksichtigt. Die vorgeschlagene hydrodynamische Dichtefunktionaltheorie ist eine nicht-lokale Theorie, die die Berechnung gewichteter (räumlich gemittelter) Dichten um jede betrachtete Ortskoordinate durch rechenintensive Faltung erfordert. In dieser Arbeit werden Fourier-Transformationen verwendet, um die gewichteten Dichten zu bestimmen. Es wird didaktisch gezeigt, wie man die in den Helmholtz-Energiefunktionalen auftretenden Faltungsintegrale in kartesischen, zylindrischen und sphärischen Koordinaten auf äquidistanten Gittern mit schnellen Fourier- und verwandten Transformationen effizient berechnen kann. Die verwendeten Standardalgorithmen erlauben es, die Dimensionalität und Komplexität vieler praktischer Probleme zu reduzieren. Weiterhin wird ein Algorithmus für eine schnelle Hankel-Transformation erster Ordnung vorgeschlagen, der schnelle und einfache Dichtefunktionaltheorie-Berechnungen in rotationssymmetrischen Systemen ermöglicht. Das hydrodynamische Dichtefunktionaltheorie-Modell wird mit Hilfe eines *well-balanced* Finite-Volumen-Verfahrens auf eindimensionale Tropfen- und Blasenkoaleszenz von Reinstoffen und binären Mischungen angewendet. Die erforderlichen Transportkoeffizienten, Scherviskosität und Maxwell-Stefan-Diffusionskoeffizienten, werden durch Anwendung von Entropieskalierung auf inhomogene Systeme bestimmt. Die betrachteten Systeme zeigen für Tropfen ein qualitativ unterschiedliches Koaleszenzverhalten im Vergleich zu Blasen. Dies ist ein erster Schritt in Richtung der Vorhersage des zur Koaleszenz führenden Phasenbruchs unter Verwendung dynamischer Dichtefunktionaltheorie.

Journal Publications

This thesis is based on the following publications:

- Chapter 3: R. Stierle, E. Sauer, J. Eller, M. Theiss, P. Rehner, P. Ackermann, and J. Gross. Guide to efficient Solution of PC-SAFT classical Density Functional Theory in various Coordinate Systems using fast Fourier and similar Transforms. *Fluid Phase Equilibria*, **504**:112306, 2020. doi:10.1016/j.fluid.2019.112306

  E. Sauer and M. Theiss co-conceptualized this work; J. Eller implemented and tested the fast sine and cosine transform; P. Rehner implemented and tested the fast Abel transform; P. Ackermann implemented and tested the fast Hankel transform of zeroth order; J. Gross supervised this work and was involved in editing the manuscript.

- Chapter 4: R. Stierle and J. Gross: A fast inverse Hankel Transform of first Order for Computing vector-valued weight Functions appearing in Fundamental Measure Theory in cylindrical Coordinates. *Fluid Phase Equilibria*, **511**:112500, 2020. doi:10.1016/j.fluid.2020.112500

  J. Gross supervised this work and was involved in editing the manuscript.

- Chapter 5: R. Stierle and J. Gross: Hydrodynamic Density Functional Theory for Mixtures from a Variational Principle and Its Application to Droplet Coalescence. *The Journal of Chemical Physics*, **155**(13):134101, 2021. doi:10.1063/5.0060088

  J. Gross supervised this work and was involved in editing the manuscript.

Chapters 3 to 5 present literal quotes of the published work. Any addition with respect to the published work is marked. Any deletion or substitution is indicated with square brackets as '[...]'. Cross-references between chapters of this thesis may have been added to the published content to increase readability. The supporting information and appendices to the published work are presented in the appendix of this thesis.

1 Necessity for Developing a Thermodynamic Coalescence Model

The hydrodynamic behavior of two droplets can be categorized into the following regimes[1]: (I) coalescence after minor deformation, (II) bouncing, (III) coalescence after substantial deformation, (IV) separation with satellite droplets, and (V) splattering of droplets. As (VI) I add to this list the growth of one droplet and the dissolution of the other through a diffusive mass transport mechanism (*Ostwald ripening*). Coalescence (I-III) is accompanied by convective mass transport, Ostwald ripening (VI) by diffusive mass transport. During coalescence, droplets merge while their positions change; during Ostwald ripening, molecules diffuse through the surrounding phase and one droplet grows at the expense of the disappearing droplet without changing their positions[2]. The behavior of two bubbles can be cast into similar categories. The hydrodynamics of each of these different regimes can be robustly reproduced by computational fluid dynamics[3–8]. However, the common question remains as to the conditions under which first rupture between approaching dispersed phases, and hence the formation of a meniscus phase bridge, occurs[†] (cf. figure 1.1).

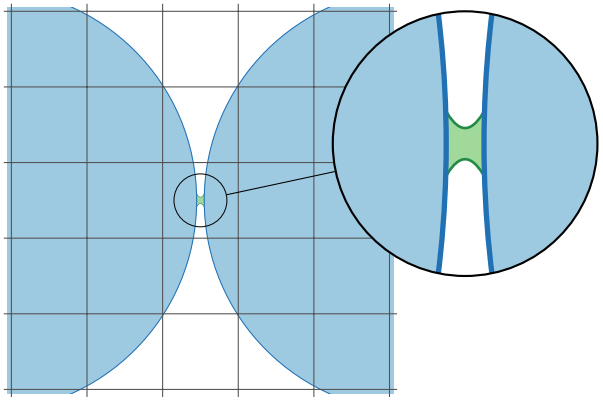

Figure 1.1: Two approaching liquid droplets (in blue) after developing a phase rupture leading to a meniscus phase bridge between the two droplets (indicated in green). A spatial volume-of-fluid grid is depicted in gray.

Mason *et al.*[4] proposed a distance criterion of less than 40 nm for the phase rupture of approaching sharp interfaces for simulations using a volume-of-fluid method in combination

[†] »[...] the reason for the first rupture is not known, so it is unclear if it can be captured by standard continuum models or if additional intermolecular forces [...] must be considered« (Focke *et al.*[5]).

with a subgrid film model. Similar length scales (10–50 nm) were proposed after experimental studies of coalescing droplets on a flat surface by Mackay and Mason[9] and droplet collisions by Bradley *et al.*[10]. Due to different capillary waves for different sized droplets, different criteria were proposed for different droplet sizes[9]. Liu and Bothe[8] suggested applying simulation criteria for volume-of-fluid simulations using piecewise linear interface calculation and a lubrication theory subgrid model for the distinction between droplet coalescence and bouncing: a threshold of liquid in a volume-of-fluid cell or collision of the reconstructed piecewise linear interfaces. Nonetheless they acknowledged that the distinction between coalescence and bouncing remains dependent on the resolution of the spatial discretization. A criterion based on the time required for the vapor film drainage between liquid droplets was used by Mohammadi *et al.*[11] in combination with volume-of-fluid simulations. Each of these different criteria share one common feature in that they must be parameterized in order to reproduce experimental results. Experimental results by Qian and Law[1] suggest that these parameterizations are not transferable to other fluids or other mixtures than those used in the study. They found that the introduction of an ambient vapor consisting of a different component than the liquid droplets affects the coalescence behavior. This conclusion is supported by molecular dynamics results of binary mixtures of different Lennard-Jones fluids by Murad and Law[12], which showed that introducing the second Lennard-Jones component leads to a different coalescence vs. bouncing behavior. The influence of surfactants on the coalescence dynamics of droplets was analyzed by Lu *et al.*[7], though limited to the time after the first phase rupture.

This demonstrates the necessity for predictive thermodynamic models, based on molecular theories, for phase rupture in coalescence processes of droplets and bubbles. These models can then be used to realize predictive hydrodynamic simulations and parameterize coarse-grained coalescence models, inter alia models for population balance equations[13], for large-scale simulations. In doing so, expensive experiments can be greatly reduced or even avoided for a wide variety of diverse applications. These include, among others, bubble or absorption columns[14–17], liquid-liquid extraction, spray breakup[18], bioreactors[19,20], spray painting, internal combustion, cleaning of oil spills, microfluidics, emulsification, and foaming.

1.1 Scope & Outline of This Thesis

The objective of this work is the development of a predictive molecular coalescence model for pure fluids and fluid mixtures employing dynamic density functional theory (DDFT) in combination with the Helmholtz energy functionals based on the perturbed-chain statistical associating fluid theory (PC-SAFT) equation of state. Density functional theory (DFT) in

conjunction with PC-SAFT Helmholtz energy functionals shows excellent predictive capabilities for inhomogeneous fluid systems in thermodynamic equilibrium, like vapor-liquid and liquid-liquid equilibria as well as adsorption phenomena on solid surfaces, predicting properties such as interfacial tension[21–24], adsorption isotherms[25], and contact angles of fluids on solid surfaces[26]. It can be expected that the predictive capabilities of DFT in combination with the PC-SAFT Helmholtz energy functionals will persist in DDFT for predicting dynamic phenomena dominated by interfacial processes like droplet or bubble coalescence and Ostwald ripening.

Such a model also provides insight into microscopic processes, the influence of additional (possibly surface active) components, and thermodynamic driving forces at interfaces leading to coalescence or Ostwald ripening, in particular the first rupture between approaching droplets or bubbles resulting in a meniscus phase bridge during coalescence. The findings obtained within this work are intended to help numerical approaches to resolve droplet or bubble coalescence in multiphase flow by enabling the development of predictive coalescence criteria for hydrodynamic simulations of pure fluids and fluid mixtures, possibly even including surfactants, for a wide range of ambient temperatures, pressures, and mixture compositions.

Chapter 2 introduces DFT for equilibrium systems and summarizes the Helmholtz energy functionals based on the PC-SAFT equation of state (which are subsequently applied to DDFT). The theoretical background of DDFT models are presented as well as models for the viscosity and diffusion coefficients required in DDFT, i.e., entropy scaling.

In chapter 3, a method for the efficient computation of the Helmholtz energy functionals in Cartesian, cylindrical, and spherical coordinate systems is presented, which is indispensable for successful practical DDFT simulations.

Chapter 4 extends the numerical procedure for the efficient computation of Helmholtz energy functionals to simplify and accelerate (D)DFT computations in cylindrical coordinates.

A DDFT model for mixtures is proposed in chapter 5. The proposed modeling framework extends a DDFT model for pure fluids to mixtures. The resulting balance equations are shown to globally satisfy the first and second law of thermodynamics. It should be noted that the balance equations for DDFT cannot be formulated in conservative form, which requires the application of a suitable well-balanced finite-volume scheme for the numerical solution. The Helmholtz energy functionals based on the PC-SAFT equation of state are used within the proposed DDFT formalism. Results for coalescence of droplets or bubbles in one dimension are presented for pure liquids and binary mixtures. The derived DDFT model is not limited to transport phenomena in fluid systems, but is capable of describing fluid-solid interactions with possible application to coalescence of droplets or bubbles on solid surfaces, prediction of

dynamic contact angles and flow through confined geometries. This includes the possibility of the analysis of inhomogeneities in the solid structure for such phenomena or time-dependent external potentials.

References

[1] J. Qian and C. K. Law. Regimes of coalescence and separation in droplet collision. *Journal of Fluid Mechanics*, **331**:59–80, 1997. doi:10.1017/S0022112096003722.

[2] A. Pototsky, U. Thiele, and A. J. Archer. Coarsening modes of clusters of aggregating particles. *Physical Review E*, **89**:032144, 2014. doi:10.1103/PhysRevE.89.032144.

[3] F. Blanchette and T. P. Bigioni. Dynamics of drop coalescence at fluid interfaces. *Journal of Fluid Mechanics*, **620**:333–352, 2009. doi:10.1017/S0022112008004801.

[4] L. Mason, G. Stevens, and D. Harvie. Multiscale volume of fluid modelling of droplet coalescence. In C. Solnordal, P. Liovic, G. Delaney, and P. Witt (editors), *Ninth International Conference on Computational Fluid Dynamics in the Minerals and Process Industries*, pages 1–6. Melbourne, 2012.

[5] C. Focke, M. Kuschel, M. Sommerfeld, and D. Bothe. Collision between high and low viscosity droplets: Direct Numerical Simulations and experiments. *International Journal of Multiphase Flow*, **56**:81–92, 2013. doi:10.1016/j.ijmultiphaseflow.2013.05.008.

[6] C. Planchette, H. Hinterbichler, M. Liu, D. Bothe, and G. Brenn. Colliding drops as coalescing and fragmenting liquid springs. *Journal of Fluid Mechanics*, **814**:277–300, 2017. doi:10.1017/jfm.2016.852.

[7] J. Lu, C. M. Corvalan, Y. J. Chew, and J.-Y. Huang. Coalescence of small bubbles with surfactants. *Chemical Engineering Science*, **196**:493–500, 2019. doi:10.1016/j.ces.2018.11.002.

[8] M. Liu and D. Bothe. Toward the predictive simulation of bouncing versus coalescence in binary droplet collisions. *Acta Mechanica*, **230**:623–644, 2019. doi:10.1007/s00707-018-2290-4.

[9] G. D. M. Mackay and S. G. Mason. The gravity approach and coalescence of fluid drops at liquid interfaces. *The Canadian Journal of Chemical Engineering*, **41**(5):203–212, 1963. doi:10.1002/cjce.5450410504.

[10] S. Bradley, C. Stow, and E. G. Bowen. Collisions between liquid drops. *Philosophical Transactions of the Royal Society of London. Series A. Mathematical and Physical Sciences*, **287**(1349):635–675, 1978. doi:10.1098/rsta.1978.0001.

[11] M. Mohammadi, S. Shahhosseini, and M. Bayat. Direct numerical simulation of water droplet coalescence in the oil. *International Journal of Heat and Fluid Flow*, **36**:58–71, 2012. doi:10.1016/j.ijheatfluidflow.2012.04.001.

[12] S. Murad and C. K. Law. Molecular simulation of droplet collision in the presence of ambient gas. *Molecular Physics*, **96**(1):81–85, 1999. doi:10.1080/00268979909482940.

[13] Y. Liao and D. Lucas. A literature review on mechanisms and models for the coalescence process of fluid particles. *Chemical Engineering Science*, **65**(10):2851–2864, 2010. doi:10.1016/j.ces.2010.02.020.

[14] E. Camarasa, C. Vial, S. Poncin, G. Wild, N. Midoux, and J. Bouillard. Influence of coalescence behaviour of the liquid and of gas sparging on hydrodynamics and bubble characteristics in a bubble column. *Chemical Engineering and Processing: Process Intensification*, **38**(4):329–344, 1999. doi:10.1016/S0255-2701(99)00024-0.

[15] E. Olmos, C. Gentric, C. Vial, G. Wild, and N. Midoux. Numerical simulation of multiphase flow in bubble column reactors. Influence of bubble coalescence and break-up. *Chemical Engineering Science*, **56**(21):6359–6365, 2001. doi:10.1016/S0009-2509(01)00204-4.

[16] P. Chen, M. P. Duduković, and J. Sanyal. Three-dimensional simulation of bubble column flows with bubble coalescence and breakup. *AIChE Journal*, **51**(3):696–712, 2005. doi:10.1002/aic.10381.

[17] B. Gourich, C. Vial, A. H. Essadki, F. Allam, M. Belhaj Soulami, and M. Ziyad. Identification of flow regimes and transition points in a bubble column through analysis of differential pressure signal-Influence of the coalescence behavior of the liquid phase. *Chemical Engineering and Processing: Process Intensification*, **45**(3):214–223, 2006. doi:10.1016/j.cep.2005.09.002.

[18] D. Loureiro, J. Reutzsch, A. Kronenburg, B. Weigand, and K. Vogiatzaki. Primary breakup regimes for cryogenic flash atomization. *International Journal of Multiphase Flow*, **132**:103405, 2020. doi:10.1016/j.ijmultiphaseflow.2020.103405.

[19] M. Laakkonen, V. Alopaeus, and J. Aittamaa. Validation of bubble breakage, coalescence and mass transfer models for gas-liquid dispersion in agitated vessel. *Chemical Engineering Science*, **61**(1):218–228, 2006. doi:10.1016/j.ces.2004.11.066.

[20] M. Kuschel and R. Takors. Simulated oxygen and glucose gradients as a prerequisite for predicting industrial scale performance a priori. *Biotechnology and Bioengineering*, **117**(9):2760–2770, 2020. doi:10.1002/bit.27457.

[21] J. Gross. A density functional theory for vapor-liquid interfaces using the PCP-SAFT equation of state. *The Journal of Chemical Physics*, **131**(20):204705, 2009. doi:10.1063/1.3263124.

[22] C. Klink and J. Gross. A Density Functional Theory for Vapor–Liquid Interfaces of Mixtures Using the Perturbed-Chain Polar Statistical Associating Fluid Theory Equation of State. *Industrial & Engineering Chemistry Research*, **53**(14):6169–6178, 2014. doi:10.1021/ie4029895.

[23] C. Klink, B. Planková, and J. Gross. Density Functional Theory for Liquid–Liquid Interfaces of Mixtures Using the Perturbed-Chain Polar Statistical Associating Fluid Theory Equation of State. *Industrial & Engineering Chemistry Research*, **54**(16):4633–4642, 2015. doi:10.1021/acs.iecr.5b00445.

[24] E. Sauer and J. Gross. Classical Density Functional Theory for Liquid–Fluid Interfaces and Confined Systems: A Functional for the Perturbed-Chain Polar Statistical Associating Fluid Theory Equation of State. *Industrial & Engineering Chemistry Research*, **56**(14):4119–4135, 2017. doi:10.1021/acs.iecr.6b04551.

[25] E. Sauer and J. Gross. Prediction of Adsorption Isotherms and Selectivities: Comparison between Classical Density Functional Theory Based on the Perturbed-Chain Statistical Associating Fluid Theory Equation of State and Ideal Adsorbed Solution Theory. *Langmuir*, **35**(36):11690–11701, 2019. doi:10.1021/acs.langmuir.9b02378.

[26] E. Sauer, A. Terzis, M. Theiss, B. Weigand, and J. Gross. Prediction of Contact Angles and Density Profiles of Sessile Droplets Using Classical Density Functional Theory Based on the PCP-SAFT Equation of State. *Langmuir*, **34**(42):12519–12531, 2018. doi:10.1021/acs.langmuir.8b01985.

2 Modeling of Equilibrium Properties and the Dynamics of Inhomogeneous Fluids

This chapter introduces the fundamentals of classical density functional theory (DFT) along with the Helmholtz energy functionals based on the perturbed-chain statistical associating fluid theory (PC-SAFT) equation of state. I then proceed to review dynamic density functional theory (DDFT). With a suitable Helmholtz energy functional, DDFT has predictive power for interfacial tensions and local enrichment or depletion of species, including adsorptive processes. Dynamic transport coefficients, such as shear viscosity or diffusion coefficients, however, need to be provided into the model. I give a brief introduction to models based on entropy scaling for determining such transport coefficients using the Helmholtz energy model of PC-SAFT.

2.1 Thermodynamic Modeling of Static Interfacial Properties

Classical DFT in combination with molecular models for inhomogeneous fluids is a powerful tool for studying and predicting thermodynamic systems in which the influence of interfaces on the thermodynamic potentials is not negligible and thermodynamic equilibrium is determined by competing contributions from bulk and interfacial effects.

2.1.1 Classical Density Functional Theory

Classical DFT describes averages of thermodynamic properties in the grand canonical ensemble with natural variables temperature T, volume V, and the chemical potentials μ_i of the various components i. Their conjugate variables entropy S, pressure p, and number of molecules N_i, are functions of these natural variables. Since only ensemble averages are described by DFT, individual microstates of the system need not be considered[†]. DFT connects the density profiles $\rho_i(\mathbf{r})$ (with spatial and potentially orientation and conformation coordinates $\mathbf{r}$) to the external potentials $V_i^{\text{ext}}(\mathbf{r})$. For fluid systems Evans[1] demonstrated that for given chemical potentials, the external potentials result uniquely from the equilibrium density profiles

[†]Or, depending on interpretation, *cannot be considered*.

$\rho_i^0(\mathbf{r})$. The reverse conclusion also applies, except for, e.g., phase equilibria where multiple equilibrium density profiles can exist for the same external potential. The equilibrium density profiles are defined by

$$\rho_i^0(\mathbf{r}) = \left\langle \sum_{j=1}^{N_i} \delta_i(\mathbf{r}-\mathbf{r}_j) \right\rangle_{\Xi} \tag{2.1}$$

where $\delta_i(\mathbf{r}-\mathbf{r}_j)$ describes the probability density of finding the j-th molecule out of N_i molecules of component i with coordinate $\mathbf{r}_j$ at coordinate $\mathbf{r}$, and the angle brackets $\langle\ldots\rangle_{\Xi}$ denote the grand canonical ensemble average. The probability density δ is merely a Dirac delta function.

DFT is based on the grand potential density functional Ω depending on the density profiles, the temperature and the chemical potentials of all components, which is defined for a mixture of N_c components as

$$\Omega([\{\rho_i(\mathbf{r})\}]; T, \{\mu_i\}) = \mathcal{F}([\{\rho_i(\mathbf{r})\}]; T) - \sum_{i=1}^{N_\mathrm{c}} \mu_i \int \rho_i(\mathbf{r})\,\mathrm{d}\mathbf{r} \tag{2.2}$$

with the total Helmholtz energy functional $\mathcal{F}$. The explicit dependence of the thermodynamic potentials on T and μ_i is omitted from here on for the sake of clarity. Square brackets '[…]' denote a functional dependence and curly brackets '{…}' indicate a vector of all components within a mixture with $i = 1,\ldots,N_\mathrm{c}$. The grand potential functional follows two theorems by Hohenberg and Kohn [2] and Mermin [3] originally developed for electron densities and later adapted by Evans [1] for fluid systems. First, the insertion of the *equilibrium density profiles* $\rho_i^0(\mathbf{r})$ into the grand potential functional yields the grand potential

$$\Omega^0 = \Omega[\{\rho_i^0(\mathbf{r})\}] \tag{2.3}$$

Second, the grand potential functional obeys a variational principle, such that the grand potential Ω^0 is the minimum of the grand potential functional

$$\Omega[\{\rho_i(\mathbf{r})\}] \geq \Omega[\{\rho_i^0(\mathbf{r})\}] = \Omega^0 \tag{2.4}$$

i.e., the grand potential functional for density profiles out of equilibrium is larger than the grand potential. A key result of the work of Evans [1] is that the total Helmholtz energy functional $\mathcal{F}$ can be uniquely separated into the intrinsic Helmholtz energy functional* F, dependent solely on the density profiles (the internal structure) and a contribution from

*From this point on referred to simply as the *Helmholtz energy functional*.

external potentials according to

$$\mathcal{F}[\{\rho_i(\mathbf{r})\}] = F[\{\rho_i(\mathbf{r})\}] + \sum_{i=1}^{N_c} \int \rho_i(\mathbf{r}) V_i^{\text{ext}}(\mathbf{r})\, \mathrm{d}\mathbf{r} \tag{2.5}$$

In particular, the Helmholtz energy functional F is a unique functional of the density profiles $\rho_i(\mathbf{r})$ (with the previously mentioned exception for phase equilibria) and is valid for all external potentials $V_i^{\text{ext}}(\mathbf{r})$, which forms the foundation of DFT. It is beneficial to split the Helmholtz energy functional into an ideal gas and a residual contribution, defined by $F \equiv F^{\text{ig}} + F^{\text{res}}$, since the structure of the the ideal gas contribution is known exactly as

$$\beta F^{\text{ig}}[\{\rho_i(\mathbf{r})\}] = \sum_{i=1}^{N_c} \int \rho_i(\mathbf{r}) \Big(\ln\big(\rho_i(\mathbf{r})\Lambda_i^3\big) - 1 \Big)\, \mathrm{d}\mathbf{r} \tag{2.6}$$

with the inverse thermodynamic temperature $\beta \equiv \frac{1}{k_B T}$, Boltzmann constant k_B, and de Broglie wavelengths Λ_i, containing all kinetic and internal degrees of freedom of the molecules of the considered components i. Combination of eqs. (2.2), (2.5), and (2.6) leads to the formally exact description of the grand potential functional

$$\beta\Omega[\{\rho_i(\mathbf{r})\}] = \sum_{i=1}^{N_c} \int \left(\rho_i(\mathbf{r}) \Big(\ln\big(\rho_i(\mathbf{r})\Lambda_i^3\big) - 1 \Big) + \rho_i(\mathbf{r}) \Big(\beta V_i^{\text{ext}}(\mathbf{r}) - \beta\mu_i \Big) \right) \mathrm{d}\mathbf{r} + \beta F^{\text{res}}[\{\rho_i(\mathbf{r})\}] \tag{2.7}$$

In general, the structure of the residual Helmholtz energy functional F^{res} (and thus, by extension, the structure of the grand potential functional Ω) is not known exactly and approximations must almost always be used*. The de Broglie wavelengths Λ_i can be eliminated from eq. (2.7) by also splitting the chemical potentials into ideal gas and residual contributions according to $\mu_i \equiv \mu_i^{\text{ig}} + \mu_i^{\text{res}}$, with the formally exact† chemical potentials for an ideal gas $\beta\mu_i^{\text{ig}}(\mathbf{r}_0) = \ln\big(\rho_i(\mathbf{r}_0)\Lambda_i^3\big)$ for any position $\mathbf{r}_0$. Note that $\mu_i^{\text{res}}(\mathbf{r}_0)$ will also depend on the choice of $\mathbf{r}_0$. Because $\mathbf{r}_0$ can even be a hypothetical position, one can always choose a bulk density $\rho_i^{\text{bulk}} \equiv \rho_i(\mathbf{r}_0)$ and the chemical potential will accordingly be $\mu_i^{\text{res,bulk}} \equiv \mu_i^{\text{res}}(\mathbf{r}_0)$, resulting in

$$\beta\Omega[\{\rho_i(\mathbf{r})\}] = \sum_{i=1}^{N_c} \int \left(\rho_i(\mathbf{r}) \left(\ln\left(\frac{\rho_i(\mathbf{r})}{\rho_i^{\text{bulk}}} \right) - 1 \right) + \rho_i(\mathbf{r}) \Big(\beta V_i^{\text{ext}}(\mathbf{r}) - \beta\mu_i^{\text{res,bulk}} \Big) \right) \mathrm{d}\mathbf{r} + \beta F^{\text{res}}[\{\rho_i(\mathbf{r})\}]$$

*With a few exceptions, e.g., the hard-rod system.

†The structure of the Helmholtz energy (functional) of an ideal gas is exact, while the de Broglie wavelengths may be not known exactly. Therefore, the exact value of the Helmholtz energy cannot be determined. Since the de Broglie wavelengths are solely functions of temperature, they can be eliminated everywhere for the isothermal conditions considered in this work.

(2.8)

To find the equilibrium density profiles $\rho_i^0(\mathbf{r})$ for a given grand potential density functional the variational principle from eq. (2.4) is exploited by applying the Euler-Lagrange equation to each component, defined by

$$\left.\frac{\delta\Omega[\{\rho_i\}]}{\delta\rho_j(\mathbf{r})}\right|_{\{\rho_i^0(\mathbf{r})\}} = 0 \qquad \forall j \tag{2.9}$$

For the grand potential density functional from eqs. (2.2) and (2.5), the Euler-Lagrange equations read

$$\left.\frac{\delta F[\{\rho_i\}]}{\delta\rho_j(\mathbf{r})}\right|_{\{\rho_i^0(\mathbf{r})\}} = \left.\left(\frac{\delta F^{\mathrm{ig}}[\{\rho_i\}]}{\delta\rho_j(\mathbf{r})} + \frac{\delta F^{\mathrm{res}}[\{\rho_i\}]}{\delta\rho_j(\mathbf{r})}\right)\right|_{\{\rho_i^0(\mathbf{r})\}} = \mu_j - V_j^{\mathrm{ext}}(\mathbf{r}) \qquad \forall j \tag{2.10}$$

or using eq. (2.8)

$$\rho_j^0(\mathbf{r}) = \rho_j^{\mathrm{bulk}} \exp\left(\beta\mu_j^{\mathrm{res,bulk}} - \beta V_j^{\mathrm{ext}}(\mathbf{r}) - \frac{\delta\beta F^{\mathrm{res}}[\{\rho_i^0\}]}{\delta\rho_j(\mathbf{r})}\right) \qquad \forall j \tag{2.11}$$

Equation (2.11) can be solved for the density profiles $\rho_i^0(\mathbf{r})$ for a given residual Helmholtz energy functional. Solutions may be found by means of simple algorithms, like Picard iteration or Anderson mixing[4], or by more sophisticated methods for nonlinear systems[5–10].

The residual Helmholtz energy functional contains all the information from intermolecular interactions which can be deduced from the Yvon-Born-Green (YBG) hierarchy[1,11–13] for mixtures[14], defined by

$$-\rho_j^0(\mathbf{r}_1)\nabla c_j^{(1)}(\mathbf{r}_1,[\{\rho_i^0\}]) = -\nabla\rho_j^0(\mathbf{r}_1) - \rho_j^0(\mathbf{r}_1)\nabla\beta V_j^{\mathrm{ext}}(\mathbf{r}_1) \tag{2.12a}$$

$$\begin{aligned} &= \sum_{k=1}^{N_c}\int \rho_{jk}^{(2),0}(\mathbf{r}_1,\mathbf{r}_2,[\{\rho_i\}])\nabla_{\mathbf{r}_1}\beta\phi_{jk}^{(2)}(\mathbf{r}_1,\mathbf{r}_2)\,\mathrm{d}\mathbf{r}_2 \\ &\quad + \sum_{k=1}^{N_c}\sum_{l=1}^{N_c}\iint \rho_{jkl}^{(3),0}(\mathbf{r}_1,\mathbf{r}_2,\mathbf{r}_3,[\{\rho_i\}])\nabla_{\mathbf{r}_1}\beta\phi_{jkl}^{(3)}(\mathbf{r}_1,\mathbf{r}_2,\mathbf{r}_3)\,\mathrm{d}\mathbf{r}_2\,\mathrm{d}\mathbf{r}_3 \\ &\quad + \ldots \end{aligned} \tag{2.12b}$$

with the two-body densities $\rho_{jk}^{(2),0}$ of components j and k, the three-body densities $\rho_{jkl}^{(3),0}$ of components j, k and l, as well as the the two- and three-body intermolecular potentials $\phi_{jk}^{(2)}$ and $\phi_{jkl}^{(3)}$ (there may also be higher multi-body contributions, which are indicated by '+ ...'),

in combination with the one-particle direct correlation function of component j, defined by[15]

$$c_j^{(1)}(\mathbf{r}, [\{\rho_i^0\}]) \equiv -\frac{\delta \beta F^{\text{res}}[\{\rho_i^0\}]}{\delta \rho_j(\mathbf{r})} \tag{2.13}$$

The YBG hierarchy, eq. (2.12), and the definition of the one-particle direct correlation function from eq. (2.13) are essential during the derivation of DDFT, as will be discussed in section 2.2.

2.1.2 Modeling Inhomogeneous Fluids Based on the PC-SAFT Equation of State

The Helmholtz energy functionals used in this work are inhomogeneous generalizations of the widely used PC-SAFT equation of state[16–21]. SAFT models[22–34], first proposed by Chapman *et al.*[22–24], are based on Wertheim's thermodynamic perturbation theory[35–38] for tangent hard chains. The PC-SAFT equation of state provides a good description of thermodynamic properties in bulk phases for a wide variety of pure components and mixtures. The robust behavior and predictive capabilities are preserved when generalized to inhomogeneous fluids by DFT[39–45]. The model parameters of the PC-SAFT equation of state allow a physical interpretation due to the strong background in statistical mechanics.

2.1.2.1 The PC-SAFT Equation of State

The PC-SAFT equation of state accounts for various interactions of real molecular fluids as additive contributions to the Helmholtz energy

$$\tilde{a} = \tilde{a}^{\text{ig}} + \tilde{a}^{\text{hs}} + \tilde{a}^{\text{hc}} + \tilde{a}^{\text{disp}} + \tilde{a}^{\text{polar}} + \tilde{a}^{\text{assoc}} \tag{2.14}$$

with the reduced Helmholtz energy $\tilde{a} \equiv \frac{A}{N k_{\text{B}} T}$* using the Helmholtz energy A and the total number of molecules N. The different contributions to the Helmholtz energy are depicted in figure 2.1: the ideal gas contribution† as well as contributions for hard-sphere, hard-chain, dispersion, multipolar, and association interactions.

Among all contributions to the Helmholtz energy, only the structure of the ideal gas contribution is explicitly known. The hard-sphere contribution is taken to be the Helmholtz energy of the Boublík-Mansoori-Carnahan-Starling-Leland[46,47] equation of state. The hard spheres

*In the bulk equation of state I use the symbol A for the Helmholtz energy to distinguish it from Helmholtz energy functionals F used in DFT.

†The ideal gas contribution contains all the kinetic and internal contributions of the molecular system to the canonical partition function. This is due to the assumption that intermolecular interactions are independent of the velocity of the individual molecules. To obtain additive contributions to the Helmholtz energy the intermolecular forces are assumed to be additive as well. This assumption is often an approximation.

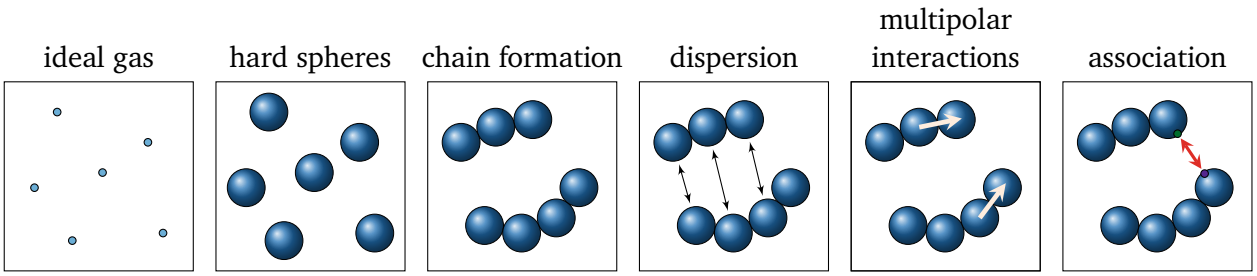

Figure 2.1: Schematic representation of the molecular model and the intermolecular interactions of the different contributions to the Helmholtz energy modeled with the PC-SAFT equation of state, cf. eq. (2.14).

are bounded to tangent hard chains[22–24] using Wertheim's thermodynamic perturbation theory (TPT1)[35–38]. The resulting hard-chain fluid is used as the reference fluid for a second order Barker-Henderson[48,49] perturbation theory to model dispersion interactions[16]. Using the hard chain as the reference fluid not only gives the PC-SAFT equation of state its name, but often improves the accuracy of the description of thermodynamic properties compared to the original SAFT equation of state.

Molecules described by the first four contributions in eq. (2.14) can be parameterized with three pure component parameters for component i: a parameter for the segment diameter σ_i, another for the number of segments in a chain m_i, and finally one for the strength of the dispersion interactions ε_i. Multipolar interactions are considered either as dipole-dipole[19], quadrupole-quadrupole[20] and dipole-quadrupole[21] interactions. These multipolar contributions are based on a third order perturbation theory with a two-centered Lennard-Jones reference fluid parameterized through the dipolar and quadrupolar moments $\breve{\mu}_i$ and Q_i, respectively. Hydrogen bonds between molecules can be considered as association contributions[18] which are modeled with TPT1[24,26] and parameterized by the interaction strengths $\varepsilon^{A_iB_j}$ and the association volumes $\kappa^{A_iB_j}$ of the interaction sites A_i and B_j.

2.1.2.2 Helmholtz Energy Functionals Based on the PC-SAFT Equation of State

The molecular model of the PC-SAFT equation of state can also be applied to inhomogeneous fluids. The individual contributions to the Helmholtz energy functional can be separated in analogy to eq. (2.14). The ideal gas contribution is given in eq. (2.6). As demonstrated in section 2.1.1, it is often advantageous to split the Helmholtz energy functional into ideal gas and residual contributions as $F \equiv F^{\mathrm{ig}} + F^{\mathrm{res}}$, with the residual contributions of the PC-SAFT functionals

$$F^{\mathrm{res}}[\{\rho_i(\mathbf{r})\}] = F^{\mathrm{hs}}[\{\rho_i(\mathbf{r})\}] + F^{\mathrm{hc}}[\{\rho_i(\mathbf{r})\}] + F^{\mathrm{disp}}[\{\rho_i(\mathbf{r})\}] + F^{\mathrm{polar}}[\{\rho_i(\mathbf{r})\}] + F^{\mathrm{assoc}}[\{\rho_i(\mathbf{r})\}]$$

(2.15)

All contributions are formulated as weighted density approximations with a similar structure. The hard-sphere contribution is modeled using the fundamental measure theory (FMT) initially introduced by Rosenfeld[50] using scaled particle theory[51,52]. For homogeneous bulk phases this functional simplifies to the Percus-Yevick equation of state for hard spheres[53–55]. Extensions to obtain the more accurate Boublík-Mansoori-Carnahan-Starling-Leland[46,47] equation of state used within the PC-SAFT model for the homogeneous case were developed independently by Roth *et al.*[56] and Yu and Wu[57]. A version corresponding to an even more accurate hard-sphere equation of state[58] also exists[15,59]. All of these different variants share a common structure with the dimensionless Helmholtz energy functional

$$\beta F^{\mathrm{hs}}[\{\rho_i\}] = \int \Phi^{\mathrm{FMT}}(\{n_\alpha(\mathbf{r})\})\,\mathrm{d}\mathbf{r} \tag{2.16}$$

formulated as an integral over the dimensionless Helmholtz energy density Φ^{FMT}, which is a function of four scalar-valued and two vector-valued weighted densities n_α with $\alpha \in \{0,1,2,3,\mathrm{V1},\mathrm{V2}\}$. The weighted densities are functionals of the density profiles and are defined as convolution integrals

$$n_\alpha(\mathbf{r}) = \sum_{i=1}^{N_\mathrm{c}} m_i \int \rho_i(\mathbf{r}')\omega_i^\alpha(\mathbf{r}-\mathbf{r}')\,\mathrm{d}\mathbf{r}' \tag{2.17}$$

with the density profiles ρ_i and weight functions ω_i^α. The number of hard-sphere segments in a hard chain m_i is already incorporated here to account for chain molecules. The weight functions are

$$\omega_i^0(\mathbf{r}) = \frac{1}{4\pi R_i^2}\delta(R_i - |\mathbf{r}|) \tag{2.18a}$$

$$\omega_i^1(\mathbf{r}) = \frac{1}{4\pi R_i}\delta(R_i - |\mathbf{r}|) \tag{2.18b}$$

$$\omega_i^2(\mathbf{r}) = \delta(R_i - |\mathbf{r}|) \tag{2.18c}$$

$$\omega_i^3(\mathbf{r}) = \Theta(R_i - |\mathbf{r}|) \tag{2.18d}$$

$$\omega_i^{\mathrm{V1}}(\mathbf{r}) = \frac{1}{4\pi R_i}\frac{\mathbf{r}}{|\mathbf{r}|}\delta(R_i - |\mathbf{r}|) \tag{2.18e}$$

$$\omega_i^{\mathrm{V2}}(\mathbf{r}) = \frac{\mathbf{r}}{|\mathbf{r}|}\delta(R_i - |\mathbf{r}|) \tag{2.18f}$$

with the hard-sphere radii R_i, the Dirac delta function δ, the Heaviside step function Θ, and spatial coordinate vector $\mathbf{r}$. This allows for an interpretation of their respective weighted

densities as averages calculated over the surface, the volume, and the direction of the outward normal on the surface of a sphere*. A FMT without using vectorial, and hence different weight functions, was proposed by Kierlik and Rosinberg [60,61]. This concept was extended to attractive interactions by Bernet *et al.* [62].

The hard-chain contribution was developed by Tripathi and Chapman [63,64] derived from an inhomogeneous formulation of the TPT1 association contribution in the limit of complete association and reads

$$\begin{aligned}\beta F^{\mathrm{hc}}[\{\rho_i(\mathbf{r})\}] = &\sum_{i=1}^{N_\mathrm{c}}(m_i-1)\int \rho_i(\mathbf{r})\Big(\ln\big(\rho_i(\mathbf{r})\Lambda_i^3\big)-1\Big)\,\mathrm{d}\mathbf{r}\\ &-\sum_{i=1}^{N_\mathrm{c}}(m_i-1)\int \rho_i(\mathbf{r})\Big(\ln\Big(y_{ii}^{dd}\big(\{\bar\rho_i^{\mathrm{hc}}(\mathbf{r})\}\big)\lambda_i^{\mathrm{hc}}(\mathbf{r})\Big)-1\Big)\,\mathrm{d}\mathbf{r}\\ &+m_i\ln\Big(\Lambda_{\mathrm{s},i}^3\Big)\sum_{i=1}^{N_\mathrm{c}}\int \rho_i(\mathbf{r})\,\mathrm{d}\mathbf{r}\end{aligned} \tag{2.19}$$

with the two weighted densities $\bar\rho_i^{\mathrm{hc}}$ and λ_i^{hc}, as well as the hard-sphere cavity correlation functions at contact distance [63,65] y_{ii}^{dd} based on the Boublík-Mansoori-Carnahan-Starling-Leland theory, evaluated from

$$y_{ii}^{dd}(\{\bar\rho_i(\mathbf{r})\}) = \frac{1}{1-\bar\zeta_3(\mathbf{r})} + \frac{1.5\,d_i\bar\zeta_2(\mathbf{r})}{(1-\bar\zeta_3(\mathbf{r}))^2} + \frac{0.5\,(d_i\bar\zeta_2(\mathbf{r}))^2}{(1-\bar\zeta_3(\mathbf{r}))^3} \tag{2.20}$$

with

$$\bar\zeta_2(\mathbf{r}) = \frac{\pi}{6}\sum_{i=1}^{N_\mathrm{c}}\bar\rho_i^{\mathrm{hc}}(\mathbf{r})m_i d_i^2 \tag{2.21a}$$

$$\bar\zeta_3(\mathbf{r}) = \frac{\pi}{6}\sum_{i=1}^{N_\mathrm{c}}\bar\rho_i^{\mathrm{hc}}(\mathbf{r})m_i d_i^3 \tag{2.21b}$$

using the hard-sphere diameters $d_i = 2R_i$. The cavity correlation function can be interpreted as a radial distribution function $g(r)$ in which the interaction potential between the reference particle and the particle at distance r is deactivated while all other interaction potentials are active†. The hard-chain contribution has been, according to Wertheim's theory [35–38,66], developed for an ideal gas reference of unbound segments. Since the PC-SAFT equation of

*Integration over the scalar-valued weight functions, $\int \omega_i^\alpha(\mathbf{r})\,\mathrm{d}\mathbf{r}$, yields the *fundamental* geometrical *measures* of a sphere in three dimensions giving FMT its name: the Euler characteristic ($\alpha=0$), the radius ($\alpha=1$), the surface area ($\alpha=2$), and the volume ($\alpha=3$). The integrals over the vector-valued weight functions ($\alpha\in\{\mathrm{V1},\mathrm{V2}\}$) vanish.

†In this case, both particles are hard spheres, and the cavity correlation function is equal to the radial distribution function for distances larger than the hard-sphere diameter.

state takes the ideal gas contribution of entire chain molecules as a reference, the ideal gas contribution of additional $(m_i - 1)$ segments needs to be accounted for in the first term. The last term contains the de Broglie wavelengths $\Lambda_{s,i}$ of unbound segments, which are irrelevant for the isothermal applications considered here[67]. The two weighted densities required for the hard-chain contribution are

$$\bar{\rho}_i^{\mathrm{hc}}(\mathbf{r}) = \int \rho_i(\mathbf{r}')\omega_i^{\mathrm{hc},\rho}(\mathbf{r}-\mathbf{r}')\,\mathrm{d}\mathbf{r}' \qquad \text{with} \qquad \omega_i^{\mathrm{hc},\rho}(\mathbf{r}) = \tfrac{3}{4\pi d_i^3}\Theta(d_i - |\mathbf{r}|) \tag{2.22a}$$

$$\lambda_i^{\mathrm{hc}}(\mathbf{r}) = \int \rho_i(\mathbf{r}')\omega_i^{\mathrm{hc},\lambda}(\mathbf{r}-\mathbf{r}')\,\mathrm{d}\mathbf{r}' \qquad \text{with} \qquad \omega_i^{\mathrm{hc},\lambda}(\mathbf{r}) = \tfrac{1}{4\pi d_i^2}\delta(d_i - |\mathbf{r}|) \tag{2.22b}$$

with the average densities at contact-distance λ_i around a segment of chain i. Considering a hard-chain reference puts all orientational and conformational degrees of freedom into the de Broglie wavelengths Λ_i of the ideal gas contribution. A further improvement considering density profiles of individual segments was developed by Jain *et al.* [68] and already applied in combination with PC-SAFT functionals[69].

The dispersion contribution to the PC-SAFT equation of state was derived from a second order Barker-Henderson[49] perturbation theory using a hard-chain reference fluid[70] with temperature-dependent hard-sphere segment diameters $d_i(T)$. In this work, the dispersion contribution is modeled as a weighted density approximation[13,71]

$$\beta F^{\mathrm{disp}}[\{\rho_i(\mathbf{r})\}] = \int \beta f^{\mathrm{disp}}(\{\bar{\rho}_i^{\mathrm{disp}}(\mathbf{r})\})\,\mathrm{d}\mathbf{r} \qquad \text{with} \qquad \bar{\rho}_i^{\mathrm{disp}} = \int \rho_i(\mathbf{r}')\omega_i^{\mathrm{disp}}(\mathbf{r}-\mathbf{r}')\,\mathrm{d}\mathbf{r}' \tag{2.23}$$

based on the Helmholtz energy density f^{disp} and the weighted densities $\bar{\rho}_i^{\mathrm{disp}}$ with weight functions ω_i^{disp} for the dispersion contribution. The applied dispersion Helmholtz energy functional contribution was developed by Sauer and Gross[67], based on preceding work by Ye *et al.* [72] and Shen *et al.* [73–75]. Their work is based on the bulk equation of state (with parameters m_i, σ_i, and ε_i) by approximating the dimensionless Helmholtz energy density as[76,77] $\beta f^{\mathrm{disp}}(\{\bar{\rho}_i^{\mathrm{disp}}\}) \approx \bar{\rho}^{\mathrm{disp}}\tilde{a}^{\mathrm{disp}}(\{\bar{\rho}_i^{\mathrm{disp}}\})$, with the reduced Helmholtz energy $\tilde{a}^{\mathrm{disp}}$ of the dispersion contribution (cf. eq. (2.14)). The weighted density approximation now reads

$$\beta F^{\mathrm{disp}}[\{\rho_i(\mathbf{r})\}] = \int \bar{\rho}^{\mathrm{disp}}(\mathbf{r})\tilde{a}^{\mathrm{disp}}(\{\bar{\rho}_i^{\mathrm{disp}}(\mathbf{r})\})\,\mathrm{d}\mathbf{r} \tag{2.24}$$

with the weighted densities for the dispersion contribution defined by

$$\bar{\rho}_i^{\mathrm{disp}}(\mathbf{r}) = \int \rho_i(\mathbf{r}')\omega_i^{\mathrm{disp}}(\mathbf{r}-\mathbf{r}')\,\mathrm{d}\mathbf{r}' \qquad \text{with} \qquad \omega_i^{\mathrm{disp}}(\mathbf{r}) = \tfrac{3}{4\pi\psi^3 d_i^3}\Theta(\psi d_i - |\mathbf{r}|) \tag{2.25}$$

where $\psi = 1.3862$ is a model constant that defines the size of the sphere in which the density is averaged[67]. This weighted density approach can be applied not only to fluid-fluid but also to fluid-solid interfaces[41,42,67]. This presents a significant advantage over previously developed Helmholtz energy functionals for the dispersion contribution based on the PC-SAFT equation of state[39,40,78] which were derived from an inhomogeneous perturbation approach. By using the bulk formulation of the Helmholtz energy density, the approach in eq. (2.24) recovers the bulk description for homogeneous profiles*.

The multipolar interactions are modeled using the same approach applied to the dispersion interactions in eqs. (2.24) and (2.25), using a weighted density approximation with the same weighted densities and a reduced bulk Helmholtz energy density (incorporating the bulk parameters for the molecular dipoles $\breve{\mu}_i$ and quadrupoles Q_i)†. Due to this simple procedure it is not possible to resolve the orientational structure at inhomogeneities typical for polar components. Helmholtz energy functionals considering orientational degrees of freedom were proposed by Frodl and Dietrich[79–82].

The work of Yu and Wu[83] proposes a perturbation theory for inhomogeneous associating fluids based on Wertheim's thermodynamic perturbation theory[35–38,84,85] with a hard-sphere reference. The contribution to the Helmholtz energy functional is formulated as a weighted density approximation using similar weighted densities as FMT. The functional formulation reads[83]

$$\beta F^{\text{assoc}}[\{\rho_i\}] = \int \sum_{i=1}^{N_c} \frac{n_{0,i}(\mathbf{r})}{m_i} \zeta_i \sum_{\{A_i\}} N_{A_i} \left(\ln\left(\chi^{A_i}(\mathbf{r})\right) - \frac{\chi^{A_i}(\mathbf{r})}{2} + \frac{1}{2} \right) \mathrm{d}\mathbf{r} \tag{2.26}$$

with the different types of association sites A_i of component i, the number of association sites N_{A_i} of type A on component i, the fraction of non-bounded association sites χ^{A_i} of type A_i (which in turn depends on the bulk parameters for the strength of the association interactions $\varepsilon^{A_iB_j}$ and the association volumes $\kappa^{A_iB_j}$; in general χ^{A_i} must be determined iteratively[22,86]), and the FMT-like component-wise weighted densities

$$n_{\alpha,i}(\mathbf{r}) = m_i \int \rho_i(\mathbf{r}') \omega_i^{\alpha}(\mathbf{r} - \mathbf{r}') \, \mathrm{d}\mathbf{r}' \tag{2.27}$$

for $\alpha \in \{0, 2, 3, \mathrm{V2}\}$ and the elementary FMT weight functions from eq. (2.18) with the shorthand $\zeta_i = 1 - \frac{\mathbf{n}_{\mathrm{V2},i} \cdot \mathbf{n}_{\mathrm{V2},i}}{n_{2,i}^2}$. The weighted densities used in FMT are recovered by summation of all components $n_\alpha = \sum_i^{N_c} n_{\alpha,i}$.

*This is not always the case as the simple and popular mean-field approach would not be able to recover the bulk description of PC-SAFT, for example.

†For a complete description of the procedure consult Sauer and Gross[67].

A further formulation for inhomogeneous associating chain fluids was developed by Bymaster and Chapman[87]. Their approach is computationally more involved, requiring more complicated internal iterations for determining the the fraction of non-bounded association sites χ^{A_i}, which is why for a DDFT approach I prefer the approach of Yu and Wu[83], eqs. (2.26) and (2.27).

2.2 Dynamic Density Functional Theory

The dynamic processes in this work are described by DDFT, combining hydrodynamics and microscopic theories of fluids. DDFT can be rigorously derived from the single-particle phase-space distribution function using assumptions for the non-equilibrium fluid structure[88]. This leads to continuum balance equations for density and velocity with the familiar transport coefficients: shear viscosity and Maxwell-Stefan diffusion coefficients, as discussed in the following section 2.3. Density and velocity are the two lowest hydrodynamic moments of the single-particle phase-space distribution function. It is assumed that the consideration of the lowest hydrodynamic moments is sufficient, since the thermodynamic non-equilibrium is not very pronounced in the considered cases within this work. This distinguishes DDFT from similar microscopic non-equilibrium descriptions using the single-particle phase-space distribution functions by truncating or approximating the Bogoliubov-Born-Green-Kirkwood-Yvon[11,12,89–91] (BBGKY) hierarchy*.

The DDFT models considered in this work are deterministic microscopic descriptions of the hydrodynamic variables density (and velocity) using balance equations very similar to the macroscopic isothermal diffusion (or Navier-Stokes) equation. DFT, as portrayed in section 2.1.1, describes equilibrium density profiles as averages of microscopic molecular coordinates in the grand canonical ensemble. In contrast, DDFT describes *non-equilibrium* ensemble averages of density and velocity profiles $\rho_i(\mathbf{r}, t)$ and $\mathbf{v}(\mathbf{r}, t)$, respectively. The time-evolution of these non-equilibrium averages can be understood as ensemble averages of different microscopic systems with different microscopic trajectories (of molecule position and potentially orientation and conformation).

The first to rigorously derive such a model for spherical particles were Marconi and Tarazona[94,95], deriving a DDFT for dense and highly structured systems where hydrodynamic modes become irrelevant and the density profile remains as the only relevant variable. Their

*This leads, for example, to the Boltzmann equation[92,93] and the numerous methods derived from it.

derivation starts from the stochastic equations for Brownian motion

$$\frac{\partial \mathbf{r}_i}{\partial t} = -\Gamma \nabla_{\mathbf{r}_i} \left(\sum_{j=1}^{N} \phi^{(2)}(\mathbf{r}_i - \mathbf{r}_j) + V^{\text{ext}}(\mathbf{r}_i) \right) + \xi_i(t) \tag{2.28}$$

with the particle position $\mathbf{r}_i$ of particle i, the mobility of each particle Γ, the pair and external potential $\phi^{(2)}$ and V^{ext}, respectively, and the stochastic noise vectors ξ_i. Considering solely Brownian dynamics limits the applicability of the resulting model to the description of *relaxational dynamics*, e.g., systems of colloidal Brownian particles in a solvent (heat bath), where the local velocity distribution function is close to Maxwellian and the density profile varies slowly in time (much slower than the velocity profile)[94–96]. By taking the ensemble average of the microscopic particle positions, similar to eq. (2.1), a deterministic equation for the isothermal density profile is obtained. This takes the form of an isothermal diffusion equation, namely

$$\frac{\partial \rho}{\partial t} = \nabla \cdot \left(\rho D^{\text{self}} \nabla \left(\frac{\delta \beta F}{\delta \rho} + \beta V^{\text{ext}} \right) \right) \tag{2.29}$$

with time t, self-diffusion coefficient D^{self} connected to the mobility Γ via the Einstein-Smoluchowski relation $\beta D^{\text{self}} = \Gamma$, the functional derivative of the Helmholtz energy functional $\frac{\delta F}{\delta \rho}$, and the external potential V^{ext}. The gradient of the pair potential in eq. (2.28) of the *non-equilibrium* system is used in conjunction with an artificial *equilibrium* state induced by an additional instantaneous external potential $U^{\text{ad},t}(\mathbf{r})$. This is a hypothetical external potential that would be necessary to obtain the instantaneous density profile in a hypothetical equilibrium state $\rho^{\text{ad},t}(\mathbf{r})$, that is identical to the instantaneous density $\rho(\mathbf{r}, t)$ of the dynamic process. This allows the use of the YBG hierarchy[1,11–13], described in eq. (2.12b), which for an instantaneous equilibrium density profile $\rho^{\text{ad},t}(\mathbf{r})$ at time t interacting only via pair potentials reads

$$-\frac{1}{\beta} \nabla \rho^{\text{ad},t}(\mathbf{r}) - \rho^{\text{ad},t}(\mathbf{r}) \nabla \left(V^{\text{ext}}(\mathbf{r}) + U^{\text{ad},t}(\mathbf{r}) \right) = \int \rho^{(2),\text{ad},t}(\mathbf{r}, \mathbf{r}', [\rho^{\text{ad},t}]) \nabla_{\mathbf{r}} \phi^{(2)}(\mathbf{r}, \mathbf{r}') \, \mathrm{d}\mathbf{r}' \tag{2.30}$$

The assumption of instantaneous equilibrium profiles, in combination with the equilibrium definitions of the one-particle direct correlation function and the functional derivative from eqs. (2.12) and (2.13), leads to the appearance of the functional derivative in eq. (2.29). This assumption implies that correlation functions at any given instant are identical to the correlation functions of the equilibrium system with the same density profile. This is usually referred to as *adiabatic approximation**.

*This term, like many in classical DFT, is borrowed from quantum mechanics, where it refers to a dynamical

In contrast to the stochastic description in eq. (2.28), the deterministic DDFT model can exhibit some shortcomings[94,95]. If the functional derivative of the Helmholtz energy landscape of the non-equilibrium density profile possesses local minima (metastable states), the deterministic equation might get trapped in such a state. The stochastic equation is able to escape said minimum. Also, the DDFT model describes the time evolution of a grand canonical system with constant ensemble average of the particle number $\langle N \rangle_{\Xi}$. The effect of the surrounding particle reservoir leads to a faster relaxation of the system compared to the purely canonical description in eq. (2.28), where these interactions do not occur. This effect is most prominent in small systems[98], noting that averages in the grand canonical and the canonical ensemble become identical in the thermodynamic limit.

Equation (2.29) can be understood as a diffusion equation[99], described by

$$\frac{\partial \rho}{\partial t} = -\nabla \cdot \mathbf{j} \qquad \text{with} \qquad \mathbf{j} = -\rho D^{\text{self}} \nabla \mu \tag{2.31}$$

with particle flux $\mathbf{j}$ using the gradient of the chemical potential μ for the *non-equilibrium* density profile defined by the result of equilibrium DFT, eq. (2.10), while the fluid structure is held in equilibrium by the vanishing instantaneous external potential $U^{\text{ad},t}(\mathbf{r})$. This means that the density profile evolves through equilibrium states of the fluid structure. From linear non-equilibrium thermodynamics[100] (which assumes local thermodynamic equilibrium) it is expected that the particle flux can be described by $\mathbf{j} = -L\nabla\mu$, with the phenomenological Onsager coefficient L. This illustrates what *local thermodynamic equilibrium* (local validity of the Gibbs-equation) means in this case: the fluid structure must be in a state of equilibrium.

While Brownian and Newtonian dynamics give the same result for $t \to \infty$, eq. (2.29) results from the assumption that the system under consideration can be described by Brownian dynamics, reducing the applicability to atomic/molecular fluids where the microscopic dynamics is Newtonian. Newtonian dynamics is accounted for in the derivation of a DDFT model for spherical particles considering inertia by Archer[88], who used Newton's equation of

system that develops so slowly that it can be considered to be in an equilibrium state. A famous example is the Born-Oppenheimer approximation[97]. In classical mechanics it refers to processes that are much slower than the time scale of temperature equilibration, and in classical thermodynamics the equivalent is a quasi-static process.

motion to describe a system of N identical particles via

$$\frac{\partial \mathbf{r}_i}{\partial t} = \frac{\mathbf{p}_i}{\check{m}} \tag{2.32a}$$

$$\frac{\partial \mathbf{p}_i}{\partial t} = -\nabla_{\mathbf{r}_i}\left(\sum_{j=1}^{N}\phi^{(2)}(\mathbf{r}_i,\mathbf{r}_j)+\sum_{j=1}^{N}\sum_{k>j}^{N}\phi^{(3)}(\mathbf{r}_i,\mathbf{r}_j,\mathbf{r}_k)+\ldots+V^{\mathrm{ext}}(\mathbf{r}_i,t)\right)-\gamma\mathbf{p}_i+\boldsymbol{\xi}_i(t) \tag{2.32b}$$

with the linear momentum vectors $\mathbf{p}_i = \check{m}\mathbf{v}_i$ (with mass $\check{m}$ and the velocities $\mathbf{v}_i$) of particle i, the friction coefficient $\gamma = \frac{1}{\check{m}\Gamma}$ which is reciprocally proportional to the mobility of the particle Γ, cf. eq. (2.28), and the stochastic noise vectors $\boldsymbol{\xi}_i$. Two- and three-body interparticle potentials, $\phi^{(2)}$ and $\phi^{(3)}$, are explicitly depicted here while higher multi-body potentials are indicated by '$+\ldots$'. In the limiting case of infinite friction coefficients γ, the Brownian equations of motion for overdamped dynamics (e.g., colloidal particles in a damping solvent), eq. (2.28), can be recovered from eq. (2.32). In the limit $\gamma \to 0$, which also yields $\boldsymbol{\xi}_i \to 0$ because both terms are linked by a fluctuation-dissipation relation, eq. (2.32) simplifies to the (deterministic) Newtonian equation of motion

$$\check{m}\frac{\partial^2 \mathbf{r}_i}{\partial t^2} = -\nabla_{\mathbf{r}_i}\left(\sum_{j=1}^{N}\phi^{(2)}(\mathbf{r}_i,\mathbf{r}_j)+\sum_{j=1}^{N}\sum_{k>j}^{N}\phi^{(3)}(\mathbf{r}_i,\mathbf{r}_j,\mathbf{r}_k)+\ldots+V^{\mathrm{ext}}(\mathbf{r}_i,t)\right) \tag{2.33}$$

which is suitable to describe atomistic/molecular fluids (without a damping solvent) that can be described by the Liouville equation[13].

Based on eq. (2.32), Archer[88] utilized the first equation of the BBGKY hierarchy[11,12,89–91] for the single-particle phase space distribution function $f^{(1)}(\mathbf{r}_1,\mathbf{p}_1,t)$ to obtain a balance equation for density and linear momentum (the first and second hydrodynamic moment of $f^{(1)}$) using a *local equilibrium* Maxwell-Boltzmann approximation for $f^{(1)}$. Instead of truncating the BBGKY hierarchy, for example by the Kirkwood superposition approximation[101], the full YBG hierarchy from eq. (2.12) was used. This is the same approach taken by Marconi and Tarazona[94,95], where the *non-equilibrium* fluid structure is approximated by the correlation structure of the fluid of the same instantaneous density profile $\rho^{\mathrm{ad},t}(\mathbf{r})$ in an artificial *equilibrium* state. This leads to an equation structure similar to the isothermal compressible Navier-Stokes equations[88]

$$\frac{\partial \rho}{\partial t} + \nabla\cdot(\rho\mathbf{v}) = 0 \tag{2.34a}$$

$$\frac{\partial(\check{m}\rho\mathbf{v})}{\partial t} + \nabla\cdot(\check{m}\rho\mathbf{v}\mathbf{v}^{\intercal}) = -\rho\nabla\left(\frac{\delta F}{\delta\rho}+V^{\mathrm{ext}}\right)-\eta\nabla^2\mathbf{v}-\gamma\check{m}\rho\mathbf{v} \tag{2.34b}$$

with the velocity profile $\mathbf{v}$ and shear viscosity η. Archer[88] obtained the viscous contribution to the pressure tensor for an incompressible colloidal fluid by using a Taylor expanded version of the Maxwell-Boltzmann distribution.

Using the same approach for colloidal particles by considering inertia but disregarding the viscous contribution to the pressure tensor, Goddard *et al.*[102] derived a DDFT model for mixtures defined by

$$\frac{\partial \rho_i}{\partial t} + \nabla \cdot (\rho_i \mathbf{v}_i) = 0 \tag{2.35a}$$

$$\frac{\partial (\check{m}_i \rho_i \mathbf{v}_i)}{\partial t} + \nabla \cdot \left(\check{m}_i \rho_i \mathbf{v}_i \mathbf{v}_i^\intercal\right) = -\rho_i \nabla \left(\frac{\delta F}{\delta \rho_i} + V_i^{\text{ext}}\right) - \gamma_i \check{m}_i \rho_i \mathbf{v}_i \tag{2.35b}$$

where each component i is described by its own momentum equation. Although the model also includes hydrodynamic interactions, they are omitted here for an easier comparison with eq. (2.34).

The introduced DDFT models can be extended for colloidal systems in solvents by hydrodynamic interactions[103–107] or fluctuations[108–111]. Fluctuations can be retained in the equations of motion by coarse-graining instead of rigorous ensemble averaging of the phase space variables[112,113]. Both hydrodynamic interactions and fluctuations are disregarded in this work, because the focus is on atomic/molecular fluids. The presented DDFT models, eqs. (2.29), (2.34), and (2.35), are based on the approximation of adiabatic dynamics, making them non-exact in contrast to their equilibrium counterpart. This approximation can be relaxed by considering *superadiabatic* forces as introduced in the formally exact *power functional theory*[114–119], which contains (adiabatic) DDFT as a limiting case. For the systems investigated in this work, superadiabatic forces are not considered under the assumption that the non-equilibrium effects on the fluid structure are negligible. For a more complete overview of the entire realm of DDFT, I refer to the review by te Vrugt *et al.*[120].

2.3 Entropy Scaling for Shear Viscosity & Diffusion Coefficients

The connection between transport coefficients, i.e., shear viscosity η, thermal conductivity λ, and self-diffusion coefficients $D_i^{\text{self},0}$ and the residual entropy*, defined by $s^{\text{res}}(T, \{\rho_i\}) \equiv -k_\text{B} T \left(\left(\frac{\partial \tilde{a}^{\text{res}}}{\partial T} \right)_{\{\rho_i\}} + \frac{\tilde{a}^{\text{res}}}{T} \right)$, was recognized by Rosenfeld[121–123], who also applied it to the scaling of radial distribution functions[124] and perturbation theories[125]. Entropy scaling states that a reduced form of the transport coefficients can, to a good approximation, be described by a univariate function of the reduced molar residual entropy $s^*(T, \{\rho_i\})$. This allows to represent

*The over ideal gas entropy, obtained from $\tilde{a}^{\text{res}} \equiv \tilde{a} - \tilde{a}^{\text{ig}}$.

the complex temperature and density dependence of the reduced transport coefficients as simple univariate relations for reduced shear viscosity $\eta^*(s^*)$, thermal conductivity $\lambda^*(s^*)$, and self-diffusion coefficients $D_i^{\mathrm{self},0,*}(s^*)$.

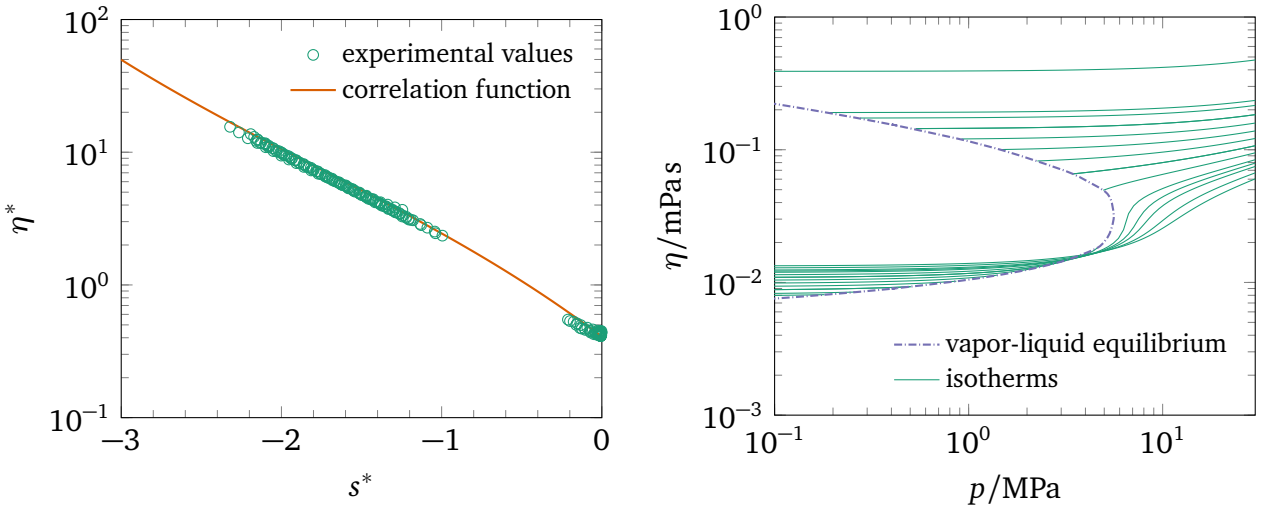

(a) Reduced viscosity η^* over residual entropy s^*.

(b) Shear viscosity η over pressure p.

Figure 2.2: Shear viscosity of dimethyl ether[126]: (a) univariate relation between logarithmic-reduced shear viscosity η^* and the reduced residual entropy s^* for experimental values and the correlation function obtained from molecular dynamics simulations[126]; (b) shear viscosity η as a function of pressure for various temperatures. The shear viscosity in both phases at vapor-liquid equilibrium is also shown.

The univariate relation between reduced transport coefficients and reduced residual entropy, obtained from the PC-SAFT equation of state, is shown exemplarily for the viscosity in figure 2.2(a). The simple univariate relation indicated by the correlation function for $\eta^*(s^*)$ is able to approximate the more complex shear viscosity behavior shown in figure 2.2(b). The same approach is applicable for self-diffusion coefficients with a different correlation function for $D_i^{\mathrm{self},0,*}(s^*)$. The application of entropy scaling for pure fluids and mixtures in combination with the PC-SAFT equation of state[16–20] was performed for viscosities by Lötgering-Lin *et al.*[127–129], and for thermal conductivities and self-diffusion coefficients by Hopp *et al.*[130–134].

The shear viscosity $\eta^*(s^*)$ and the self-diffusion coefficients $D_i^{\mathrm{self},0,*}(s^*)$ are modeled by

$$\ln(\eta^*) = \ln\left(\frac{\eta}{\eta_{\mathrm{CE}}}\right) = \breve{f}(s^*) \tag{2.36a}$$

$$\ln(D_i^{\mathrm{self},0,*}) = \ln\left(\frac{\rho D_i^{\mathrm{self},0}}{\rho D_{i,\mathrm{CE}}^{\mathrm{self},0}}\right) = \breve{g}(s^*) \tag{2.36b}$$

where the transport coefficients η and $D_i^{\mathrm{self},0}$ are reduced by their Chapman-Enskog counter-

parts[135,136], η_{CE} and $D_{i,\mathrm{CE}}^{\mathrm{self},0}$. The univariate correlation functions $\breve{f}(s^*)$ and $\breve{g}(s^*)$ depend only on the reduced residual entropy $s^* = \frac{s^{\mathrm{res}}(T,\{\rho_i\})}{k_{\mathrm{B}}\bar{m}}$, reduced by the Boltzmann constant k_{B} and the average chain-length parameter of the PC-SAFT equation of state $\bar{m} = \sum_i^{N_c} x_i m_i$ defined using the mole fractions x_i and number of segments per chain m_i of component i. The correlation functions are parameterized such that the resulting transport coefficients match experimental or simulation data of pure components[126,127,133]. The shear viscosity of mixtures can be obtained using combining rules for the parameters of the correlation function $\breve{f}$.

The Maxwell-Stefan diffusion coefficients can be obtained from the self-diffusion coefficients using the combined methods of Zmpitas *et al.* [137], Liu *et al.* [138], Darken [139] and Sridhar [140].

References

[1] R. Evans. The nature of the liquid-vapour interface and other topics in the statistical mechanics of non-uniform, classical fluids. *Advances in Physics*, **28**(2):143–200, 1979. doi:10.1080/00018737900101365.

[2] P. Hohenberg and W. Kohn. Inhomogeneous Electron Gas. *Physical Review*, **136**:B864–B871, 1964. doi:10.1103/PhysRev.136.B864.

[3] N. D. Mermin. Thermal Properties of the Inhomogeneous Electron Gas. *Physical Review*, **137**:A1441–A1443, 1965. doi:10.1103/PhysRev.137.A1441.

[4] A. Kovalenko, S. Ten-no, and F. Hirata. Solution of three-dimensional reference interaction site model and hypernetted chain equations for simple point charge water by modified method of direct inversion in iterative subspace. *Journal of Computational Chemistry*, **20**(9):928–936, 1999. doi:10.1002/(SICI)1096-987X(19990715)20:9<928::AID-JCC4>3.0.CO;2-X.

[5] L. J. D. Frink and A. G. Salinger. Two- and Three-Dimensional Nonlocal Density Functional Theory for Inhomogeneous Fluids. *Journal of Computational Physics*, **159**(2):407–424, 2000. doi:10.1006/jcph.2000.6454.

[6] L. J. D. Frink and A. G. Salinger. Two- and Three-Dimensional Nonlocal Density Functional Theory for Inhomogeneous Fluids. *Journal of Computational Physics*, **159**(2):425–439, 2000. doi:10.1006/jcph.2000.6455.

[7] L. J. D. Frink, A. G. Salinger, M. P. Sears, J. D. Weinhold, and A. L. Frischknecht. Numerical challenges in the application of density functional theory to biology and nanotechnology. *Journal of Physics: Condensed Matter*, **14**(46):12167, 2002. doi:10.1088/0953-8984/14/46/320.

[8] L. J. D. Frink, M. G. Martin, A. G. Salinger, and M. A. Heroux. High performance computing for the application of molecular theories to biological systems. *Journal of Physics: Conference Series*, **46**(1):304–306, 2006. doi:10.1088/1742-6596/46/1/042.

[9] L. J. D. Frink, A. L. Frischknecht, M. A. Heroux, M. L. Parks, and A. G. Salinger. Toward Quantitative Coarse-Grained Models of Lipids with Fluids Density Functional Theory. *Journal of Chemical Theory and Computation*, **8**(4):1393–1408, 2012. doi:10.1021/ct200707b.

[10] J. Mairhofer and J. Gross. Numerical aspects of classical density functional theory for one-dimensional vapor-liquid interfaces. *Fluid Phase Equilibria*, **444**:1–12, 2017. doi:10.1016/j.fluid.2017.03.023.

[11] J. Yvon. *La théorie statistique des fluides et l'équation d'état*, volume 203 of *Actualités scientifiques et industrielles*. Hermann & Cie, Paris, 1935.

[12] M. Born and H. Green. A general kinetic theory of liquids I. The molecular distribution functions. *Proceedings of the Royal Society of London. Series A. Mathematical and Physical Sciences*, **188**(1012):10–18, 1946. doi:10.1098/rspa.1946.0093.

[13] J.-P. Hansen and I. R. McDonald. *Theory of Simple Liquids*. Academic Press, Oxford, 4th edition, 2013. doi:10.1016/C2010-0-66723-X.

[14] M. Werdland, U. Heinbuch, and J. Fischer. Adsorption of simple gas mixtures on a plane wall: Born-Green-Yvon for structure, adsorption isotherms and selectivity. *Fluid Phase Equilibria*, **48**:259–277, 1989. doi:10.1016/0378-3812(89)80206-7.

[15] R. Roth. Fundamental measure theory for hard-sphere mixtures: a review. *Journal of Physics: Condensed Matter*, **22**(6):063102, 2010. doi:10.1088/0953-8984/22/6/063102.

[16] J. Gross and G. Sadowski. Perturbed-Chain SAFT: An Equation of State Based on a Perturbation Theory for Chain Molecules. *Industrial & Engineering Chemistry Research*, **40**(4):1244–1260, 2001. doi:10.1021/ie0003887.

[17] J. Gross and G. Sadowski. Modeling Polymer Systems Using the Perturbed-Chain Statistical Associating Fluid Theory Equation of State. *Industrial & Engineering Chemistry Research*, **41**(5):1084–1093, 2002. doi:10.1021/ie010449g.

[18] J. Gross and G. Sadowski. Application of the Perturbed-Chain SAFT Equation of State to Associating Systems. *Industrial & Engineering Chemistry Research*, **41**(22):5510–5515, 2002. doi:10.1021/ie010954d.

[19] J. Gross and J. Vrabec. An equation-of-state contribution for polar components: Dipolar molecules. *AIChE Journal*, **52**(3):1194–1204, 2006. doi:10.1002/aic.10683.

[20] J. Gross. An equation-of-state contribution for polar components: Quadrupolar molecules. *AIChE Journal*, **51**(9):2556–2568, 2005. doi:10.1002/aic.10502.

[21] J. Vrabec and J. Gross. Vapor–Liquid Equilibria Simulation and an Equation of State Contribution for Dipole–Quadrupole Interactions. *The Journal of Physical Chemistry B*, **112**(1):51–60, 2008. doi:10.1021/jp072619u.

[22] W. G. Chapman, G. Jackson, and K. E. Gubbins. Phase equilibria of associating fluids: Chain molecules with multiple bonding sites. *Molecular Physics*, **65**(5):1057–1079, 1988. doi:10.1080/00268978800101601.

[23] W. Chapman, K. Gubbins, G. Jackson, and M. Radosz. SAFT: Equation-of-state solution model for associating fluids. *Fluid Phase Equilibria*, **52**:31–38, 1989. doi:10.1016/0378-3812(89)80308-5.

[24] W. G. Chapman, K. E. Gubbins, G. Jackson, and M. Radosz. New reference equation of state for associating liquids. *Industrial & Engineering Chemistry Research*, **29**(8):1709–1721, 1990. doi:10.1021/ie00104a021.

[25] S. H. Huang and M. Radosz. Equation of state for small, large, polydisperse, and associating molecules. *Industrial & Engineering Chemistry Research*, **29**(11):2284–2294, 1990. doi:10.1021/ie00107a014.

[26] S. H. Huang and M. Radosz. Equation of state for small, large, polydisperse, and associating molecules: extension to fluid mixtures. *Industrial & Engineering Chemistry Research*, **30**(8):1994–2005, 1991. doi:10.1021/ie00056a050.

[27] F. J. Blas and L. F. Vega. Thermodynamic behaviour of homonuclear and heteronuclear Lennard-Jones chains with association sites from simulation and theory. *Molecular Physics*, **92**(1):135–150, 1997. doi:10.1080/002689797170707.

[28] F. J. Blas and L. F. Vega. Prediction of Binary and Ternary Diagrams Using the Statistical Associating Fluid Theory (SAFT) Equation of State. *Industrial & Engineering Chemistry Research*, **37**(2):660–674, 1998. doi:10.1021/ie970449+.

[29] A. Gil-Villegas, A. Galindo, P. J. Whitehead, S. J. Mills, G. Jackson, and A. N. Burgess. Statistical associating fluid theory for chain molecules with attractive potentials of variable range. *The Journal of Chemical Physics*, **106**(10):4168–4186, 1997. doi:10.1063/1.473101.

[30] A. Galindo, L. A. Davies, A. Gil-Villegas, and G. Jackson. The thermodynamics of mixtures and the corresponding mixing rules in the SAFT-VR approach for potentials of variable range. *Molecular Physics*, **93**(2):241–252, 1998. doi:10.1080/002689798169249.

[31] A. Galindo, A. Gil-Villegas, G. Jackson, and A. N. Burgess. SAFT-VRE: Phase Behavior of Electrolyte Solutions with the Statistical Associating Fluid Theory for Potentials of Variable Range. *The Journal of Physical Chemistry B*, **103**(46):10272–10281, 1999. doi:10.1021/jp991959f.

[32] A. Gil-Villegas, A. Galindo, and G. Jackson. A statistical associating fluid theory for electrolyte solutions(SAFT-VRE). *Molecular Physics*, **99**(6):531–546, 2001. doi:10.1080/00268970010018666.

[33] A. Lymperiadis, C. S. Adjiman, A. Galindo, and G. Jackson. A group contribution method for associating chain molecules based on the statistical associating fluid theory (SAFT-γ). *The Journal of Chemical Physics*, **127**(23):234903, 2007. doi:10.1063/1.2813894.

[34] V. Papaioannou, T. Lafitte, C. Avendaño, C. S. Adjiman, G. Jackson, E. A. Müller, and A. Galindo. Group contribution methodology based on the statistical associating fluid theory for heteronuclear molecules formed from Mie segments. *The Journal of Chemical Physics*, **140**(5):054107, 2014. doi:10.1063/1.4851455.

[35] M. S. Wertheim. Fluids with highly directional attractive forces. I. Statistical thermodynamics. *Journal of Statistical Physics*, **35**(1):19–34, 1984. doi:10.1007/BF01017362.

[36] M. S. Wertheim. Fluids with highly directional attractive forces. II. Thermodynamic perturbation theory and integral equations. *Journal of Statistical Physics*, **35**(1):35–47, 1984. doi:10.1007/BF01017363.

[37] M. S. Wertheim. Fluids with highly directional attractive forces. III. Multiple attraction sites. *Journal of Statistical Physics*, **42**(3):459–476, 1986. doi:10.1007/BF01127721.

[38] M. S. Wertheim. Fluids with highly directional attractive forces. IV. Equilibrium polymerization. *Journal of Statistical Physics*, **42**(3):477–492, 1986. doi:10.1007/BF01127722.

[39] C. Klink and J. Gross. A Density Functional Theory for Vapor–Liquid Interfaces of Mixtures Using the Perturbed-Chain Polar Statistical Associating Fluid Theory Equation of State. *Industrial & Engineering Chemistry Research*, **53**(14):6169–6178, 2014. doi:10.1021/ie4029895.

[40] C. Klink, B. Planková, and J. Gross. Density Functional Theory for Liquid–Liquid Interfaces of Mixtures Using the Perturbed-Chain Polar Statistical Associating Fluid Theory Equation of State. *Industrial & Engineering Chemistry Research*, **54**(16):4633–4642, 2015. doi:10.1021/acs.iecr.5b00445.

[41] E. Sauer, A. Terzis, M. Theiss, B. Weigand, and J. Gross. Prediction of Contact Angles and Density Profiles of Sessile Droplets Using Classical Density Functional Theory Based on the PCP-SAFT Equation of State. *Langmuir*, **34**(42):12519–12531, 2018. doi:10.1021/acs.langmuir.8b01985.

[42] E. Sauer and J. Gross. Prediction of Adsorption Isotherms and Selectivities: Comparison between Classical Density Functional Theory Based on the Perturbed-Chain Statistical Associating Fluid Theory Equation of State and Ideal Adsorbed Solution Theory. *Langmuir*, **35**(36):11690–11701, 2019. doi:10.1021/acs.langmuir.9b02378.

[43] J. Mairhofer and J. Gross. Modeling properties of the one-dimensional vapor-liquid interface: Application of classical density functional and density gradient theory. *Fluid Phase Equilibria*, **458**:243–252, 2018. doi:10.1016/j.fluid.2017.11.032.

[44] C. Klink, C. Waibel, and J. Gross. Analysis of Interfacial Transport Resistivities of Pure Components and Mixtures Based on Density Functional Theory. *Industrial & Engineering Chemistry Research*, **54**(45):11483–11492, 2015. doi:10.1021/acs.iecr.5b03270.

[45] P. Rehner and J. Gross. Surface tension of droplets and Tolman lengths of real substances and mixtures from density functional theory. *The Journal of Chemical Physics*, **148**(16):164703, 2018. doi:10.1063/1.5020421.

[46] T. Boublík. Hard-Sphere Equation of State. *The Journal of Chemical Physics*, **53**(1):471–472, 1970. doi:10.1063/1.1673824.

[47] G. A. Mansoori, N. F. Carnahan, K. E. Starling, and T. W. Leland Jr. Equilibrium Thermodynamic Properties of the Mixture of Hard Spheres. *The Journal of Chemical Physics*, **54**(4):1523–1525, 1971. doi:10.1063/1.1675048.

[48] J. A. Barker and D. Henderson. Perturbation Theory and Equation of State for Fluids: The Square-Well Potential. *The Journal of Chemical Physics*, **47**(8):2856–2861, 1967. doi:10.1063/1.1712308.

[49] J. A. Barker and D. Henderson. Perturbation Theory and Equation of State for Fluids. II. A Successful Theory of Liquids. *The Journal of Chemical Physics*, **47**(11):4714–4721, 1967. doi:10.1063/1.1701689.

[50] Y. Rosenfeld. Free-energy model for the inhomogeneous hard-sphere fluid mixture and density-functional theory of freezing. *Physical Review Letters*, **63**:980–983, 1989. doi:10.1103/PhysRevLett.63.980.

[51] H. Reiss, H. L. Frisch, and J. L. Lebowitz. Statistical Mechanics of Rigid Spheres. *The Journal of Chemical Physics*, **31**(2):369–380, 1959. doi:10.1063/1.1730361.

[52] J. A. Barker and D. Henderson. What is "liquid"? Understanding the states of matter. *Reviews of Modern Physics*, **48**:587–671, 1976. doi:10.1103/RevModPhys.48.587.

[53] M. S. Wertheim. Exact Solution of the Percus-Yevick Integral Equation for Hard Spheres. *Physical Review Letters*, **10**:321–323, 1963. doi:10.1103/PhysRevLett.10.321.

[54] M. S. Wertheim. Analytic Solution of the Percus-Yevick Equation. *Journal of Mathematical Physics*, **5**(5):643–651, 1964. doi:10.1063/1.1704158.

[55] J. L. Lebowitz. Exact Solution of Generalized Percus-Yevick Equation for a Mixture of Hard Spheres. *Physical Review*, **133**:A895–A899, 1964. doi:10.1103/PhysRev.133.A895.

[56] R. Roth, R. Evans, A. Lang, and G. Kahl. Fundamental measure theory for hard-sphere mixtures revisited: the White Bear version. *Journal of Physics: Condensed Matter*, **14**(46):12063, 2002. doi:10.1088/0953-8984/14/46/313.

[57] Y.-X. Yu and J. Wu. Structures of hard-sphere fluids from a modified fundamental-measure theory. *The Journal of Chemical Physics*, **117**(22):10156–10164, 2002. doi:10.1063/1.1520530.

[58] H. Hansen-Goos and R. Roth. A new generalization of the Carnahan-Starling equation of state to additive mixtures of hard spheres. *The Journal of Chemical Physics*, **124**(15):154506, 2006. doi:10.1063/1.2187491.

[59] H. Hansen-Goos and R. Roth. Density functional theory for hard-sphere mixtures: the White Bear version mark II. *Journal of Physics: Condensed Matter*, **18**(37):8413–8425, 2006. doi:10.1088/0953-8984/18/37/002.

[60] E. Kierlik and M. L. Rosinberg. Free-energy density functional for the inhomogeneous hard-sphere fluid: Application to interfacial adsorption. *Physical Review A*, **42**:3382–3387, 1990. doi:10.1103/PhysRevA.42.3382.

[61] E. Kierlik and M. L. Rosinberg. Density-functional theory for inhomogeneous fluids: Adsorption of binary mixtures. *Physical Review A*, **44**:5025–5037, 1991. doi:10.1103/PhysRevA.44.5025.

[62] T. Bernet, M. M. Piñeiro, F. Plantier, and C. Miqueu. Generalization of the Fundamental-Measure Theory Beyond Hard Potentials: The Square-Well Fluid Case. *The Journal of Physical Chemistry C*, **121**(11):6184–6190, 2017. doi:10.1021/acs.jpcc.7b00797.

[63] S. Tripathi and W. G. Chapman. Microstructure and Thermodynamics of Inhomogeneous Polymer Blends and Solutions. *Physical Review Letters*, **94**:087801, 2005. doi:10.1103/PhysRevLett.94.087801.

[64] S. Tripathi and W. G. Chapman. Microstructure of inhomogeneous polyatomic mixtures from a density functional formalism for atomic mixtures. *The Journal of Chemical Physics*, **122**(9):094506, 2005. doi:10.1063/1.1853371.

[65] E. Kierlik and M. L. Rosinberg. A perturbation density functional theory for polyatomic fluids. II. Flexible molecules. *The Journal of Chemical Physics*, **99**(5):3950–3965, 1993. doi:10.1063/1.466142.

[66] W. Zmpitas and J. Gross. Detailed pedagogical review and analysis of Wertheim's thermodynamic perturbation theory. *Fluid Phase Equilibria*, **428**:121–152, 2016. doi:10.1016/j.fluid.2016.07.033.

[67] E. Sauer and J. Gross. Classical Density Functional Theory for Liquid–Fluid Interfaces and Confined Systems: A Functional for the Perturbed-Chain Polar Statistical Associating Fluid Theory Equation of State. *Industrial & Engineering Chemistry Research*, **56**(14):4119–4135, 2017. doi:10.1021/acs.iecr.6b04551.

[68] S. Jain, A. Dominik, and W. G. Chapman. Modified interfacial statistical associating fluid theory: A perturbation density functional theory for inhomogeneous complex fluids. *The Journal of Chemical Physics*, **127**(24):244904, 2007. doi:10.1063/1.2806932.

[69] J. Mairhofer, B. Xiao, and J. Gross. A classical density functional theory for vapor-liquid interfaces consistent with the heterosegmented group-contribution perturbed-chain polar statistical associating fluid theory. *Fluid Phase Equilibria*, **472**:117–127, 2018. doi:10.1016/j.fluid.2018.05.016.

[70] J. Gross and G. Sadowski. Application of perturbation theory to a hard-chain reference fluid: an equation of state for square-well chains. *Fluid Phase Equilibria*, **168**(2):183–199, 2000. doi:10.1016/S0378-3812(00)00302-2.

[71] R. Evans. Density Functionals in the Theory of inhomogeneous Fluids. In D. Henderson (editor), *Fundamentals of Inhomogeneous Fluids*, pages 85–175. CRC Press, New York, 1992.

[72] Z. Ye, J. Cai, H. Liu, and Y. Hu. Density and chain conformation profiles of square-well chains confined in a slit by density-functional theory. *The Journal of Chemical Physics*, **123**(19):194902, 2005. doi:10.1063/1.2117009.

[73] G. Shen, X. Ji, and X. Lu. A hybrid perturbed-chain SAFT density functional theory for representing fluid behavior in nanopores. *The Journal of Chemical Physics*, **138**(22):224706, 2013. doi:10.1063/1.4808160.

[74] G. Shen, X. Ji, S. Öberg, and X. Lu. A hybrid perturbed-chain SAFT density functional theory for representing fluid behavior in nanopores: Mixtures. *The Journal of Chemical Physics*, **139**(19):194705, 2013. doi:10.1063/1.4825078.

[75] G. Shen, X. Lu, and X. Ji. Modeling of molecular gas adsorption isotherms on porous materials with hybrid PC-SAFT-DFT. *Fluid Phase Equilibria*, **382**:116–126, 2014. doi:10.1016/j.fluid.2014.09.002.

[76] B. Peng and Y.-X. Yu. A Density Functional Theory for Lennard-Jones Fluids in Cylindrical Pores and Its Applications to Adsorption of Nitrogen on MCM-41 Materials. *Langmuir*, **24**(21):12431–12439, 2008. doi:10.1021/la8024099.

[77] B. Peng and Y.-X. Yu. A Density Functional Theory with a Mean-field Weight Function: Applications to Surface Tension, Adsorption, and Phase Transition of a Lennard-Jones Fluid in a Slit-like Pore. *The Journal of Physical Chemistry B*, **112**(48):15407–15416, 2008. doi:10.1021/jp805697p.

[78] J. Gross. A density functional theory for vapor-liquid interfaces using the PCP-SAFT equation of state. *The Journal of Chemical Physics*, **131**(20):204705, 2009. doi:10.1063/1.3263124.

[79] P. Frodl and S. Dietrich. Bulk and interfacial properties of polar and molecular fluids. *Physical Review A*, **45**:7330–7354, 1992. doi:10.1103/PhysRevA.45.7330.

[80] P. Frodl and S. Dietrich. Erratum: Bulk and interfacial properties of polar and molecular fluids. *Physical Review E*, **48**:3203–3203, 1993. doi:10.1103/PhysRevE.48.3203.

[81] P. Frodl and S. Dietrich. Thermal and structural properties of the liquid-vapor interface in dipolar fluids. *Physical Review E*, **48**:3741–3759, 1993. doi:10.1103/PhysRevE.48.3741.

[82] P. Frodl and S. Dietrich. Erratum: Thermal and structural properties of the liquid-vapor interface in dipolar fluids [Phys. Rev. E 48, 3741 (1993)]. *Physical Review E*, **49**:4755–4755, 1994. doi:10.1103/PhysRevE.49.4755.2.

[83] Y.-X. Yu and J. Wu. A fundamental-measure theory for inhomogeneous associating fluids. *The Journal of Chemical Physics*, **116**(16):7094–7103, 2002. doi:10.1063/1.1463435.

[84] M. S. Wertheim. Fluids of dimerizing hard spheres, and fluid mixtures of hard spheres and dispheres. *The Journal of Chemical Physics*, **85**(5):2929–2936, 1986. doi:10.1063/1.451002.

[85] M. S. Wertheim. Integral equation for the Smith–Nezbeda model of associated fluids. *The Journal of Chemical Physics*, **88**(2):1145–1155, 1988. doi:10.1063/1.454233.

[86] G. Jackson, W. G. Chapman, and K. E. Gubbins. Phase equilibria of associating fluids: Spherical molecules with multiple bonding sites. *Molecular Physics*, **65**(1):1–31, 1988. doi:10.1080/00268978800100821.

[87] A. Bymaster and W. G. Chapman. An iSAFT Density Functional Theory for Associating Polyatomic Molecules. *The Journal of Physical Chemistry B*, **114**(38):12298–12307, 2010. doi:10.1021/jp102677m.

[88] A. J. Archer. Dynamical density functional theory for molecular and colloidal fluids: A microscopic approach to fluid mechanics. *The Journal of Chemical Physics*, **130**(1):014509, 2009. doi:10.1063/1.3054633.

[89] N. N. Bogoliubov. Kinetic Equations. *Journal of Physics USSR*, **10**(3):265–274, 1946.

[90] J. G. Kirkwood. The Statistical Mechanical Theory of Transport Processes I. General Theory.

The Journal of Chemical Physics, **14**(3):180–201, 1946. doi:10.1063/1.1724117.

[91] J. G. Kirkwood. The Statistical Mechanical Theory of Transport Processes II. Transport in Gases. *The Journal of Chemical Physics*, **15**(1):72–76, 1947. doi:10.1063/1.1746292.

[92] L. Boltzmann. *Vorlesungen über Gastheorie: I. Theil*. Barth, Leipzig, 1896.

[93] L. Boltzmann. *Vorlesungen über Gastheorie: II. Theil*. Barth, Leipzig, 1898.

[94] U. M. B. Marconi and P. Tarazona. Dynamic density functional theory of fluids. *The Journal of Chemical Physics*, **110**(16):8032–8044, 1999. doi:10.1063/1.478705.

[95] U. M. B. Marconi and P. Tarazona. Dynamic density functional theory of fluids. *Journal of Physics: Condensed Matter*, **12**(8A):A413–A418, 2000. doi:10.1088/0953-8984/12/8a/356.

[96] A. J. Archer and R. Evans. Dynamical density functional theory and its application to spinodal decomposition. *The Journal of Chemical Physics*, **121**(9):4246–4254, 2004. doi:10.1063/1.1778374.

[97] M. Born and J. R. Oppenheimer. Zur Quantentheorie der Molekeln. *Annalen der Physik*, **389**(20):457–484, 1927. doi:10.1002/andp.19273892002.

[98] D. de las Heras and M. Schmidt. Full Canonical Information from Grand-Potential Density-Functional Theory. *Physical Review Letters*, **113**:238304, 2014. doi:10.1103/PhysRevLett.113.238304.

[99] J. F. Lutsko. Recent Developments in Classical Density Functional Theory. In *Advances in Chemical Physics*, pages 1–92. John Wiley & Sons, 2010. doi:10.1002/9780470564318.ch1.

[100] S. Kjelstrup, D. Bedeaux, E. Johannessen, and J. Gross. *Non-Equilibrium Thermodynamics for Engineers*. World Scientific Publishing, 2nd edition, 2016. ISBN 9789813200302, 9789813200319. doi:10.1142/10286.

[101] J. G. Kirkwood. Statistical Mechanics of Fluid Mixtures. *The Journal of Chemical Physics*, **3**(5):300–313, 1935. doi:10.1063/1.1749657.

[102] B. D. Goddard, A. Nold, and S. Kalliadasis. Multi-species dynamical density functional theory. *The Journal of Chemical Physics*, **138**(14):144904, 2013. doi:10.1063/1.4800109.

[103] B. D. Goddard, A. Nold, N. Savva, P. Yatsyshin, and S. Kalliadasis. Unification of dynamic density functional theory for colloidal fluids to include inertia and hydrodynamic interactions: derivation and numerical experiments. *Journal of Physics: Condensed Matter*, **25**(3):035101, 2012. doi:10.1088/0953-8984/25/3/035101.

[104] B. D. Goddard, A. Nold, N. Savva, G. A. Pavliotis, and S. Kalliadasis. General Dynamical Density Functional Theory for Classical Fluids. *Physical Review Letters*, **109**:120603, 2012. doi:10.1103/PhysRevLett.109.120603.

[105] B. D. Goddard, A. Nold, and S. Kalliadasis. Dynamical density functional theory with hydrody-

namic interactions in confined geometries. *The Journal of Chemical Physics*, **145**(21):214106, 2016. doi:10.1063/1.4968565.

[106] M. A. Durán-Olivencia, B. D. Goddard, and S. Kalliadasis. Dynamical Density Functional Theory for Orientable Colloids Including Inertia and Hydrodynamic Interactions. *Journal of Statistical Physics*, **164**:785–809, 2016. doi:10.1007/s10955-016-1545-5.

[107] J. Bleibel, A. Domínguez, and M. Oettel. A dynamic DFT approach to generalized diffusion equations in a system with long-ranged and hydrodynamic interactions. *Journal of Physics: Condensed Matter*, **28**(24):244021, 2016. doi:10.1088/0953-8984/28/24/244021.

[108] A. Donev and E. Vanden-Eijnden. Dynamic density functional theory with hydrodynamic interactions and fluctuations. *The Journal of Chemical Physics*, **140**(23):234115, 2014. doi:10.1063/1.4883520.

[109] A. Russo, M. A. Durán-Olivencia, P. Yatsyshin, and S. Kalliadasis. Memory effects in fluctuating dynamic density-functional theory: theory and simulations. *Journal of Physics A: Mathematical and Theoretical*, **53**(44):445007, 2020. doi:10.1088/1751-8121/ab9e8d.

[110] F. Giavazzi, G. Savorana, A. Vailati, and R. Cerbino. Structure and dynamics of concentration fluctuations in a non-equilibrium dense colloidal suspension. *Soft Matter*, **12**:6588–6600, 2016. doi:10.1039/C6SM00935B.

[111] R. P. Peláez, F. B. Usabiaga, S. Panzuela, Q. Xiao, R. Delgado-Buscalioni, and A. Donev. Hydrodynamic fluctuations in quasi-two dimensional diffusion. *Journal of Statistical Mechanics: Theory and Experiment*, **2018**(6):063207, 2018. doi:10.1088/1742-5468/aac2fb.

[112] A. J. Archer and M. Rauscher. Dynamical density functional theory for interacting Brownian particles: stochastic or deterministic? *Journal of Physics A: Mathematical and General*, **37**(40):9325–9333, 2004. doi:10.1088/0305-4470/37/40/001.

[113] M. A. Durán-Olivencia, P. Yatsyshin, B. D. Goddard, and S. Kalliadasis. General framework for fluctuating dynamic density functional theory. *New Journal of Physics*, **19**(12):123022, 2017. doi:10.1088/1367-2630/aa9041.

[114] M. Schmidt and J. M. Brader. Power functional theory for Brownian dynamics. *The Journal of Chemical Physics*, **138**(21):214101, 2013. doi:10.1063/1.4807586.

[115] J. M. Brader and M. Schmidt. Power functional theory for the dynamic test particle limit. *Journal of Physics: Condensed Matter*, **27**(19):194106, 2015. doi:10.1088/0953-8984/27/19/194106.

[116] P. Krinninger, M. Schmidt, and J. M. Brader. Nonequilibrium Phase Behavior from Minimization of Free Power Dissipation. *Physical Review Letters*, **117**:208003, 2016. doi:10.1103/PhysRevLett.117.208003.

[117] P. Krinninger, M. Schmidt, and J. M. Brader. Erratum: Nonequilibrium Phase Behavior from Minimization of Free Power Dissipation [Phys. Rev. Lett. 117, 208003 (2016)]. *Physical Review*

Letters, **119**:029902, 2017. doi:10.1103/PhysRevLett.119.029902.

[118] D. de las Heras and M. Schmidt. Velocity Gradient Power Functional for Brownian Dynamics. *Physocal Review Letters*, **120**:028001, 2018. doi:10.1103/PhysRevLett.120.028001.

[119] M. Schmidt. Power functional theory for Newtonian many-body dynamics. *The Journal of Chemical Physics*, **148**(4):044502, 2018. doi:10.1063/1.5008608.

[120] M. te Vrugt, H. Löwen, and R. Wittkowski. Classical dynamical density functional theory: from fundamentals to applications. *Advances in Physics*, **69**(2):121–247, 2020. doi:10.1080/00018732.2020.1854965.

[121] Y. Rosenfeld. Relation between the transport coefficients and the internal entropy of simple systems. *Physical Review A*, **15**:2545–2549, 1977. doi:10.1103/PhysRevA.15.2545.

[122] Y. Rosenfeld. Comments on the transport coefficients of dense hard core systems. *Chemical Physics Letters*, **48**(3):467–468, 1977. doi:10.1016/0009-2614(77)85071-9.

[123] Y. Rosenfeld. A quasi-universal scaling law for atomic transport in simple fluids. *Journal of Physics: Condensed Matter*, **11**(28):5415–5427, 1999. doi:10.1088/0953-8984/11/28/303.

[124] Y. Rosenfeld. New method for equation-of-state calculations: Linear combinations of basis potentials. *Physical Review A*, **26**:3633–3645, 1982. doi:10.1103/PhysRevA.26.3633.

[125] Y. Rosenfeld. Variational soft-sphere perturbation theory and conditions for a Grüneisen equation of state for dense fluids. *Physical Review A*, **28**:3063–3069, 1983. doi:10.1103/PhysRevA.28.3063.

[126] M. Fischer, G. Bauer, and J. Gross. Transferable Anisotropic United-Atom Mie (TAMie) Force Field: Transport Properties from Equilibrium Molecular Dynamic Simulations. *Industrial & Engineering Chemistry Research*, **59**(18):8855–8869, 2020. doi:10.1021/acs.iecr.0c00848.

[127] O. Lötgering-Lin, M. Fischer, M. Hopp, and J. Gross. Pure Substance and Mixture Viscosities Based on Entropy Scaling and an Analytic Equation of State. *Industrial & Engineering Chemistry Research*, **57**(11):4095–4114, 2018. doi:10.1021/acs.iecr.7b04871.

[128] O. Lötgering-Lin and J. Gross. Group Contribution Method for Viscosities Based on Entropy Scaling Using the Perturbed-Chain Polar Statistical Associating Fluid Theory. *Industrial & Engineering Chemistry Research*, **54**(32):7942–7952, 2015. doi:10.1021/acs.iecr.5b01698.

[129] O. Lötgering-Lin, A. Schöniger, W. Nowak, and J. Gross. Bayesian Model Selection Helps To Choose Objectively between Thermodynamic Models: A Demonstration of Selecting a Viscosity Model Based on Entropy Scaling. *Industrial & Engineering Chemistry Research*, **55**(38):10191–10207, 2016. doi:10.1021/acs.iecr.6b02671.

[130] M. Hopp, J. Mele, R. Hellmann, and J. Gross. Thermal Conductivity via Entropy Scaling: An Approach That Captures the Effect of Intramolecular Degrees of Freedom. *Industrial & Engineering Chemistry Research*, **58**(39):18432–18438, 2019. doi:10.1021/acs.iecr.9b03998.

[131] M. Hopp and J. Gross. Thermal Conductivity of Real Substances from Excess Entropy Scaling Using PCP-SAFT. *Industrial & Engineering Chemistry Research*, **56**(15):4527–4538, 2017. doi:10.1021/acs.iecr.6b04289.

[132] M. Hopp and J. Gross. Thermal Conductivity from Entropy Scaling: A Group-Contribution Method. *Industrial & Engineering Chemistry Research*, **58**(44):20441–20449, 2019. doi:10.1021/acs.iecr.9b04289.

[133] M. Hopp, J. Mele, and J. Gross. Self-Diffusion Coefficients from Entropy Scaling Using the PCP-SAFT Equation of State. *Industrial & Engineering Chemistry Research*, **57**(38):12942–12950, 2018. doi:10.1021/acs.iecr.8b02406.

[134] M. Hopp, J. Mele, and J. Gross. Erratum to "Self-Diffusion Coefficients from Entropy Scaling Using the PCP-SAFT Equation of State". *Industrial & Engineering Chemistry Research*, **58**(45):20857–20857, 2019. doi:10.1021/acs.iecr.9b05731.

[135] S. Chapman and T. G. Cowling. *The Mathematical Theory of Non-uniform Gases: An Account of the Kinetic Theory of Viscosity, Thermal Conduction and Diffusion in Gases*. Cambridge University Press, Cambridge, 3rd edition, 1990.

[136] J. O. Hirschfelder, C. F. Curtiss, and R. B. Bird. *Molecular theory of gases and liquids*. John Wiley & Sons, New York, 4th edition, 1967.

[137] J. Zmpitas, A. Bardow, and J. Gross. Prediction of Mutual Diffusion Coefficients based on Stokes-Einstein Equation and the Entropy Scaling Method, 2021. Work in progress.

[138] X. Liu, T. J. Vlugt, and A. Bardow. Predictive Darken Equation for Maxwell-Stefan Diffusivities in Multicomponent Mixtures. *Industrial & Engineering Chemistry Research*, **50**(17):10350–10358, 2011. doi:10.1021/ie201008a.

[139] L. S. Darken. Diffusion, Mobility and Their Interrelation through Free Energy in Binary Metallic Systems. *Transactions of the Metallurgical Society of AIME*, **175**:184–201, 1948.

[140] S. Sridhar. A Commentary on "Diffusion, Mobility and Their Interrelation through Free Energy in Binary Metallic Systems", L.S. Darken: Trans. AIME, 1948, vol. 175, p. 184ff. *Metallurgical and Materials Transactions A*, **41**:543–562, 2010. doi:10.1007/s11661-010-0177-7.

3 Guide to Efficient Solution of PC-SAFT Classical Density Functional Theory in Various Coordinate Systems Using Fast Fourier and Similar Transforms

The content of this chapter is a literal quote of the publication:

R. Stierle, E. Sauer, J. Eller, M. Theiss, P. Rehner, P. Ackermann, and J. Gross. Guide to efficient Solution of PC-SAFT classical Density Functional Theory in various Coordinate Systems using fast Fourier and similar Transforms. *Fluid Phase Equilibria*, **504**:112306, 2020. doi:10.1016/j.fluid.2019.112306

Abstract

Classical density functional theory (DFT) is a powerful tool for studying solvation or problems where resolution of interfacial domains or interfacial properties among phases (or thin films) is required. Many interesting problems necessitate multi-dimensional modeling, which calls for robust and efficient algorithmic implementations of the Helmholtz energy functionals. A possible approach for achieving efficient numerical solutions is using the convolution theorem of the Fourier transform. This study is meant to facilitate research and application of DFT methods, by providing a detailed guide on solving DFT problems in multi-dimensional domains. Methods for efficiently solving the convolution integrals in Fourier space are presented for Cartesian, cylindrical, and spherical coordinates. For cylindrical and spherical coordinate systems, rotational and spherical symmetry is exploited, respectively. To enable easy implementation, our approach is based on fast Fourier, fast Hankel, fast sine and cosine transforms on equidistant grids, all of which can be applied using off-the-shelf algorithms. Subtle details for implementing algorithms in cylindrical and spherical coordinate systems are emphasized. The work covers functionals based on weighted densities exemplarily. Functionals according to fundamental measure theory (FMT) as well as a Helmholtz energy functional based on the perturbed-chain statistical associating fluid theory (PC-SAFT) equation of state are worked out in detail (and given as supporting information[†]).

[†]in appendices A and B

3.1 Introduction

Efficient numerical solution of convolution integrals is important for solving classical density functional theory (DFT) or dynamic density functional theory (DDFT) in multidimensional problems. The solution of a DFT model, namely the densities of all species, is obtained iteratively. The computational demand for the iterative solution is the repetitive computation of numerous convolution integrals. Naïve numerical convolution through integration leads to long computation times and complicated integration schemes, especially for multidimensional DFT problems. One approach to address this problem is the utilization of the convolution theorem of the Fourier transform. The $\mathcal{O}(N \log N)$ computational complexity of fast Fourier transform (FFT) algorithms (compared to $\mathcal{O}(N^2)$ for numerical convolution) leads to a significant advantage regarding computational performance. Additionally, working with integral transforms like FFT simplifies multidimensional convolutions, because each dimension can be treated separately which averts multidimensional integration schemes.

Several authors applied integral transforms to convolution integrals appearing in DFT. Knepley *et al.* [1] used the FFT approach for convolutions in a DFT for ionic solutions. A short introduction to usage of FFT for Rosenfeld's fundamental measure theory[2] (FMT) was also given. Frink *et al.* [3,4] proposed Fourier space convolution on a multidimensional Cartesian grid in combination with nonlinear iterative solvers and Sears and Frink[5] proposed using FFT in combination with a matrix-free scheme and compared computational efficiency for one-, two- and three-dimensional systems. Hlushak *et al.* [6] employed the FFT on a two-dimensional Cartesian grid to analyze flexible chain molecules at curved surfaces, whereas Hlushak *et al.* [7,8] studied attractive particles in nanopores. While analyzing rotationally symmetric systems, rotational symmetry was not exploited in the computation of the convolution integrals, leading to unnecessary computational overhead. Oettel *et al.* applied the Fourier convolution approach within the framework of three-dimensional FMT and compared results to those obtained by phase-field models[10] and Monte Carlo simulations[9]. A similar analysis of crystal structures and solid-liquid interfaces using three-dimensional FMT combined with a Helmholtz energy contribution to account for attractive interactions was conducted by Wang *et al.* [11]. Solvation effects in water were studied by Levesque *et al.* [12]; solvation energies of amino acid side chains by Liu *et al.* [13], both by three-dimensional DFT. Zhou *et al.* [14] applied three-dimensional Cartesian DFT to heterogeneous nucleation of Lennard-Jones fluids on solid walls.

For cylindrical systems, rotational symmetry can be exploited to reduce dimensionality of the DFT problem. In one-dimensional cylindrical coordinates, González *et al.* [15] proposed using the Hankel transform for computation of the convolution in Fourier space. The fast Hankel

transform was not employed, however. Malijevský[16] and Mariani *et al.*[17] took advantage of rotational symmetry to formulate the convolution integrals of FMT for cylindrical coordinates in real space. In Fourier space this was done by Boţan *et al.*[18] for the analysis of hard-sphere fluids in annular wedges. In cylindrical coordinates the Fourier transform can not be computed using FFT, but requires a, preferably fast, Hankel transform algorithm for the radial direction. Boţan *et al.*[18] reformulated the DFT problem on a logarithmic grid to apply a fast Hankel transform.

Spherical symmetry can be exploited to efficiently compute spherical DFT systems in one dimension. This was applied by González *et al.*[15] to hard spheres in a spherical cavity, utilizing Fourier space convolution. For FMT in spherical coordinates projection of the weight functions onto one dimension was described by Roth[19].

Convolution in Fourier space by exploiting the FFT or similar algorithms is not the only approach to speed up the computation of the convolution integrals appearing in DFT problems. Yatsyshin *et al.* introduced a Chebyshev pseudo-spectral collocation method in combination with Clenshaw-Curtis quadrature for computation of the convolution integrals in one[20] and two dimensions[21] of a Cartesian grid, extended by Nold *et al.*[22]. Contrary to FFT convolution, equidistant grid spacing is not required, but possible. Problem-specific grid spacing has potential to reduce computational effort. Xu and Cao[23] used a two-dimensional multiscale finite element approach to reduce computational complexity for the convolution integrals.

Computation time, of course, not only depends on the performance of the Helmholtz functional computation and the involved convolution integrals but also depends on the algorithm used to solve the system of nonlinear equations as well. Previous work on numerical algorithms can be found in Frink *et al.*[3,4], Kovalenko *et al.*[24], Frink and Salinger[25,26], Frink *et al.*[27], a comparison of different nonlinear solvers in Mairhofer and Gross[28].

Classical DFT or DDFT are theoretical approaches that carry molecular detail through averaged quantities. DFT approaches are predictive when a suitable Helmholtz energy functional is applied. We aim at applying FFT convolution to a functional consistent with the perturbed-chain statistical associating fluid theory (PC-SAFT) equation of state[29,30]. The PC-SAFT equation of state is formulated in terms of the Helmholtz energy allowing easy generalization to Helmholtz energy functionals. PC-SAFT provides good descriptions of thermodynamic properties in bulk phases for a wide variety of real substances and mixtures, including components of low molecular mass[30], but also complex species like polymers[31] or associating substances[32]. The underlying molecular model regards molecules as hard chains with attractive van der Waals segment-segment interactions or hydrogen-bonding (associating)[32–37] or dipolar and quadrupolar interactions[38–40]. Several approaches combining PC-SAFT and DFT have been proposed. Gross[41] described a DFT for pure substances which was generalized by Klink and

Gross for mixtures and successfully applied to vapor-liquid[42], liquid-liquid interfaces[43]. Klink *et al.*[44] and Lamanna *et al.*[45] applied this PC-SAFT DFT to interfacial transport resistivities. Sauer and Gross[46] suggested a Helmholtz energy functional for the dispersion contribution based on a weighted density approximation suitable for confined systems, predicting physical phenomena like surface tension, contact angles[47] and adsorption isotherms. Similar approaches were taken by Shen *et al.*[48,49], Ye *et al.*[50] and Xu *et al.*[51].

This work provides a practical guide to implementing and solving DFT models that are based on weighted densities. We wish to facilitate the use of DFT approaches in engineering applications. More specifically we demonstrate implementation of the ideal gas, hard-sphere, hard-chain and dispersion contribution of PC-SAFT DFT in Cartesian, cylindrical and spherical coordinate systems. We use the FFT algorithm for Cartesian coordinates and the axial contribution to cylindrical systems, the fast Hankel transform is applied for the radial contribution to cylindrical systems and the fast sine and cosine transform is adopted for systems described in spherical coordinates. In contrast to previous work using cylindrical coordinates[18], we apply the fast Hankel transform of Hansen[52,53], which allows computation of Hankel transforms on equidistant (rather than logarithmic) grids by using a combination of fast Abel[54] and fast sine and cosine transforms. Equidistant grids reduce computational overhead because a smaller number of overall grid points is usually possible, while maintaining the same worst-case grid density as compared to logarithmic grids. Fourier space convolution is easier to implement than naïve real space convolution, which allows writing robust simulation codes.

The general procedure is shown for weighted density approximations in the main part of this work. A detailed description of equations for Helmholtz energy functionals based on the PC-SAFT equation of state is provided in the supporting information*, including functional derivatives of the model as well as a comprehensive introduction to Fourier space convolution.

3.2 Classical Density Functional Theory

The starting point for classical DFT is the grand potential functional Ω, which, for a mixture of N_c components is written as

$$\Omega[\{\rho_i(\mathbf{r})\}] = F[\{\rho_i(\mathbf{r})\}] + \sum_{i=1}^{N_c} \int \rho_i(\mathbf{r}) \left(V_i^{\text{ext}}(\mathbf{r}) - \mu_i \right) \mathrm{d}\mathbf{r} \tag{3.1}$$

with Helmholtz energy functional F, chemical potential μ_i of component i and the external potential V_i^{ext}, acting on component i. Although not made explicit in this notation, the

*in appendix A

specified variables of Ω are temperature T, volume V, and chemical potentials μ_i of all species. Square brackets denote a functional dependence and curly brackets around $\{\rho_i(\mathbf{r})\}$ indicate a vector of all densities within a mixture, $i = 1, \ldots, N_c$.

In equilibrium the grand potential functional is minimal and the value of the grand potential functional reduces to the grand potential $\Omega^0 = \Omega[\{\rho_i^0\}]$. The minimum implies, that for the equilibrium density profile $\{\rho_i^0(\mathbf{r})\}$, the functional derivatives of the grand potential functional Ω with respect to the density profiles $\{\rho_i(\mathbf{r})\}$ vanish according to

$$\left.\frac{\delta\Omega[\{\rho_i\}]}{\delta\rho_j(\mathbf{r})}\right|_{\{\rho_i^0(\mathbf{r})\}} = 0 \tag{3.2}$$

which leads to the main equation of DFT

$$\frac{\delta F[\{\rho_i\}]}{\delta\rho_j(\mathbf{r})} = \mu_j - V_j^{\mathrm{ext}}(\mathbf{r}) \qquad \forall j \tag{3.3}$$

that can be solved for the density profiles $\{\rho_i^0(\mathbf{r})\}$ in the considered volume, provided a model for the Helmholtz energy functional is available.

3.2.1 Weighted Density Approximation Functionals

Weighted density approximation functionals can be constructed generically as

$$\beta F[\{\rho_i(\mathbf{r})\}] = \int \Phi(\{n_\alpha(\mathbf{r}), \mathbf{n}_\beta(\mathbf{r})\})\,\mathrm{d}\mathbf{r} \tag{3.4}$$

where $\alpha \in \{1, \ldots\}$ is a generic index that denotes the scalar-valued weighted densities and $\beta \in \{\mathrm{V1}, \ldots\}$ points at the vector-valued weighted densities, with $\beta F = \frac{F}{k_\mathrm{B}T}$, where k_B is the Boltzmann constant, and with the reduced Helmholtz energy density Φ, which is solely a function of the weighted densities $n_{\alpha,\beta}$. The weighted densities $n_{\alpha,\beta}$ are calculated via convolution of the density profile $\{\rho_i\}$ as

$$n_{\alpha,\beta}(\mathbf{r}) = \sum_{i=1}^{N_c} \int \rho_i(\mathbf{r}')\omega_i^{\alpha,\beta}(\mathbf{r}-\mathbf{r}')\,\mathrm{d}\mathbf{r}' \equiv \sum_{i=1}^{N_c} \rho_i(\mathbf{r}) \otimes \omega_i^{\alpha,\beta}(\mathbf{r}) \tag{3.5}$$

The respective weight functions ω_i^α are typically defined as functions including Heaviside step functions Θ, Dirac delta functions δ, or derivatives thereof δ' as shown for scalar-valued

weight functions

$$\omega_i^\alpha(\mathbf{r}) \propto \Theta(R_i - |\mathbf{r}|) \tag{3.6a}$$
$$\omega_i^\alpha(\mathbf{r}) \propto \delta(R_i - |\mathbf{r}|) \tag{3.6b}$$
$$\omega_i^\alpha(\mathbf{r}) \propto \delta'(R_i - |\mathbf{r}|) \tag{3.6c}$$

Vector-valued weight functions are expressed as combinations of the previous weights with the position vector $\mathbf{r}$ as

$$\omega_i^\beta(\mathbf{r}) \propto \frac{\mathbf{r}}{|\mathbf{r}|}\omega_i^\alpha(\mathbf{r}) \tag{3.7}$$

For the case of eq. (3.6a) one averages over a spherical volume, whereas for the case of eq. (3.6b), the weighting is defined on the surface of a sphere with radius R_i. The functional derivative is calculated as

$$\frac{\delta\beta F^{\mathrm{hs}}[\{\rho_i\}]}{\delta\rho_j(\mathbf{r})} = \int \frac{\delta\Phi}{\delta\rho_j(\mathbf{r})}\,\mathrm{d}\mathbf{r}' = \int \sum_{\alpha,\beta} \frac{\partial\Phi}{\partial n_{\alpha,\beta}(\mathbf{r}')} \cdot \frac{\delta n_{\alpha,\beta}(\mathbf{r}')}{\delta\rho_j(\mathbf{r})}\,\mathrm{d}\mathbf{r}' \tag{3.8}$$

with the functional derivative of the weighted densities according to

$$\begin{aligned}\frac{\delta n_{\alpha,\beta}(\mathbf{r}')}{\delta\rho_j(\mathbf{r})} &= \frac{\delta}{\delta\rho_j(\mathbf{r})}\sum_{i=1}^{N_c}\int \rho_i(\mathbf{r}'')\omega_i^{\alpha,\beta}(\mathbf{r}'-\mathbf{r}'')\,\mathrm{d}\mathbf{r}'' \\ &= \sum_{i=1}^{N_c}\int \delta_{ij}\delta(\mathbf{r}''-\mathbf{r})\omega_i^{\alpha,\beta}(\mathbf{r}'-\mathbf{r}'')\,\mathrm{d}\mathbf{r}'' = \omega_j^{\alpha,\beta}(\mathbf{r}'-\mathbf{r})\end{aligned} \tag{3.9}$$

with δ_{ij} as the Kronecker delta and δ as the Dirac delta function. Substitution of eq. (3.9) in eq. (3.8) allows the functional derivative to be rewritten as a sum of convolution integrals according to

$$\frac{\delta\beta F^{\mathrm{hs}}[\{\rho_i\}]}{\delta\rho_j(\mathbf{r})} = \sum_{\alpha,\beta}\int \frac{\partial\Phi}{\partial n_{\alpha,\beta}}\omega_j^{\alpha,\beta}(\mathbf{r}'-\mathbf{r})\,\mathrm{d}\mathbf{r}' = \sum_\alpha \frac{\partial\Phi}{\partial n_\alpha}\otimes\omega_j^\alpha - \sum_\beta \frac{\partial\Phi}{\partial \mathbf{n}_\beta}\otimes\omega_j^\beta \tag{3.10}$$

The scalar-valued weight functions are even, with

$$\omega_i^\alpha(\mathbf{r}'-\mathbf{r}) = \omega_i^\alpha(\mathbf{r}-\mathbf{r}') \qquad \text{for } \alpha \in \{1,\dots\} \tag{3.11}$$

while the vector-valued weight functions are odd functions

$$\boldsymbol{\omega}_i^{\beta}(\mathbf{r}'-\mathbf{r}) = -\boldsymbol{\omega}_i^{\beta}(\mathbf{r}-\mathbf{r}') \qquad \text{for } \beta \in \{\mathrm{V1}, \dots\} \tag{3.12}$$

leading to the minus signs in eq. (3.10).

3.3 Fourier Space Convolutions

Weighted density approximation functionals and functional derivatives can be calculated efficiently in Fourier space, by making use of the convolution theorem of the Fourier transform. In this section, we show how to compute the required Fourier transforms in various coordinate systems using off-the-shelf FFT, fast Hankel, fast sine/cosine transform algorithms.

We show the procedure by considering weighted densities as convolutions of density ρ_i with weight function ω_i. One transforms the density profile ρ_i to Fourier space using a discrete transform scheme and, after multiplication in Fourier space with the analytically transformed weight function, transforms the result back to real space using the inverse discrete transform scheme according to

$$\begin{aligned} n_{\alpha,\beta}(\mathbf{r}) &= \int \rho_i(\mathbf{r}')\omega_i^{\alpha,\beta}(\mathbf{r}-\mathbf{r}')\,\mathrm{d}\mathbf{r}' = \rho_i(\mathbf{r}) \otimes \omega_i^{\alpha,\beta}(\mathbf{r}) \\ &= \mathcal{F}^{-1}\left[\mathcal{F}\left[\rho_i(\mathbf{r})\right]\mathcal{F}\left[\omega_i^{\alpha,\beta}(\mathbf{r})\right]\right] = \mathcal{F}^{-1}\left[\hat{\rho}_i(\mathbf{k})\hat{\omega}_i^{\alpha,\beta}(\mathbf{k})\right] \end{aligned} \tag{3.13}$$

with the Fourier space vector $\mathbf{k}$, and introducing the Fourier transform $\mathcal{F}$ and inverse Fourier transform operator $\mathcal{F}^{-1}$. The circumflex ($\hat{}$) above quantities indicates them being the Fourier transforms of the respective quantity.

The scalar-valued weight functions in Fourier space, eq. (3.6), are obtained using

$$\hat{\omega}_i^{\alpha}(\mathbf{k}) = \mathcal{F}\left[\omega_i^{\alpha}(\mathbf{r})\right] \tag{3.14}$$

The vector-valued weight functions in Fourier space can be described by

$$\hat{\omega}_i^{\beta}(\mathbf{k}) \propto -\mathrm{i}\,\mathbf{k}\hat{\omega}_i^{\alpha}(\mathbf{k}) \tag{3.15}$$

where the position vector $\frac{\mathbf{r}}{|\mathbf{r}|}$ in eq. (3.7) transforms to $(-\mathrm{i}\,\mathbf{k})$ in Fourier space, with the imaginary unit i.

3.3.1 Convolution in Cartesian Coordinates

For Cartesian coordinates we substitute $\mathbf{r} = [x, y, z]^\intercal$ and $\mathbf{k} = [k_x, k_y, k_z]^\intercal$. The Fourier transform of the density profiles is computed as

$$\hat{\rho}_i(k_x, k_y, k_z) = \mathcal{F}_x \mathcal{F}_y \mathcal{F}_z \left[\rho_i(x, y, z)\right] \tag{3.16}$$

just as presented in appendix B.2 in eq. (B.11). For computation of the scalar-valued weighted densities

$$n_\alpha(x, y, z) = \sum_{i=1}^{N_c} \mathcal{F}_x^{-1} \mathcal{F}_y^{-1} \mathcal{F}_z^{-1} \left[\hat{\rho}_i(k_x, k_y, k_z) \hat{\omega}_i^\alpha(k_x, k_y, k_z)\right] \tag{3.17}$$

the inverse Fourier transform for scalar functions, eq. (B.12), is needed. For the vector-valued weighted densities we use the vector-valued weight functions in Fourier space from eq. (3.15). The inverse Fourier transform is obtained as

$$\mathbf{n}_\beta(x, y, z) = \sum_{i=1}^{N_c} \mathcal{F}^{-1} \left[-\mathrm{i}\, \mathbf{k} \hat{\omega}_i^\alpha(\mathbf{k}) \hat{\rho}_i(\mathbf{k})\right] \tag{3.18}$$

with

$$\mathcal{F}^{-1} \left[-\mathrm{i}\, \mathbf{k} \hat{\omega}_i^\alpha(\mathbf{k}) \hat{\rho}_i(\mathbf{k})\right] = \begin{pmatrix} \mathcal{F}_x^{-1} \mathcal{F}_y^{-1} \mathcal{F}_z^{-1} \left[-\mathrm{i}\, k_x\, \hat{\omega}_i^\alpha(k_x, k_y, k_z) \hat{\rho}_i(k_x, k_y, k_z)\right] \\ \mathcal{F}_x^{-1} \mathcal{F}_y^{-1} \mathcal{F}_z^{-1} \left[-\mathrm{i}\, k_y\, \hat{\omega}_i^\alpha(k_x, k_y, k_z) \hat{\rho}_i(k_x, k_y, k_z)\right] \\ \mathcal{F}_x^{-1} \mathcal{F}_y^{-1} \mathcal{F}_z^{-1} \left[-\mathrm{i}\, k_z\, \hat{\omega}_i^\alpha(k_x, k_y, k_z) \hat{\rho}_i(k_x, k_y, k_z)\right] \end{pmatrix} \tag{3.19}$$

using the inverse Fourier transform for vector-valued functions from eq. (B.19). The convolution integrals of the Helmholtz energy density derivatives $\frac{\partial \Phi}{\partial n_\alpha}$ with the weight functions ω_i^α are computed similarly.

The scalar-valued convolution integrals in eq. (3.10) are obtained using the scalar inverse Fourier transform from eq. (B.12), leading to

$$\frac{\partial \Phi}{\partial n_\alpha} \otimes \omega_i^\alpha = \mathcal{F}_x^{-1} \mathcal{F}_y^{-1} \mathcal{F}_z^{-1} \left[\frac{\hat{\partial \Phi}}{\partial n_\alpha}(k_x, k_y, k_z) \hat{\omega}_i^\alpha(k_x, k_y, k_z)\right] \tag{3.20}$$

with the scalar Fourier transform of the partial derivative of the Helmholtz energy density, eq. (B.11), computed according to

$$\frac{\hat{\partial \Phi}}{\partial n_\alpha}(k_x, k_y, k_z) = \mathcal{F}_x \mathcal{F}_y \mathcal{F}_z \left[\frac{\partial \Phi}{\partial n_\alpha}(x, y, z)\right] \tag{3.21}$$

The vector-valued convolution integrals in eq. (3.10) can be handled using the inverse Fourier transform of scalar-valued functions, eq. (B.12), leading to

$$\frac{\partial \Phi}{\partial \mathbf{n}_\beta} \otimes \omega_i^\beta = \mathcal{F}_x^{-1}\mathcal{F}_y^{-1}\mathcal{F}_z^{-1}\left[\left.\frac{\partial \hat{\Phi}}{\partial \mathbf{n}_\beta}\right|_{k_x} \hat{\omega}_i^\beta|_{k_x} + \left.\frac{\partial \hat{\Phi}}{\partial \mathbf{n}_\beta}\right|_{k_y} \hat{\omega}_i^\beta|_{k_y} + \left.\frac{\partial \hat{\Phi}}{\partial \mathbf{n}_\beta}\right|_{k_z} \hat{\omega}_i^\beta|_{k_z} \right] \tag{3.22}$$

where the dot product in Fourier space is used, calculated according to

$$\frac{\partial \hat{\Phi}}{\partial \mathbf{n}_\beta} \cdot \hat{\omega}_i^\beta = \begin{pmatrix} \left.\frac{\partial \hat{\Phi}}{\partial \mathbf{n}_\beta}\right|_{k_x} \\ \left.\frac{\partial \hat{\Phi}}{\partial \mathbf{n}_\beta}\right|_{k_y} \\ \left.\frac{\partial \hat{\Phi}}{\partial \mathbf{n}_\beta}\right|_{k_z} \end{pmatrix} \cdot \begin{pmatrix} \hat{\omega}_i^\beta|_{k_x} \\ \hat{\omega}_i^\beta|_{k_y} \\ \hat{\omega}_i^\beta|_{k_z} \end{pmatrix} = \left.\frac{\partial \hat{\Phi}}{\partial \mathbf{n}_\beta}\right|_{k_x} \hat{\omega}_i^\beta|_{k_x} + \left.\frac{\partial \hat{\Phi}}{\partial \mathbf{n}_\beta}\right|_{k_y} \hat{\omega}_i^\beta|_{k_y} + \left.\frac{\partial \hat{\Phi}}{\partial \mathbf{n}_\beta}\right|_{k_z} \hat{\omega}_i^\beta|_{k_z} \tag{3.23}$$

whereby the vector-valued weight functions, eq. (3.15), in Fourier space in each direction are defined as

$$\hat{\omega}_i^\beta|_{k_x}(k_x,k_y,k_z) = -\mathrm{i}\,k_x \hat{\omega}_i^\alpha(k_x,k_y,k_z) \tag{3.24a}$$
$$\hat{\omega}_i^\beta|_{k_y}(k_x,k_y,k_z) = -\mathrm{i}\,k_y \hat{\omega}_i^\alpha(k_x,k_y,k_z) \tag{3.24b}$$
$$\hat{\omega}_i^\beta|_{k_z}(k_x,k_y,k_z) = -\mathrm{i}\,k_z \hat{\omega}_i^\alpha(k_x,k_y,k_z) \tag{3.24c}$$

The vector-valued Fourier transform, eq. (B.16), of the vector-valued derivatives of the reduced Helmholtz energy yields

$$\frac{\partial \hat{\Phi}}{\partial \mathbf{n}_\beta}(k_x,k_y,k_z) = \begin{pmatrix} \mathcal{F}_x\mathcal{F}_y\mathcal{F}_z\left[\left.\frac{\partial \Phi}{\partial \mathbf{n}_\beta}\right|_x(x,y,z)\right] \\ \mathcal{F}_x\mathcal{F}_y\mathcal{F}_z\left[\left.\frac{\partial \Phi}{\partial \mathbf{n}_\beta}\right|_y(x,y,z)\right] \\ \mathcal{F}_x\mathcal{F}_y\mathcal{F}_z\left[\left.\frac{\partial \Phi}{\partial \mathbf{n}_\beta}\right|_z(x,y,z)\right] \end{pmatrix} \tag{3.25}$$

3.3.2 Convolution in Cylindrical Coordinates

We regard problems in cylindrical coordinates with angular symmetry, leading to two-dimensional problems. The presented formalism follows Boţan *et al.* [18], but instead of separating the external potential to obtain vanishing boundary conditions, we separate the density profile directly. The fast Hankel transform algorithm used for computing the Fourier transform requires the function to vanish for large values of the radial coordinate r. That is why we decompose the density profile into a part that approaches zero at large $r = r_{\max}$ and a part that only depends on the axial coordinate according to

$$\rho_i(r,z) = \rho_i^\Delta(r,z) + \rho_i^\infty(z) \tag{3.26}$$

The contribution that shifts the density profiles is defined at the r-boundary $\rho_i^\infty(z) \equiv \rho_i(r = r_{\max}, z)$. The remaining contribution $\rho_i^\Delta(r,z)$ is well-behaved for a treatment with the fast Hankel transform.

The Fourier transform of the density profiles is computed according to eq. (B.29) as presented in appendix B.2

$$\hat{\rho}_i(k_r,k_z) = \mathcal{F}_z\mathcal{H}_0\left[\rho_i^\Delta(r,z)\right] + \mathcal{F}_z\left[\rho_i^\infty(z)\right]\frac{\delta(k_r)}{2\pi k_r} \tag{3.27}$$

with the Hankel transform of order zero $\mathcal{H}_0$. The solely z-dependent contribution ρ_i^∞ is transformed via a Fourier transform in z-direction, while the analytical Hankel transform in the constant r-direction yields $\frac{\delta(k_r)}{2\pi k_r}$.

The scalar-valued weighted densities n_α, are calculated using the inverse Fourier transform for scalar functions, eq. (B.30), leading to

$$n_\alpha(r,z) = \sum_{i=1}^{N_c}\left(\mathcal{F}_z^{-1}\mathcal{H}_0^{-1}\left[\hat{\rho}_i^\Delta(k_r,k_z)\hat{\omega}_i^\alpha(k_r,k_z)\right] + \mathcal{F}_z^{-1}\left[\hat{\rho}^\infty(k_z)\hat{\omega}_i^\alpha(k_r=0,k_z)\right]\right) \tag{3.28}$$

For the vector-valued weighted densities we use the vector-valued weight functions from eq. (3.15). The inverse Fourier transform is obtained as

$$\begin{aligned}\mathbf{n}_\beta(r,z) = \sum_{i=1}^{N_c}\Bigg(&\begin{pmatrix}\mathcal{F}_z^{-1}\mathcal{H}_1^{-1}\left[k_r\,\hat{\omega}_i^\alpha(k_r,k_z)\hat{\rho}_i^\Delta(k_r,k_z)\right]\\ 0\\ \mathcal{F}_z^{-1}\mathcal{H}_0^{-1}\left[-\mathrm{i}\,k_z\,\hat{\omega}_i^\alpha(k_r,k_z)\hat{\rho}_i^\Delta(k_r,k_z)\right]\end{pmatrix}\\ &+\begin{pmatrix}0\\0\\ \mathcal{F}_z^{-1}\left[-\mathrm{i}\,k_z\,\hat{\omega}_i^\alpha(k_r=0,k_z)\hat{\rho}_i^\infty(k_z)\right]\end{pmatrix}\Bigg)\end{aligned} \tag{3.29}$$

with the Hankel transform of zeroth and first order, $\mathcal{H}_0$ and $\mathcal{H}_1$, respectively. For this result we made use of the inverse Fourier transform for vector-valued functions, eq. (B.45). The convolution integrals of the Helmholtz energy density derivatives $\frac{\partial\Phi}{\partial n_{\alpha,\beta}}$ with the weight functions $\omega_i^{\alpha,\beta}$ are computed similarly. The partial derivatives $\frac{\partial\Phi}{\partial n_{\alpha,\beta}}$ at the r-boundary do not approach zero in general. Analogous to eq. (3.26), we therefore shift the profile by splitting the partial derivatives into a r- and z-dependent contribution $\frac{\partial\Phi^\Delta}{\partial n_{\alpha,\beta}}(r,z)$, which approaches

zero at the r-boundary, and the z-dependent value at the r-boundary $\frac{\partial \Phi^\infty}{\partial n_{\alpha,\beta}}(z)$ according to

$$\frac{\partial \Phi}{\partial n_{\alpha,\beta}}(r,z) = \frac{\partial \Phi^\Delta}{\partial n_{\alpha,\beta}}(r,z) + \frac{\partial \Phi^\infty}{\partial n_{\alpha,\beta}}(z) \tag{3.30}$$

For the scalar terms one obtains

$$\frac{\partial \Phi}{\partial n_\alpha} \otimes \omega_i^\alpha = \mathcal{F}_z^{-1}\mathcal{H}_0^{-1}\left[\frac{\partial \hat{\Phi}^\Delta}{\partial n_\alpha}(k_r,k_z)\hat{\omega}_i^\alpha(k_r,k_z)\right] + \mathcal{F}_z^{-1}\left[\frac{\partial \hat{\Phi}^\infty}{\partial n_\alpha}(k_z)\hat{\omega}_i^\alpha(k_r=0,k_z)\right] \tag{3.31}$$

using the scalar inverse Fourier transform from eq. (B.30). With the scalar Fourier transform of the partial derivative of the Helmholtz energy density, eq. (B.29), according to

$$\hat{\frac{\partial \Phi}{\partial n_\alpha}}(k_r,k_z) = \mathcal{F}_z\mathcal{H}_0\left[\frac{\partial \Phi^\Delta}{\partial n_\alpha}(r,z)\right] + \mathcal{F}_z\left[\frac{\partial \Phi^\infty}{\partial n_\alpha}(z)\right]\frac{\delta(k_r)}{2\pi k_r} \tag{3.32}$$

For the vector-valued contributions we have

$$\frac{\partial \Phi}{\partial \mathbf{n}_\beta} \otimes \omega_i^\beta = \mathcal{F}_z^{-1}\mathcal{H}_0^{-1}\left[\hat{\frac{\partial \Phi}{\partial \mathbf{n}_\alpha}}\Big|_{k_r}\hat{\omega}_i^\alpha|_{k_r} + \hat{\frac{\partial \Phi}{\partial \mathbf{n}_\alpha}}\Big|_{k_z}\hat{\omega}_i^\alpha|_{k_z}\right] \tag{3.33}$$

where the expression in angular brackets results from the dot product in Fourier space

$$\hat{\frac{\partial \Phi}{\partial \mathbf{n}_\beta}} \cdot \hat{\omega}_i^\beta = \begin{pmatrix} \hat{\frac{\partial \Phi}{\partial \mathbf{n}_\beta}}\big|_{k_r} \\ 0 \\ \hat{\frac{\partial \Phi}{\partial \mathbf{n}_\beta}}\big|_{k_z} \end{pmatrix} \cdot \begin{pmatrix} \hat{\omega}_i^\beta|_{k_r} \\ 0 \\ \hat{\omega}_i^\beta|_{k_z} \end{pmatrix} = \hat{\frac{\partial \Phi}{\partial \mathbf{n}_\beta}}\Big|_{k_r}\hat{\omega}_i^\beta|_{k_r} + \hat{\frac{\partial \Phi}{\partial \mathbf{n}_\beta}}\Big|_{k_z}\hat{\omega}_i^\beta|_{k_z} \tag{3.34}$$

requiring the weight functions from eq. (3.15)

$$\hat{\omega}_i^\beta|_{k_r}(k_r,k_z) = -\mathrm{i}\,k_r\hat{\omega}_i^\alpha(k_r,k_z) \tag{3.35a}$$
$$\hat{\omega}_i^\beta|_{k_z}(k_r,k_z) = -\mathrm{i}\,k_z\hat{\omega}_i^\alpha(k_r,k_z) \tag{3.35b}$$

using the inverse Fourier transform for scalar functions from eq. (B.30). Equation (3.33) further requires the vector-valued Fourier transform, eq. (B.38), of the vector-valued derivatives

$$\hat{\frac{\partial \Phi}{\partial \mathbf{n}_\beta}}(k_r,k_z) = \begin{pmatrix} \mathcal{F}_z\mathcal{H}_1\left[-\mathrm{i}\,\frac{\partial \Phi^\Delta}{\partial \mathbf{n}_\beta}\big|_r(r,z)\right] \\ 0 \\ \mathcal{F}_z\mathcal{H}_0\left[\frac{\partial \Phi^\Delta}{\partial \mathbf{n}_\beta}\big|_z(r,z)\right] \end{pmatrix} + \begin{pmatrix} 0 \\ 0 \\ \mathcal{F}_z\left[\frac{\partial \Phi^\infty}{\partial \mathbf{n}_\beta}(z)\right]\frac{\delta(k_r)}{2\pi k_r} \end{pmatrix} \tag{3.36}$$

Combining eqs. (3.35) and (3.36) in eq. (3.33) we obtain for the vector-valued contributions

$$\frac{\partial\Phi}{\partial\mathbf{n}_\beta}\otimes\omega_i^\beta=\mathcal{F}_z^{-1}\mathcal{H}_0^{-1}\Bigg[-\mathrm{i}\,\hat{\omega}_i^\alpha(k_r,k_z)\Bigg(k_r\frac{\partial\hat{\Phi}^\Delta}{\partial\mathbf{n}_\beta}\Big|_{k_r}(k_r,k_z)+k_z\frac{\partial\hat{\Phi}^\Delta}{\partial\mathbf{n}_\beta}\Big|_{k_z}(k_r,k_z)\Bigg)\Bigg]$$
$$+\mathcal{F}_z^{-1}\Bigg[-\mathrm{i}\,k_z\,\hat{\omega}_i^\alpha(k_r=0,k_z)\frac{\partial\hat{\Phi}^\infty}{\partial\mathbf{n}_\beta}\Big|_{k_z}(k_z)\Bigg] \tag{3.37}$$

3.3.3 Convolution in Spherical Coordinates

The fast sine/cosine transform algorithms used for computing the Fourier transform in spherical coordinates require the function to vanish for large values of r. If the density profiles $\rho_i(r)$ do not approach zero, we define shifted profiles $\rho_i^\Delta(r)$ which do approach zero at large radial distances $r=r_{\max}$ by splitting the density profile

$$\rho_i(r)=\rho_i^\Delta(r)+\rho_i^\infty \tag{3.38}$$

into a r-dependent contribution $\rho_i^\Delta(r)$, vanishing at the boundary, and the constant value at the boundary $\rho_i^\infty(r=r_{\max})$. The Fourier transform of the density profiles is computed as presented in appendix B.2 according to eq. (B.53) while the constant boundary value can be computed analytically, leading to

$$\hat{\rho}_i(k_r)=\frac{2}{k_r}\mathcal{SIN}\left[\rho_i^\Delta(r)\,r\right]+\rho_i^\infty\delta(k_r) \tag{3.39}$$

The scalar-valued weighted densities n_α, are then calculated based on the inverse Fourier transform for scalar functions, eq. (B.54), leading to

$$n_\alpha(r)=\sum_{i=1}^{N_c}\left(\frac{2}{r}\mathcal{SIN}\left[k_r\,\hat{\omega}_i^\alpha(k_r)\hat{\rho}_i^\Delta(k_r)\right]+\hat{\omega}_i^\alpha(k_r=0)\rho_i^\infty\right) \tag{3.40}$$

For the vector-valued weighted densities we use the vector-valued weight functions, eq. (3.15), and transform them back to real space using the inverse Fourier transform for vector-valued functions from eq. (B.72). For the vector-valued weight functions

$$\mathbf{n}_\beta(r)=\sum_{i=1}^{N_c}\left(\mathbf{e}_r\frac{\mathrm{i}}{\pi r^2}\mathcal{SIN}\left[-\mathrm{i}\,k_r\,\hat{\omega}_i^\alpha(k_r)\hat{\rho}_i^\Delta(k_r)\right]-\mathbf{e}_r\frac{2\mathrm{i}}{r}\mathcal{COS}\left[-\mathrm{i}\,k_r\,\hat{\omega}_i^\alpha(k_r)\,k_r\hat{\rho}_i^\Delta(k_r)\right]\right) \tag{3.41}$$

the convolution with the constant value from shifting the density profile vanishes due to $\hat{\omega}_i^\beta(k_r=0)=0$. The convolution integrals of the Helmholtz energy density derivatives $\frac{\partial\Phi}{\partial n_{\alpha,\beta}}$ with the weight functions $\omega_i^{\alpha,\beta}$ are computed similarly. If the partial derivatives $\frac{\partial\Phi}{\partial n_{\alpha,\beta}}$ do not

vanish, we shift the profile to zero by splitting the partial derivatives into a r-dependent contribution $\frac{\partial \Phi^\Delta}{\partial n_{\alpha,\beta}}(r)$, vanishing at the boundary, and the constant value at the boundary $\frac{\partial \Phi^\infty}{\partial n_{\alpha,\beta}}$ according to

$$\frac{\partial \Phi}{\partial n_{\alpha,\beta}}(r) = \frac{\partial \Phi^\Delta}{\partial n_{\alpha,\beta}}(r) + \frac{\partial \Phi^\infty}{\partial n_{\alpha,\beta}} \tag{3.42}$$

For the scalar terms one obtains

$$\frac{\partial \Phi}{\partial n_\alpha} \otimes \omega_i^\alpha = \frac{2}{r} \mathcal{SIN}\left[\frac{\partial \hat{\Phi}^\Delta}{\partial n_\alpha}(k_r)\hat{\omega}_i^\alpha(k_r)\, k_r\right] + \frac{\partial \Phi^\infty}{\partial n_\alpha}\hat{\omega}_i^\alpha(k_r = 0) \tag{3.43}$$

using the scalar inverse Fourier transform from eq. (B.54). With the scalar Fourier transform of the partial derivative of the Helmholtz energy density, eq. (B.53), obtained from

$$\widehat{\frac{\partial \Phi}{\partial n_\alpha}}(k_r) = \frac{2}{k_r}\mathcal{SIN}\left[\frac{\partial \Phi^\Delta}{\partial n_\alpha}(r)\, r\right] + \frac{\partial \Phi^\infty}{\partial n_\alpha}\delta(k_r) \tag{3.44}$$

For the vector-valued derivatives we compute the dot product

$$\begin{aligned}\widehat{\frac{\partial \Phi}{\partial \mathbf{n}_\beta}} \cdot \hat{\omega}_i^\beta &= \left.\frac{\partial \hat{\Phi}^\Delta}{\partial \mathbf{n}_\beta}\right|_{k_r} \mathbf{e}_{k_r} \cdot \hat{\omega}_i^\beta|_{k_r}\mathbf{e}_{k_r} + \left.\frac{\partial \Phi^\infty}{\partial \mathbf{n}_\beta}\right|_{k_r}\delta(k_r)\mathbf{e}_{k_r}\cdot\hat{\omega}_i^\beta|_{k_r}\mathbf{e}_{k_r} \\ &= \left.\frac{\partial \hat{\Phi}^\Delta}{\partial \mathbf{n}_\beta}\right|_{k_r}\hat{\omega}_i^\beta|_{k_r} + \left.\frac{\partial \Phi^\infty}{\partial \mathbf{n}_\beta}\right|_{k_r}\delta(k_r)\hat{\omega}_i^\beta|_{k_r}\end{aligned} \tag{3.45}$$

in Fourier space, the convolution with the constant value from shifting the density profile vanishes due to $\hat{\omega}_i^\beta(k_r = 0) = 0$. The weight functions, eq. (3.15), are obtained from

$$\hat{\omega}_i^\beta|_{k_r}(k_r) = -\mathrm{i}\, k_r \hat{\omega}_i^\alpha(k_r) \tag{3.46}$$

In real space, this results in

$$\frac{\partial \Phi}{\partial \mathbf{n}_\beta} \otimes \omega_i^\beta = \frac{2}{r}\mathcal{SIN}\left[\left.\frac{\partial \hat{\Phi}^\Delta}{\partial \mathbf{n}_\beta}\right|_{k_r}\hat{\omega}_i^\beta|_{k_r} k_r\right] \tag{3.47}$$

with the inverse Fourier transform for scalar functions, eq. (B.54). With the vector-valued Fourier transform, eq. (B.63), of the vector-valued derivatives obtained from

$$\widehat{\frac{\partial \Phi}{\partial \mathbf{n}_\beta}}(k_r) = \mathbf{e}_{k_r}\frac{2\mathrm{i}}{k_r}\mathcal{COS}\left[\left.\frac{\partial \Phi^\Delta}{\partial \mathbf{n}_\beta}\right|_r(r)\, r\right] - \mathbf{e}_{k_r}\frac{\mathrm{i}}{\pi k_r^2}\mathcal{SIN}\left[\left.\frac{\partial \Phi^\Delta}{\partial \mathbf{n}_\beta}\right|_r(r)\right] + \mathbf{e}_{k_r}\left.\frac{\partial \Phi^\infty}{\partial \mathbf{n}_\beta}\right|_{k_r}\delta(k_r) \tag{3.48}$$

Combining the above equations for the vector-valued convolution, we obtain

$$\frac{\partial \Phi}{\partial \mathbf{n}_\beta} \otimes \omega_i^\beta = \frac{2}{r} \mathcal{SIN}\left[-\mathrm{i}\, k_r \hat{\omega}_i^\alpha(k_r) \frac{\partial \hat{\Phi}^\Delta}{\partial \mathbf{n}_\beta}\Big|_{k_r} k_r \right] \tag{3.49}$$

3.4 From Integral Transform to Discretized Representation

In this section, we discuss the transition from continuous integral transforms to discrete representations of the inhomogeneous field variables (e.g., ρ_i). For Cartesian coordinates, the fast Fourier transform is used. For cylindrical coordinates we apply a combination of the fast Fourier and the fast Hankel transform (from a combination of fast Abel and fast Fourier transform, appearing as fast sine and cosine transform). For spherical coordinates the fast sine and cosine transforms are utilized. Because the weight functions from the weighted density approaches ω_i are transformed to Fourier space analytically, we also show the connection of the **r**-grid in real space to the **k**-grid in Fourier space. The fast Fourier, fast sine and fast cosine transforms are taken from *FFTPACK*[55,56], while the fast Abel transform follows Hansen[53] and Hansen and Law[54], described in detail in appendix B.4. Strategies to minimize Gibbs phenomenon are presented in appendix B.6.

3.4.1 Cartesian Grid

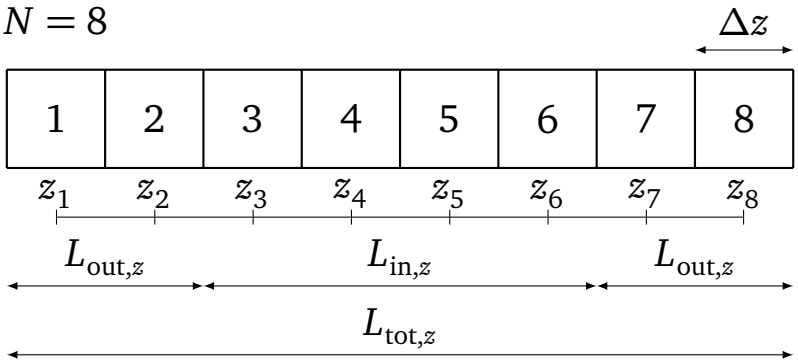

Figure 3.1: Schematic equidistant Cartesian grid with $N = 8$ grid points and grid spacing Δz. The partitioned elements represent a discretization used for finite volume methods, while the function to be transformed is evaluated at the center of those elements z_i. The density profiles are computed on the inner domain $L_{\mathrm{in},z}$, while the buffer zones $L_{\mathrm{out},z}$ compensate the periodic continuation of the FFT and serve as boundary conditions.

For Cartesian coordinates, we use the FFT in each dimension. A schematic grid is visualized in figure 3.1. FFT algorithms require real space samples evaluated on an equidistant grid. Even though a physical problem may be non-periodic in the domain of interest $L_{\mathrm{in},z}$, fast Fourier

transforms will treat the considered domain as is it was surrounded by infinitely many (i.e., periodic) images of itself. To suppress the unwanted effect of periodic copies of the regarded domain, definition of a buffer region $L_{\text{out},z}$ on each side of the domain is needed. The two outer buffer regions $L_{\text{out},z}$ also serve as constant boundary conditions for the evaluation of the weighted densities at the boundary. Due to the functional nature of the problem a buffer domain is required as boundary condition, in contrast to boundary conditions for functions where information about a single point is sufficient.

3.4.1.1 Grid and Boundary Conditions

We thus consider a grid covering three domains, the two outer buffer domains with length $L_{\text{out},z}$, and the inner domain of interest with length $L_{\text{in},z}$, where the density profiles are iterated. To better connect this section to the previous one, we remind that the grand potential functional Ω is a functional of density profiles $\{\rho_i\}$ and a function of the variables $(\{\mu_i\}, T, V)$, whereby the system volume V is defined by the domain length $L_{\text{in},z}$ in z-direction. The choice for the value of the buffer length $L_{\text{out},z}$ is determined by the *influence length* of the weight functions. Here, the weight functions, eq. (3.6), have an influence length of R_i. For the hard-sphere fluid as described with the modified FMT[57,58], two times the influence length corresponds to the closest approach of two hard spheres of type i. Because two types of convolutions are computed (one for computation of the weighted density profiles and one for the convolution of the reduced Helmholtz energy with the weight functions), the buffer length $L_{\text{out},z}$ has to be at least twice the value of R_i. After each of the two convolutions, a fraction of the buffer domain with length R_i is tainted due to possible inhomogeneous boundary conditions and periodic continuation of the FFT, which leads to the length of the buffer zone, as

$$L_{\text{out},z} \geq \max_i \{2R_i(T)\} \tag{3.50}$$

3.4.1.2 Discrete Representation for FFT Algorithm

We now explain the $\mathbf{k}$-grid in Fourier space for the computation of the weight functions, eqs. (3.14) and (3.15). The approach is shown for one dimension only. Higher dimensions are the result of multiple consecutive Fourier transforms and can be treated analogously.

The discrete Fourier transform with Fourier variable k as used in FFT algorithms is defined as

the following sum

$$\hat{f}_k = \sum_{j=0}^{N-1} f_j \, \mathrm{e}^{-2\pi \mathrm{i} \frac{jk}{N}} \qquad \text{with } k = 0, \ldots, (N-1) \tag{3.51}$$

which transforms a finite series of N equally-spaced samples $z_j = j\,\Delta z$ of a function f_j into a series of equally-spaced samples of the function in Fourier space $\hat{f}_k$. Index j denotes the discrete grid points in real space, while k denotes the grid points in Fourier space.

In comparison, the continuous Fourier transform can be discretized as well with $z_j = j\Delta z$ and $f(z_j) = f_j$. The continuous Fourier transform then leads to a similar equation as the discretization of the Fourier transform, eq. (3.51), namely to

$$\hat{f}(k_z) = \int_{z=-\infty}^{\infty} f(z) \, \mathrm{e}^{-2\pi \mathrm{i} z k_z} \, \mathrm{d}z \approx \sum_{j=0}^{N-1} f_j \, \mathrm{e}^{-2\pi \mathrm{i} j \Delta z k_z} \, \Delta z \tag{3.52}$$

where the result is multiplied with Δz compared to the unscaled version in eq. (3.51). Comparison of the arguments of the exponential functions in eqs. (3.51) and (3.52), $\frac{jk}{N} = j\Delta z k_z$, yields the discretization in Fourier space, as

$$k_z = \frac{k}{N\Delta z} = \frac{k}{L_{\mathrm{tot},z}} \qquad \text{with } k = 0, \ldots, (N-1) \tag{3.53}$$

At first glance, this result differs from the one proposed by Knepley *et al.* [1], because we define $L_{\mathrm{tot},z}$ differently. We evaluate the function to be transformed at the center of the elements in figure 3.1 instead of the edges, as done by Knepley *et al.* [1], so that the regarded overall domain for the work of Knepley *et al.* ($\tilde{L}_{\mathrm{tot},z} = L_{\mathrm{tot},z} - \Delta z$) is different to our overall domain length ($L_{\mathrm{tot},z}$) for the same number of grid points N and the same discretization step size Δz. Complex-valued FFT algorithms include negative k-values as well. For an even number of grid points, the k-vector for the computation of the discrete representation of the weight functions, eqs. (3.14) and (3.15), is

$$k_z = \frac{1}{L_{\mathrm{tot},z}} \left[0, 1, \ldots, \left(\frac{N}{2} - 1\right), \left(-\frac{N}{2}\right), \ldots, -1 \right] \tag{3.54}$$

For real-valued FFT algorithms, the k-vector looks differently

$$k_z = \frac{1}{L_{\mathrm{tot},z}} \left[0, 1, 1, 2, 2, \ldots, \left(\frac{N}{2}\right) \right] \tag{3.55}$$

This yields a k_z-grid in Fourier space which is used for the analytical computation of the

weight functions $\hat{\omega}_i$, eqs. (3.14) and (3.15). These weight functions $\hat{\omega}_i$ are then multiplied in Fourier space with the FFT output of the function to be convolved, the result of which is transformed back to real space using the inverse FFT. For higher dimensions, the k-grid becomes a two- or three-dimensional array, while k_x and k_y are constructed equivalently to eq. (3.54) or eq. (3.55) with their respective length scale $L_{\text{tot},x}$ and $L_{\text{tot},y}$. The absolute value of $\mathbf{k}$ is calculated as

$$|\mathbf{k}| = \sqrt{k_x^2 + k_y^2 + k_z^2} \tag{3.56}$$

3.4.2 Cylindrical Grid

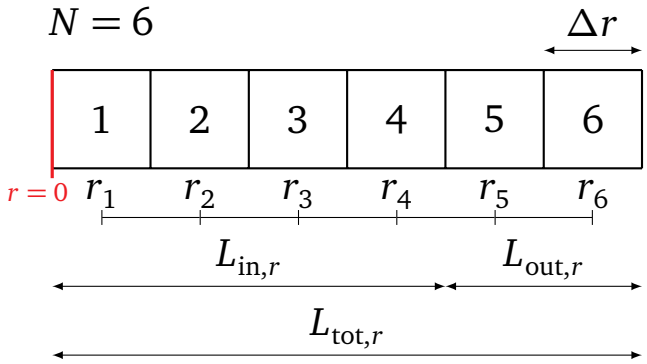

Figure 3.2: Schematic equidistant radial grid with $N = 6$ grid points and grid spacing Δr. The partitioned elements represent a discretization used for finite volume methods, while the function to be transformed is evaluated at the center of those elements r_i. The density profiles are computed on the inner domain $L_{\text{in},r}$, while the buffer zone $L_{\text{tot},r}$ serves as boundary condition, where the density profiles ρ_i^{Δ} go to zero.

For cylindrical coordinates, we use the fast Fourier in axial and the fast Hankel transform (as a combination of fast Abel and fast sine and cosine transform) in radial direction. The procedure of the axial direction is equivalent to the approach for Cartesian coordinates as described in the previous section, therefore, only the radial direction is regarded here. A schematic grid is visualized in figure 3.2. As opposed to the approach of Boţan *et al.* [18], who computed discrete Hankel transform on a logarithmic grid, we adopt the ideas of Hansen [52,53] and Hansen and Law [54], using a combination of Abel and Fourier transforms, which allows computation of the Hankel transform on equidistant grids.

3.4.2.1 Grid and Boundary Conditions

The radial grid is divided into two domains, the outer domain with length $L_{\text{out},r}$, which is needed as boundary condition for the evaluation of the weighted densities at the boundary,

and the inner domain with length $L_{\mathrm{in},r}$, where the density profiles are iterated. Due to even and odd continuation of the fast sine and fast cosine transform, respectively, no boundary domain for $r < 0$ is needed. The size of the outer domain $L_{\mathrm{out},r}$ is determined as described in section 3.4.1.1. Therefore, the size of the outer domain is determined as

$$L_{\mathrm{out},r} \geq \max_i \{2R_i(T)\} \tag{3.57}$$

3.4.2.2 Discrete Representation for FFT and Fast Hankel Transform Algorithms

The **k**-grid in Fourier space for the computation of the weight functions, eqs. (3.14) and (3.15), is computed as follows. The axial direction is equivalent to the Cartesian grid, eq. (3.53), whereas for the radial component the k-values correspond to twice the domain shown in figure 3.2. Instead of the Fourier, the discrete sine and cosine transform are used, which exploit symmetry and, therefore, require only half of the Fourier domain. The length of the whole Fourier domain in radial direction is $(2L_{\mathrm{tot},r})$. This leads to the following k-grid for the radial component

$$k_r = \frac{k}{2N\Delta r} = \frac{k}{2L_{\mathrm{tot},r}} \qquad \text{with } k = 0, \ldots, (N-1) \tag{3.58}$$

This yields a k_r-grid in Fourier space which, together with the k_z-grid, is used for the analytical computation of the weight functions $\hat{\omega}_i$, eqs. (3.14) and (3.15). These weight functions $\hat{\omega}_i$ are then multiplied in Fourier space with the FFT and fast Hankel transform output of the function to be convolved, and this result can be transformed back to real space using the inverse FFT and inverse fast Hankel transform algorithms. For two dimensional problems in cylindrical coordinates, the **k**-grid becomes a two-dimensional array. The absolute value of **k** is calculated as

$$|\mathbf{k}| = \sqrt{k_r^2 + k_z^2} \tag{3.59}$$

In this work, we utilize the projection-slice theorem for the computation of the Hankel transform, where the Hankel transform is replaced by

$$\mathcal{H}_0[f(r)] = \mathcal{F}_r \mathcal{A}[f(r)] \tag{3.60}$$

a combination of Fourier $\mathcal{F}$ and Abel transform $\mathcal{A}$. The algorithm for computation of the fast Hankel transform is based on work of Hansen[52] and described in detail in appendix B.4. The inverse transform is computed from a combination of inverse Abel and inverse Fourier

transform, as

$$\mathcal{H}_0^{-1}\left[\hat{f}(k_r)\right] = \mathcal{A}^{-1}\mathcal{F}_r^{-1}\left[\hat{f}(k_r)\right] \tag{3.61}$$

The Abel transform is computed as described in appendix B.4. As a result of rotational symmetry, all density profiles are even with respect to $r = 0$. This allows using the cosine instead of the Fourier transform. Because some calculations require a division by the radius r, we locate the first grid point at $r = \frac{\Delta r}{2}$. For this grid distribution, we require the discrete cosine transform II ($\mathcal{DCT}_{\mathrm{II}}$) which is available in *FFTPACK* as subroutine *COSQ1B*. More details on the discrete cosine transform are presented in appendix B.5. The Fourier transform of scalar functions $f(r,z)$, using the Hankel transform of zeroth order as in eq. (B.29), is computed from

$$\hat{f}(k_r,k_z) = \mathcal{F}_z\,\mathcal{DCT}_{\mathrm{II}}\,\mathcal{A}[f(r,z)] \tag{3.62}$$

with the Abel transform $\mathcal{A}$. The inverse transform uses the discrete cosine transform III ($\mathcal{DCT}_{\mathrm{III}} = \mathcal{DCT}_{\mathrm{II}}^{-1}$) which is available in *FFTPACK* as subroutine *COSQ1F* and can be computed via

$$f(r,z) = \mathcal{A}^{-1}\,\mathcal{DCT}_{\mathrm{III}}\,\mathcal{F}_z^{-1}\left[\hat{f}(k_r,k_z)\right] \tag{3.63}$$

For vector-valued functions, the Hankel transform of first order is computed from the zeroth order Hankel transform with eq. (B.75) from appendix B.3, leading to

$$\hat{f}(k_r,k_z)|_{k_r} = \mathcal{F}_z\mathcal{H}_1\left[f(r,z)|_r\right] = \mathcal{F}_z\left[\frac{1}{2\pi k_r}\mathcal{DCT}_{\mathrm{II}}\mathcal{A}\left[\frac{f(r,z)|_r}{r} + \frac{\partial f(r,z)|_r}{\partial r}\right]\right] \tag{3.64}$$

The application of this is limited to the radial contribution in eq. (3.36), where $f(r,z)|_r = -\mathrm{i}\,\frac{\partial \Phi^{\Delta}}{\partial \mathbf{n}_\beta}\Big|_r(r,z)$ is an odd function in r. This leads to the derivative $\frac{\partial f(r,z)|_r}{\partial r}$ being an even function. Even continuation of the $\mathcal{DCT}_{\mathrm{II}}$ allows neglecting the odd contribution $\frac{f(r,z)|_r}{r}$, which leads to the simpler form

$$\hat{f}(k_r,k_z)|_{k_r} = \mathcal{F}_z\left[\frac{1}{2\pi k_r}\mathcal{DCT}_{\mathrm{II}}\mathcal{A}\left[\frac{\partial f(r,z)|_r}{\partial r}\right]\right] \tag{3.65}$$

The derivative $\frac{\partial f(r,z)}{\partial r}$ can be approximated using central differences with vanishing boundary conditions from

$$\frac{\partial f(z,r^{(n)})}{\partial r} \approx \frac{f(r^{(n+1)},z) - f(r^{(n-1)},z)}{r^{(n+1)} - r^{(n-1)}} \tag{3.66}$$

The inverse transform is computed similarly according to

$$f(r,z)|_r = \mathcal{H}_1^{-1}\mathcal{F}_z^{-1}\left[\hat{f}(k_r,k_z)|_{k_r}\right] = \frac{1}{r}\mathcal{H}_0^{-1}\left[\frac{\mathcal{F}_z^{-1}\left[\hat{f}(k_r,k_z)|_{k_r}\right]}{2\pi k_r} + \frac{\partial\mathcal{F}_z^{-1}\left[\hat{f}(k_r,k_z)|_{k_r}\right]}{\partial k_r}\right]$$
$$= \frac{1}{r}\mathcal{A}^{-1}\mathcal{F}_r^{-1}\left[\frac{\mathcal{F}_z^{-1}\left[\hat{f}(k_r,k_z)|_{k_r}\right]}{2\pi k_r} + \frac{\partial\mathcal{F}_z^{-1}\left[\hat{f}(k_r,k_z)|_{k_r}\right]}{\partial k_r}\right] \tag{3.67}$$

The derivative in the second term of eq. (3.67) can be replaced using the identity

$$\mathcal{F}_r^{-1}\left[\frac{\partial\hat{g}(k_r,z)}{\partial k_r}\mathrm{i}\right] = 2\pi r\mathcal{F}_r^{-1}\left[\hat{g}(k_r,z)\right] \tag{3.68}$$

with $\hat{g}(k_r,z) = \mathcal{F}_z^{-1}\left[\hat{f}(k_r,k_z)|_{k_r}\right]$. This is applied to eq. (3.29) where $\hat{g}(k_r,z)$ is a real even function in k_r, making $\left(\frac{\partial\hat{g}(k_r,z)}{\partial k_r}\mathrm{i}\right)$ purely imaginary and odd in k_r. The purely imaginary and odd inverse Fourier transform $\mathcal{F}_r^{-1}\left[\frac{\partial\hat{g}(k_r,z)}{\partial k_r}\mathrm{i}\right]$ can, therefore, be replaced by the sine transform $2\pi r\mathcal{DST}_{\mathrm{III}}[\hat{g}(k_r,z)]$. The first term in eq. (3.67) transforms an even function and allows for replacing the Fourier transform $\mathcal{F}_r^{-1}$ with the $\mathcal{DCT}_{\mathrm{III}}$ according to

$$f(r,z)|_r = \frac{1}{r}\mathcal{A}^{-1}\left[\mathcal{DCT}_{\mathrm{III}}\mathcal{F}_z^{-1}\left[\frac{\hat{f}(k_r,k_z)|_{k_r}}{2\pi k_r}\right] + 2\pi r\mathcal{DST}_{\mathrm{III}}\mathcal{F}_z^{-1}\left[\hat{f}(k_r,k_z)|_{k_r}\right]\right] \tag{3.69}$$

Equation (3.65) with eqs. (3.66) and (3.69) are our final equations for the forward and inverse transform in radial direction, respectively.

Here we require the discrete sine transform III ($\mathcal{DST}_{\mathrm{III}}$) which is available in *FFTPACK* as subroutine *SINQ1F*. The grid for the $\mathcal{DST}_{\mathrm{III}}$ algorithm has to be shifted in Fourier space. The procedure is described in section 3.4.3.2 and visualized in figure 3.5. More details on the discrete sine and cosine transform are presented in appendix B.5.

3.4.3 Spherical Grid

In spherical coordinates we only consider one-dimensional problems, where angular symmetry exists. We use the fast sine and fast cosine transform. A schematic grid is visualized in figure 3.3. Fast sine and cosine transform algorithms require real space samples evaluated on an equidistant grid.

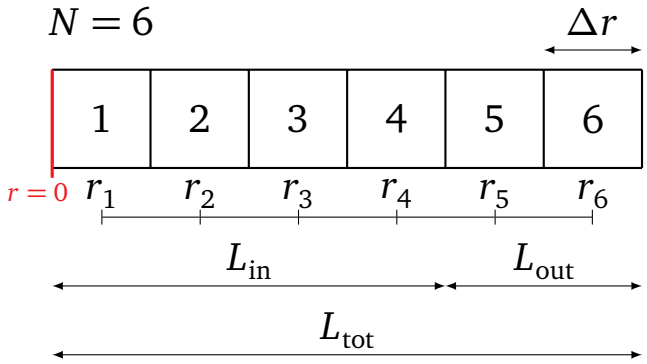

Figure 3.3: Schematic equidistant spherical grid with $N = 6$ grid points and grid spacing Δr. The partitioned elements represent a discretization used for finite volume methods, while the function to be transformed is evaluated at the center of those elements r_i. The density profiles are computed on the inner domain L_{in}, while the buffer zone L_{out} compensates for periodic continuation of the fast sine and cosine transform, and serves as boundary condition, where the density profiles ρ_i^{Δ} go to zero.

3.4.3.1 Grid and Boundary Conditions

Similar to cylindrical coordinates, no boundary domain for $r < 0$ is needed, because the used algorithms for the discrete sine and cosine transform assume odd and even continuation, respectively, which can be exploited here due to spherical symmetry requirements. The size of the outer domain L_{out} is determined as described in section 3.4.1.1. Therefore, the size of the outer domain is determined as

$$L_{\text{out}} \geq \max_i \{2R_i(T)\} \tag{3.70}$$

3.4.3.2 Discrete Representation for Sine and Cosine Transform Algorithms

The **k**-grid in Fourier space for the computation of the weight functions, eqs. (3.14) and (3.15), is computed as follows. The discrete sine and cosine transform are recovered by discretization of the derived Fourier transform in spherical coordinates. There are four relevant variants of the sine and cosine transform, each with a set of different boundary conditions and discretization schemes. Due to the singularity at the origin in spherical coordinates, we locate the first grid point at $r = \frac{\Delta r}{2}$. For this grid distribution, we need the discrete sine transform II ($\mathcal{DST}_{\text{II}}$) according to

$$\hat{f}_{k^*} = \sum_{j=0}^{N-1} f_j \sin\left(\frac{\pi}{N}\left(j + \frac{1}{2}\right)(k^* + 1)\right) \qquad \text{with } k^* = 0, \ldots, (N-1) \tag{3.71}$$

which is available in *FFTPACK* as subroutine *SINQ1B*. More details on the discrete sine transform are presented in appendix B.5. The iteration variable k^* does not represent the true Fourier variable k, which for the $\mathcal{DST}_{\text{II}}$ is obtained from $k = k^* + 1$.

The matching discrete cosine transform is the $\mathcal{DCT}_{\text{II}}$, computed as

$$\hat{f}_k = \sum_{j=0}^{N-1} f_j \cos\left(\frac{\pi}{N}\left(j+\frac{1}{2}\right)k\right) \qquad \text{with } k = 0,\ldots,(N-1) \tag{3.72}$$

which is available in *FFTPACK* as subroutine *COSQ1B*. More details on the discrete cosine transform are presented in appendix B.5. Both transforms transform a finite series of equally-spaced samples $z_j = \frac{1}{N}(j+\frac{1}{2})$ of a function f_j into a series of equal length in Fourier space $\hat{f}_k$. The index j denotes the discrete grid points in real space, while k denotes the grid points in Fourier space.

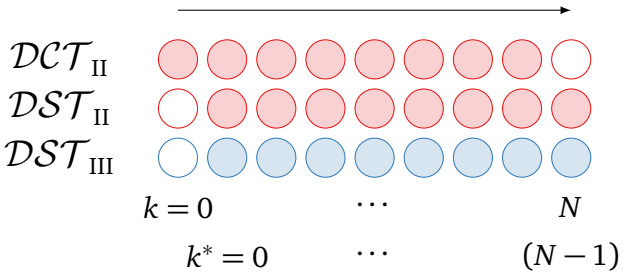

Figure 3.4: Shift of indices to match $\mathcal{DST}_{\text{II}}$ and $\mathcal{DCT}_{\text{II}}$ to $\mathcal{DST}_{\text{III}}$. Filled spheres represent the k-grid of the respective forward (red) and inverse (blue) transform.

For both transforms, indices k and k^* run from $0,\ldots,(N-1)$ in Fourier space, but the $\mathcal{DST}_{\text{II}}$ treats the point $k = 0$ implicitly as $\hat{f}_{k=0}^{\mathcal{DST}} = 0$, while the $\mathcal{DCT}_{\text{II}}$ treats the value $\hat{f}_{k=0}^{\mathcal{DCT}}$ explicitly. In contrast, the $\mathcal{DCT}_{\text{II}}$ does not provide a value for $k = N$, while the $\mathcal{DST}_{\text{II}}$ does (as $k^* = N-1$). Because the transformation to Fourier space in eqs. (3.41) and (3.48) requires $f(r)$ to be multiplied with r, the argument of the sine and cosine transform are always zero at $r = 0$, which leads to $\hat{f}_{k=0}^{\mathcal{DCT}} = 0$.

For the computation of eq. (3.48) a combination of $\mathcal{DST}_{\text{II}}$ and $\mathcal{DCT}_{\text{II}}$ is needed. Because the inverse transform, eq. (3.47), uses solely the $\mathcal{DST}_{\text{III}}$ the value $\hat{f}_{k=0}^{\mathcal{DCT}} = 0$ can be neglected, but the value for $k = N$ (or $k^* = N-1$) for the $\mathcal{DST}_{\text{III}}$ has to be added: $\hat{f}_{k=N}^{\mathcal{DST}} = 0$. This approach is not exact, but a reasonable approximation as $\hat{f}_{k\to\infty}^{\mathcal{DCT}} \to 0$ for smooth functions and appropriate number of grid points. This procedure is necessary to match the different k-values of the $\mathcal{DST}_{\text{II}}$, $\mathcal{DCT}_{\text{II}}$ and $\mathcal{DST}_{\text{III}}$. The shifting of indices is visualized in figure 3.4.

The inverse of the $\mathcal{DST}_{\text{II}}$ and $\mathcal{DCT}_{\text{II}}$ are the $\mathcal{DST}_{\text{III}}$ and $\mathcal{DCT}_{\text{III}}$, respectively. The $\mathcal{DST}_{\text{III}}$ is available from *FFTPACK* as subroutine *SINQ1F* and $\mathcal{DCT}_{\text{III}}$ as subroutine *COSQ1F*. Again, the k-values of the $\mathcal{DST}_{\text{III}}$ and $\mathcal{DCT}_{\text{III}}$ do not match. For computation of eq. (3.41), a function

in Fourier space as result of a $\mathcal{DST}_{\text{II}}$ is transformed back to real space using the $\mathcal{DST}_{\text{III}}$ and $\mathcal{DCT}_{\text{III}}$. The $\mathcal{DST}_{\text{III}}$ can be performed immediately. For the inverse transform using the $\mathcal{DCT}_{\text{III}}$, the exact value $\hat{f}_{k=0}^{\mathcal{DCT}} = 0$ has to be added. Therefore, $\hat{f}_{k=N}^{\mathcal{DST}}$ is disregarded, which has negligible effect as $\hat{f}_{k\to\infty}^{\mathcal{DCT}} \to 0$ for smooth functions and appropriate number of grid points. The shifting of indices is visualized in figure 3.5.

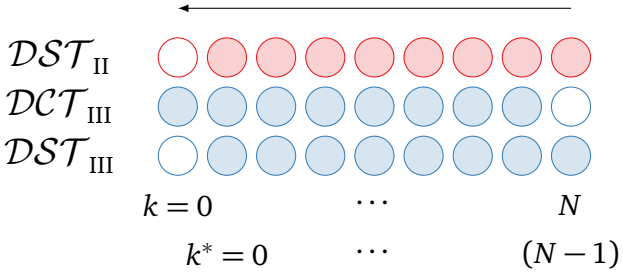

Figure 3.5: Shift of indices to match $\mathcal{DST}_{\text{II}}$ and $\mathcal{DCT}_{\text{III}}$ to $\mathcal{DST}_{\text{II}}$. Filled spheres represent the k-grid of the respective forward (red) and inverse (blue) transform.

For computation of the appropriate discrete k-grid, the analytical sine transform can be discretized with $r_j = (j + \frac{1}{2})\Delta z$ and $f(r_j) = f_j$. This leads to a similar equation as the discrete sine transform, eq. (3.71), according to

$$\hat{f}(k_r) = \int_{r=0}^{\infty} f(r) \sin(2\pi r k_r)\, \mathrm{d}r \approx \sum_{j=0}^{N-1} f_j \sin\left(2\pi\left(j + \frac{1}{2}\right)\Delta r k_r\right)\Delta r \tag{3.73}$$

Comparison of the arguments of the sine functions in eqs. (3.72) and (3.73), $\frac{\pi}{N}(j + \frac{1}{2})(k^* + 1) = 2\pi(j + \frac{1}{2})\Delta r k_r$, yields the discretization in Fourier space according to

$$k_r = \frac{k^* + 1}{2N\Delta z} = \frac{k^* + 1}{2L_{\text{tot}}} \qquad \text{with } k^* = 0, \ldots, (N-1) \tag{3.74}$$

In contrast to eq. (3.53), we divide by $(2L_{\text{tot}})$, because the $\mathcal{DST}_{\text{II}}$ assumes odd continuation by considering only half of the domain compared to the corresponding Fourier transform. For N grid points, the k-vector for the computation of the discrete representation of the weight functions, eqs. (3.14) and (3.15), is

$$k_r^{\mathcal{DST}} = \frac{1}{2L_{\text{tot}}}[1, \ldots, N] \tag{3.75}$$

while the same approach leads to a k-vector for the $\mathcal{DCT}_{\text{II}}$ according to

$$k_r^{\mathcal{DCT}} = \frac{1}{2L_{\text{tot}}}[0, \ldots, (N-1)] \tag{3.76}$$

This yields a k_r-grid in Fourier space which is used for the analytical computation of the weight functions $\hat{\omega}_i$, eqs. (3.14) and (3.15). These weight functions $\hat{\omega}_i$ are then multiplied in Fourier space with the $\mathcal{DST}_{\text{II}}$ and $\mathcal{DCT}_{\text{II}}$ output of the function to be convolved, while this result can be directly transformed back to real space using the $\mathcal{DST}_{\text{III}}$ and $\mathcal{DCT}_{\text{III}}$ algorithms.

3.5 Performance Analysis of FFT Convolution

To compare the efficiency of convolution algorithms using fast Fourier or similar transforms (i.e., discrete sine, cosine and Abel transforms), we compare the performance of one-dimensional FFT convolutions, computed via

$$\rho \otimes \omega = \mathcal{F}_z^{-1}\left[\mathcal{F}_z\left[\rho(z)\right]\hat{\omega}(k_z)\right] \tag{3.77}$$

with three real space convolution algorithms. We adapt the notation of the weighted densities defined in eq. (3.5).

The first real space convolution algorithm, hereafter referred to as *naïve* convolution, approximates the convolution integral of a density profile ρ with the weight function ω (each with N discretization points) over the whole discrete domain, where the value for the i-th element of the discrete sequence is computed according to[59]

$$(\rho \otimes \omega)_i = \frac{1}{N}\sum_{k=0}^{N-1} \omega_k \rho_{i-k} \qquad \forall i \tag{3.78}$$

The second real space algorithm, referred to as *compact* convolution, exploits the fact that weight functions are nonzero on a finite domain. As a consequence, the sequence for the weight function is shorter (length $M < N$) than the sequence for the density profile. Therefore, the value for the i-th element is computed as

$$(\rho \otimes \omega)_i = \frac{1}{M}\sum_{k=-\frac{M-1}{2}}^{\frac{M-1}{2}} \omega_k \rho_{i-k} \qquad \forall i \tag{3.79}$$

with the number of discretization points $M \in \{2n+1 | n \in \mathbb{N}^+\}$ for the weight function, which is always an odd number due to the symmetry of the weight function.

The third real space algorithm uses dense *matrix* multiplication

$$\rho \otimes \omega = \boldsymbol{\omega}\boldsymbol{\rho} \tag{3.80}$$

with the convolution matrix $\boldsymbol{\omega}$ and the density profile vector $\boldsymbol{\rho}$.

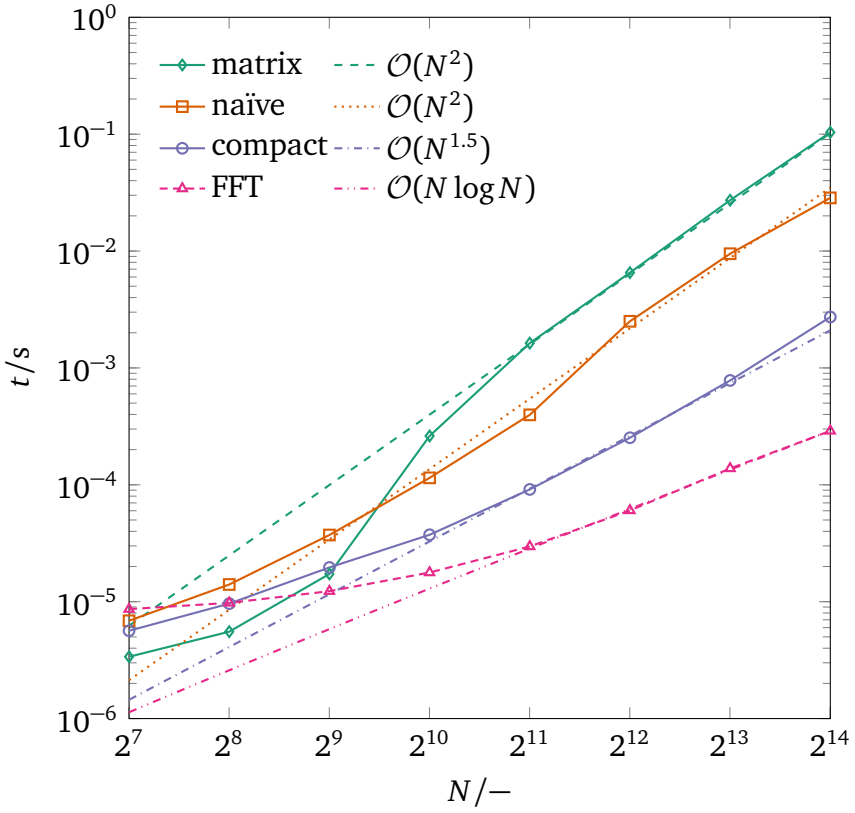

Figure 3.6: Comparison of computing time t for one convolution using Fourier space, naïve, compact and matrix multiplication convolution, eqs. (3.77)–(3.80) respectively, for different number of grid points N, including scaling behavior $\mathcal{O}$. Length of the inner domain is $L_{\text{in},z} = 100\,\text{Å}$ and the radius for convolution is $R = 1.8\,\text{Å}$.

Figure 3.6 depicts the computing time for one convolution using the four algorithms defined in eqs. (3.77)–(3.80) with respect to the number of spatial discretization points N. Additionally, scaling behavior $\mathcal{O}$ of the used algorithms is presented (non-continuous lines).

For small system sizes N, convolutions with convolution matrices perform best, while computing times for naïve, compact and FFT convolutions are higher (staying in the same order of magnitude). For $N = 2^{14}$, the scaling behavior of the FFT, $\mathcal{O}(N \log N)$, renders the FFT convolution at least one order of magnitude faster than the remaining algorithms. For a large number of discretization points, convolutions using a matrix product, eq. (3.80), take the longest, while naïve convolutions, eq. (3.78), compute faster; both scaling with $\mathcal{O}(N^2)$. Compact convolutions, eq. (3.79), scale better with respect to approximately $\mathcal{O}(N^{1.5})$, making this convolution algorithm for large systems superior to the matrix product and naïve approach. FFT convolutions, eq. (3.77), scale best for large systems (here $N = 2^{14}$) according to $\mathcal{O}(N \log N)$, performing at least one order of magnitude better than the remaining algorithms. Even for typical number of discretization points $N = 2^{10} = 1024$ convolution algorithms ex-

ploiting fast Fourier or similar transforms perform best among the four considered numerical convolution approaches.

To summarize, convolution algorithms exploiting fast Fourier or similar transforms perform best for relevant systems among the four considered numerical convolution approaches.

3.6 Conclusion

This work serves as a guide on efficient numerical implementations of classical DFT methods in Cartesian, cylindrical and spherical coordinates using the convolution theorem of the Fourier transform. Applied to Helmholtz energy functionals expressed in terms of weighted densities, this allows for fast and easy DFT calculations using off-the-shelf algorithms: fast Fourier, Hankel, sine and cosine transforms. Especially for two- and three-dimensional problems, using Fourier space convolution simplifies computation of multi-dimensional convolution integrals compared to real space methods. The main text describes scalar-valued and vector-valued weighted densities that appear with FMT. The equations for a Helmholtz energy functional based on the perturbed-chain statistical associating fluid theory are explicitly written out in the supporting information*.

*in appendix A

References

[1] M. G. Knepley, D. A. Karpeev, S. Davidovits, R. S. Eisenberg, and D. Gillespie. An efficient algorithm for classical density functional theory in three dimensions: Ionic solutions. *The Journal of Chemical Physics*, **132**(12):124101, 2010. doi:10.1063/1.3357981.

[2] Y. Rosenfeld. Free-energy model for the inhomogeneous hard-sphere fluid mixture and density-functional theory of freezing. *Physical Review Letters*, **63**:980–983, 1989. doi:10.1103/PhysRevLett.63.980.

[3] L. J. D. Frink, A. G. Salinger, M. P. Sears, J. D. Weinhold, and A. L. Frischknecht. Numerical challenges in the application of density functional theory to biology and nanotechnology. *Journal of Physics: Condensed Matter*, **14**(46):12167, 2002. doi:10.1088/0953-8984/14/46/320.

[4] L. J. D. Frink, M. G. Martin, A. G. Salinger, and M. A. Heroux. High performance computing for the application of molecular theories to biological systems. *Journal of Physics: Conference Series*, **46**(1):304–306, 2006. doi:10.1088/1742-6596/46/1/042.

[5] M. P. Sears and L. J. Frink. A new efficient method for density functional theory calculations of inhomogeneous fluids. *Journal of Computational Physics*, **190**(1):184–200, 2003. doi:10.1016/S0021-9991(03)00270-5.

[6] S. P. Hlushak, W. Rżysko, and S. Sokołowski. Density functional study of flexible chain molecules at curved surfaces. *The Journal of Chemical Physics*, **131**(9):094904, 2009. doi:10.1063/1.3213623.

[7] S. P. Hlushak, C. McCabe, and P. T. Cummings. Fourier space approach to the classical density functional theory for multi-Yukawa and square-well fluids. *The Journal of Chemical Physics*, **137**(10):104104, 2012. doi:10.1063/1.4749381.

[8] S. P. Hlushak, P. T. Cummings, and C. McCabe. Comparison of several classical density functional theories for the adsorption of flexible chain molecules into cylindrical nanopores. *The Journal of Chemical Physics*, **139**(23):234902, 2013. doi:10.1063/1.4843655.

[9] M. Oettel, S. Görig, A. Härtel, H. Löwen, M. Radu, and T. Schilling. Free energies, vacancy concentrations, and density distribution anisotropies in hard-sphere crystals: A combined density functional and simulation study. *Physical Review E*, **82**:051404, 2010. doi:10.1103/PhysRevE.82.051404.

[10] M. Oettel, S. Dorosz, M. Berghoff, B. Nestler, and T. Schilling. Description of hard-sphere crystals and crystal-fluid interfaces: A comparison between density functional approaches and a phase-field crystal model. *Physical Review E*, **86**:021404, 2012. doi:10.1103/PhysRevE.86.021404.

[11] X. Wang, J. Mi, and C. Zhong. Density functional theory for crystal-liquid interfaces of Lennard-Jones fluid. *The Journal of Chemical Physics*, **138**(16):164704, 2013. doi:10.1063/1.4802633.

[12] M. Levesque, R. Vuilleumier, and D. Borgis. Scalar fundamental measure theory for hard spheres

in three dimensions: Application to hydrophobic solvation. *The Journal of Chemical Physics*, **137**(3):034115, 2012. doi:10.1063/1.4734009.

[13] Y. Liu, S. Zhao, and J. Wu. A Site Density Functional Theory for Water: Application to Solvation of Amino Acid Side Chains. *Journal of Chemical Theory and Computation*, **9**(4):1896–1908, 2013. doi:10.1021/ct3010936.

[14] D. Zhou, J. Mi, and C. Zhong. Three-Dimensional Density Functional Study of Heterogeneous Nucleation of Droplets on Solid Surfaces. *The Journal of Physical Chemistry B*, **116**(48):14100–14106, 2012. doi:10.1021/jp307820w.

[15] A. González, J. A. White, F. L. Román, and S. Velasco. Density functional theory of fluids in nanopores: Analysis of the fundamental measures theory in extreme dimensional-crossover situations. *The Journal of Chemical Physics*, **125**(6):064703, 2006. doi:10.1063/1.2227389.

[16] A. Malijevský. Fundamental measure theory in cylindrical geometry. *The Journal of Chemical Physics*, **126**(13):134710, 2007. doi:10.1063/1.2713106.

[17] N. J. Mariani, C. Mocciaro, M. A. Campesi, and G. F. Barreto. On the computation of fundamental measure theory in pores with cylindrical symmetry. *The Journal of Chemical Physics*, **132**(20):204104, 2010. doi:10.1063/1.3425873.

[18] V. Boţan, F. Pesth, T. Schilling, and M. Oettel. Hard-sphere fluids in annular wedges: Density distributions and depletion potentials. *Physical Review E*, **79**:061402, 2009. doi:10.1103/PhysRevE.79.061402.

[19] R. Roth. Fundamental measure theory for hard-sphere mixtures: a review. *Journal of Physics: Condensed Matter*, **22**(6):063102, 2010. doi:10.1088/0953-8984/22/6/063102.

[20] P. Yatsyshin, N. Savva, and S. Kalliadasis. Spectral methods for the equations of classical density-functional theory: Relaxation dynamics of microscopic films. *The Journal of Chemical Physics*, **136**(12):124113, 2012. doi:10.1063/1.3697471.

[21] P. Yatsyshin, N. Savva, and S. Kalliadasis. Wetting of prototypical one- and two-dimensional systems: Thermodynamics and density functional theory. *The Journal of Chemical Physics*, **142**(3):034708, 2015. doi:10.1063/1.4905605.

[22] A. Nold, B. D. Goddard, P. Yatsyshin, N. Savva, and S. Kalliadasis. Pseudospectral methods for density functional theory in bounded and unbounded domains. *Journal of Computational Physics*, **334**:639–664, 2017. doi:10.1016/j.jcp.2016.12.023.

[23] X. Xu and D. Cao. Multiscaled density-functional theory for helical polymers. *The Journal of Chemical Physics*, **131**(5):054901, 2009. doi:10.1063/1.3197004.

[24] A. Kovalenko, S. Ten-no, and F. Hirata. Solution of three-dimensional reference interaction site model and hypernetted chain equations for simple point charge water by modified method of direct inversion in iterative subspace. *Journal of Computational Chemistry*, **20**(9):928–936, 1999.

doi:10.1002/(SICI)1096-987X(19990715)20:9<928::AID-JCC4>3.0.CO;2-X.

[25] L. J. D. Frink and A. G. Salinger. Two- and Three-Dimensional Nonlocal Density Functional Theory for Inhomogeneous Fluids. *Journal of Computational Physics*, **159**(2):407–424, 2000. doi:10.1006/jcph.2000.6454.

[26] L. J. D. Frink and A. G. Salinger. Two- and Three-Dimensional Nonlocal Density Functional Theory for Inhomogeneous Fluids. *Journal of Computational Physics*, **159**(2):425–439, 2000. doi:10.1006/jcph.2000.6455.

[27] L. J. D. Frink, A. L. Frischknecht, M. A. Heroux, M. L. Parks, and A. G. Salinger. Toward Quantitative Coarse-Grained Models of Lipids with Fluids Density Functional Theory. *Journal of Chemical Theory and Computation*, **8**(4):1393–1408, 2012. doi:10.1021/ct200707b.

[28] J. Mairhofer and J. Gross. Numerical aspects of classical density functional theory for one-dimensional vapor-liquid interfaces. *Fluid Phase Equilibria*, **444**:1–12, 2017. doi:10.1016/j.fluid.2017.03.023.

[29] J. Gross and G. Sadowski. Application of perturbation theory to a hard-chain reference fluid: an equation of state for square-well chains. *Fluid Phase Equilibria*, **168**(2):183–199, 2000. doi:10.1016/S0378-3812(00)00302-2.

[30] J. Gross and G. Sadowski. Perturbed-Chain SAFT: An Equation of State Based on a Perturbation Theory for Chain Molecules. *Industrial & Engineering Chemistry Research*, **40**(4):1244–1260, 2001. doi:10.1021/ie0003887.

[31] J. Gross and G. Sadowski. Modeling Polymer Systems Using the Perturbed-Chain Statistical Associating Fluid Theory Equation of State. *Industrial & Engineering Chemistry Research*, **41**(5):1084–1093, 2002. doi:10.1021/ie010449g.

[32] J. Gross and G. Sadowski. Application of the Perturbed-Chain SAFT Equation of State to Associating Systems. *Industrial & Engineering Chemistry Research*, **41**(22):5510–5515, 2002. doi:10.1021/ie010954d.

[33] M. S. Wertheim. Fluids with highly directional attractive forces. I. Statistical thermodynamics. *Journal of Statistical Physics*, **35**(1):19–34, 1984. doi:10.1007/BF01017362.

[34] M. S. Wertheim. Fluids with highly directional attractive forces. II. Thermodynamic perturbation theory and integral equations. *Journal of Statistical Physics*, **35**(1):35–47, 1984. doi:10.1007/BF01017363.

[35] M. S. Wertheim. Fluids with highly directional attractive forces. III. Multiple attraction sites. *Journal of Statistical Physics*, **42**(3):459–476, 1986. doi:10.1007/BF01127721.

[36] M. S. Wertheim. Fluids with highly directional attractive forces. IV. Equilibrium polymerization. *Journal of Statistical Physics*, **42**(3):477–492, 1986. doi:10.1007/BF01127722.

[37] W. G. Chapman, G. Jackson, and K. E. Gubbins. Phase equilibria of associating fluids. *Molecular*

Physics, **65**(5):1057–1079, 1988. doi:10.1080/00268978800101601.

[38] J. Gross. An equation-of-state contribution for polar components: Quadrupolar molecules. *AIChE Journal*, **51**(9):2556–2568, 2005. doi:10.1002/aic.10502.

[39] J. Gross and J. Vrabec. An equation-of-state contribution for polar components: Dipolar molecules. *AIChE Journal*, **52**(3):1194–1204, 2006. doi:10.1002/aic.10683.

[40] J. Vrabec and J. Gross. Vapor–Liquid Equilibria Simulation and an Equation of State Contribution for Dipole–Quadrupole Interactions. *The Journal of Physical Chemistry B*, **112**(1):51–60, 2008. doi:10.1021/jp072619u.

[41] J. Gross. A density functional theory for vapor–liquid interfaces using the PCP-SAFT equation of state. *The Journal of Chemical Physics*, **131**(20):204705, 2009. doi:10.1063/1.3263124.

[42] C. Klink and J. Gross. A Density Functional Theory for Vapor–Liquid Interfaces of Mixtures Using the Perturbed-Chain Polar Statistical Associating Fluid Theory Equation of State. *Industrial & Engineering Chemistry Research*, **53**(14):6169–6178, 2014. doi:10.1021/ie4029895.

[43] C. Klink, B. Planková, and J. Gross. Density Functional Theory for Liquid–Liquid Interfaces of Mixtures Using the Perturbed-Chain Polar Statistical Associating Fluid Theory Equation of State. *Industrial & Engineering Chemistry Research*, **54**(16):4633–4642, 2015. doi:10.1021/acs.iecr.5b00445.

[44] C. Klink, C. Waibel, and J. Gross. Analysis of Interfacial Transport Resistivities of Pure Components and Mixtures Based on Density Functional Theory. *Industrial & Engineering Chemistry Research*, **54**(45):11483–11492, 2015. doi:10.1021/acs.iecr.5b03270.

[45] G. Lamanna, C. Steinhausen, B. Weigand, A. Preusche, B. Bork, A. Dreizler, R. Stierle, and J. Gross. On the importance of non-equilibrium models for describing the coupling of heat and mass transfer at high pressure. *International Communications in Heat and Mass Transfer*, **98**:49–58, 2018. doi:10.1016/j.icheatmasstransfer.2018.07.012.

[46] E. Sauer and J. Gross. Classical Density Functional Theory for Liquid–Fluid Interfaces and Confined Systems: A Functional for the Perturbed-Chain Polar Statistical Associating Fluid Theory Equation of State. *Industrial & Engineering Chemistry Research*, **56**(14):4119–4135, 2017. doi:10.1021/acs.iecr.6b04551.

[47] E. Sauer, A. Terzis, M. Theiss, B. Weigand, and J. Gross. Prediction of Contact Angles and Density Profiles of Sessile Droplets Using Classical Density Functional Theory Based on the PCP-SAFT Equation of State. *Langmuir*, **34**(42):12519–12531, 2018. doi:10.1021/acs.langmuir.8b01985.

[48] G. Shen, X. Ji, and X. Lu. A hybrid perturbed-chain SAFT density functional theory for representing fluid behavior in nanopores. *The Journal of Chemical Physics*, **138**(22):224706, 2013. doi:10.1063/1.4808160.

[49] G. Shen, X. Ji, S. Öberg, and X. Lu. A hybrid perturbed-chain SAFT density functional the-

ory for representing fluid behavior in nanopores: Mixtures. *The Journal of Chemical Physics*, **139**(19):194705, 2013. doi:10.1063/1.4825078.

[50] Z. Ye, J. Cai, H. Liu, and Y. Hu. Density and chain conformation profiles of square-well chains confined in a slit by density-functional theory. *The Journal of Chemical Physics*, **123**(19):194902, 2005. doi:10.1063/1.2117009.

[51] X. Xu, D. E. Cristancho, S. Costeux, and Z.-G. Wang. Density-functional theory for polymer-carbon dioxide mixtures: A perturbed-chain SAFT approach. *The Journal of Chemical Physics*, **137**(5):054902, 2012. doi:10.1063/1.4742346.

[52] E. W. Hansen. Fast Hankel transform algorithm. *IEEE Transactions on Acoustics, Speech, and Signal Processing*, **33**(3):666–671, 1985. doi:10.1109/TASSP.1985.1164579.

[53] E. W. Hansen. Correction to "Fast Hankel transform algorithm". *IEEE Transactions on Acoustics, Speech, and Signal Processing*, **34**(3):623–624, 1986. doi:10.1109/TASSP.1986.1164860.

[54] E. W. Hansen and P.-L. Law. Recursive methods for computing the Abel transform and its inverse. *Journal of the Optical Society of America A*, **2**(4):510–520, 1985. doi:10.1364/JOSAA.2.000510.

[55] P. N. Swarztrauber. Vectorizing the FFTs. In G. Rodrigue (editor), *Parallel Computations*, pages 51–83. Academic Press, New York, 1982. doi:10.1016/B978-0-12-592101-5.50007-5.

[56] P. N. Swarztrauber. FFT algorithms for vector computers. *Parallel Computing*, **1**(1):45–63, 1984. doi:10.1016/S0167-8191(84)90413-7.

[57] R. Roth, R. Evans, A. Lang, and G. Kahl. Fundamental measure theory for hard-sphere mixtures revisited: the White Bear version. *Journal of Physics: Condensed Matter*, **14**(46):12063, 2002. doi:10.1088/0953-8984/14/46/313.

[58] Y.-X. Yu and J. Wu. Structures of hard-sphere fluids from a modified fundamental-measure theory. *The Journal of Chemical Physics*, **117**(22):10156–10164, 2002. doi:10.1063/1.1520530.

[59] T. Butz. *Fourier Transformation for Pedestrians*. Springer, 2006. doi:10.1007/978-3-319-16985-9.

4 A Fast Inverse Hankel Transform of First Order for Computing Vector-Valued Weight Functions Appearing in Fundamental Measure Theory in Cylindrical Coordinates

The content of this chapter is a literal quote of the publication:

R. Stierle and J. Gross. A fast inverse Hankel Transform of first Order for Computing vector-valued weight Functions appearing in Fundamental Measure Theory in cylindrical Coordinates. *Fluid Phase Equilibria*, **511**:112500, 2020. doi:10.1016/j.fluid.2020.112500

Abstract

Application of classical density functional theory in cylindrical coordinates requires a fast Hankel transform algorithm of order zero and its inverse, when the involved convolution integrals are solved in Fourier space. Vector-valued fundamental measure theory requires a fast Hankel transform of first order and its inverse. Compared to naïve real space convolution, this not only reduces complexity of the required computer code, but also increases computational performance due to the efficiency of the fast Hankel transform. This study proposes a new approach to compute the inverse of the first order fast Hankel transform on equidistant grids as a combination of a modified inverse Abel transform and a fast sine transform. Equidistant grids have a significant advantage over alternative implementations that require logarithmic grid spacing, since most problems, such as pores or droplets, require a certain resolution in the outer region of the radial domain, which in the case of a logarithmic grid necessitates an overly high number of grid points in the inner region of the radial domain. The proposed algorithm for the modified inverse Abel transform is straightforward to implement, while for the fast sine transform off-the-shelf algorithms can be used.

4.1 Introduction

Classical density functional theories (DFT) commonly involve several convolution integrals. Any DFT model based on the fundamental measure theory (FMT)[1–4] for modeling the hard-sphere contribution to the fluid behavior, for example, implies such convolutions. The convolution integrals can be calculated efficiently using fast Fourier transform algorithms, which is especially useful for multidimensional problems. For cylindrical coordinates, the Fourier transform in the radial direction converts to a Hankel transform of order zero or of first order for scalar-valued and for vector-valued weight functions, respectively. Efficient solution of the DFT models in cylindrical coordinates thus requires a fast Hankel transform algorithm.

For logarithmic grids, algorithms for the Hankel transform can be constructed using a coordinate transform[5] and a fast Fourier transform algorithm[6]. As noted by Sauer *et al.*[7], logarithmic grids have a significant disadvantage over equidistant grids, since most applications, such as pores or droplets, require a certain grid resolution in the outer region of the radial domain, resulting in an overly dense resolution for small radii (implying concomitant increase in computational effort).

Alternatively, in [chapter 3]* we applied the fast Hankel transform proposed by Hansen[9,10] to the Helmholtz functionals of the perturbed-chain statistical associating fluid theory (PC-SAFT)[11–16], which includes FMT. This algorithm[9,10] allows computation of the fast Hankel transform of zeroth order, and its inverse, on equidistant grids utilizing a combination of a fast Abel transform[17] (by solving a nine-dimensional state-space model[18]) and fast cosine transform[19]. We thereby reformulated the Hankel transform of order one as a Hankel transform of order zero, which involves a combination of fast Abel, fast sine, and fast cosine transforms[8].

A different algorithm for computing a fast Hankel transform of first order based on the method proposed by Hansen[9,10] was developed by Kim[20], using a combination of a modified Abel and sine transform. Due to the self-inverse nature of the Hankel transforms, the algorithm developed by Kim[20] can, theoretically, be applied in both directions, for transformations to Fourier space and back to real space. However, due to poor resolution and high oscillations in Fourier space, the transformation back to real space leads to substantial errors. Even extensive zero padding to increase Fourier space resolution leads to minor improvements only. The inverse zeroth order fast Hankel transform proposed by Hansen[9,10] does not suffer from this issue, because the order of cosine and Abel transform can be reversed with respect to the forward transform, due to availability of the inverse Abel transform. Subsequently, the

*The text in the original publication reads: [our earlier work[8]].

inverse Hankel transform of zeroth order is computed by a combination of fast cosine and inverse Abel transform.

In this work, we derive the inverse of the modified Abel transform proposed by Kim[20], which allows easy computation of the inverse of the Hankel transform of first order on equidistant grids. The inverse is computed using a combination of a modified inverse Abel transform and the sine transform. For ease of implementation, we provide real and Fourier space discretizations suitable for off-the-shelf algorithms of the sine transform. The proposed algorithm makes FMT calculations in cylindrical coordinates conceptually easy and computationally efficient. In this study, we use sine transform algorithms provided by *FFTPACK*[19,21].

This work is structured as follows. In section 4.2, we illustrate the method of Kim[20] for calculating the Hankel transform of first order based on the Hankel and inverse Hankel transform of order zero proposed by Hansen[9,10]. Then, we derive the projection method for the inverse fast Hankel transform of first order. In section 4.3, we discuss the transition from a continuous to a discrete transform and we introduce the algorithm for the inverse of the modified Abel transform and the inverse Hankel transform of first order. Numerical accuracy of the algorithm is evaluated in section 4.4 for two analytically known transform pairs.

4.2 Projection Method for Hankel Transforms

The Hankel transform $\mathcal{H}_\nu$ of order ν of the rotationally symmetric function f, is defined as

$$\mathcal{H}_\nu[f(r)] = 2\pi \int_{r=0}^{\infty} f(r)\, r\, \mathrm{J}_\nu(2\pi r k_r)\, \mathrm{d}r \tag{4.1}$$

with J_ν as the Bessel function of first kind and order ν, the radial coordinate in real space r, and the radial coordinate in Fourier space k_r. Cree and Bones[22] rewrote the Hankel transform as

$$\mathcal{H}_\nu[f(r)] = \mathrm{i}^{-\nu} \int_{-\infty}^{\infty} \underbrace{\int_{|\tilde{r}|}^{\infty} \frac{2f(r)T_\nu\left(\frac{\tilde{r}}{r}\right)}{\sqrt{1-\left(\frac{\tilde{r}}{r}\right)^2}}\, \mathrm{d}r}_{\equiv F_\nu(\tilde{r})}\, \mathrm{e}^{-2\pi \mathrm{i}\tilde{r}k_r}\, \mathrm{d}\tilde{r} \tag{4.2}$$

with the imaginary unit i, the ν-th order Chebyshev polynomial $T_\nu(x) = \cos\left(\nu \cos^{-1}(x)\right)$, the generalized Abel transform F_ν, and the integration variable of the Abel transform $\tilde{r}$. Kim[20]

separated the Fourier transform for even or odd order ν, expressing eq. (4.2) as

$$\mathcal{H}_\nu[f(r)] = \mathrm{i}^{-\nu}\mathcal{F}[F_\nu(\tilde{r})] = \begin{cases} \mathrm{i}^{-\nu}\mathcal{F}_{\mathcal{SIN}}[F_\nu(\tilde{r})], & \nu \text{ odd} \\ \mathrm{i}^{-\nu}\mathcal{F}_{\mathcal{COS}}[F_\nu(\tilde{r})], & \nu \text{ even} \end{cases} \tag{4.3}$$

with Fourier transform $\mathcal{F}$ and the Fourier sine and cosine transform, $\mathcal{F}_{\mathcal{SIN}}$ (imaginary part of the Fourier transform) and $\mathcal{F}_{\mathcal{COS}}$ (real part of the Fourier transform), respectively. For the Hankel transform of zeroth and first order, this leads to

$$\mathcal{H}_0[f(r)] = \mathcal{COS}[F_0(\tilde{r})] \tag{4.4a}$$

$$\mathcal{H}_1[f(r)] = \mathcal{SIN}[F_1(\tilde{r})] \tag{4.4b}$$

with the sine and cosine transform $\mathcal{SIN}$ and $\mathcal{COS}$, respectively, defined as

$$\mathcal{COS}[f(r)] = \int_{r=0}^{\infty} f(r)\, r\, \cos(2\pi r k_r)\, \mathrm{d}r \tag{4.5a}$$

$$\mathcal{SIN}[f(r)] = \int_{r=0}^{\infty} f(r)\, r\, \sin(2\pi r k_r)\, \mathrm{d}r \tag{4.5b}$$

We note here, that the sine and cosine transform are self-inverse.

4.2.1 Projection Method for Zeroth Order Hankel Transform

For order $\nu = 0$, with the Chebyshev polynomial $T_0(x) = 1$, the generalized Abel transform F_ν, defined in eq. (4.2), becomes the Abel transform. Insertion of $T_0(x) = 1$ into the Hankel transform defined in eq. (4.2) thus results in a combination of cosine $\mathcal{COS}$ and Abel transform $\mathcal{A}$, as $\mathcal{H}_0[f(r)] = \mathcal{COS}[F_0(\tilde{r})]$, with the Abel transform defined by

$$\mathcal{A}[f(r)] = 2\int_{\tilde{r}}^{\infty} \frac{f(r)}{\sqrt{1-\left(\frac{\tilde{r}}{r}\right)^2}}\, \mathrm{d}r \tag{4.6}$$

while the inverse Abel transform $\mathcal{A}^{-1}$ is obtained from

$$\mathcal{A}^{-1}\left[\tilde{f}(\tilde{r})\right] = -\frac{1}{\pi}\int_{r}^{\infty} \frac{\tilde{f}'(\tilde{r})}{\tilde{r}\sqrt{1-\left(\frac{r}{\tilde{r}}\right)^2}}\, \mathrm{d}\tilde{r} \tag{4.7}$$

where the prime ($'$) denotes the derivative with respect to $\tilde{r}$. Combination of eq. (4.4a) with eqs. (4.6) and (4.7) leads to the Hankel and inverse Hankel transform of zeroth order, respectively

$$\hat{f}(k_r) = \mathcal{H}_0[f(r)] = \mathcal{COS}\,\mathcal{A}[f(r)] \tag{4.8a}$$
$$f(r) = \mathcal{H}_0^{-1}\left[\hat{f}(k_r)\right] = \mathcal{A}^{-1}\,\mathcal{COS}\left[\hat{f}(k_r)\right] \tag{4.8b}$$

with $\hat{f}$ as the function in Fourier space. Equation (4.8) leads to the algorithms proposed by Hansen[9,10].

4.2.2 Projection Method for First-Order Hankel Transform

For order $\nu = 1$, with the Chebyshev polynomial $T_1(x) = x$, the generalized Abel transform F_ν, defined in eq. (4.2), becomes a modification of the Abel transform $\tilde{\mathcal{A}}$, defined by

$$\tilde{f}(\tilde{r}) = \tilde{\mathcal{A}}[f(r)] \equiv 2\int_{\tilde{r}}^{\infty} \frac{f(r)\left(\frac{\tilde{r}}{r}\right)}{\sqrt{1-\left(\frac{\tilde{r}}{r}\right)^2}}\,\mathrm{d}r \tag{4.9}$$

which, in combination with eq. (4.4b), leads to the Hankel transform of first order $\mathcal{H}_1$, while the inverse of eq. (4.9) is obtained from

$$f(r) = \tilde{\mathcal{A}}^{-1}\left[\tilde{f}(\tilde{r})\right] \equiv -\frac{1}{\pi}\int_{r}^{\infty} \frac{\left(\tilde{f}(\tilde{r})\left(\frac{r}{\tilde{r}}\right)\right)'}{\tilde{r}\sqrt{1-\left(\frac{r}{\tilde{r}}\right)^2}}\,\mathrm{d}\tilde{r} \tag{4.10}$$

which, in combination with eq. (4.4b), leads to the inverse of the Hankel transform of first order $\mathcal{H}_1^{-1}$, both obtained from

$$\hat{f}(k_r) = \mathcal{H}_1[f(r)] = \mathcal{SIN}\,\tilde{\mathcal{A}}[f(r)] \tag{4.11a}$$
$$f(r) = \mathcal{H}_1^{-1}\left[\hat{f}(k_r)\right] = \tilde{\mathcal{A}}^{-1}\mathcal{SIN}\left[\hat{f}(k_r)\right] \tag{4.11b}$$

This allows for a much easier first-order Hankel transform and inverse Hankel transform than the one proposed in [section 3.4.2.2]*, which for convenience we restate in appendix C, as eqs. (C.1) and (C.2). Equations (4.9) and (4.11a) represent the algorithm for the Hankel transform of first order proposed by Kim[20]. This work proposes an algorithm for the inverse Hankel transform of first order through eq. (4.11b) using eq. (4.10) (the inverse of the algorithm proposed by Kim[20]).

*The text in the original publication reads: [our earlier work[8]].

4.3 Discrete Modified Abel & Inverse Abel Transform

In this section, we proceed with converting the continuous integral transform to a discrete representation. We ensure that established fast sine transform algorithms provided by *FFTPACK*[19,21] can be used for applications of classical DFT, especially FMT. Therefore, we show the connection between the sample grid in real and Fourier space. Notation and application is based on [chapter 3]*.

4.3.1 From Integral Transform to Discrete Representation

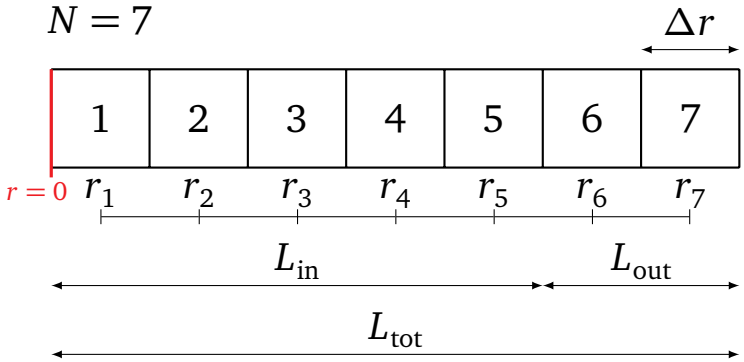

Figure 4.1: Schematic equidistant radial grid with $N = 7$ grid points and grid spacing Δr. The partitioned elements represent a discretization used for finite volume methods, while the function to be transformed is evaluated at the center of those elements r_i. The density profiles are computed on the inner domain L_{in}, while the buffer zone L_{out} serves as boundary condition, where function f approaches zero.

The majority of the computational effort in DFT is required for calculating convolutions with weight functions ω. The weight functions have a finite convolution kernel in real space, which can be transformed to Fourier space analytically (which is why, we require the grid spacing in Fourier space).

The radial grid is divided into two domains, as illustrated in figure 4.1. The inner domain of length L_{in} is the domain of physical interest and the domain for which the convolutions are desired. An outer domain with length L_{out} is needed because the functions f in DFT applications are usually non-periodic in the considered radial direction of a cylindrical coordinate system. The outer domain is introduced as a buffer zone for convolutions and additionally serves as a boundary condition. On the outer domain, the function f approaches zero. The size of the outer domain depends on the used weight functions, for FMT the outer domain

*The text in the original publication reads: [our previous work[8]].

has to fulfill the following relation

$$L_{\text{out},r} \geq \max_i \{2R_i\} \tag{4.12}$$

with the hard-sphere radius R_i of component i. Different weight functions lead to different requirements for the outer domain, as described in [section 3.4.1.1]*. The sampling grid in Fourier space is defined by[8]

$$k_r = \frac{k}{2N\Delta r} = \frac{k}{2L_{\text{tot}}} \qquad \text{with } k = 0, \ldots, (N-1) \tag{4.13}$$

with the integer samples k, the number of grid points N, and the grid spacing Δr.

The discrete version of the sine transform, eq. (4.5b), is the discrete sine transform ($\mathcal{DST}$). Several versions of the discrete sine transform exist, depending on what symmetry properties are exploited. The first grid point of the grid presented in figure 4.1 is located at $\frac{\Delta r}{2}$. For this grid distribution, we require the discrete sine transform II ($\mathcal{DST}_{\text{II}}$), available from *FFTPACK* as subroutine *SINQ1B*. The Hankel transform of first order, eq. (4.11a), is then computed from

$$\hat{f}(k_r) = \mathcal{H}_1[f(r)] = \mathcal{DST}_{\text{II}} \tilde{\mathcal{A}}[f(r)] \tag{4.14}$$

It is important to note, that the output of the $\mathcal{DST}_{\text{II}}$ algorithm excludes the vanishing result for $k = 0$ but adds one for $k = N$. Hence, the first element in the solution vector represents the value for $k = 1$. The implementation of the $\mathcal{DST}_{\text{III}}$ algorithm used for the inverse transform also requires a sequence excluding the value for $k = 0$. As a result, for FMT weight functions defined on the grid described in eq. (4.13), a shift in index is required. That is visualized in figure 4.2. A more detailed description is given in [section 3.4.3.2]†.

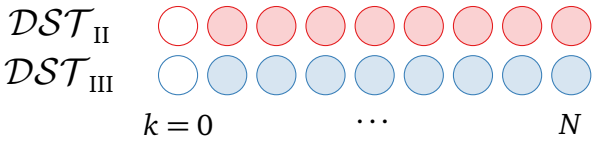

Figure 4.2: Algorithm output of $\mathcal{DST}_{\text{II}}$ and input of $\mathcal{DST}_{\text{III}}$. Filled spheres represent the k-grid of the respective forward (red) and inverse (blue) transform.

The inverse of the discrete sine transform II is the discrete sine transform III ($\mathcal{DST}_{\text{III}} = \mathcal{DST}_{\text{II}}^{-1}$), which is available from *FFTPACK* as subroutine *SINQ1F*. The inverse Hankel trans-

*The text in the original publication reads: [previous work[8]].
†The text in the original publication reads: [previous work[8]].

form of first order, eq. (4.11b), is then obtained from

$$f(r) = \mathcal{H}_1^{-1}\left[\hat{f}(k_r)\right] = \tilde{\mathcal{A}}^{-1}\mathcal{DST}_{\mathrm{III}}\left[\hat{f}(k_r)\right] \tag{4.15}$$

Using eq. (4.14) in combination with eq. (4.15) allows easy computation of convolutions with vector-valued weight functions appearing in FMT in cylindrical coordinates.

Numerical details on how to apply the $\mathcal{DST}$ algorithms can be found in [appendix B.5]*.

4.3.2 Algorithm for Modified Abel & Inverse Abel Transform

The following algorithm for the modified Abel transform, eq. (4.9), and its inverse, eq. (4.10), is derived following Hansen[9,10] and Kim[20]. The forward modified Abel transform describes the algorithm of Kim[20] for equidistant grids, while the modified inverse Abel transform is the result of this work. The derivation of the forward transform is well documented in literature[20], which is why in the following we solely describe the derivation of the modified inverse Abel transform $\tilde{\mathcal{A}}^{-1}$. An algorithm for computing both, the modified Abel and its inverse transform, is given at the end of this section.

Solving the product rule in eq. (4.10) and conducting the coordinate transforms $r = \exp(-\tau)$ and $\tilde{r} = \exp(-t)$ leads to

$$\tilde{\mathcal{A}}^{-1}\left[\tilde{f}(\tilde{r})\right] = \int_{-\infty}^{\infty} \frac{-\tilde{f}'(t)}{\pi} \frac{\exp(-(\tau-t))\Theta(\tau-t)}{\sqrt{1-\exp(-2(\tau-t))}}\,\mathrm{d}t + \int_{-\infty}^{\infty} \frac{\tilde{f}(t)}{\pi\exp(-t)} \frac{\exp(-(\tau-t))\Theta(\tau-t)}{\sqrt{1-\exp(-2(\tau-t))}}\,\mathrm{d}t \tag{4.16}$$

with the Heaviside step function Θ. Both terms on the right-hand-side of eq. (4.16) are convolution integrals of two different inputs. For the following analysis we use the short-hand notation $u(t)$ to represent both inputs, i.e.,

$$u(t) \equiv \begin{cases} \frac{-\tilde{f}'(t)}{\pi} \\ \frac{\tilde{f}(t)}{\pi\exp(-t)} \end{cases} \tag{4.17}$$

for the first and for the second convolution integral of eq. (4.16), respectively. For the transfer function we introduce the notation

$$g(t) \equiv \frac{\exp(-t)}{\sqrt{1-\exp(-2t)}} \tag{4.18}$$

*The text in the original publication reads: [our previous work[8] appendix D].

Hansen and Jablokow[18] showed, that this kind of convolution can be approximated by a low order state-space representation (here the order of the state-space model is $K = 9$), as

$$\dot{\mathbf{x}}(\tilde{r}) = \mathbf{A}\mathbf{x}(\tilde{r}) + \mathbf{b}u(\tilde{r}) \tag{4.19a}$$

$$y = \mathbf{c}^{\mathsf{T}}\mathbf{x}(\tilde{r}) \tag{4.19b}$$

with states $\mathbf{x}$ and input u, as well as

$$\mathbf{A} = \operatorname{diag}[(\lambda_1 - 1), \ldots, (\lambda_K - 1)] \tag{4.20a}$$

$$\mathbf{b} = [h_1, \ldots, h_K]^{\mathsf{T}} \tag{4.20b}$$

$$\mathbf{c} = [1, \ldots, 1]^{\mathsf{T}} \tag{4.20c}$$

with system matrix $\mathbf{A}$, input vector $\mathbf{b}$, and output vector $\mathbf{c}^{\mathsf{T}}$. The output y of the state-space model, eq. (4.19), corresponds to the solution of the convolution integral in eq. (4.16), i.e., the transfer function, eq. (4.18), is equivalent to the combination of state matrix $\mathbf{A}$, input vector $\mathbf{c}$, and output vector $\mathbf{c}^{\mathsf{T}}$. The model parameters[9,17] of the system, λ_k and h_k are listed in table 4.1. Solution of the state-space convolution, defined by[9]

$$\mathbf{x}(\tilde{r}) = \mathrm{e}^{\mathbf{A}(\tilde{r}-\tilde{r}_0)}\mathbf{x}(\tilde{r}_0) + \int_{\tilde{r}_0}^{\tilde{r}} \mathrm{e}^{\mathbf{A}(\tilde{r}-\xi)}\mathbf{b}u(\xi)\,\mathrm{d}\xi \tag{4.21}$$

and substituting the input with a piecewise linear function (first-order hold approximation)[9], obtained from

$$u(\xi) = p + q\xi \qquad \text{with } \tilde{r} < \xi \leq \tilde{r}_0 \tag{4.22a}$$

$$p = \frac{\tilde{r}\,u(\tilde{r}_0) - \tilde{r}_0\,u(\tilde{r})}{\tilde{r} - \tilde{r}_0} \tag{4.22b}$$

$$q = \frac{u(\tilde{r}) - u(\tilde{r}_0)}{\tilde{r} - \tilde{r}_0} \tag{4.22c}$$

leads to the following recursive algorithm for the modified (inverse) Abel transform $\tilde{F}_n$

Table 4.1: Parameters for Abel transform[9,17].

k	h_k/π	λ_k
1	0.318	0
2	0.19	-2.1
3	0.35	-6.2
4	0.82	-22.4
5	1.8	-92.5
6	3.9	-414.5
7	8.3	-1889.4
8	19.6	-8990.9
9	48.3	-47391.1

according to

$$\mathbf{x}_{n-1} = \tilde{\Phi}_n \mathbf{x}_n + \tilde{B}_{0,n} f_n + \tilde{B}_{1,n} f_{n-1} \tag{4.23a}$$

$$\tilde{F}_n = \tilde{C}\mathbf{x}_n \tag{4.23b}$$

$$\mathbf{x}_N = 0 \tag{4.23c}$$

$$\tilde{\Phi}_n = \operatorname{diag}\left\{\left(\frac{r_n}{r_{n-1}}\right)^{\lambda_1 - 1}, \ldots, \left(\frac{r_n}{r_{n-1}}\right)^{\lambda_K - 1}\right\} \tag{4.23d}$$

$$\tilde{C} = [1, \ldots, 1] \tag{4.23e}$$

$$\tilde{B}_{0,n} = \left[h_1 \tilde{\beta}_{0,n}(\lambda_1), \ldots, h_K \tilde{\beta}_{0,n}(\lambda_K)\right]^\intercal \tag{4.23f}$$

$$\tilde{B}_{1,n} = \left[h_1 \tilde{\beta}_{1,n}(\lambda_1), \ldots, h_K \tilde{\beta}_{1,n}(\lambda_K)\right]^\intercal \tag{4.23g}$$

with the modified (inverse) discrete Abel transform $\tilde{F}_n$ at grid point index n, the grid dependent state transition matrix $\tilde{\Phi}_n$, the grid dependent states of the state-space model $\mathbf{x}_n$, the grid dependent discrete input vectors $\tilde{B}_{0,n}$ and $\tilde{B}_{1,n}$, as well as model parameters from Hansen[9,10], λ_k and h_k (see table 4.1). The recursion is started at the outermost grid point r_N with $\mathbf{x}_N = 0$ and is continued inwards towards the origin of the radial grid. For r_{n-1} this method cannot be used.

The forward Hankel transform of first order $\mathcal{H}_1$, as proposed by Kim[20], is obtained by using

$$\tilde{\beta}^{\mathrm{f}}_{0,n}(\lambda_1 = 0) = \frac{2r_{n-1}}{r_n - r_{n-1}}\left(r_n - r_{n-1} - r_{n-1}\ln\left(\frac{r_n}{r_{n-1}}\right)\right) \tag{4.24a}$$

$$\tilde{\beta}^{\mathrm{f}}_{1,n}(\lambda_1 = 0) = \frac{2r_{n-1}}{r_n - r_{n-1}}\left(r_{n-1} - r_n + r_n\ln\left(\frac{r_n}{r_{n-1}}\right)\right) \tag{4.24b}$$

for $\lambda_{k=1} = 0$, and

$$\tilde{\beta}^{\mathrm{f}}_{0,n}(\lambda_k) = \frac{2r_{n-1}}{r_n - r_{n-1}} \frac{r_{n-1} + [r_n\lambda_k - r_{n-1}(\lambda_k+1)]\left(\frac{r_n}{r_{n-1}}\right)^{\lambda_k}}{\lambda_k(\lambda_k+1)} \quad \lambda_k \neq 0 \tag{4.25a}$$

$$\tilde{\beta}^{\mathrm{f}}_{1,n}(\lambda_k) = \frac{2r_{n-1}}{r_n - r_{n-1}} \frac{[r_{n-1}\lambda_k - r_n(\lambda_k+1)] + r_n\left(\frac{r_n}{r_{n-1}}\right)^{\lambda_k}}{\lambda_k(\lambda_k+1)} \quad \lambda_k \neq 0 \tag{4.25b}$$

for $k \in \{2, \ldots, 9\}$, in combination with the $\mathcal{DST}_{\mathrm{II}}$ according to eq. (4.14). The inverse Hankel transform of first order $\mathcal{H}_1^{-1}$ is obtained by performing the $\mathcal{DST}_{\mathrm{III}}$ before computing the modified inverse Abel transform using

$$\tilde{\beta}^{\mathrm{b}}_{0,n}(\lambda_k) = \frac{1 - \left(\frac{r_n}{r_{n-1}}\right)^{\lambda_k - 1}}{\pi(\lambda_k - 1)(r_n - r_{n-1})} + \frac{1 + \left(\frac{r_n}{r_{n-1}}\right)^{\lambda_k - 1}\left((\lambda_k - 2) - (\lambda_k - 1)\left(\frac{r_{n-1}}{r_n}\right)\right)}{\pi(\lambda_k - 1)(\lambda_k - 2)(r_n - r_{n-1})} \tag{4.26a}$$

$$\tilde{\beta}^{\mathrm{b}}_{1,n}(\lambda_k) = \frac{\left(\frac{r_n}{r_{n-1}}\right)^{\lambda_k - 1} - 1}{\pi(\lambda_k - 1)(r_n - r_{n-1})} + \frac{\left(\frac{r_n}{r_{n-1}}\right)^{\lambda_k - 1} + \left((\lambda_k - 2) - (\lambda_k - 1)\left(\frac{r_n}{r_{n-1}}\right)\right)}{\pi(\lambda_k - 1)(\lambda_k - 2)(r_n - r_{n-1})} \tag{4.26b}$$

4.4 Numerical Results & Accuracy

In order to test the accuracy of the proposed algorithm, eqs. (4.15) and (4.23), we chose two analytically known transform pairs. The first test case was chosen as an example of a continuous function. The second test case transforms a function with a discontinuity and we test how well the algorithm can handle such discontinuities. The first test case is defined as

$$\hat{f}(k_r) = \frac{2\pi k_r}{(2a)^2} \exp\left(-\frac{(2\pi k_r)^2}{4a}\right) \tag{4.27a}$$

$$\mathcal{H}_1^{-1}\left[\hat{f}(k_r)\right] = r \exp\left(-ar^2\right) \tag{4.27b}$$

with parameter $a = \frac{1}{10}$, and

$$\hat{f}(k_r) = \frac{1}{2} \frac{\mathrm{J}_2(2\pi k_r b)}{2\pi k_r} \tag{4.28a}$$

$$\mathcal{H}_1^{-1}\left[\hat{f}(k_r)\right] = \begin{cases} \frac{1}{2}\frac{r}{b^2}, & 0 < r < b \\ 0, & b \leq r < \infty \end{cases} \tag{4.28b}$$

with the Bessel function of the first kind and second order J_2 and parameter $b = 8$. The procedure is divided into the following steps. First, the function $\hat{f}$ is transformed by a $\mathcal{DST}_{\mathrm{III}}$ before being transformed with the algorithm for the modified Abel transform $\tilde{\mathcal{A}}^{-1}$, proposed

in eq. (4.23). The results of the transform are shown for eq. (4.27) in figure 4.3 and eq. (4.28) in figure 4.4.

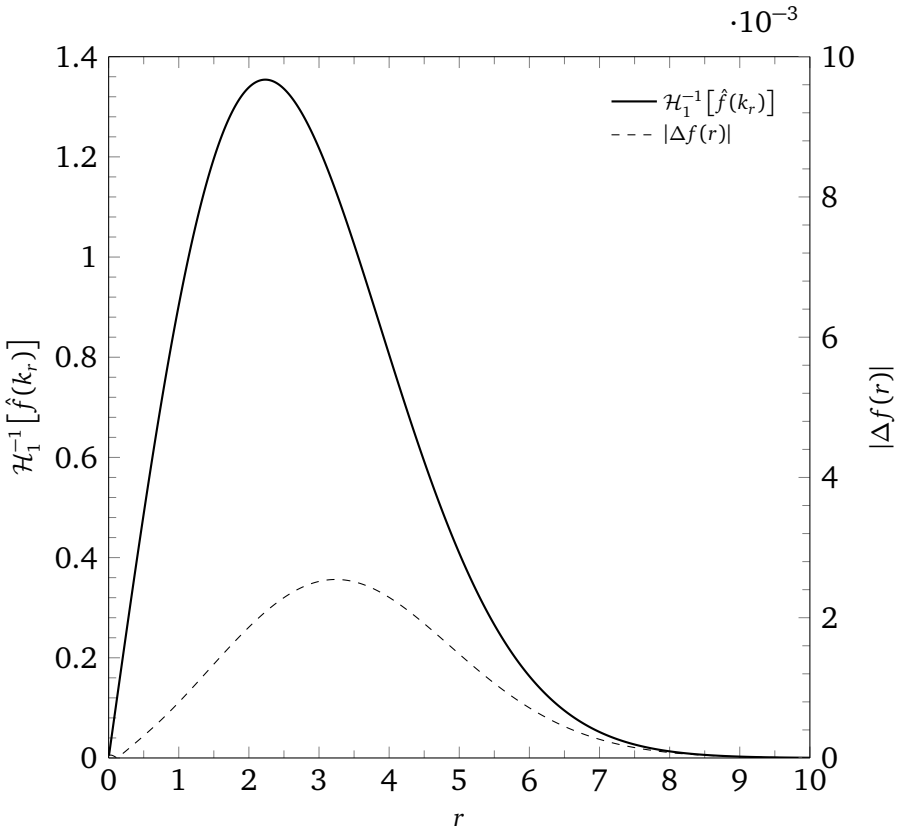

Figure 4.3: Result of inverse fast Hankel transform of first order with absolute deviation from analytical solution for eq. (4.27) using $N = 1024$ grid points.

For the first transform pair, eq. (4.27), depicted in figure 4.3, the here proposed algorithm leads to satisfactory results with small but smooth deviations. The numerical result is shifted somewhat to the left, probably caused by the inward iteration and the inertia of the dynamical system leading to the modified Abel transform.

The second transform pair, eq. (4.28), depicted in figure 4.4, shows a jump at $r = 8$. This jump causes Gibbs phenomenon at the singularity in the output of the fast sine transform algorithm which are directly adopted by the inverse modified Abel transform.

Despite large local deviations, the algorithm is still able to describe the shape of the transform. This is in accordance with results obtained by Hansen[9] for the zeroth order inverse Hankel transform. Fortunately, no profile jumps have to be resolved by this transform applied to FMT. Gibbs phenomenon occurring for very steep profiles can be reduced applying the Lanczos σ-factor[23] in Fourier space, a short guide on how to apply the σ-factor to DFT can be found in [appendix B.6]*.

*The text in the original publication reads: [our previous work[8] appendix E].

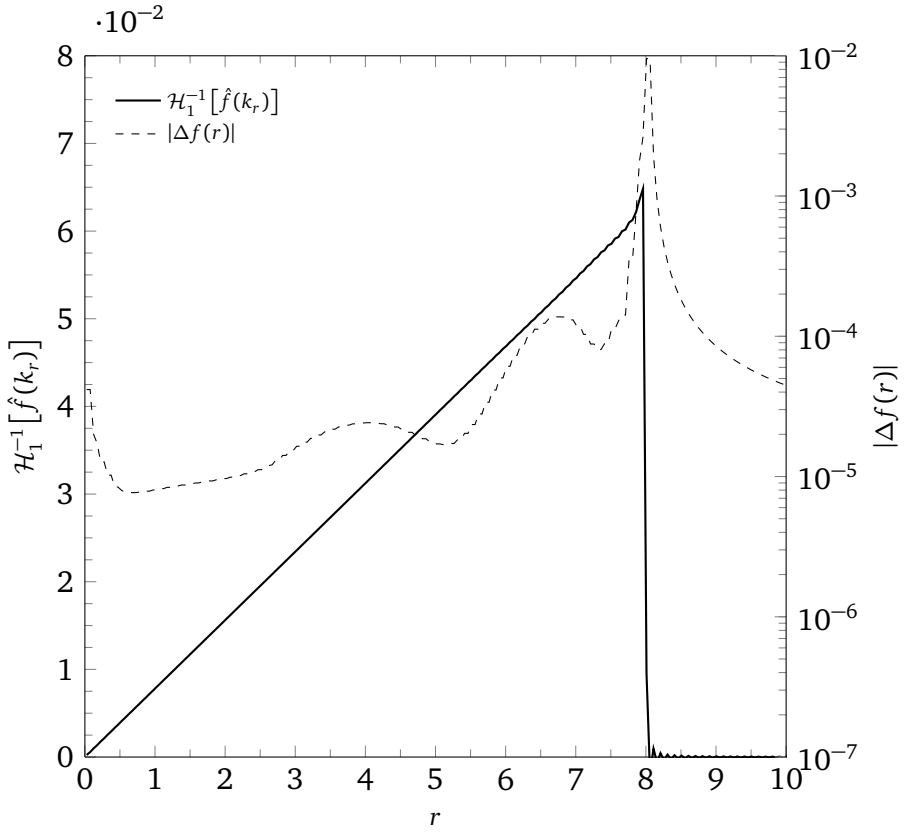

Figure 4.4: Result of inverse fast Hankel transform of first order with absolute deviation from analytical on a logarithmic scale for eq. (4.28) using $N = 1024$ grid points. Due to Gibbs phenomenon, the maximum contour of the error is visualized as a conservative estimate.

FMT using tensor-valued weight functions as proposed by Tarazona[24], Tarazona *et al.*[25] requires fast Hankel transform algorithms of zeroth, first and second order as well as their respective inverse transforms for application to cylindrical coordinates. While the algorithms for Hankel transforms of zeroth and first order are already derived, the approach of Kim[20] and the one applied in this work can also be used to derive an algorithm for a fast Hankel transform of second order and its inverse. This development is left to future work.

4.5 Conclusion

A new method for computing the inverse fast Hankel transform of first order on equidistant grids is presented for solving convolution integrals in polar or cylindrical coordinates appearing in vector-valued DFT, for example vector-valued FMT. This allows much easier and more efficient computation of the above convolution integrals compared to the method proposed in [chapter 3]*. Numerical accuracy for continuous functions, as found in FMT, is satisfactory.

*The text in the original publication reads: [our previous work[8]].

References

[1] Y. Rosenfeld. Free-energy model for the inhomogeneous hard-sphere fluid mixture and density-functional theory of freezing. *Physical Review Letters*, **63**:980–983, 1989. doi:10.1103/PhysRevLett.63.980.

[2] R. Roth, R. Evans, A. Lang, and G. Kahl. Fundamental measure theory for hard-sphere mixtures revisited: the White Bear version. *Journal of Physics: Condensed Matter*, **14**(46):12063, 2002. doi:10.1088/0953-8984/14/46/313.

[3] R. Roth. Fundamental measure theory for hard-sphere mixtures: a review. *Journal of Physics: Condensed Matter*, **22**(6):063102, 2010. doi:10.1088/0953-8984/22/6/063102.

[4] Y.-X. Yu and J. Wu. Structures of hard-sphere fluids from a modified fundamental-measure theory. *The Journal of Chemical Physics*, **117**(22):10156–10164, 2002. doi:10.1063/1.1520530.

[5] V. Boţan, F. Pesth, T. Schilling, and M. Oettel. Hard-sphere fluids in annular wedges: Density distributions and depletion potentials. *Physical Review E*, **79**:061402, 2009. doi:10.1103/PhysRevE.79.061402.

[6] A. J. S. Hamilton. Uncorrelated modes of the non-linear power spectrum. *Monthly Notices of the Royal Astronomical Society*, **312**(2):257–284, 2000. doi:10.1046/j.1365-8711.2000.03071.x.

[7] E. Sauer, A. Terzis, M. Theiss, B. Weigand, and J. Gross. Prediction of Contact Angles and Density Profiles of Sessile Droplets Using Classical Density Functional Theory Based on the PCP-SAFT Equation of State. *Langmuir*, **34**(42):12519–12531, 2018. doi:10.1021/acs.langmuir.8b01985.

[8] R. Stierle, E. Sauer, J. Eller, M. Theiss, P. Rehner, P. Ackermann, and J. Gross. Guide to efficient solution of PC-SAFT classical Density Functional Theory in various Coordinate Systems using fast Fourier and similar Transforms. *Fluid Phase Equilibria*, **504**:112306, 2020. doi:10.1016/j.fluid.2019.112306.

[9] E. W. Hansen. Fast Hankel transform algorithm. *IEEE Transactions on Acoustics, Speech, and Signal Processing*, **33**(3):666–671, 1985. doi:10.1109/TASSP.1985.1164579.

[10] E. W. Hansen. Correction to "Fast Hankel transform algorithm". *IEEE Transactions on Acoustics, Speech, and Signal Processing*, **34**(3):623–624, 1986. doi:10.1109/TASSP.1986.1164860.

[11] J. Gross and G. Sadowski. Perturbed-Chain SAFT: An Equation of State Based on a Perturbation Theory for Chain Molecules. *Industrial & Engineering Chemistry Research*, **40**(4):1244–1260, 2001. doi:10.1021/ie0003887.

[12] J. Gross and G. Sadowski. Modeling Polymer Systems Using the Perturbed-Chain Statistical Associating Fluid Theory Equation of State. *Industrial & Engineering Chemistry Research*, **41**(5):1084–1093, 2002. doi:10.1021/ie010449g.

[13] J. Gross and G. Sadowski. Application of the Perturbed-Chain SAFT Equation of State to Associating Systems. *Industrial & Engineering Chemistry Research*, **41**(22):5510–5515, 2002.

doi:10.1021/ie010954d.

[14] J. Gross. A density functional theory for vapor–liquid interfaces using the PCP-SAFT equation of state. *The Journal of Chemical Physics*, **131**(20):204705, 2009. doi:10.1063/1.3263124.

[15] C. Klink and J. Gross. A Density Functional Theory for Vapor–Liquid Interfaces of Mixtures Using the Perturbed-Chain Polar Statistical Associating Fluid Theory Equation of State. *Industrial & Engineering Chemistry Research*, **53**(14):6169–6178, 2014. doi:10.1021/ie4029895.

[16] C. Klink, B. Planková, and J. Gross. Density Functional Theory for Liquid–Liquid Interfaces of Mixtures Using the Perturbed-Chain Polar Statistical Associating Fluid Theory Equation of State. *Industrial & Engineering Chemistry Research*, **54**(16):4633–4642, 2015. doi:10.1021/acs.iecr.5b00445.

[17] E. W. Hansen and P.-L. Law. Recursive methods for computing the Abel transform and its inverse. *Journal of the Optical Society of America A*, **2**(4):510–520, 1985. doi:10.1364/JOSAA.2.000510.

[18] E. Hansen and A. Jablokow. State variable representation of a class of linear shift-variant systems. *IEEE Transactions on Acoustics, Speech, and Signal Processing*, **30**(6):874–880, 1982. doi:10.1109/TASSP.1982.1163978.

[19] P. N. Swarztrauber. FFT algorithms for vector computers. *Parallel Computing*, **1**(1):45–63, 1984. doi:10.1016/S0167-8191(84)90413-7.

[20] H. J. Kim. A fast algorithm for computing the Hankel transform of order 1. *IEEE Transactions on Acoustics, Speech, and Signal Processing*, **37**(8):1291–1293, 1989. doi:10.1109/29.31279.

[21] P. N. Swarztrauber. Vectorizing the FFTs. In G. Rodrigue (editor), *Parallel Computations*, pages 51–83. Academic Press, New York, 1982. doi:10.1016/B978-0-12-592101-5.50007-5.

[22] M. Cree and P. Bones. Algorithms to numerically evaluate the Hankel transform. *Computers & Mathematics with Applications*, **26**(1):1–12, 1993. doi:10.1016/0898-1221(93)90081-6.

[23] C. Lanczos. *Applied Analysis*. Prentice-Hall Mathematics Series. Prentice-Hall, 1956.

[24] P. Tarazona. Density Functional for Hard Sphere Crystals: A Fundamental Measure Approach. *Physical Review Letters*, **84**:694–697, 2000. doi:10.1103/PhysRevLett.84.694.

[25] P. Tarazona, J. Cuesta, and Y. Martínez-Ratón. Density Functional Theories of Hard Particle Systems. In Á. Mulero (editor), *Theory and Simulation of Hard-Sphere Fluids and Related Systems*, pages 247–341. Springer Berlin Heidelberg, 2008. doi:10.1007/978-3-540-78767-9_7.

5 Hydrodynamic Density Functional Theory for Mixtures from a Variational Principle and Its Application to Droplet Coalescence

The content of this chapter is a literal quote of the publication:

R. Stierle and J. Gross. Hydrodynamic Density Functional Theory for Mixtures from a Variational Principle and Its Application to Droplet Coalescence. *The Journal of Chemical Physics*, **155**(13):134101, 2021. doi:10.1063/5.0060088

Abstract

Dynamic density functional theory (DDFT) allows the description of microscopic dynamical processes on the molecular scale extending classical density functional theory (DFT) to non-equilibrium situations. Since DDFT and DFT use the same Helmholtz energy functionals, both predict the same density profiles in thermodynamic equilibrium. We propose a molecular DDFT model, in this work also referred to as hydrodynamic DFT, for mixtures based on a variational principle that accounts for viscous forces as well as diffusive molecular transport via the generalized Maxwell-Stefan diffusion. Our work identifies a suitable expression for driving forces for molecular diffusion of inhomogeneous systems. These driving forces contain a contribution due to the interfacial tension. The hydrodynamic DFT model simplifies to the isothermal multicomponent Navier-Stokes equation in continuum situations when Helmholtz energies can be used instead of Helmholtz energy functionals, closing the gap between micro- and macroscopic scales. We show that the hydrodynamic DFT model, although not formulated in conservative form, globally satisfies the first and second law of thermodynamics. Shear viscosities and Maxwell-Stefan diffusion coefficients are predicted using an entropy scaling approach. As an example, we apply the hydrodynamic DFT model with a Helmholtz energy density functional based on the perturbed-chain statistical associating fluid theory (PC-SAFT) equation of state to droplet and bubble coalescence in one dimension and analyze the influence of additional components on coalescence phenomena.

5.1 Introduction

Following the work of Rohde [1], we show a derivation of the molecular dynamic density functional theory (DDFT), in this work also referred to as hydrodynamic DFT, proposed by Archer [2] for pure molecular fluids and extended to colloidal mixtures by Goddard *et al.* [3], by means of a variational principle (which automatically incorporates the adiabatic approximation leading to DDFT) put forward by Herivel and Lin[4,5]. Our derivation naturally leads to a diffuse interface model that incorporates established Helmholtz energy functionals into microscopic hydrodynamics. We model the convective flux by a momentum balance for the barycentric velocity of the mixture and diffusive molecular fluxes for each individual component, similar to the Navier-Stokes-Korteweg equations for mixtures; in distinction to the work of Goddard *et al.* [3], who instead described each component in a colloidal mixture with its own momentum balance. We demonstrate that the resulting system of equations globally obeys the first and second law of thermodynamics, even though the momentum balance cannot be expressed in conservative form*. The description of molecular transport by applying a hydrodynamic DFT model with a structure related to the macroscopic Navier-Stokes equations is motivated by the work of Hitz *et al.* [6,7], who were able to show that the results of non-equilibrium molecular dynamics simulations of shock tube flow can be reproduced surprisingly well with hydrodynamic methods.

The principle of stationary action, which we use for our derivation, is formulated such that the difference between kinetic and *Helmholtz* plus potential energy becomes stationary. While the original formulation of the Herivel-Lin principle[4,5] uses the difference between kinetic and *internal* plus potential energy in the variational principle, we follow the procedure proposed by Rohde [1], where we use the Helmholtz energy instead of the internal energy. The resulting reformulation of the Navier-Stokes-Korteweg equations by Rohde [1] can be considered as a hydrodynamic DFT with a simple Helmholtz energy functional. With the exception of the Helmholtz energy functional, no other prerequisites are required for the derivation. In this work, we use a Helmholtz energy functional based on the perturbed-chain statistical associating fluid theory (PC-SAFT) equation of state[8–19] for quantitative modeling of the fluid behavior [see appendix A].

DDFT was first developed by Marconi and Tarazona[20,21] for colloidal systems of Brownian particles in an isothermal system and put on a more rigorous theoretical foundation by Chan and Finken[22]. Since then, it has been applied not only to spinodal decomposition[23], phase separation of colloidal fluids in a cavity[24], but also to the relaxation dynamics of colloidal systems of Brownian particles by means of the van Hove correlation function[25–28]

*All spatial derivatives in the balance equations can be formulated as divergences.

or non-equilibrium phase transition of colloids[29]. Besides to colloidal systems, DDFT for molecular fluids incorporating inertia[2,30] or considering hydrodynamic interactions[31–34] and fluctuations[35–39] gained attention. While DDFT, unlike its equilibrium counterpart, is not exact and requires approximations, power functional theory[40–43] formally removes these approximations.

The focus of this work is on microscopic hydrodynamics of molecular systems based on the work of Archer[2]. Hydrodynamics describes thermodynamic non-equilibrium by a set of local variables, namely, density, momentum, and temperature of the fluid. Phenomena that do not vary slowly enough in space do not justify such a description and necessitate a finer level of characterization, such as the time-evolution equations for the phase-space density distribution functions of molecules. Similar hydrodynamic approaches have been followed by Burghardt and Bagchi[44] who coupled the solvent dynamics to a quantum subsystem using a molecular hydrodynamic description; when investigating wetting with a DDFT/phase field method by Mickel *et al.*[45], or by Marconi and Melchionna[46–48] who solve the time-evolution equations of the single-particle phase-space distribution function of colloids and molecular fluids using a lattice Boltzmann method. Baskaran *et al.*[49] obtained a hydrodynamic DFT for pure hard spheres from the integration of the Bogoliubov-Born-Green-Kirkwood-Yvon (BBGKY) hierarchy[50–55] to study the fluid-solid phase transition of hard spheres. All approaches using the single-particle phase-space distribution function starting from the Liouville equation require an approximation or closure relation for the BBGKY hierarchy; Hughes and Burghardt[56] applied a maximum entropy closure to derive hydrodynamic equations from the hydrodynamic moments of the single-particle phase-space distribution function.

Microscopic hydrodynamic systems of mixtures have been studied by Rotenberg *et al.*[57] for binary mixtures of charged particles, and by Okamoto and Onuki[58] who studied the stability of bubbles in a binary system, and extensively by Marconi and Melchionna[59,60] and Marconi[61] who analyzed multicomponent diffusion in nanosystems by employing the multicomponent Boltzmann-Enskog equation. Microscopic hydrodynamics at the liquid-solid interface, in particular the Navier slip condition was analyzed by Camargo *et al.*[62,63] for solid spheres, while the time-dependent average of a fluid confined by planar walls was studied by Duque-Zumajo *et al.*[64,65]. Further details on DDFT can be found in the review articles by Lutsko[66] and te Vrugt *et al.*[67].

This [chapter]* is organized as follows. In section 5.2 we derive a hydrodynamic DFT model for microscopic hydrodynamics of mixtures using a generalization of the Herivel-Lin variational principle. We incorporate diffusive phenomena into the component and momentum balance, viscous momentum transport and generalized Maxwell-Stefan diffusion[68–70], respectively.

*The text in the original publication reads: [paper].

We propose generalized expressions for the driving forces of molecular diffusion for inhomogeneous systems (section 5.2.4.5). Since the focus of this work is on model synthesis and analysis, we show that the hydrodynamic DFT model satisfies the integral version of the first and second law of thermodynamics. Section 5.3 illustrates the modeling of the required mixture viscosities and Maxwell-Stefan diffusion coefficients using entropy scaling. The applied well-balanced numerical discretization scheme is described along with implementation details in section 5.4. For this purpose, the hydrodynamic DFT model is reformulated to apply numerical methods for hyperbolic-parabolic conservation laws. The hydrodynamic DFT model in combination with a Helmholtz energy functional based on the PC-SAFT equation of state is applied to droplet and bubble coalescence of binary mixtures in section 5.5 to show that the proposed model allows predictions for typically difficult problems.

5.2 Dynamic Density Functional Theory from a Variational Principle

This section introduces classical density functional theory (DFT) before deriving the hydrodynamic DFT equations for viscous mixtures using a generalization of the Herivel-Lin principle[4,5]. We then analyze the hydrodynamic DFT model equations with respect to the first and second law of thermodynamics.

5.2.1 Classical Density Functional Theory

Classical (equilibrium) DFT is formulated as a variational principle using a grand potential functional Ω, which is defined for a mixture of N_c components as

$$\Omega[\{\rho_i(\mathbf{r})\}] = F[\{\rho_i(\mathbf{r})\}] + \sum_{i=1}^{N_\mathrm{c}} \int \rho_i(\mathbf{r}) \left(V_i^\mathrm{ext}(\mathbf{r}) - \mu_i\right) \mathrm{d}\mathbf{r} \tag{5.1}$$

with Helmholtz energy functional F, molecular density $\rho_i(\mathbf{r})$ of component i at coordinate $\mathbf{r}$, chemical potential μ_i, and external potential V_i^ext acting on component i. The Helmholtz energy functional describes interactions between the fluid molecules. Solid structures are, in the spirit of DFT, represented as external potentials $V_i^\mathrm{ext}(\mathbf{r})$ acting on all components i of the fluid. The external potentials model interactions of the fluid with, e.g., solid structures. Although not made explicit in this notation, the specified variables of Ω are temperature T, volume V, and chemical potentials μ_i of all components. Square brackets denote a functional dependence, and curly brackets around $\{\rho_i(\mathbf{r})\}$ indicate a vector of all components within a mixture, $i = 1, \ldots, N_\mathrm{c}$.

In equilibrium the grand potential functional is minimal with respect to all density profiles $\{\rho_i(\mathbf{r})\}$, and the value of the grand potential functional becomes equal to the grand potential $\Omega^0 = \Omega[\{\rho_i^0\}]$. The minimum implies that for the equilibrium density profiles $\{\rho_i^0\}$, the functional derivatives of the grand potential functional Ω with respect to the density profiles $\{\rho_i(\mathbf{r})\}$ vanish according to

$$\left.\frac{\delta\Omega}{\delta\rho_i}\right|_{\{\rho_i^0\}} = 0 \tag{5.2}$$

which leads to the main equation of DFT

$$\mu_i = \frac{\delta F}{\delta\rho_i} + V_i^{\mathrm{ext}} \tag{5.3}$$

that can be solved for the equilibrium density profiles $\{\rho_i^0(\mathbf{r})\}$ in the volume under consideration, if a model for the Helmholtz energy functional is available. The equilibrium theory, eqs. (5.1)–(5.3), is exact and can be derived without approximations (approximate models are usually required for the Helmholtz energy functional $F[\{\rho_i(\mathbf{r})\}]$ of real fluids). In equilibrium, the chemical potential μ_i is constant over the whole domain; the imposed (constant) variables are $(T, V, \{\mu_i\})$.

For DDFT under non-equilibrium conditions, eq. (5.3) can be used to define a chemical potential profile $\mu_i(\mathbf{r})$, the gradients of which we can use as the thermodynamic driving forces in diffusion models for molecular transport. This approach is no longer exact, since it assumes that the functional form of the Helmholtz energy functional for the *non-equilibrium* density is the same as the Helmholtz energy functional in equilibrium, i.e., the higher order *non-equilibrium* multi-body densities $\rho_i^{(n)}(\mathbf{r}_1, \ldots, \mathbf{r}_n)$ can be approximated by the ones of the equilibrium fluid[2,20,21,23] (*adiabatic* approximation); dynamic intramolecular correlations are thus also neglected.

In the above considerations, the coordinate $\mathbf{r}$ may contain, in addition to spatial coordinates, orientational and conformational coordinates that are relevant for describing molecular microstates. In this work, we use a Helmholtz energy functional based on the PC-SAFT equation of state[13–16], for which the coordinate $\mathbf{r}$ denotes only the center-of-mass position of the molecules*, while the orientational and conformational degrees of freedom are absorbed in the de Broglie wavelength $\Lambda_i(T)$, which is irrelevant in all equations due to the isothermal conditions considered in this work.

*In a more elaborate variant of the PC-SAFT functional, the single-particle density of each segment is described individually, which is advantageous, for example, for surfactants, where the polar head-groups are spatially resolved[71].

5.2.2 Generalization of the Herivel-Lin Variational Principle

The Herivel-Lin variational principle[4,5] is based on the action functional $\mathcal{S}$, defined by

$$\mathcal{S}[\{\rho_i(\mathbf{r},t),\mathbf{v}_i(\mathbf{r},t)\}] = \iint \mathcal{L}([\{\rho_i(\mathbf{r},t),\mathbf{v}_i(\mathbf{r},t)\}])\,\mathrm{d}\mathbf{r}\,\mathrm{d}t \tag{5.4}$$

with the Lagrangian $\mathcal{L}$ as a function of the molecular densities ρ_i and the molecular velocities $\mathbf{v}_i$ of components i. Both depend on the position vector $\mathbf{r}$ and time t. By applying this variational principle, the adiabatic approximation of DDFT is automatically incorporated. Following Rohde[1], the Lagrangian is defined as

$$\mathcal{L}(\{\rho_i,\mathbf{v}_i\}) = \sum_{i=1}^{N_c} \frac{\check{m}_i}{2}\rho_i|\mathbf{v}_i|^2 - \rho a(\{\bar{\rho}_i\}) - \sum_{i=1}^{N_c}\rho_i V_i^{\mathrm{ext}} \tag{5.5}$$

with the difference between the kinetic energy density $\frac{\check{m}_i}{2}\rho|\mathbf{v}_i|^2$ including the molecular mass $\check{m}_i$ of component i and the Helmholtz energy density ρa, with the overall molecular density $\rho = \sum_i^{N_c}\rho_i$ and the Helmholtz energy per molecule $a = \frac{F}{N}$ using the number of molecules N and the weighted densities $\{\bar{\rho}_i\}$. Using the Helmholtz energy density instead of the internal energy density later leads to a system of balance equations that obey the first and second law of thermodynamics without an additional constraint for the time evolution of entropy in the system (as the Helmholtz energy already incorporates this entropy constraint for isothermal systems). In order to show that easily, we assume that there are no fluxes across the fixed system boundary and the external potential V^{ext} is conservative (has no time dependence). These assumptions can be relaxed by considering surface fluxes across the system boundary as well as time-dependent source terms for time-dependent external potentials. We omit these here for the sake of clarity and brevity.

With exception of the Helmholtz energy functional $F[\{\rho_i(\mathbf{r})\}] = \int \rho(\mathbf{r})a(\{\bar{\rho}_i(\mathbf{r})\})\,\mathrm{d}\mathbf{r}$ we do not require any prior knowledge of the system. In this work, we propose using Helmholtz energy functionals $F[\{\rho_i(\mathbf{r})\}]$ appearing in classical DFT (cf. section 5.2.1). In the action functional $\mathcal{S}$ the Helmholtz energy now appears as

$$\iint \rho a(\{\bar{\rho}_i(\mathbf{r})\})\,\mathrm{d}\mathbf{r}\,\mathrm{d}t = \int F[\{\rho_i(\mathbf{r})\}]\,\mathrm{d}t \tag{5.6}$$

The vector/matrix notation used below is clarified in appendix D.1.

5.2.2.1 Incorporating Constraints into the Variational Principle

We obtain the equations of motion for the system from the stationary path of the action functional $\mathcal{S}$. The stationary path is subject to the constraint that the identity of the molecules is preserved. This can be expressed as

$$\frac{\mathrm{d}\mathbf{x}_i}{\mathrm{d}t} \equiv \frac{\partial \mathbf{x}_i}{\partial t} + \mathbf{v}_i \cdot \nabla \mathbf{x}_i = 0 \tag{5.7}$$

which corresponds to the Lagrangian coordinates $\mathbf{x}_i$ of the molecules of component i. This results in the constraints[1] in Eulerian coordinates as

$$\frac{\partial \rho_i}{\partial t} + \nabla \cdot (\rho_i \mathbf{v}_i) = 0 \tag{5.8a}$$

$$\frac{\partial \mathbf{x}_i}{\partial t} + \mathbf{v}_i \cdot \nabla \mathbf{x}_i = 0 \tag{5.8b}$$

which represents the conservation of molecules of each component and the preservation of the identity of the molecules of each component. Equation (5.8b) denotes the material derivative of component i, eq. (5.7), in Eulerian coordinates.

Hence, the hydrodynamic DFT model is obtained by choosing $(\{\rho_i, \mathbf{v}_i\})$ such that $(\{\rho_i, \mathbf{v}_i, \mathbf{x}_i\})$ is a stationary point of the action functional $\mathcal{S}$, eq. (5.4), while the constraints from eq. (5.8) hold. This problem is the same as searching for the stationary point with respect to $(\{\rho_i, \mathbf{v}_i, \mathbf{x}_i, \delta_i, \mathbf{q}_i\})$ for the functional

$$\int_{t_0}^{t_1} \int_{\mathbb{R}^d} \mathcal{L}[\{\rho_i, \mathbf{v}_i\}] + \sum_{i=1}^{N_c} \delta_i \left(\frac{\partial \rho_i}{\partial t} + \nabla \cdot \left(\rho_i \mathbf{v}_i \right) \right) - \sum_{i=1}^{N_c} \rho_i \mathbf{q}_i \cdot \left(\frac{\partial \mathbf{x}_i}{\partial t} + \mathbf{v}_i \cdot \nabla \mathbf{x}_i \right) \mathrm{d}\mathbf{r}\, \mathrm{d}t \tag{5.9}$$

with the Lagrange multipliers $\delta_i(\mathbf{r}, t)$ and $\mathbf{q}_i(\mathbf{r}, t)$. Multiplication of the second Lagrange multiplier $\mathbf{q}_i$ with the molecular density profile ρ_i does not change the result[1], but subsequently leads to simplifications during the calculation.

In contrast to the original work of Herivel[4] and the depiction of Serrin[5], we use the Helmholtz instead of the internal energy which allows us to neglect a constraint for constant entropy of each individual molecule.

5.2.2.2 Stationary Paths from the Euler-Lagrange Equation

Solutions of the Euler-Lagrange equation

$$\frac{\partial L}{\partial f} - \sum_{j=1}^{d} \frac{\partial}{\partial r_j}\left(\frac{\partial L}{\partial\left(\frac{\partial f}{\partial r_j}\right)}\right) - \frac{\partial}{\partial t}\left(\frac{\partial L}{\partial\left(\frac{\partial f}{\partial t}\right)}\right) = 0 \tag{5.10}$$

are stationary paths for the action functionals of the type $\mathcal{S} = \iint L[f, \nabla f, \frac{\partial f}{\partial t}]\,\mathrm{d}\mathbf{r}\,\mathrm{d}t$ using the Lagrangian with incorporated constraints L. In this work, this means the stationary path for the integration argument of eq. (5.9) with respect to $f \in \{\rho_i, \mathbf{v}_i, \mathbf{x}_i, \delta_i, \mathbf{q}_i\}$.

The Euler-Lagrange equation with respect to the elements of the vector $\mathbf{x}_i$ yields

$$\frac{\partial(\rho_i \mathbf{q}_i)}{\partial t} + \nabla \cdot \left(\rho_i \mathbf{v}_i \mathbf{q}_i^{\intercal}\right) = 0 \tag{5.11}$$

This result can be simplified using the component balance from eq. (5.8a), which leads to

$$\frac{\partial \mathbf{q}_i}{\partial t} + \mathbf{v}_i \cdot \nabla \mathbf{q}_i = 0 \tag{5.12}$$

The Euler-Lagrange equation with respect to the molecular densities ρ_i results in

$$\frac{\check{m}_i}{2}|\mathbf{v}_i|^2 - \left(\frac{\delta F}{\delta \rho_i} + V_i^{\mathrm{ext}}\right) - \frac{\partial \delta_i}{\partial t} - \mathbf{v}_i \cdot \nabla \delta_i + \mathbf{q}_i \cdot \left(\frac{\partial \mathbf{x}_i}{\partial t} + \mathbf{v}_i \cdot \nabla \mathbf{x}_i\right) = 0 \tag{5.13}$$

taking advantage of the fact that there is no flux over the boundaries of the considered domain. This result can be further simplified by using eq. (5.8b), to

$$\frac{\mathrm{d}\delta_i}{\mathrm{d}t} = \frac{\partial \delta_i}{\partial t} + \mathbf{v}_i \cdot \nabla \delta_i = \frac{\check{m}_i}{2}|\mathbf{v}_i|^2 - \left(\frac{\delta F}{\delta \rho_i} + V_i^{\mathrm{ext}}\right) \tag{5.14}$$

The Euler-Lagrange equation with respect to the velocities $\mathbf{v}_i$ gives

$$\begin{aligned} \check{m}_i \rho_i \mathbf{v}_i - \rho_i \nabla \delta_i - \rho_i \nabla \mathbf{x}_i \cdot \mathbf{q}_i &= 0 \\ \check{m}_i \mathbf{v}_i - \nabla \delta_i - \nabla \mathbf{x}_i \cdot \mathbf{q}_i &= 0 \end{aligned} \tag{5.15}$$

The material derivative of eq. (5.15) yields

$$\frac{\mathrm{d}(\check{m}_i \mathbf{v}_i)}{\mathrm{d}t} = \frac{\mathrm{d}\nabla \delta_i}{\mathrm{d}t} + \nabla \mathbf{x}_i \cdot \frac{\mathrm{d}\mathbf{q}_i}{\mathrm{d}t} + \frac{\mathrm{d}\nabla \mathbf{x}_i}{\mathrm{d}t} \cdot \mathbf{q}_i \tag{5.16}$$

which can be simplified with $\frac{\mathrm{d}\mathbf{q}_i}{\mathrm{d}t} = 0$ from eq. (5.12), and

$$\frac{\mathrm{d}\nabla\mathbf{x}_i}{\mathrm{d}t} = \frac{\partial\nabla\mathbf{x}_i}{\partial t} + \mathbf{v}_i\cdot\nabla\nabla\mathbf{x}_i = \nabla\frac{\partial\mathbf{x}_i}{\partial t} + \nabla(\mathbf{v}_i\cdot\nabla\mathbf{x}_i) - \nabla\mathbf{v}_i\cdot\nabla\mathbf{x}_i = \nabla\frac{\mathrm{d}\mathbf{x}_i}{\mathrm{d}t} - \nabla\mathbf{v}_i\cdot\nabla\mathbf{x}_i \tag{5.17}$$

with $\frac{\partial\nabla\mathbf{x}_i}{\partial t} = \nabla\frac{\partial\mathbf{x}_i}{\partial t}$ as well as $\frac{\mathrm{d}\mathbf{x}_i}{\mathrm{d}t} = 0$ from eqs. (5.7) and (5.8b). This results in

$$\frac{\mathrm{d}(\check{m}_i\mathbf{v}_i)}{\mathrm{d}t} = \nabla\frac{\mathrm{d}\delta_i}{\mathrm{d}t} - \nabla\mathbf{v}_i\cdot\nabla\delta_i - \nabla\mathbf{v}_i\cdot\nabla\mathbf{x}_i\cdot\mathbf{q}_i \tag{5.18}$$

Replacing $\frac{\mathrm{d}\delta_i}{\mathrm{d}t}$ in the first summand with eq. (5.14) and $\nabla\delta_i$ in the second summand with eq. (5.15) yields

$$\frac{\mathrm{d}(\check{m}_i\mathbf{v}_i)}{\mathrm{d}t} = \frac{\partial(\check{m}_i\mathbf{v}_i)}{\partial t} + \mathbf{v}_i\cdot\nabla(\check{m}_i\mathbf{v}_i) = -\nabla\left(\frac{\delta F}{\delta\rho_i} + V_i^{\mathrm{ext}}\right) \tag{5.19}$$

where we have used the identity $\nabla\frac{\check{m}_i}{2}|\mathbf{v}_i|^2 = \check{m}_i\mathbf{v}_i\cdot\nabla\mathbf{v}_i$. Multiplication of eq. (5.19) with ρ_i and using the component balance, eq. (5.8a), leads to the component-wise momentum balance

$$\frac{\partial(\check{m}_i\rho_i\mathbf{v}_i)}{\partial t} + \nabla\cdot\left(\check{m}_i\rho_i\mathbf{v}_i\mathbf{v}_i^{\intercal}\right) = -\rho_i\nabla\left(\frac{\delta F}{\delta\rho_i} + V_i^{\mathrm{ext}}\right) \tag{5.20}$$

This system contains only the reversible dynamics due to the derivation from a variational principle. All intermolecular interactions, including those between different components of the mixture, are described by the Helmholtz energy functional F. The irreversible effects of viscosity and molecular diffusion are not yet included.

In this work, we only consider molecular systems and therefore disregard drag and hydrodynamic interactions (which are used to model colloidal systems), unlike in the work of Goddard *et al.*[3], for which the component-wise momentum balance for mixtures agrees with this work. The same applies to previous results by Archer[2] for pure substances.

5.2.3 Hydrodynamic Density Functional Theory Including Diffusive Transport of Momentum and Molecules

If we add the divergence of the Cauchy pressure tensors ($-\nabla\cdot\boldsymbol{\tau}_i$) of each individual component i on the right-hand side of eq. (5.20) and sum up all components, we obtain

$$\frac{\partial(\check{m}\rho\mathbf{v})}{\partial t} + \nabla\cdot(\check{m}\rho\mathbf{v}\mathbf{v}^{\intercal}) = -\sum_{i=1}^{N_c}\rho_i\nabla\left(\frac{\delta F}{\delta\rho_i} + V_i^{\mathrm{ext}}\right) - \nabla\cdot\boldsymbol{\tau} \tag{5.21}$$

with the mean molecular mass in the mixture defined by $\check{m} \equiv \sum_i^{N_c} x_i \check{m}_i$ using the mole fraction x_i, the barycentric velocity $\mathbf{v} \equiv \frac{1}{\check{m}\rho} \sum_i^{N_c} \check{m}_i \rho_i \mathbf{v}_i$* with the shorthand $\check{m}\rho \equiv \sum_i^{N_c} \check{m}_i \rho_i$, as well as the Cauchy pressure tensor of the mixture

$$\boldsymbol{\tau} \equiv \sum_{i=1}^{N_c} \left(\boldsymbol{\tau}_i + \check{m}_i \rho_i (\mathbf{v}_i - \mathbf{v})(\mathbf{v}_i - \mathbf{v})^\intercal \right) = \sum_{i=1}^{N_c} \left(\boldsymbol{\tau}_i + \check{m}_i \rho_i (\mathbf{v}_i - \mathbf{v}) \mathbf{v}_i^\intercal \right) \tag{5.22}$$

which is composed of the Cauchy pressure tensors of the individual components $\boldsymbol{\tau}_i$ and a contribution from the diffusive molecular fluxes†. The sum of the momentum transfer between the components needs to be zero for eq. (5.22) to maintain the conservative character of the momentum balance[72,73]. For pure components, eq. (5.21) is the hydrodynamic DFT model proposed by Archer[2]. Because we only consider molecular systems, we do not consider drag. In this work, we model the Cauchy pressure tensor as a Newtonian fluid defined by

$$\boldsymbol{\tau} = -\lambda (\nabla \cdot \mathbf{v}) \mathbb{I} - 2\eta \left(\frac{1}{2} \nabla \mathbf{v} + \frac{1}{2} (\nabla \mathbf{v})^\intercal \right) \tag{5.23a}$$

$$= -\zeta (\nabla \cdot \mathbf{v}) \mathbb{I} - \eta \left(\nabla \mathbf{v} + (\nabla \mathbf{v})^\intercal - \frac{2}{3} (\nabla \cdot \mathbf{v}) \mathbb{I} \right) \tag{5.23b}$$

with the identity matrix $\mathbb{I}$, the first Lamé constant λ, the dynamic shear viscosity η (second Lamé constant), and the volume viscosity $\zeta \equiv \lambda + \frac{2}{3}\eta$, which is often neglected in liquid systems. The decomposition in eq. (5.23b) represents the dilatation and the viscous shear contribution to the Cauchy pressure tensor separately. The viscous shear contribution is symmetrical and traceless, which motivates this decomposition. All viscosities are mixture properties.

5.2.3.1 Hydrodynamic Density Functional Theory – Model Equations

The complete hydrodynamic DFT model can be expressed as

$$\frac{\partial (\check{m}\rho)}{\partial t} + \nabla \cdot (\check{m}\rho \mathbf{v}) = 0 \tag{5.24a}$$

$$\frac{\partial \rho_i}{\partial t} + \nabla \cdot (\rho_i \mathbf{v} + \mathbf{j}_i^{\mathrm{diff}}) = 0 \tag{5.24b}$$

$$\frac{\partial (\check{m}\rho \mathbf{v})}{\partial t} + \nabla \cdot (\check{m}\rho \mathbf{v}\mathbf{v}^\intercal) = -\sum_{i=1}^{N_c} \rho_i \nabla \left(\frac{\delta F}{\delta \rho_i} + V_i^{\mathrm{ext}} \right) - \nabla \cdot \boldsymbol{\tau} \tag{5.24c}$$

*This expression can be reformulated to the more straightforward definition $\mathbf{v} \equiv \sum_i^{N_c} w_i \mathbf{v}_i$, using the mass fraction $w_i = \frac{x_i \check{m}_i}{\sum_j^{N_c} x_j \check{m}_j}$.

†The [last equality] can be obtained using eq. (5.25).

where we introduced diffusive molecular fluxes $\mathbf{j}_i^{\mathrm{diff}} \equiv \rho_i(\mathbf{v}_i - \mathbf{v})$ of components i with respect to the barycentric velocity $\mathbf{v}$. The diffusive fluxes need to be described by a constitutive equation. In this work, we propose using the generalized Maxwell-Stefan diffusion[68–70], as described in detail in appendix D.3. Due to eq. (5.24a), eq. (5.24b) is considered for all but one component, i.e., for $i = 1, \ldots, (N_\mathrm{c} - 1)$, noting also that the diffusive fluxes are not independent, but are connected by

$$\check{m}_{N_\mathrm{c}} \mathbf{j}_{N_\mathrm{c}}^{\mathrm{diff}} = -\sum_{i=1}^{N_\mathrm{c}-1} \check{m}_i \mathbf{j}_i^{\mathrm{diff}} \tag{5.25}$$

The hydrodynamic DFT model in eq. (5.24) is characterized by a similar structure to diffuse interface models, such as the isothermal Navier-Stokes-Korteweg equations. However, the interfacial thickness is typically on the nanometer scale (in agreement with molecular simulations). Moreover, the effect of fluid-fluid interfaces is captured by the DFT term $\sum_i^{N_\mathrm{c}} \rho_i \nabla\left(\frac{\delta F}{\delta \rho_i}\right)$ without the need for specifying interfacial tension or adsorption behavior. The effect of solid walls or confinement is captured by external potentials V_i^{ext}, as a field acting on the fluid. In fact, the DFT term in eq. (5.24c) is predictive for interfacial properties and agrees well with experimental data for interfacial tensions of mixtures[13–16,74] including surfactants[71], adsorption isotherms of multicomponent systems[75], and contact angles of sessile droplets[17], without any additional parameters. For sufficiently large distances from vapor-liquid, liquid-liquid, or fluid-solid interfaces, the term $\sum_i^{N_\mathrm{c}} \rho_i \nabla\left(\frac{\delta F}{\delta \rho_i}\right)$ in eq. (5.24c) simplifies to the pressure gradient ∇p, yielding the familiar momentum balance of the Navier-Stokes equations.

5.2.3.2 Assumptions of the Hydrodynamic Density Functional Theory

The hydrodynamic DFT model proposed in eq. (5.24) is based on several model assumptions that we point out by comparison with the exact formulation of Chan and Finken[22].

The proposed hydrodynamic DFT model considers only the two lowest hydrodynamic moments of the phase-space distribution function (component and momentum balance) in an infinite hierarchy (viz., the BBGKY hierarchy[50–54]), which is justified if the system is not too far from equilibrium. The Yvon-Born-Green hierarchy[55,76] is used as a closure relation for the BBGKY hierarchy. This takes into account all multi-body correlations but is exact only in thermodynamic equilibrium. This so-called *adiabatic* approximation implies that at any given instant, all molecular correlation functions are equal to the correlation functions of the equilibrium system (which exhibits no time correlation) with the same density profile. This allows replacing the *action functional* used by Chan and Finken[22] with the Helmholtz energy functional $F[\{\rho_i\}]$ from equilibrium DFT (which is exact for equilibrium situations since it is

based on the Yvon-Born-Green hierarchy).

Orientational and conformational relaxation as well as dynamic intramolecular correlations are neglected in the hydrodynamic DFT model, which is consistent with the PC-SAFT Helmholtz energy functional used in this work, that also does not resolve orientational and conformational degrees of freedom.

Moreover, the pressure tensor functional that represents hydrodynamic effects, defined by Chan and Finken[22] as $\boldsymbol{\sigma}[\{\rho_i\}]$, is approximated by $\boldsymbol{\sigma} \equiv \nabla \cdot \left(\check{m}\rho \mathbf{v}\mathbf{v}^\intercal + \boldsymbol{\tau} + p^{\mathrm{ig}}\mathbb{I}\right)$, which results from the application of the generalized Herivel-Lin principle[1] (which is a continuum approach)*. The description of the convective momentum transport $\nabla \cdot (\check{m}\rho \mathbf{v}\mathbf{v}^\intercal)$ and the viscous contribution to the pressure tensor $\nabla \cdot \boldsymbol{\tau}$ in the hydrodynamic DFT model stems from the continuum treatment of the fluid, which, however, is only an approximation for the hydrodynamic effects on the molecular scale. An interaction of the two terms can already be observed in eq. (5.22). A more complex relationship is not explored in this work.

5.2.4 Non-Equilibrium Thermodynamics, First & Second Law of Thermodynamics, Energy Inequalities

In the following, we show that for the hydrodynamic DFT model for mixtures, proposed in eq. (5.24), the integral versions of the first and second law of thermodynamics are fulfilled. The previously used assumption (cf. appendix D.2) that no fluxes are allowed across the system boundary, corresponds to an isolated thermodynamic system.

5.2.4.1 Isothermal Non-Equilibrium Thermodynamics

The volume specific entropy production $\dot{\sigma}$ in an isothermal system without chemical reactions and in the absence of an electrical field can be described by[77]

$$\dot{\sigma} = \sum_{i=1}^{N_\mathrm{c}} \mathbf{j}_i^{\mathrm{diff}} \cdot \left(-\frac{1}{T}\nabla_T \mu_i^{\mathrm{diff}}\right) + \boldsymbol{\tau} : \left(-\frac{1}{T}\nabla \mathbf{v}\right) \tag{5.26}$$

with the absolute temperature T and the thermodynamic driving force for diffusion $\nabla_T \mu_i^{\mathrm{diff}}$ in the direction of constant temperature defined by $\nabla_T \mu_i^{\mathrm{diff}} = \nabla \mu_i^{\mathrm{diff}} + s_i \nabla T$, with partial molar entropies s_i. For the isothermal systems considered in this work follows $\nabla_T \mu_i^{\mathrm{diff}} = \nabla \mu_i^{\mathrm{diff}}$, thence we omit the temperature index in the gradients from here on. For suitable definition of

*The notation of the pressure tensor functional $\boldsymbol{\sigma}[\{\rho_i\}]$ corresponds to ref. 22 and should not be confused with the entropy production $\dot{\sigma}$, the PC-SAFT segment size parameter σ_i, or the Lanczos σ-factor used in this work.

a driving force for molecular diffusion in inhomogeneous systems, we introduce quantity μ_i^{diff}, which is different from the chemical potential μ_i (as expressed in eq. (5.3)). The driving force is identified below as eq. (5.45).

Entropy production $\dot{\sigma}$ is the central quantity of linear non-equilibrium thermodynamics[77]. Equation (5.26) can be reformulated as a sum of products of all independent fluxes $\mathbf{J}_k \in \left\{\{\mathbf{j}_i^{\mathrm{diff}}\}, \boldsymbol{\tau}\right\}$ and their conjugate driving forces $\mathbf{X}_k \in \left\{\{-\frac{1}{T}\nabla\mu_i^{\mathrm{diff}}\}, -\frac{1}{T}\nabla\mathbf{v}\right\}$ according to

$$\dot{\sigma}(\mathbf{r},t) = \sum_k \mathbf{J}_k \cdot \mathbf{X}_k \tag{5.27}$$

where the index k denotes different types of transport. Fluxes and driving forces have the same tensorial rank. Entropy production is a local and time-dependent quantity, indicated by the positional and time coordinate $\mathbf{r}$ and t in eq. (5.27).

Equation (5.27) contains no information about the relation between fluxes and conjugate driving forces. Linear relations of the form

$$\mathbf{J}_i = \sum_j L_{ij}\mathbf{X}_j \tag{5.28a}$$

$$\mathbf{X}_j = \sum_k R_{jk}\mathbf{J}_k \tag{5.28b}$$

can be assumed in conductivity, eq. (5.28a), or resistivity form, eq. (5.28b), including the matrices for the phenomenological Onsager coefficients $\mathbf{L}$ and resistivities $\mathbf{R}$, which must be symmetric and positive semi-definite for thermodynamic consistency, as demonstrated by Onsager[78,79].

The non-equilibrium thermodynamics framework described above rests upon the assumption that the Gibbs equation is locally satisfied. This is compatible with the adiabatic approximation of DDFT, which assumes that the dynamic processes occur quasi-statically, i.e., the fluid structure can be assumed to be in an equilibrium state (induced by an additional instantaneous external potential, satisfying the Yvon-Born-Green hierarchy[55,76]).

5.2.4.2 Entropy Balance/Second Law & Entropy Production

The entropy balance of a isothermal system of mixtures can be expressed as

$$\frac{\partial(\rho s)}{\partial t} + \nabla\cdot\left(\sum_{i=1}^{N_c}\rho_i s_i \mathbf{v}_i\right) = \dot{\sigma} \tag{5.29a}$$

$$\frac{\partial(\rho s)}{\partial t} + \nabla\cdot\left(\sum_{i=1}^{N_c}\rho_i s_i \mathbf{v} + \sum_{i=1}^{N_c}\mathbf{j}_i^{\mathrm{diff}} s_i\right) = \dot{\sigma} \tag{5.29b}$$

with the entropy per molecule s, the partial molar entropies s_i with entropy density $\rho s = \sum_i^{N_c}\rho_i s_i$, and the entropy production per unit volume $\dot{\sigma}$. From integration of eq. (5.29) over the entire domain and assuming that no transport across the stationary boundary of the domain occurs (cf. appendix D.2), we obtain

$$\frac{\partial}{\partial t}\int \rho s \,\mathrm{d}\mathbf{r} = \int \dot{\sigma}\,\mathrm{d}\mathbf{r} = \int \sum_{i=1}^{N_c}\mathbf{j}_i^{\mathrm{diff}}\cdot\left(-\frac{1}{T}\nabla\mu_i^{\mathrm{diff}}\right) + \boldsymbol{\tau} : \left(-\frac{1}{T}\nabla\mathbf{v}\right)\mathrm{d}\mathbf{r} \tag{5.30}$$

where the convective entropy fluxes were eliminated by applying eq. (D.6). We can interpret this result, namely, the change in entropy of the considered isolated system is solely due to entropy production by molecular diffusion and viscous shear within the system.

In the following, we show in sections 5.2.4.3 and 5.2.4.4 that the right-hand side of eq. (5.30) is non-negative so that for entropy production, $\dot{\sigma} \geq 0$ holds, and the hydrodynamic DFT model thus obeys the second law of thermodynamics. To show this, however, we first need to be concerned with molecular diffusion, which we do below in section 5.2.4.5.

5.2.4.3 Entropy Production for Viscous Dissipation

In the following, we show under which circumstances entropy production in isothermal systems, defined in eq. (5.26), is positive to satisfy the Clausius-Duhem inequality $\dot{\sigma} \geq 0$.

The viscous dissipation in eq. (5.26) can be reformulated into

$$-\boldsymbol{\tau} : \nabla\mathbf{v} = 2\eta\left(\boldsymbol{\Gamma} - \frac{1}{3}(\nabla\cdot\mathbf{v})\,\mathbb{I}\right) : \left(\boldsymbol{\Gamma} - \frac{1}{3}(\nabla\cdot\mathbf{v})\,\mathbb{I}\right) + \zeta\,(\nabla\cdot\mathbf{v})^2 \geq 0 \tag{5.31}$$

using the definition of the shear pressure tensor, eq. (5.23), and a decomposition of the velocity gradient into a scalar invariant, a symmetric traceless part, and an antisymmetric part according to $\nabla\mathbf{v} = \frac{1}{3}(\nabla\cdot\mathbf{v})\mathbb{I} + \left(\boldsymbol{\Gamma} - \frac{1}{3}(\nabla\cdot\mathbf{v})\mathbb{I}\right) + \boldsymbol{\Omega}$, with the rate of strain tensor $\boldsymbol{\Gamma} = \frac{1}{2}\left(\nabla\mathbf{v} + (\nabla\mathbf{v})^{\intercal}\right)$ and the vorticity tensor $\boldsymbol{\Omega} = \frac{1}{2}\left(\nabla\mathbf{v} - (\nabla\mathbf{v})^{\intercal}\right)$. Note that both the double dot product of the scalar invariant with the traceless part and the vorticity tensor with the traceless part vanish.

From eq. (5.31), it can easily be seen that for positive volume and shear viscosities, $\zeta = \lambda + \frac{2}{3}\eta \geq 0$ and $\eta \geq 0$, the viscous contributions individually are always positive, as required by the Curie principle[77] (the scalar-valued dilatation contribution to entropy production does not couple with the vector-valued shear contribution), since the rate of shear pressure tensor and the divergence of the velocity both occur quadratically.

5.2.4.4 Entropy Production for Maxwell-Stefan Diffusion

In this work, we propose using Maxwell-Stefan diffusion, which is formulated in resistivity form, cf. eq. (5.28b), according to

$$-\frac{\rho_i \nabla \mu_i^{\mathrm{diff}}}{k_{\mathrm{B}} T} = \sum_{j \neq i}^{N_{\mathrm{c}}} \frac{1}{\mathcal{D}_{ij}} \left(x_j \mathbf{j}_i^{\mathrm{diff}} - x_i \mathbf{j}_j^{\mathrm{diff}} \right) \tag{5.32}$$

with binary Maxwell-Stefan diffusion coefficients $\mathcal{D}_{ij}$ connected to the phenomenological Onsager resistivities defined in eq. (5.28b) via $R_{ij} = -\frac{k_{\mathrm{B}}}{\rho \mathcal{D}_{ij}}$. We already set the frame of reference to the barycentric velocity. We consider the generalized Maxwell-Stefan diffusion[68–70].

Let us consider the entropy production, eq. (5.26), and more specifically the contribution from molecular diffusion, defined as

$$\sum_{i=1}^{N_{\mathrm{c}}} \mathbf{j}_i^{\mathrm{diff}} \cdot \left(-\frac{1}{T} \nabla \mu_i^{\mathrm{diff}} \right) \tag{5.33}$$

and the thermodynamic driving force from eq. (5.28b) for isothermal systems, we obtain

$$\mathbf{X}_i = \left(-\frac{1}{T} \nabla \mu_i^{\mathrm{diff}} \right) = \sum_{j=1}^{N_{\mathrm{c}}} R_{ij} \mathbf{j}_j^{\mathrm{diff}} \tag{5.34}$$

which leads to

$$\sum_{i=1}^{N_{\mathrm{c}}} \sum_{j=1}^{N_{\mathrm{c}}} \mathbf{j}_i^{\mathrm{diff}} R_{ij} \mathbf{j}_j^{\mathrm{diff}} \geq 0 \tag{5.35}$$

For thermodynamic consistency, the resistivity matrix $\mathbf{R}$ must be at least positive semi-definite (cf. section 5.2.4.1; for binary systems, as considered in this work, this implies $\mathcal{D}_{12} \geq 0$). Since the Maxwell-Stefan diffusion coefficients $\mathcal{D}_{ij}$ can be directly obtained from the resistivity matrix $\mathbf{R}$, we can argue that entropy production for the generalized Maxwell-Stefan diffusion leads to positive entropy production when $\mathbf{R}$ is chosen to be thermodynamically consistent[77].

The same can be shown for the conductivity form by using eqs. (5.3), (5.28a), and (5.33), which leads to

$$\sum_{i=1}^{N_c}\sum_{j=1}^{N_c}\left(-\frac{1}{T}\nabla\mu_i^{\mathrm{diff}}\right)L_{ij}\left(-\frac{1}{T}\nabla\mu_j^{\mathrm{diff}}\right)\geq 0 \tag{5.36}$$

with the semi-definite conductivity matrix $\mathbf{L}$ of phenomenological Onsager coefficients[78,79].

The analysis confirms that the second law of thermodynamics is obeyed; entropy production as determined from the hydrodynamic DFT model for an adiabatic system cannot become negative.

5.2.4.5 Combination of First & Second Law of Thermodynamics

Having shown that the proposed hydrodynamic DFT model obeys the second law of thermodynamics (non-negative entropy production), we will show below that, although not formulated in a conservative form, it conserves the sum of kinetic, internal, and potential energy in an isolated system (integral version of the first law of thermodynamics).

Calculation of the dot product of eq. (5.24c) with the velocity and using $\mathbf{v}\cdot\nabla\cdot\boldsymbol{\tau}=\nabla\cdot(\boldsymbol{\tau}\cdot\mathbf{v})-\boldsymbol{\tau}:\nabla\mathbf{v}$ and the continuity equation, eq. (5.24a), leads to

$$\frac{\partial\left(\frac{\check{m}}{2}\rho|\mathbf{v}|^2\right)}{\partial t}+\nabla\cdot\left(\frac{\check{m}}{2}\rho|\mathbf{v}|^2\mathbf{v}\right)=-\sum_{i=1}^{N_c}\rho_i\mathbf{v}\cdot\nabla\left(\frac{\delta F}{\delta\rho_i}+V_i^{\mathrm{ext}}\right)-\nabla\cdot(\boldsymbol{\tau}\cdot\mathbf{v})+\boldsymbol{\tau}:\nabla\mathbf{v} \tag{5.37}$$

which represents the balance equation of the kinetic energy density.

By integrating eq. (5.37) and assuming there is no transport across the domain boundary (cf. appendix D.2), we obtain

$$\int\frac{\partial\left(\frac{\check{m}}{2}\rho|\mathbf{v}|^2\right)}{\partial t}\,\mathrm{d}\mathbf{r}=-\int\sum_{i=1}^{N_c}\rho_i\mathbf{v}\cdot\nabla\left(\frac{\delta F}{\delta\rho_i}+V_i^{\mathrm{ext}}\right)\mathrm{d}\mathbf{r}+\int\boldsymbol{\tau}:\nabla\mathbf{v}\,\mathrm{d}\mathbf{r} \tag{5.38}$$

where we already applied eq. (D.6) to eliminate the convective fluxes of kinetic energy and shear pressure. The first integral on the right-hand side of eq. (5.38) simplifies using eq. (D.7), where we assume that there is no flux over the boundary of the considered domain, to

$$\int\frac{\partial\left(\frac{\check{m}}{2}\rho|\mathbf{v}|^2\right)}{\partial t}\,\mathrm{d}\mathbf{r}=\int\sum_{i=1}^{N_c}\big(\nabla\cdot(\rho_i\mathbf{v})\big)\left(\frac{\delta F}{\delta\rho_i}+V_i^{\mathrm{ext}}\right)\mathrm{d}\mathbf{r}+\int\boldsymbol{\tau}:\nabla\mathbf{v}\,\mathrm{d}\mathbf{r} \tag{5.39}$$

On the right-hand side, by replacing the divergence in the first integral with eq. (5.24b), we

get

$$\int \frac{\partial\left(\frac{\check{m}}{2}\rho|\mathbf{v}|^2\right)}{\partial t}\,\mathrm{d}\mathbf{r} = -\int \sum_{i=1}^{N_c}\left(\frac{\delta F}{\delta\rho_i}+V_i^{\mathrm{ext}}\right)\frac{\partial\rho_i}{\partial t}\,\mathrm{d}\mathbf{r} - \int \sum_{i=1}^{N_c}\left(\nabla\cdot\mathbf{j}_i^{\mathrm{diff}}\right)\left(\frac{\delta F}{\delta\rho_i}+V_i^{\mathrm{ext}}\right)\mathrm{d}\mathbf{r} + \int \boldsymbol{\tau}:\nabla\mathbf{v}\,\mathrm{d}\mathbf{r} \quad (5.40)$$

where the first term on the right-hand side simplifies to

$$\int \sum_{i=1}^{N_c}\left(\frac{\delta F}{\delta\rho_i}+V_i^{\mathrm{ext}}\right)\frac{\partial\rho_i}{\partial t}\,\mathrm{d}\mathbf{r} = \frac{\partial}{\partial t}\left(F[\{\rho_i\}]+\int \sum_{i=1}^{N_c}\rho_i V_i^{\mathrm{ext}}\,\mathrm{d}\mathbf{r}\right) \quad (5.41)$$

where we used the chain rule and eq. (5.6) (for more details, consult appendix D.4). The second term of eq. (5.40) simplifies using eq. (D.7), assuming no flux across the domain boundary, leading to rewrite eq. (5.40) as

$$\frac{\partial}{\partial t}\int\left(\frac{\check{m}}{2}\rho|\mathbf{v}|^2+\rho a+\sum_{i=1}^{N_c}\rho_i V_i^{\mathrm{ext}}\right)\mathrm{d}\mathbf{r} + T\int\sum_{i=1}^{N_c}\mathbf{j}_i^{\mathrm{diff}}\cdot\left(-\frac{1}{T}\nabla\left(\frac{\delta F}{\delta\rho_i}+V_i^{\mathrm{ext}}\right)\right)\mathrm{d}\mathbf{r} + T\int\sum_{i=1}^{N_c}\mathbf{j}_i^{\mathrm{diff}}\cdot\left(\frac{1}{T}\frac{w_i}{\rho_i}\sum_{j=1}^{N_c}\rho_j\nabla\left(\frac{\delta F}{\delta\rho_j}+V_j^{\mathrm{ext}}\right)\right)\mathrm{d}\mathbf{r} + T\int\boldsymbol{\tau}:\left(-\frac{1}{T}\nabla\mathbf{v}\right)\mathrm{d}\mathbf{r}=0 \quad (5.42)$$

where (for a reason that is given below) we added a complicated zero as the third [integral term]*

$$\left(\sum_{i=1}^{N_c}\mathbf{j}_i^{\mathrm{diff}}\frac{w_i}{\rho_i}\right)\cdot\left(\sum_{j=1}^{N_c}\rho_j\nabla\left(\frac{\delta F}{\delta\rho_j}+V_j^{\mathrm{ext}}\right)\right)=0 \quad (5.43)$$

which is zero because $\sum_i^{N_c}\mathbf{j}_i^{\mathrm{diff}}\frac{w_i}{\rho_i}=\sum_i^{N_c}w_i(\mathbf{v}_i-\mathbf{v})=\mathbf{v}-\mathbf{v}=0$, with the mass fractions $w_i\equiv\frac{\check{m}_i\rho_i}{\check{m}\rho}$, as well as the definition of the diffusive molecular fluxes and the barycentric velocity from section 5.2.3. We reformulate the dissipative terms of eq. (5.42) to match eq. (5.26), yielding

$$\frac{\partial}{\partial t}\int\left(\frac{\check{m}}{2}\rho|\mathbf{v}|^2+\rho a+\sum_{i=1}^{N_c}\rho_i V_i^{\mathrm{ext}}\right)\mathrm{d}\mathbf{r} + T\int\sum_{i=1}^{N_c}\mathbf{j}_i^{\mathrm{diff}}\cdot\left(-\frac{1}{T}\nabla\mu_i^{\mathrm{diff}}\right)\mathrm{d}\mathbf{r} + T\int\boldsymbol{\tau}:\left(-\frac{1}{T}\nabla\mathbf{v}\right)\mathrm{d}\mathbf{r}=0 \quad (5.44)$$

where the driving force for molecular diffusion of component i for inhomogeneous fluids can

*The text in the original publication reads: [line].

be identified as

$$\rho_i \nabla \mu_i^{\mathrm{diff}} \equiv \rho_i \nabla \left(\frac{\delta F}{\delta \rho_i} + V_i^{\mathrm{ext}} \right) - w_i \sum_{j=1}^{N_c} \rho_j \nabla \left(\frac{\delta F}{\delta \rho_j} + V_j^{\mathrm{ext}} \right) \tag{5.45}$$

We recall that the DFT formalism, eq. (5.3), states that $\left(\frac{\delta F}{\delta \rho_i} + V_i^{\mathrm{ext}} \right) = \mu_i$. Thus, the driving force expressed as $\nabla \mu_i^{\mathrm{diff}}$ contains an additional term (on the right-hand side of eq. (5.45)) that accounts for pressures/tensions that contribute considerably at interfaces. The structure of eq. (5.45) is in agreement with refs. 68–70 considering the definition of the DFT chemical potential from eq. (5.3) and the external forces $\mathbf{F}_i \equiv -\nabla \left(\frac{\delta F}{\delta \rho_j} + V_i^{\mathrm{ext}} \right)$ from the momentum balance of the hydrodynamic DFT model, eq. (5.24c).

Driving forces for molecular diffusion, as defined in eq. (5.45), have the important property

$$\sum_i^{N_c} \rho_i \nabla \mu_i^{\mathrm{diff}} = 0 \tag{5.46}$$

which is a prerequisite for deriving Maxwell-Stefan equations, where the diagonal elements of the resistivity (or diffusion) coefficients are eliminated due to this relation. Equation (5.46) implies the Gibbs-Duhem equation for inhomogeneous fluids. The requirement to obey eq. (5.46) for the driving force led us to introduce a complicated zero: eq. (5.43) within eq. (5.42). For fluids sufficiently far from interfaces, a comparable form, namely, the *generalized driving force*, was proposed by Curtiss and Bird [68,69]. Their expression reads in our notation as

$$\rho_i \nabla \mu_i^{\mathrm{diff}} = \rho_i \nabla \mu_i - w_i \left(\nabla p + \sum_{j=1}^{N_c} \rho_j \nabla V_j^{\mathrm{ext}} \right) \tag{5.47}$$

which also satisfies the condition in eq. (5.46). The chemical potential μ_i is also defined by eq. (5.3), now for homogeneous fluids, which includes the contribution due to external potentials. The pressure gradient ∇p corresponds to the homogeneous version of $\sum_j^{N_c} \rho_j \nabla \left(\frac{\delta F}{\delta \rho_j} \right)$ in eq. (5.45). In that sense, eq. (5.45) can be regarded as a generalization of the *generalized driving force* to inhomogeneous fluids.

The Helmholtz energy density in eq. (5.44) can be reformulated as

$$\sum_{i=1}^{N_c} \rho_i a_i = \rho a = \rho u - T \rho s = \sum_{i=1}^{N_c} (\rho_i u_i - T \rho_i s_i) \tag{5.48}$$

with the partial molar Helmholtz energies a_i, the internal energy density ρu, and the partial

molar internal energies u_i. Combining eqs. (5.3), (5.30), (5.44), and (5.48) leads to

$$\frac{\partial}{\partial t}\int\left(\frac{\check{m}}{2}\rho|\mathbf{v}|^2+\rho u+\sum_{i=1}^{N_c}\rho_i V_i^{\mathrm{ext}}\right)\mathrm{d}\mathbf{r}=0 \tag{5.49}$$

where the entropy balance cancels with the integrals describing dissipation from molecular diffusion and viscosity. This shows global conservation of the sum of kinetic, internal and potential energy in an isolated system. This means that the hydrodynamic DFT model proposed in eq. (5.24), although not written in local conservative form, satisfies integral versions of the first and second law of thermodynamics.

5.2.4.6 Dissipation Relation

The total energy of the whole system remains constant without any fluxes across the system boundary and constant external potential as shown in eq. (5.49). Combining eq. (5.44) with the results from sections 5.2.4.3 and 5.2.4.4 shows that the right-hand side of the global dissipation relation

$$\begin{aligned}\frac{\partial}{\partial t}\left(\int\frac{\check{m}}{2}\rho|\mathbf{v}|^2\,\mathrm{d}\mathbf{r}+F[\{\rho_i\}]+\int\sum_{i=1}^{N_c}\rho_i V_i^{\mathrm{ext}}\,\mathrm{d}\mathbf{r}\right)&\\ =-T\int\sum_{i=1}^{N_c}\mathbf{j}_i^{\mathrm{diff}}\cdot\left(-\frac{1}{T}\nabla\mu_i^{\mathrm{diff}}\right)\mathrm{d}\mathbf{r}-T\int\boldsymbol{\tau}:\left(-\frac{1}{T}\nabla\mathbf{v}\right)\mathrm{d}\mathbf{r}\leq 0&\end{aligned} \tag{5.50}$$

is non-positive (due to dissipation from molecular diffusion and viscous momentum diffusion).

After rewriting the left-hand side into separate terms for reasons of clarity, this indicates that for the overall system, the sum of kinetic energy, Helmholtz energy, and energy from an external potential decreases monotonically over time, establishing a natural Lyapunov functional. For an isothermal system without fluxes across the boundary and in mechanical and thermodynamic equilibrium, this corresponds to the minimum principle of the Helmholtz energy.

5.3 Modeling of Transport Coefficients

Knowledge of the transport coefficients, namely, shear viscosity η (in this work, we neglect the effect of the volume viscosity ζ) and Maxwell-Stefan diffusion coefficients $\mathcal{D}_{ij}$, is required to solve the proposed hydrodynamic DFT model. We model the shear viscosity in mixtures and the self-diffusion coefficients of pure components by entropy scaling based on the

PC-SAFT equation of state[80–83]. The Maxwell-Stefan diffusion coefficients are determined from an approximation for the self-diffusion coefficients in a mixture combined with the Darken equation[84,85]. Entropy scaling methods originally developed by Rosenfeld[86–88] suggest a simple, univariable correlation of transport coefficients with the residual entropy per molecule $s^{\mathrm{res}}(\{\rho_i\}, T)$.

These methods were developed for bulk fluids. We assume that the entropy scaling approach is also predictive for inhomogeneous fluids. We calculate the residual entropy from the Helmholtz energy functional according to

$$s^{\mathrm{res}} = -\frac{1}{\bar{\rho}(\mathbf{r})}\left(\frac{\partial\left(\rho a^{\mathrm{res}}\right)}{\partial T}\right)_{\rho} \overset{!}{\leq} 0 \tag{5.51}$$

with the residual Helmholtz energy per molecule a^{res} defined by $F^{\mathrm{res}} \equiv \int \rho a^{\mathrm{res}}\,\mathrm{d}\mathbf{r}$ and the weighted density $\bar{\rho}(\mathbf{r})$ computed with the appropriate convolution radius for each PC-SAFT contribution to the residual Helmholtz energy functional (we use the weighted density because otherwise we get unreasonable values for the residual entropy and hence the transport coefficients in the entropy scaling approaches that follow).

To exclude unexpected results in the transport coefficients for positive residual entropies, noting the model equations were fitted to non-positive residual entropies only, we limit the residual entropy to negative values ($s^{\mathrm{res}} = 0$ corresponds to the ideal gas state).

By using a Helmholtz energy functional based on the PC-SAFT equation of state, the same limitations apply to the determination of transport properties as to the determination of density profiles in the inhomogeneous regions: since the thermodynamic modeling of the non-equilibrium fluid is based on the molecular correlation functions of the equilibrium system, dynamic intramolecular correlations are not considered; orientational and conformational degrees of freedom are not resolved and therefore only considered in a bulk manner. The tensorial rank of the transport properties is also neglected for simplicity because only the density profiles of the center of mass and not the orientation profiles are available for transport property modeling.

5.3.1 Entropy Scaling for Shear Viscosity & Self-Diffusion Coefficients

The shear viscosity η and the self-diffusion coefficients $D_i^{\mathrm{self},0}$ of (hypothetical) pure components are modeled by[81–83,89]

$$\ln\left(\frac{\eta}{\eta_{\mathrm{CE}}}\right) = \sum_{i=1}^{N_\mathrm{c}} x_i A_i + \sum_{i=1}^{N_\mathrm{c}} \frac{x_i m_i}{\bar{m}} B_i s^* + \sum_{i=1}^{N_\mathrm{c}} \frac{x_i m_i}{\bar{m}} C_i (s^*)^2 + \sum_{i=1}^{N_\mathrm{c}} \frac{x_i m_i}{\bar{m}} D_i (s^*)^3 \tag{5.52a}$$

$$\ln\left(\frac{\rho D_i^{\mathrm{self},0}}{\rho D_{i,\mathrm{CE}}^{\mathrm{self},0}}\right) = A_i + B_i s^* - C_i\big(1-\exp(s^*)\big)(s^*)^2 - D_i (s^*)^4 - E_i (s^*)^8 \tag{5.52b}$$

with the reduced residual entropy $s^* \equiv \frac{s^{\mathrm{res}}(\{\rho_i\},T)}{k_\mathrm{B}\bar{m}}$, the Boltzmann constant k_B, and the average chain length parameter of the PC-SAFT equation of state $\bar{m} = \sum_i^{N_\mathrm{c}} x_i m_i$ defined in terms of the number of segments per chain m_i of component i. The component-specific parameters A_i, B_i, C_i, D_i, and E_i were fitted to experimental data of pure component bulk systems[81–83,89].

The self-diffusion coefficient $D_i^{\mathrm{self},0}$ requires some explanation. Let us consider a binary mixture with a volatile component (incapable of forming a liquid phase as a pure fluid), forming a vapor-liquid interface. Furthermore, we consider a location where a liquid-like density is observed, with the volatile component dissolved. Then, $D_i^{\mathrm{self},0}$ of the volatile component is the self-diffusion coefficient of a hypothetical liquid (noting that the pure volatile component is vaporous under the considered conditions) because we assess $D_i^{\mathrm{self},0}$ using the residual entropy $s^*(\{\rho_i\},T)$, which corresponds to a liquid phase in the considered scenario. In this sense, the volatile component is considered in a hypothetical liquid state. For this approach to work robustly, it is important that the typical ranges of s^* are comparable for various (potentially very different) components. In our definition of s^*, this is the case (cf. refs. 80–83,89).

The transport coefficients are reduced by their Chapman-Enskog counterpart[90,91], defined by

$$\eta_{\mathrm{CE}} = \sum_{i=1}^{N_\mathrm{c}} \frac{x_i \eta_{\mathrm{CE},i}}{\sum_{j=1}^{N_\mathrm{c}} x_j \phi_{ij}} \qquad \eta_{\mathrm{CE},i} = \frac{5}{16}\frac{\sqrt{\frac{M_i k_\mathrm{B} T}{N_\mathrm{A}\pi}}}{\sigma_i^2 \Omega_i^{(2,2)*}} \qquad \phi_{ij} = \frac{\left(1+\sqrt{\frac{\eta_{\mathrm{CE},i}}{\eta_{\mathrm{CE},j}}}\sqrt[4]{\frac{M_j}{M_i}}\right)^2}{\sqrt{8\left(1+\frac{M_i}{M_j}\right)}} \tag{5.53a}$$

$$\rho D_{i,\mathrm{CE}}^{\mathrm{self},0} = \frac{3}{8}\frac{\sqrt{\frac{\mathbb{R}T}{\pi M_i}}}{\sigma_i^2 \Omega_i^{(1,1)*}} \tag{5.53b}$$

with the pure-component Chapman-Enskog viscosities $\eta_{\mathrm{CE},i}$ of components i, the mixture reference for shear viscosities η_{CE}[92,93] with factors ϕ_{ij}, the Chapman-Enskog self-diffusion coefficients $D_{i,\mathrm{CE}}^{\mathrm{self},0}$ the molar masses M_i, the Avogadro constant N_A (so that $\check{m}_i = \frac{M_i}{N_\mathrm{A}}$), the universal gas constant $\mathbb{R}$, the dimensionless collision integrals[94] $\Omega_i^{(1,1)*}$ and $\Omega_i^{(2,2)*}$, and the

PC-SAFT segment size parameters σ_i.

5.3.2 Maxwell-Stefan Diffusion Coefficients Estimated from Self-Diffusion Coefficients Using the Darken Equation

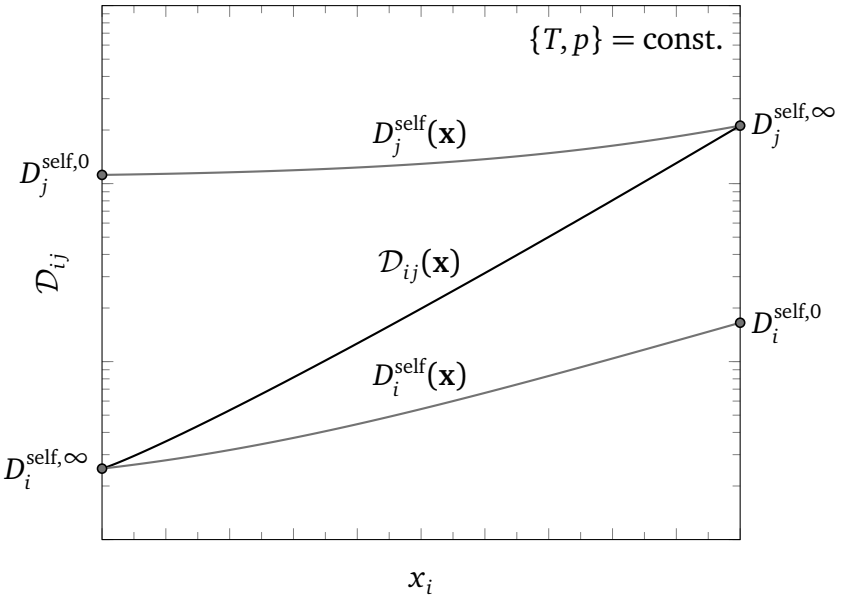

Figure 5.1: Schematic illustration of different diffusion coefficients in a binary mixture of components i and j at constant temperature and pressure: the self-diffusion coefficients in a pure fluid $D_i^{\text{self},0}$, the self-diffusion coefficients at infinite dilution $D_i^{\text{self},\infty}$, the self-diffusion coefficients in a mixture D_i^{self}, and the Maxwell-Stefan binary diffusion coefficient $\mathcal{D}_{ij}$.

The Maxwell-Stefan diffusion coefficients in fluid mixtures are obtained from the self-diffusion coefficients. The relationship between the self-diffusion coefficients and the Maxwell-Stefan diffusion coefficients is illustrated in figure 5.1.

The self-diffusion coefficients at infinite dilution $D_i^{\text{self},\infty}$ are estimated following the method by Zmpitas *et al.* [89], namely,

$$D_i^{\text{self},\infty} = D_j^{\text{self},0} \left(\frac{d_j}{d_i} \right)^{2.23} \tag{5.54}$$

using the effective molecular diameters

$$\frac{d_i}{\text{Å}} = \left(\frac{\rho_i^{\text{pure}}(T_i^{\text{sat}}(p^{\circ}), p^{\circ})}{\#\,\text{Å}^{-3}} \right)^{-\frac{0.71}{3}} \tag{5.55}$$

inspired by Wilke and Chang [95], from the liquid densities of the pure components ρ_i^{pure} at their normal boiling temperatures $T_i^{\text{sat}}(p^{\circ})$ with $p^{\circ} = 1.013\,25\,\text{bar}$. The self-diffusion coefficients

for the binary mixtures considered in this work are estimated using the approach of Liu *et al.* [96],

$$\frac{1}{D_i^{\mathrm{self}}(\mathbf{x})} = \frac{x_i}{D_i^{\mathrm{self},0}} + \frac{(1-x_i)}{D_i^{\mathrm{self},\infty}} \tag{5.56}$$

Then, the binary Maxwell-Stefan diffusion coefficient is approximated by the Darken equation [84,85] according to

$$\mathcal{D}_{ij}(\mathbf{x}) = \left(x_i D_j^{\mathrm{self}}(\mathbf{x}) + x_j D_i^{\mathrm{self}}(\mathbf{x})\right)\Gamma_{ij}^{\alpha} \tag{5.57}$$

with $\Gamma_{ij} = \frac{x_i}{k_\mathrm{B}T}\left(\frac{\partial \mu_i}{\partial x_j}\right)_{T,p,\sum_i x_i=1}$ as the thermodynamic factor and an empirical parameter α. In this work, for simplicity, we neglect the influence of the non-ideality of the mixtures and set the thermodynamic factor to unity, $\Gamma_{ij} = 1$.

5.4 Well-Balanced Finite-Volume Discretization Scheme

The well-balanced finite-volume discretization scheme used in this work is the first-order scheme developed by Carrillo *et al.* [97] applied to mixtures. The rationale behind this discretization scheme is to preserve the stationary states of the original system, eq. (5.3), on the discrete level. The dissipation relations, eqs. (5.44) and (5.50), ensure that the sum of kinetic, Helmholtz, and potential energy decreases monotonically with time. Assuming there are no fluxes across the system boundary as specified in section 5.2, this yields $\mathbf{v} = 0$ and thus the stationary state described in eq. (5.3), which we can rewrite for each component i as

$$\mu_i = \frac{\delta F}{\delta \rho_i} + V_i^{\mathrm{ext}} = \frac{\delta F^{\mathrm{ig}}}{\delta \rho_i} + \frac{\delta F^{\mathrm{res}}}{\delta \rho_i} + V_i^{\mathrm{ext}} = k_\mathrm{B}T \ln(\rho_i \Lambda_i^3) + \frac{\delta F^{\mathrm{res}}}{\delta \rho_i} + V_i^{\mathrm{ext}} \quad \forall i \tag{5.58}$$

The effective de Broglie wavelength $\Lambda_i(T)$ cancels out of our isothermal model, and we can simply set it to unity $\Lambda_i = 1\,\text{Å}$. On the discrete level, eq. (5.58) translates to

$$(\mu_i)_k = k_\mathrm{B}T \ln\big((\rho_i \Lambda_i^3)_k\big) + \left(\frac{\delta F^{\mathrm{res}}}{\delta \rho_i} + V_i^{\mathrm{ext}}\right)_k \quad \forall i,k \tag{5.59}$$

for each discrete cell with index k.

5.4.1 Reformulation of the Hydrodynamic DFT Model

The hydrodynamic DFT model as described in eq. (5.24) does not incorporate a pressure-term as required by the well-balanced finite-volume scheme[97]. To obtain a pressure-term for the convective flux, we employ the ideal gas contribution to the Helmholtz energy functional, defined by

$$F^{\mathrm{ig}}[\{\rho_i\}] = \int \rho a^{\mathrm{ig}}(\{\rho_i(\mathbf{r}')\})\,\mathrm{d}\mathbf{r}' = k_{\mathrm{B}}T \int \sum_{i=1}^{N_{\mathrm{c}}} \rho_i(\mathbf{r}')\Big(\ln\big(\rho_i(\mathbf{r}')\Lambda_i^3\big) - 1\Big)\,\mathrm{d}\mathbf{r}' \tag{5.60}$$

with the Helmholtz energy density of the ideal gas ρa^{ig}. The ideal gas contribution is the only local Helmholtz energy contribution of the employed PC-SAFT Helmholtz energy functional[8,13,16] used in this work. For the (local) ideal gas contribution, the functional derivative simplifies to a partial derivative according to

$$\frac{\delta F^{\mathrm{ig}}}{\delta \rho_i(\mathbf{r})} \equiv \mu_i^{\mathrm{ig}}(\mathbf{r}) = k_{\mathrm{B}}T \ln\big(\rho_i(\mathbf{r})\Lambda_i^3\big) = \frac{\partial(\rho a^{\mathrm{ig}})}{\partial \rho_i(\mathbf{r})} \tag{5.61}$$

with the chemical potential of the ideal gas contribution μ_i^{ig}. This motivates the separation of the Helmholtz energy functionals $F = F^{\mathrm{ig}} + F^{\mathrm{res}}$ into the ideal gas contribution F^{ig} (local) and the residual contributions F^{res} (non-local), which allows rewriting the momentum balance of eq. (5.24c) as

$$\frac{\partial(\check{m}\rho\mathbf{v})}{\partial t} + \nabla\cdot\big(\check{m}\rho\mathbf{v}\mathbf{v}^{\intercal} + p^{\mathrm{ig}}\mathbb{I}\big) = -\sum_{i=1}^{N_{\mathrm{c}}} \rho_i \nabla\left(\frac{\delta F^{\mathrm{res}}}{\delta \rho_i} + V_i^{\mathrm{ext}}\right) - \nabla\cdot\boldsymbol{\tau} \tag{5.62}$$

where we used the Gibbs-Duhem equation (which also assumes a local form as $\sum_i^{N_{\mathrm{c}}} \rho_i \nabla_T \mu_i^{\mathrm{ig}} = \nabla p^{\mathrm{ig}}$), and introducing the pressure of the ideal gas contribution $p^{\mathrm{ig}} \equiv \rho k_{\mathrm{B}}T$, that represents the purely kinetic contribution to the static pressure. The influence from intermolecular interactions is represented in the functional derivative of the residual Helmholtz energy functional $\frac{\delta F^{\mathrm{res}}}{\delta \rho_i}$.

With eq. (5.62), the balance equations of the hydrodynamic DFT model for mixtures, eq. (5.24), can be written in a manner in which the pressure of the ideal gas contribution is considered in the convective flux in the following way

$$\frac{\partial \mathbf{U}}{\partial t} + \nabla\cdot\mathbf{F}^{\mathrm{conv}}(\mathbf{U}) + \nabla\cdot\mathbf{F}^{\mathrm{diff}}(\mathbf{U}, \nabla\mathbf{U}) = \mathbf{S}(\mathbf{r}, \mathbf{U}) \tag{5.63}$$

with the vector of unknowns $\mathbf{U}$, the convective and diffusive fluxes $\mathbf{F}^{\mathrm{conv}}$ and $\mathbf{F}^{\mathrm{diff}}$, and the

source $\mathbf{S}$, defined by

$$\mathbf{U} = \begin{pmatrix} \check{m}\rho \\ \{\rho_i\} \\ \check{m}\rho\mathbf{v} \end{pmatrix} \tag{5.64a}$$

$$\mathbf{F}^{\text{conv}}(\mathbf{U}) = \begin{pmatrix} \check{m}\rho\mathbf{v} \\ \{\rho_i\}\mathbf{v} \\ \check{m}\rho\mathbf{v}\mathbf{v}^\intercal + p^{\text{ig}}(\rho)\mathbb{I} \end{pmatrix} \tag{5.64b}$$

$$\mathbf{F}^{\text{diff}}(\mathbf{U}, \nabla\mathbf{U}) = \begin{pmatrix} 0 \\ \mathbf{j}_i^{\text{diff}}(\{\rho_i\}) \\ \boldsymbol{\tau}(\{\rho_i\}, \nabla\mathbf{v}) \end{pmatrix} \tag{5.64c}$$

$$\mathbf{S}(\mathbf{r}, \mathbf{U}) = \begin{pmatrix} 0 \\ 0 \\ -\sum_{i=1}^{N_c} \rho_i \nabla\left(\frac{\delta F^{\text{res}}[\{\rho_i\}]}{\delta\rho_i} + V_i^{\text{ext}}(\mathbf{r})\right) \end{pmatrix} \tag{5.64d}$$

where we explicitly included the dependencies of the unknowns for clarity.

To satisfy the well-balanced property on the discrete level, the pressure of the ideal gas contribution p^{ig} must be balanced with the source $\mathbf{S}$ using eq. (5.59). Due to the structure of the Helmholtz energy functional used in this work, only the ideal gas contribution (the only local contribution) can be extracted in a (local) pressure p^{ig}.

Not taking the 'correct' system pressure into account for the numerical flux approximations using a numerical Riemann solver might not seem convincing at first, but, as it turns out, has several advantages. The ideal gas pressure $p^{\text{ig}}(\rho)$ is a convex function of density ρ for all physical densities $\rho \geq 0$ and temperatures $T \geq 0$. The ideal gas does not show a two-phase region and hence no van der Waals loop and thus no non-convex (unstable) region with $\left(\frac{\partial p}{\partial \rho}\right)_T \leq 0$, which would require additional attention because in these cases, the type of the non-viscous momentum equation becomes mixed hyperbolic-elliptic. The loss of pure hyperbolicity would prevent the straightforward application of upwind schemes that use numerical Riemann solvers. This problem and how it can be circumvented is described in refs. 98–101.

5.4.2 First-order Discretization Scheme for Convective Fluxes

The first-order well-balanced finite-volume scheme used in this work developed by Carrillo *et al.*[97] (for cell-centered nodes identified by indices k) uses the discrete stationary state

relation from eq. (5.59) to define interface values at the cell faces (identified by half-numbered indices $k+\frac{1}{2}$) from

$$k_\mathrm{B}T\ln\left((\rho_i\Lambda_i^3)^-_{k+\frac{1}{2}}\right)+\left(\frac{\delta F^\mathrm{res}}{\delta\rho_i}+V_i^\mathrm{ext}\right)_{k+\frac{1}{2}}=\left(k_\mathrm{B}T\ln(\rho_i\Lambda_i^3)+\frac{\delta F^\mathrm{res}}{\delta\rho_i}+V_i^\mathrm{ext}\right)_k \quad \text{and} \quad \mathbf{v}^-_{k+\frac{1}{2}}=\mathbf{v}_k \tag{5.65a}$$

$$k_\mathrm{B}T\ln\left((\rho_i\Lambda_i^3)^+_{k+\frac{1}{2}}\right)+\left(\frac{\delta F^\mathrm{res}}{\delta\rho_i}+V_i^\mathrm{ext}\right)_{k+\frac{1}{2}}=\left(k_\mathrm{B}T\ln(\rho_i\Lambda_i^3)+\frac{\delta F^\mathrm{res}}{\delta\rho_i}+V_i^\mathrm{ext}\right)_{k+1} \text{ and } \mathbf{v}^+_{k+\frac{1}{2}}=\mathbf{v}_{k+1} \tag{5.65b}$$

where $()^\pm_{k+\frac{1}{2}}$ denotes the reconstruction of the left ($^-$) and right ($^+$) boundary value of the molecular density ρ_i and the velocity $\mathbf{v}$ at the cell face located at $k+\frac{1}{2}$, and the choice of average value

$$\left(\frac{\delta F^\mathrm{res}}{\delta\rho_i}+V_i^\mathrm{ext}\right)_{k+\frac{1}{2}}=\max\left(\left(\frac{\delta F^\mathrm{res}}{\delta\rho_i}+V_i^\mathrm{ext}\right)_k,\left(\frac{\delta F^\mathrm{res}}{\delta\rho_i}+V_i^\mathrm{ext}\right)_{k+1}\right) \tag{5.66a}$$

$$\text{or}\quad \left(\frac{\delta F^\mathrm{res}}{\delta\rho_i}+V_i^\mathrm{ext}\right)_{k+\frac{1}{2}}=\frac{1}{2}\left(\left(\frac{\delta F^\mathrm{res}}{\delta\rho_i}+V_i^\mathrm{ext}\right)_k+\left(\frac{\delta F^\mathrm{res}}{\delta\rho_i}+V_i^\mathrm{ext}\right)_{k+1}\right) \tag{5.66b}$$

Solving for the reconstructed values at the cell face leads to

$$(\rho_i)^-_{k+\frac{1}{2}}=(\rho_i)_k\exp\left(\left(\frac{\delta\beta F^\mathrm{res}}{\delta\rho_i}+\beta V_i^\mathrm{ext}\right)_k-\left(\frac{\delta\beta F^\mathrm{res}}{\delta\rho_i}+\beta V_i^\mathrm{ext}\right)_{k+\frac{1}{2}}\right) \quad \text{and} \quad \mathbf{v}^-_{k+\frac{1}{2}}=\mathbf{v}_k \tag{5.67a}$$

$$(\rho_i)^+_{k+\frac{1}{2}}=(\rho_i)_{k+1}\exp\left(\left(\frac{\delta\beta F^\mathrm{res}}{\delta\rho_i}+\beta V_i^\mathrm{ext}\right)_{k+1}-\left(\frac{\delta\beta F^\mathrm{res}}{\delta\rho_i}+\beta V_i^\mathrm{ext}\right)_{k+\frac{1}{2}}\right) \text{ and } \mathbf{v}^+_{k+\frac{1}{2}}=\mathbf{v}_{k+1} \tag{5.67b}$$

with the inverse thermodynamic temperature $\beta\equiv\frac{1}{k_\mathrm{B}T}$.

The reconstructed values $()^\pm_{k+\frac{1}{2}}$ are then used for the convective flux calculation at the interface according to

$$\mathbf{F}^\mathrm{conv}_{k+\frac{1}{2}}=\mathfrak{F}\left(\mathbf{U}^-_{k+\frac{1}{2}},\mathbf{U}^+_{k+\frac{1}{2}}\right) \qquad \text{with } \mathbf{U}^\pm_{k+\frac{1}{2}}=\begin{pmatrix}\check{m}^\pm_{k+\frac{1}{2}}\rho^\pm_{k+\frac{1}{2}}\\ \left\{(\rho_i)^\pm_{k+\frac{1}{2}}\right\}\\ \check{m}^\pm_{k+\frac{1}{2}}\rho^\pm_{k+\frac{1}{2}}\mathbf{v}^\pm_{k+\frac{1}{2}}\end{pmatrix} \tag{5.68}$$

with the numerical flux $\mathfrak{F}$ (approximate Riemann solver).

The source $\mathbf{S}$ is discretized to preserve a stationary state on the discrete level. The system described in eq. (5.64) simplifies for the stationary state ($\mathbf{v} = 0$) to

$$\mathbf{S} = -\sum_{i=1}^{N_c} \rho_i \nabla \left(\frac{\delta F^{\mathrm{res}}[\{\rho_i\}]}{\delta \rho_i} + V_i^{\mathrm{ext}}(\mathbf{r}) \right) = \nabla \cdot \left(p^{\mathrm{ig}} \mathbb{I} \right) \tag{5.69}$$

which must be satisfied on the discrete level. This motivated replacing the original source term with the pressure gradient $\nabla p^{\mathrm{ig}} = \nabla \cdot \left(p^{\mathrm{ig}} \mathbb{I} \right)$. Integrating eq. (5.69) over finite-volume cells k yields

$$\int_{\Omega_k} \mathbf{S} \, \mathrm{d}\mathbf{r} = \int_{\Omega_k} \nabla \cdot \left(p^{\mathrm{ig}} \mathbb{I} \right) \mathrm{d}\mathbf{r} = \int_{\partial \Omega_k} \left(p^{\mathrm{ig}} \mathbb{I} \right) \cdot \mathbf{n} \, \mathrm{d}A \tag{5.70}$$

where Ω_k and $\partial \Omega_k$ denote the volume and surface of cell k, respectively. In the following, we show exemplarily the procedure for two dimensions; the extension to three dimensions follows analogously. Equation (5.70) for Cartesian cells leads to

$$\iint_{\Omega_k} \mathbf{S}_k \, \mathrm{d}x \, \mathrm{d}y = \begin{pmatrix} \left((p^{\mathrm{ig}})^-_{k+\frac{1}{2},x} - (p^{\mathrm{ig}})^+_{k-\frac{1}{2},x} \right) \Delta y \\ \left((p^{\mathrm{ig}})^-_{k+\frac{1}{2},y} - (p^{\mathrm{ig}})^+_{k-\frac{1}{2},y} \right) \Delta x \end{pmatrix} \tag{5.71}$$

where the subscripts x and y indicate from which cell faces the values are taken and $(p^{\mathrm{ig}})^{\pm}_{k+\frac{1}{2},x} \equiv p^{\mathrm{ig}}\left(\rho^{\pm}_{k+\frac{1}{2},x}\right)$. This discretization for the source $\mathbf{S}_k$ is not only used for stationary states but out of global equilibrium as well.

For discrete stationary states, conservation of the following property needs to be satisfied for each dimension. For the x-component of the momentum flux $F_x^{\mathrm{conv},\rho\mathbf{v}}$ using eq. (5.71), it reads

$$F^{\mathrm{conv},\rho\mathbf{v}}_{k+\frac{1}{2},x} - F^{\mathrm{conv},\rho\mathbf{v}}_{k-\frac{1}{2},x} = S_{k,x} \Delta x = (p^{\mathrm{ig}})^-_{k+\frac{1}{2},x} - (p^{\mathrm{ig}})^+_{k-\frac{1}{2},x} \tag{5.72}$$

Equations (5.65a) and (5.65b) in combination with the discrete stationary state relation from eq. (5.59) show that $(\rho_i)^-_{k+\frac{1}{2}} = (\rho_i)^+_{k+\frac{1}{2}}$ holds for stationary states. Exploiting this, the convective momentum flux $F^{\mathrm{conv},\rho\mathbf{v}}_{k+\frac{1}{2},x}$ in a stationary state ($\mathbf{v} = 0$) is calculated using eq. (5.68). Exploiting consistency of the numerical flux (approximate Riemann solver), $\mathfrak{F}(\mathbf{U}, \mathbf{U}) = F(\mathbf{U})$,

yields

$$F^{\mathrm{conv},\rho\mathbf{v}}_{k+\frac{1}{2},x} = \mathfrak{F}^{\rho\mathbf{v}}\left(\begin{pmatrix} \check{m}^{-}_{k+\frac{1}{2},x}\rho^{-}_{k+\frac{1}{2},x} \\ \left\{(\rho_i)^{-}_{k+\frac{1}{2},x}\right\} \\ 0 \end{pmatrix}, \begin{pmatrix} \check{m}^{+}_{k+\frac{1}{2},x}\rho^{+}_{k+\frac{1}{2},x} \\ \left\{(\rho_i)^{+}_{k+\frac{1}{2},x}\right\} \\ 0 \end{pmatrix}\right) = (p^{\mathrm{ig}})^{-}_{k+\frac{1}{2},x} = (p^{\mathrm{ig}})^{+}_{k+\frac{1}{2},x} \tag{5.73}$$

The same can be shown for $F^{\mathrm{conv},\rho\mathbf{v}}_{k-\frac{1}{2},x}$, which confirms that eq. (5.72) is satisfied on a discrete level. The y-component can be treated analogously.

Although specialized Riemann solvers tailored to diffusive transport equations have already been proposed[102,103], we follow the approach taken by Carrillo *et al.*[97] and apply simple and versatile approximations to the Riemann problem: the local Lax-Friedrichs flux for the convective transport, defined by

$$\mathfrak{F}_{k+\frac{1}{2},x}\left(\mathbf{U}^{-}_{k+\frac{1}{2},x}, \mathbf{U}^{+}_{k+\frac{1}{2},x}\right) = \frac{1}{2}\left(F^{-}_{k+\frac{1}{2},x} + F^{+}_{k+\frac{1}{2},x}\right) - \frac{\lambda_{k+\frac{1}{2},x}}{2}\left(\mathbf{U}^{+}_{k+\frac{1}{2},x} - \mathbf{U}^{-}_{k+\frac{1}{2},x}\right) \tag{5.74}$$

with the maximum absolute value of the eigenvalues of the Jacobian of the equation system (cf. appendix D.5) at the cell faces, defined by

$$\lambda_{k+\frac{1}{2},x} \equiv \max_{\mathbf{U}^{\pm}_{k+\frac{1}{2},x}} \left\{\left|v_x + c_{\mathrm{s}}^{\mathrm{ig}}\right|, \left|v_x - c_{\mathrm{s}}^{\mathrm{ig}}\right|\right\} \tag{5.75}$$

with the isothermal speed of sound of the ideal gas contribution $c_{\mathrm{s}}^{\mathrm{ig}} \equiv \sqrt{\frac{k_{\mathrm{B}}T}{\check{m}}}$, which, in the isothermal system considered here, depends only on the composition of the mixture (cf. eq. (D.34)). Equation (5.75) selects the maximum information speed of the positive and negative characteristic of the system of equations for the negative ($^-$) and positive ($^+$) side of the cell face, i.e., the maximum out of four values.

Using the same discretization scheme for mixtures as Carrillo *et al.*[97] used for pure fluids is motivated in appendix D.6.

5.4.3 Discretization for Diffusive Fluxes

The diffusive fluxes $\mathbf{j}_i^{\mathrm{diff}}$ and $\boldsymbol{\tau}$ of the left ($^-$) and right ($^+$) side of the cell face located at $k+\frac{1}{2}$ are naïvely approximated with their respective cell values for the velocities and the projected densities at the cell faces (equivalent to the convective fluxes, cf. eq. (5.67)). For viscous momentum transports we use

$$\boldsymbol{\tau}^{-}_{k+\frac{1}{2},x} = \boldsymbol{\tau}_k \qquad \text{and} \qquad \boldsymbol{\tau}^{+}_{k+\frac{1}{2},x} = \boldsymbol{\tau}_{k+1} \tag{5.76}$$

For the diffusive molecular fluxes $\mathbf{j}_i^{\text{diff}} \equiv \rho_i(\mathbf{v}_i - \mathbf{v})$, we choose a similar approach as for the convective transport, namely

$$\left(\mathbf{j}_i^{\text{diff}}\right)^-_{k+\frac{1}{2}} = (\rho_i)^-_{k+\frac{1}{2}} (\mathbf{v}_i - \mathbf{v})_k \qquad \text{and} \qquad \left(\mathbf{j}_i^{\text{diff}}\right)^+_{k+\frac{1}{2}} = (\rho_i)^+_{k+\frac{1}{2}} (\mathbf{v}_i - \mathbf{v})_{k+1} \tag{5.77}$$

where the density at the cell faces is determined by eq. (5.67).

Like for the convective fluxes (cf. eq. (5.68)) we use an approximate Riemann solver. For diffusive fluxes, we apply the central flux, defined by

$$F^{\text{diff},\tau}_{k+\frac{1}{2},x} = \mathfrak{F}\left(\boldsymbol{\tau}^-_{k+\frac{1}{2},x}, \boldsymbol{\tau}^+_{k+\frac{1}{2},x}\right)\mathbf{e}_x = \frac{1}{2}(\boldsymbol{\tau}_k + \boldsymbol{\tau}_{k+1})\,\mathbf{e}_x \tag{5.78}$$

for the viscous momentum transport at the face in the positive x-direction, and by

$$F^{\text{diff},\mathbf{j}_i^{\text{diff}}}_{k+\frac{1}{2},x} = \mathfrak{F}\left(\left(\mathbf{j}_i^{\text{diff}}\right)^-_{k+\frac{1}{2},x}, \left(\mathbf{j}_i^{\text{diff}}\right)^+_{k+\frac{1}{2},x}\right) = \frac{1}{2}\left(\left(\mathbf{j}_i^{\text{diff}}\right)_k + \left(\mathbf{j}_i^{\text{diff}}\right)_{k+1}\right) \tag{5.79}$$

for molecular diffusion.

Approximation of the gradients $\left\{\{-\nabla\mu_i\}, -\nabla\mathbf{v}\right\}$ at the cell centers k occurring in the thermodynamic driving forces for molecular and momentum transport (cf. section 5.2.4.1) is described in detail in appendix D.7.

5.5 Application of Hydrodynamic Density Functional Theory Model to Droplet/Bubble Coalescence

The main result of this work is the synthesis and analysis of the hydrodynamic DFT model, eq. (5.24), with a suitable driving force for molecular diffusion, eq. (5.45), to be used with the Maxwell-Stefan diffusion model, eq. (5.32). In this section, we show that the proposed model allows predictions for typically difficult problems. Therefore, we apply the hydrodynamic DFT model to one-dimensional droplet and bubble coalescence of mixtures.

We model the fluid mixtures with a Helmholtz energy functional based on the PC-SAFT equation of state[13,14,16]. The required PC-SAFT and entropy scaling parameters are listed in tables 5.1 and 5.2. No external potentials are considered for the coalescence computations.

The arising convolution integrals are computed using fast Fourier methods[19] [see chapter 3], where symmetry at the left edge of the computational domain can be exploited by using fast sine and cosine transforms (the full symmetric results are depicted for clarity). To improve stability of the convolution calculation, we apply the Lanczos σ-factor[19,104] once

Table 5.1: Used PC-SAFT parameters for chain length m_i, segment size parameter σ_i, segment energy parameter $\frac{\varepsilon_i}{k_B}$, quadrupole moment Q_i, molecular mass $\check{m}_i$, and binary interaction parameters $k_{N_2,j}$ of nitrogen with the *n*-alkanes.

	propane	nitrogen	*n*-dodecane
m_i / –	2.0018	1.1504	5.3058
σ_i / Å	3.6184	3.3848	3.8959
$\frac{\varepsilon_i}{k_B}$ / K	208.1101	91.4	249.2145
Q_i / D Å	–	1.43	–
$\check{m}_i$ / u $\#^{-1}$	44.0962	28.0134	170.3374
$k_{N_2,j}$ / –	0.0251	–	0.1661

Table 5.2: Entropy scaling parameters for shear viscosity and self-diffusion coefficients, consistent with the PC-SAFT parameters in table 5.1.

	propane		nitrogen		*n*-dodecane	
	viscosity	self-diffusion	viscosity	self-diffusion	viscosity	self-diffusion
A_i	−0.8013	−0.6752	−0.1964	−0.1286	−1.6719	−1.7100
B_i	−1.9972	0.3212	−0.9461	0.2489	−3.3902	0.4350
C_i	−0.2907	0.1002	−0.0310	0.0805	−0.6956	0.3567
D_i	−0.0467	–	−0.0303	–	−0.1546	–
E_i	–	–	–	–	–	–

during the calculation*. The semi-discrete system of ordinary differential equations (obtained by discretizing the system of partial differential equations) is solved using the backward differentiation formula (BDF) method[105–107] implemented in the Python library SciPy[108]. All results are computed with 256 grid points (taking advantage of symmetry, the following plots therefore effectively consist of 512 grid points), and the integrator parameters listed in table 5.3.

The considered coalescence systems are described by droplets/bubbles with their respective *equivalent diameter* and an *equivalent distance* between them. The equivalent diameter d_{eq} is determined as the diameter of a droplet/bubble with sharp (equivalent) vapor-liquid interfaces and the same number of enclosed molecules. The equivalent distance between two droplets/bubbles describes the distances between two equivalent interfaces. Note that enrichment of the volatile component at the interface reduces the equivalent diameter and thus increases the equivalent distance between two droplets/bubbles compared to a monotonic vapor-liquid interface.

*[For details on the Lanczos σ-factor consult appendix B.6.]

Table 5.3: Integrator parameters for the BDF integrator used for the different systems considered in this work: absolute tolerance for the molecular densities and the velocities (`atol`$_{\rho_i}$ and `atol`$_{\mathbf{v}}$, respectively), relative tolerance (`rtol`), initial step size (`first_step`), and the maximum allowed step size (`max_step`).

	`atol`$_{\rho_i}$ $\#\,\text{Å}^{-3}$	`atol`$_{\mathbf{v}}$ $\text{Å}\,\text{ps}^{-1}$	`rtol` –	`first_step` ps	`max_step` ps
Figure 5.2	1e−4	1e−3	1e−6	1e−10	1e−2
Figure 5.3	1e−4	1e−3	1e−6	1e−10	1e−2
Figure 5.4	1e−6	1e−4	1e−8	1e−12	20e−2
Figure 5.5	1e−6	1e−4	1e−8	1e−12	15e−2

5.5.1 Coalescence of Pure Propane Droplets/Bubbles

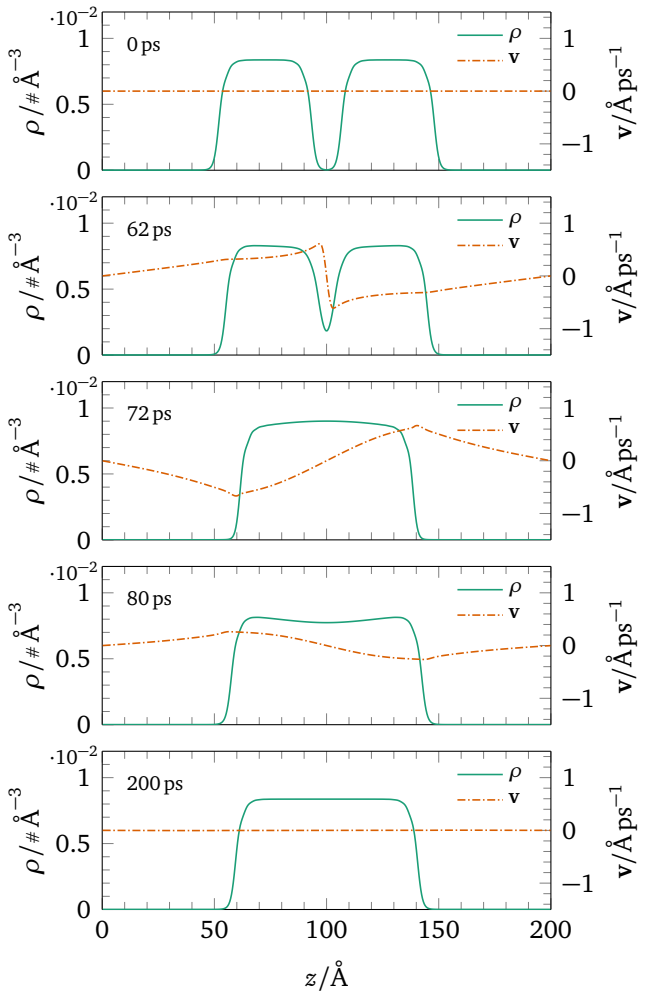

Figure 5.2: Density and velocity profiles for the coalescence of two one-dimensional propane droplets at $T = 200\,\text{K}$ and $p = 0.201\,95\,\text{bar}$ with equivalent diameter $d_{\text{eq}} = 40\,\text{Å}$ and initial distance of 15 Å. For the definition of atomic units, see appendix D.8.

The coalescence of two pure propane droplets is depicted in figure 5.2. The initial conditions are obtained by equilibrating a single droplet in vapor-liquid equilibrium. The two-droplet system is created by moving the droplet in the direction of the symmetry axis on the left edge of the domain. The initial velocity profile is set to zero.

The driving force for coalescence is the source term $-\rho\nabla\left(\frac{\delta F}{\delta\rho}\right)$ in the momentum balance, eq. (5.24c), resulting in a velocity that pulls both droplets together. After coalescence (see figure 5.2 at 72 ps), the density in the center of the domain is compressed to a value higher than the equilibrium liquid density (giving an idea of the large forces at work). The inertia of the system leads to oscillatory behavior, best observed in the velocity profile. The shear viscosity damps the oscillation, which is no longer visible after 200 ps at the latest.

5.5.2 Influence of Second Component on Propane Droplet Coalescence

How a second component affects the coalescence behavior is depicted in figure 5.3 for the addition of nitrogen to the propane system considered previously (for the same temperature and pressure conditions). The temperature, equivalent droplet diameter, and the distance between the droplets are maintained compared to the pure propane droplets; to preserve vapor-liquid equilibrium, the pressure of the binary system deviates from the pure fluid case. This system shows a small temporary enrichment of nitrogen at the vapor-liquid interface.

For mixtures, the driving force leading to coalescence consists of two contributions: $-\rho_{\mathrm{C_3H_8}}\nabla\left(\frac{\delta F}{\delta\rho_{\mathrm{C_3H_8}}}\right)$ and $-\rho_{\mathrm{N_2}}\nabla\left(\frac{\delta F}{\delta\rho_{\mathrm{N_2}}}\right)$. We can see that the additional component, in this case nitrogen, formally has an influence on the coalescence behavior. The influence is small, but this might well be due to the small concentration of nitrogen at these vapor-liquid equilibrium conditions.

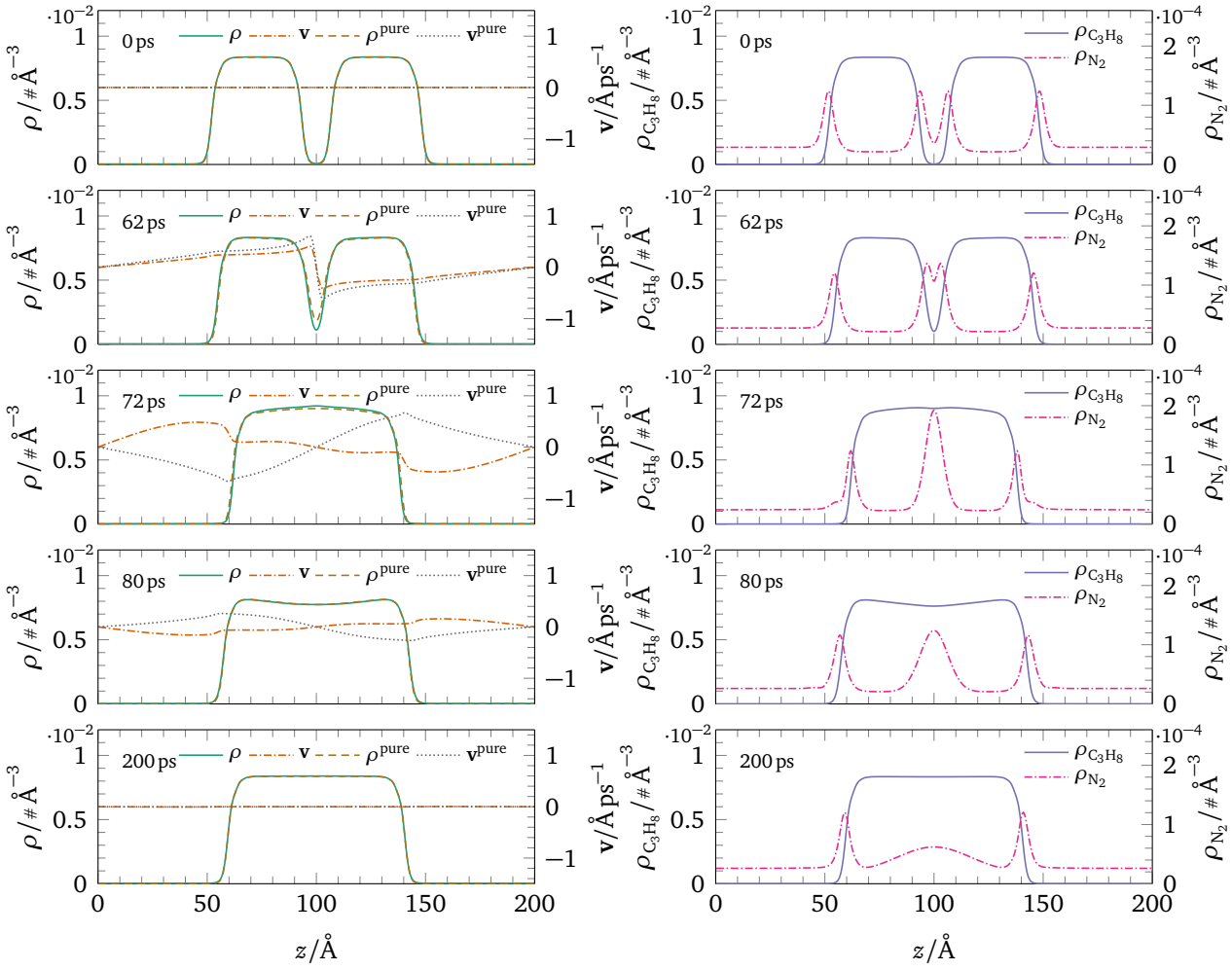

Figure 5.3: Coalescence of two one-dimensional propane/nitrogen droplets with equivalent diameter $d_{eq} = 40\,\text{Å}$ and initial distance of 15 Å at $T = 200\,\text{K}$ and $p = 1\,\text{bar}$. The left panels show the density and velocity profiles of the mixture, labeled ρ and $\mathbf{v}$, and of the pure propane system, ρ^{pure} and $\mathbf{v}^{\text{pure}}$, respectively (cf. figure 5.2). The molecular densities of propane (C_3H_8) and nitrogen (N_2) are shown on the right; the molecular densities of nitrogen are magnified. Note that the mixture is not yet in thermodynamic equilibrium at 200 ps.

5.5.3 Droplet Coalescence of Dodecane/Nitrogen Mixture

The coalescence of two *n*-dodecane/nitrogen droplets is depicted in figure 5.4. Compared to the previously examined propane/nitrogen mixture shown in figure 5.3, the system regarded here shows a more pronounced enrichment of nitrogen at the vapor-liquid interface.

Similar to the two systems considered previously, the *n*-dodecane/nitrogen system shows a density higher than the equilibrium liquid density in the middle of the domain after coalescence (cf. figure 5.4 at 135 ps). This can be attributed to the temporary enrichment of nitrogen between the vapor-liquid interfaces. The nitrogen layer between the two droplets does not prevent coalescence. It is noticeable that the interdiffusion of both components is

much slower than the convective processes, as can be seen in figure 5.4 at 500 ps, where the velocity is already damped by the shear viscosity, but the molecular density profiles have not reached their equilibrium values yet.

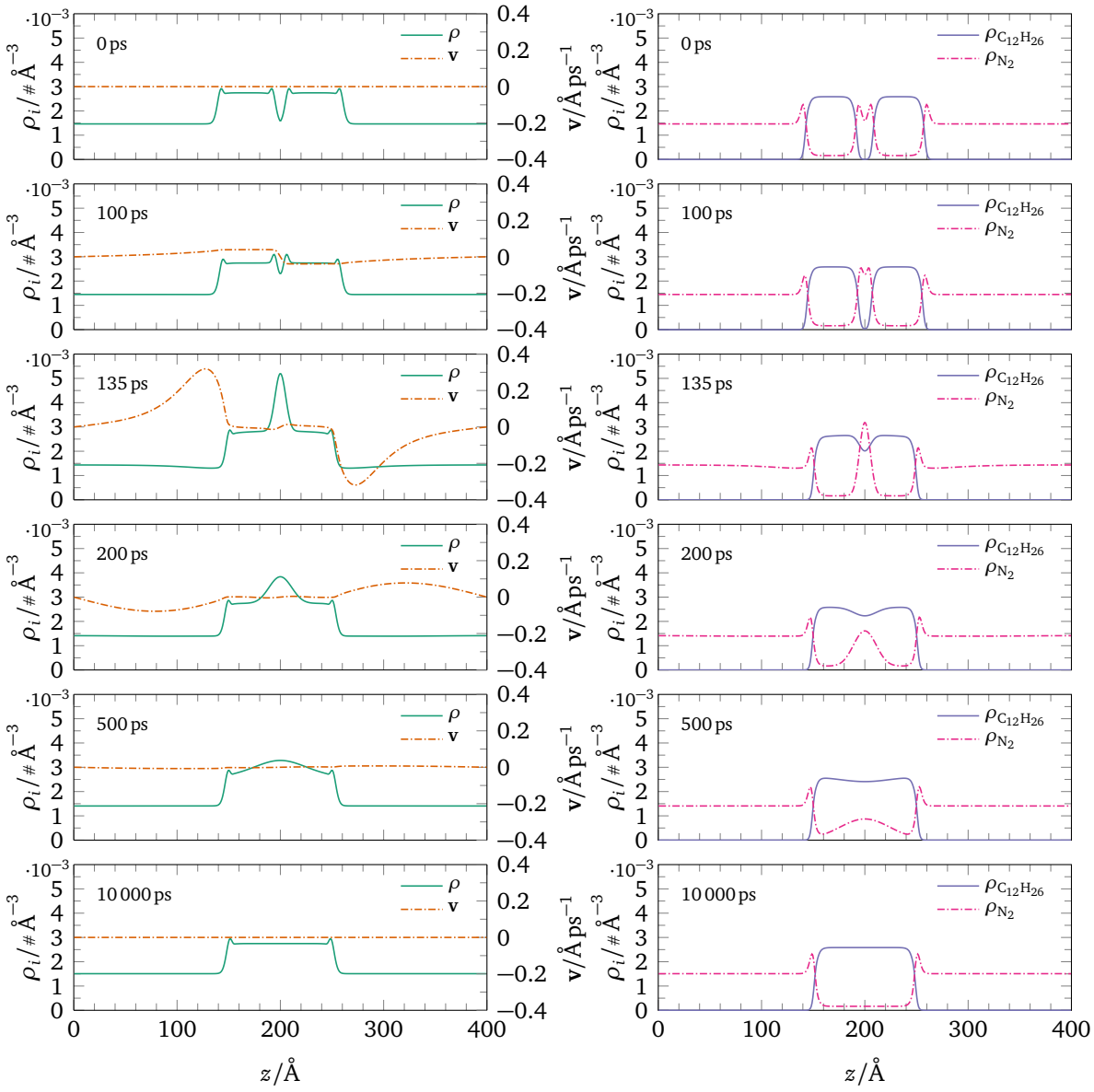

Figure 5.4: Coalescence of two one-dimensional *n*-dodecane/nitrogen droplets with equivalent diameter $d_{eq} = 40\,\text{Å}$ and initial distance of 15 Å at $T = 300\,\text{K}$ and $p = 60\,\text{bar}$. The left panels show the density and velocity profiles, and the right panels show the molecular density profiles of nitrogen (N_2) and *n*-dodecane ($C_{12}H_{26}$).

5.5.4 Bubble Coalescence of Dodecane/Nitrogen Mixture

The coalescence of two *n*-dodecane/nitrogen bubbles is depicted in figure 5.5. For the considered systems, bubble coalescence shows different characteristics than the droplet

system illustrated in figure 5.4. Unlike the droplet system, there is no over-/undershoot of the density profile in the middle of the domain after coalescence. Temporary enrichment or depletion of one component between the bubbles is not visible due to larger diffusive molecular fluxes (larger Maxwell-Stefan diffusion coefficients) in the vapor phase. In addition, oscillations are much less pronounced than in the droplet system. This might be caused by the surrounding liquid phase, which has a high viscosity compared to the bubble and effectively damps the oscillation.

For this system, bubble coalescence occurs in three distinguishable stages: (I) fast convective transport in the vapor phase (cf. 4 ps) followed by small oscillations (cf. 40 ps); (II) slow diffusive molecular transport (cf. 2400 ps, where the barycentric velocity starts to build up again); and (III) simultaneous convective and diffusive molecular transport until complete coalescence.

5.6 Conclusion & Outlook

A variational principle is used to derive a hydrodynamic DFT model for mixtures that simplifies to the isothermal Navier-Stokes equations for local Helmholtz energy functionals, similar to diffuse interface models such as the Navier-Stokes-Korteweg equations. The applied variational principle already incorporates the adiabatic approximation of DDFT. Molecular diffusion is described by generalized Maxwell-Stefan diffusion. We derived a suitable expression for the driving force of diffusion for inhomogeneous systems. Our expression can be regarded as an extension of the *generalized driving force* of the Maxwell-Stefan approach to inhomogeneous systems. Diffusive momentum transport is described by the Cauchy pressure tensor of a Newtonian fluid.

The proposed hydrodynamic DFT model is characterized by its predictive power regarding interfacial properties. The underlying DFT model predicts interfacial tensions and the structure of interfaces of mixtures in thermodynamic equilibrium without additional parameterization. The influence of walls or confinement can be described by external potentials, as fields acting on the fluid. Thus, not only the adsorption behavior of mixtures can be predicted but also hydrodynamics interacting with solid walls. The required transport coefficients, shear viscosity, and Maxwell-Stefan Diffusion coefficients can be described using entropy scaling. The required parameters are fitted to single-phase pure substances only. This allows the transport coefficients in mixtures to be predicted. Our approach is an application of entropy scaling to inhomogeneous fluids that deserves further assessment in future work.

We are able to show that the hydrodynamic DFT model globally satisfies the first and second

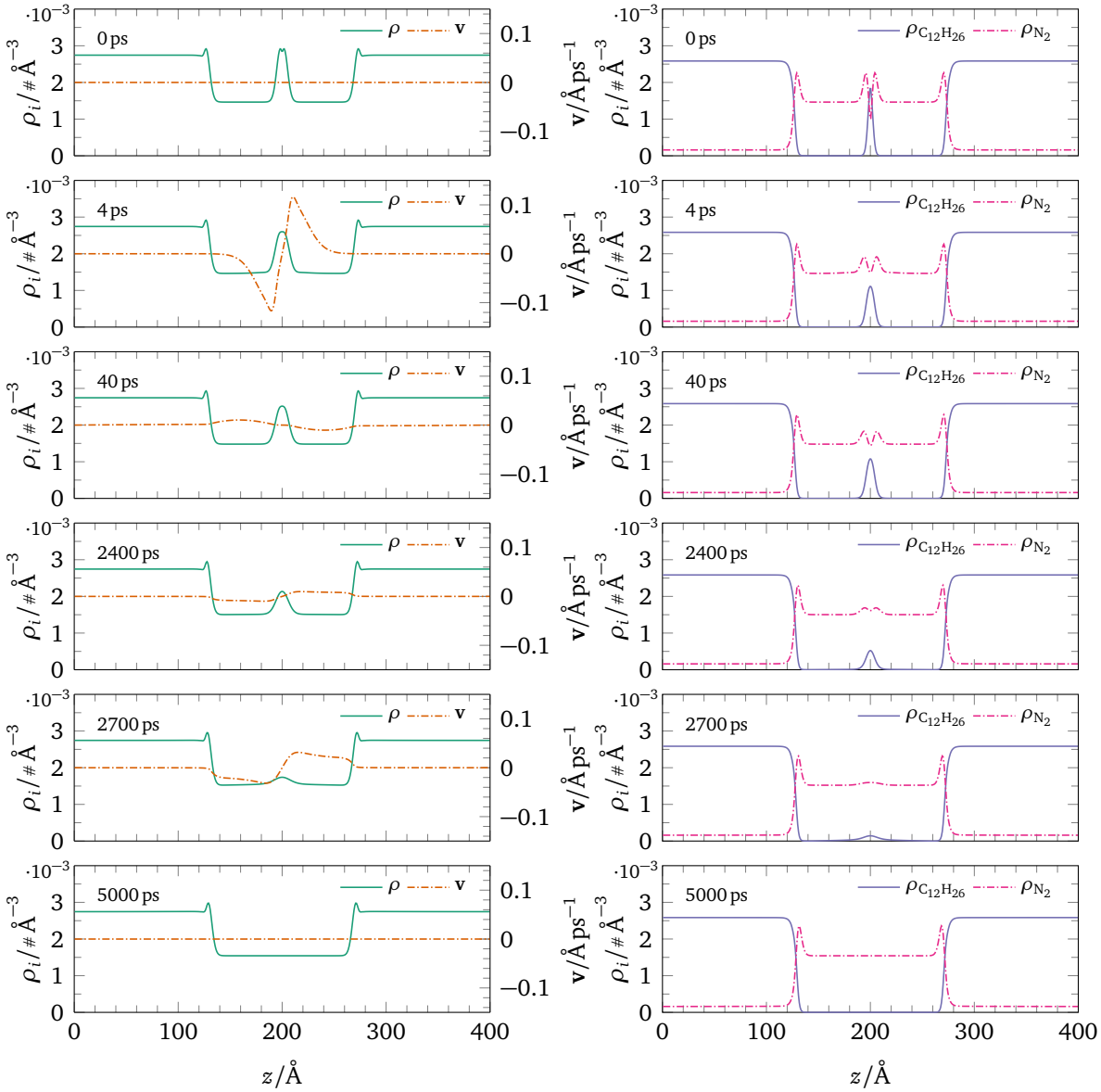

Figure 5.5: Coalescence of two one-dimensional *n*-dodecane/nitrogen bubbles with equivalent diameter $d_{eq} = 40\,\text{Å}$ and initial distance of 15 Å at $T = 300\,\text{K}$ and $p = 60\,\text{bar}$. The left panels show the density and velocity profiles, and the right panels show the molecular density profiles of nitrogen (N_2) and *n*-dodecane ($C_{12}H_{26}$).

law of thermodynamics, provided the transport coefficients are chosen such that the matrices of phenomenological Onsager coefficients are positive semi-definite*.

We applied the derived hydrodynamic DFT model to droplet and bubble coalescence of binary mixtures. The fluid and transport coefficients were modeled with entropy scaling using a Helmholtz energy functional based on the PC-SAFT equation of state. The model equations

*In particular, this implies that volume and shear viscosity are non-negative and the Maxwell-Stefan diffusion coefficients lead to a semi-definite matrix of phenomenological Onsager coefficients.

were semi-discretized with a well-balanced finite-volume scheme and solved with a BDF integrator.

We were able to describe droplet and bubble coalescence of binary mixtures in one dimension with the hydrodynamic DFT, observing phenomena such as temporary enrichment of one component between the droplet interfaces, the influence of a second component on coalescence phenomena (although the effect was small for the chosen system), and different stages of coalescence as in the bubble coalescence example.

In the future, the following aspects should be addressed. The considered systems represent only a small subset of possible applications. For a more realistic prediction of droplet and bubble coalescence, the hydrodynamic DFT model should be solved in two or, for real physical droplets, three dimensions.

An off-the-shelf integrator not tailored to fluid dynamic problems, such as the used BDF implementation, is probably not the best choice. In particular, in higher dimensions, the fully implicit numerical treatment of the system of ordinary differential equations could prove unreasonably time-consuming.

A higher-order extension to the used well-balanced finite-volume scheme already exists[109]. Its use may allow for a coarser spatial discretization, which is particularly advantageous when considering higher-dimensional cases. With the current discretization of the gradients appearing in the driving forces of the diffusive fluxes, a discrete stationary state cannot be exactly satisfied due to the naïve central differentiation scheme; therefore, a different gradient approximation is desirable. Since the gradient of the non-local contributions to the Helmholtz energy functional is required for the diffusive molecular fluxes, a cell-wise entropy inequality as proved for the convective fluxes[97] seems difficult to obtain.

References

[1] C. Rohde. On local and non-local Navier-Stokes-Korteweg systems for liquid-vapour phase transitions. *Journal of Applied Mathematics and Mechanics*, **85**(12):839–857, 2005. doi:10.1002/zamm.200410211.

[2] A. J. Archer. Dynamical density functional theory for molecular and colloidal fluids: A microscopic approach to fluid mechanics. *The Journal of Chemical Physics*, **130**(1):014509, 2009. doi:10.1063/1.3054633.

[3] B. D. Goddard, A. Nold, and S. Kalliadasis. Multi-species dynamical density functional theory. *The Journal of Chemical Physics*, **138**(14):144904, 2013. doi:10.1063/1.4800109.

[4] J. W. Herivel. The derivation of the equations of motion of an ideal fluid by Hamilton's principle. *Mathematical Proceedings of the Cambridge Philosophical Society*, **51**(2):344–349, 1955. doi:10.1017/S0305004100030267.

[5] J. Serrin. Mathematical Principles of Classical Fluid Mechanics. In C. Truesdell (editor), *Fluid Dynamics I / Strömungsmechanik I*, pages 125–263. Springer Berlin Heidelberg, Berlin, Heidelberg, 1959. doi:10.1007/978-3-642-45914-6_2.

[6] T. Hitz, M. Heinen, J. Vrabec, and C.-D. Munz. Comparison of macro- and microscopic solutions of the Riemann problem I. Supercritical shock tube and expansion into vacuum. *Journal of Computational Physics*, **402**:109077, 2020. doi:10.1016/j.jcp.2019.109077.

[7] T. Hitz, S. Jöns, M. Heinen, J. Vrabec, and C.-D. Munz. Comparison of macro- and microscopic solutions of the Riemann problem II. Two-phase shock tube. *Journal of Computational Physics*, **429**:110027, 2021. doi:10.1016/j.jcp.2020.110027.

[8] J. Gross and G. Sadowski. Perturbed-Chain SAFT: An Equation of State Based on a Perturbation Theory for Chain Molecules. *Industrial & Engineering Chemistry Research*, **40**(4):1244–1260, 2001. doi:10.1021/ie0003887.

[9] J. Gross and G. Sadowski. Application of the Perturbed-Chain SAFT Equation of State to Associating Systems. *Industrial & Engineering Chemistry Research*, **41**(22):5510–5515, 2002. doi:10.1021/ie010954d.

[10] J. Gross. An equation-of-state contribution for polar components: Quadrupolar molecules. *AIChE Journal*, **51**(9):2556–2568, 2005. doi:10.1002/aic.10502.

[11] J. Gross and J. Vrabec. An equation-of-state contribution for polar components: Dipolar molecules. *AIChE Journal*, **52**(3):1194–1204, 2006. doi:10.1002/aic.10683.

[12] J. Vrabec and J. Gross. Vapor–Liquid Equilibria Simulation and an Equation of State Contribution for Dipole–Quadrupole Interactions. *The Journal of Physical Chemistry B*, **112**(1):51–60, 2008. doi:10.1021/jp072619u.

[13] J. Gross. A density functional theory for vapor-liquid interfaces using the PCP-SAFT equation

of state. *The Journal of Chemical Physics*, **131**(20):204705, 2009. doi:10.1063/1.3263124.

[14] C. Klink and J. Gross. A Density Functional Theory for Vapor–Liquid Interfaces of Mixtures Using the Perturbed-Chain Polar Statistical Associating Fluid Theory Equation of State. *Industrial & Engineering Chemistry Research*, **53**(14):6169–6178, 2014. doi:10.1021/ie4029895.

[15] C. Klink, B. Planková, and J. Gross. Density Functional Theory for Liquid–Liquid Interfaces of Mixtures Using the Perturbed-Chain Polar Statistical Associating Fluid Theory Equation of State. *Industrial & Engineering Chemistry Research*, **54**(16):4633–4642, 2015. doi:10.1021/acs.iecr.5b00445.

[16] E. Sauer and J. Gross. Classical Density Functional Theory for Liquid–Fluid Interfaces and Confined Systems: A Functional for the Perturbed-Chain Polar Statistical Associating Fluid Theory Equation of State. *Industrial & Engineering Chemistry Research*, **56**(14):4119–4135, 2017. doi:10.1021/acs.iecr.6b04551.

[17] E. Sauer, A. Terzis, M. Theiss, B. Weigand, and J. Gross. Prediction of Contact Angles and Density Profiles of Sessile Droplets Using Classical Density Functional Theory Based on the PCP-SAFT Equation of State. *Langmuir*, **34**(42):12519–12531, 2018. doi:10.1021/acs.langmuir.8b01985.

[18] P. Rehner and J. Gross. Predictive density gradient theory based on nonlocal density functional theory. *Physical Review E*, **98**:063312, 2018. doi:10.1103/PhysRevE.98.063312.

[19] R. Stierle, E. Sauer, J. Eller, M. Theiss, P. Rehner, P. Ackermann, and J. Gross. Guide to efficient solution of PC-SAFT classical Density Functional Theory in various Coordinate Systems using fast Fourier and similar Transforms. *Fluid Phase Equilibria*, **504**:112306, 2020. doi:10.1016/j.fluid.2019.112306.

[20] U. M. B. Marconi and P. Tarazona. Dynamic density functional theory of fluids. *The Journal of Chemical Physics*, **110**(16):8032–8044, 1999. doi:10.1063/1.478705.

[21] U. M. B. Marconi and P. Tarazona. Dynamic density functional theory of fluids. *Journal of Physics: Condensed Matter*, **12**(8A):A413–A418, 2000. doi:10.1088/0953-8984/12/8a/356.

[22] G. K.-L. Chan and R. Finken. Time-Dependent Density Functional Theory of Classical Fluids. *Physical Review Letters*, **94**:183001, 2005. doi:10.1103/PhysRevLett.94.183001.

[23] A. J. Archer and R. Evans. Dynamical density functional theory and its application to spinodal decomposition. *The Journal of Chemical Physics*, **121**(9):4246–4254, 2004. doi:10.1063/1.1778374.

[24] A. J. Archer. Dynamical density functional theory: binary phase-separating colloidal fluid in a cavity. *Journal of Physics: Condensed Matter*, **17**(10):1405–1427, 2005. doi:10.1088/0953-8984/17/10/001.

[25] P. Hopkins, A. Fortini, A. J. Archer, and M. Schmidt. The van Hove distribution function for Brownian hard spheres: Dynamical test particle theory and computer simulations for bulk

dynamics. *The Journal of Chemical Physics*, **133**(22):224505, 2010. doi:10.1063/1.3511719.

[26] D. Stopper, K. Marolt, R. Roth, and H. Hansen-Goos. Modeling diffusion in colloidal suspensions by dynamical density functional theory using fundamental measure theory of hard spheres. *Physical Review E*, **92**:022151, 2015. doi:10.1103/PhysRevE.92.022151.

[27] D. Stopper, R. Roth, and H. Hansen-Goos. Communication: Dynamical density functional theory for dense suspensions of colloidal hard spheres. *The Journal of Chemical Physics*, **143**(18):181105, 2015. doi:10.1063/1.4935967.

[28] D. Stopper, R. Roth, and H. Hansen-Goos. Structural relaxation and diffusion in a model colloid-polymer mixture: dynamical density functional theory and simulation. *Journal of Physics: Condensed Matter*, **28**(45):455101, 2016. doi:10.1088/0953-8984/28/45/455101.

[29] D. Stopper and R. Roth. Nonequilibrium phase transitions of sheared colloidal microphases: Results from dynamical density functional theory. *Physical Review E*, **97**:062602, 2018. doi:10.1103/PhysRevE.97.062602.

[30] A. J. Archer. Dynamical density functional theory for dense atomic liquids. *Journal of Physics: Condensed Matter*, **18**(24):5617–5628, 2006. doi:10.1088/0953-8984/18/24/004.

[31] B. D. Goddard, A. Nold, N. Savva, P. Yatsyshin, and S. Kalliadasis. Unification of dynamic density functional theory for colloidal fluids to include inertia and hydrodynamic interactions: derivation and numerical experiments. *Journal of Physics: Condensed Matter*, **25**(3):035101, 2012. doi:10.1088/0953-8984/25/3/035101.

[32] B. D. Goddard, A. Nold, N. Savva, G. A. Pavliotis, and S. Kalliadasis. General Dynamical Density Functional Theory for Classical Fluids. *Physical Review Letters*, **109**:120603, 2012. doi:10.1103/PhysRevLett.109.120603.

[33] M. A. Durán-Olivencia, B. D. Goddard, and S. Kalliadasis. Dynamical Density Functional Theory for Orientable Colloids Including Inertia and Hydrodynamic Interactions. *Journal of Statistical Physics*, **164**:785–809, 2016. doi:10.1007/s10955-016-1545-5.

[34] B. D. Goddard, A. Nold, and S. Kalliadasis. Dynamical density functional theory with hydrodynamic interactions in confined geometries. *The Journal of Chemical Physics*, **145**(21):214106, 2016. doi:10.1063/1.4968565.

[35] A. Donev and E. Vanden-Eijnden. Dynamic density functional theory with hydrodynamic interactions and fluctuations. *The Journal of Chemical Physics*, **140**(23):234115, 2014. doi:10.1063/1.4883520.

[36] A. J. Archer and M. Rauscher. Dynamical density functional theory for interacting Brownian particles: stochastic or deterministic? *Journal of Physics A: Mathematical and General*, **37**(40):9325–9333, 2004. doi:10.1088/0305-4470/37/40/001.

[37] M. A. Durán-Olivencia, P. Yatsyshin, B. D. Goddard, and S. Kalliadasis. General framework for

fluctuating dynamic density functional theory. *New Journal of Physics*, **19**(12):123022, 2017. doi:10.1088/1367-2630/aa9041.

[38] A. Russo, S. P. Perez, M. A. Durán-Olivencia, P. Yatsyshin, J. A. Carrillo, and S. Kalliadasis. A finite-volume method for fluctuating dynamical density functional theory. *Journal of Computational Physics*, **428**:109796, 2020. doi:10.1016/j.jcp.2020.109796.

[39] A. Russo, M. A. Durán-Olivencia, P. Yatsyshin, and S. Kalliadasis. Memory effects in fluctuating dynamic density-functional theory: theory and simulations. *Journal of Physics A: Mathematical and Theoretical*, **53**(44):445007, 2020. doi:10.1088/1751-8121/ab9e8d.

[40] J. M. Brader and M. Schmidt. Power functional theory for the dynamic test particle limit. *Journal of Physics: Condensed Matter*, **27**(19):194106, 2015. doi:10.1088/0953-8984/27/19/194106.

[41] M. Schmidt and J. M. Brader. Power functional theory for Brownian dynamics. *The Journal of Chemical Physics*, **138**(21):214101, 2013. doi:10.1063/1.4807586.

[42] D. de las Heras and M. Schmidt. Velocity Gradient Power Functional for Brownian Dynamics. *Physical Review Letters*, **120**:028001, 2018. doi:10.1103/PhysRevLett.120.028001.

[43] M. Schmidt. Power functional theory for Newtonian many-body dynamics. *The Journal of Chemical Physics*, **148**(4):044502, 2018. doi:10.1063/1.5008608.

[44] I. Burghardt and B. Bagchi. On the non-adiabatic dynamics of solvation: A molecular hydrodynamic formulation. *Chemical Physics*, **329**(1):343–356, 2006. doi:10.1016/j.chemphys.2006.07.014.

[45] W. Mickel, L. Joly, and T. Biben. Transport, phase transitions, and wetting in micro/nanochannels: A phase field/DDFT approach. *The Journal of Chemical Physics*, **134**(9):094105, 2011. doi:10.1063/1.3557061.

[46] U. M. B. Marconi and S. Melchionna. Kinetic theory of correlated fluids: From dynamic density functional to Lattice Boltzmann methods. *The Journal of Chemical Physics*, **131**(1):014105, 2009. doi:10.1063/1.3166865.

[47] U. M. B. Marconi and S. Melchionna. Dynamic density functional theory versus kinetic theory of simple fluids. *Journal of Physics: Condensed Matter*, **22**(36):364110, 2010. doi:10.1088/0953-8984/22/36/364110.

[48] U. M. B. Marconi and S. Melchionna. Kinetic Density Functional Theory: A Microscopic Approach to Fluid Mechanics. *Communications in Theoretical Physics*, **62**(4):596–606, 2014. doi:10.1088/0253-6102/62/4/17.

[49] A. Baskaran, A. Baskaran, and J. Lowengrub. Kinetic density functional theory of freezing. *The Journal of Chemical Physics*, **141**(17):174506, 2014. doi:10.1063/1.4900499.

[50] J. Yvon. *La théorie statistique des fluides et l'équation d'état*, volume 203 of *Actualités scientifiques et industrielles*. Hermann & Cie, Paris, 1935.

[51] M. Born and H. Green. A general kinetic theory of liquids I. The molecular distribution functions. *Proceedings of the Royal Society of London. Series A. Mathematical and Physical Sciences*, **188**(1012):10–18, 1946. doi:10.1098/rspa.1946.0093.

[52] N. N. Bogoliubov. Kinetic Equations. *Journal of Physics USSR*, **10**(3):265–274, 1946.

[53] J. G. Kirkwood. The Statistical Mechanical Theory of Transport Processes I. General Theory. *The Journal of Chemical Physics*, **14**(3):180–201, 1946. doi:10.1063/1.1724117.

[54] J. G. Kirkwood. The Statistical Mechanical Theory of Transport Processes II. Transport in Gases. *The Journal of Chemical Physics*, **15**(1):72–76, 1947. doi:10.1063/1.1746292.

[55] R. Evans. The nature of the liquid-vapour interface and other topics in the statistical mechanics of non-uniform, classical fluids. *Advances in Physics*, **28**(2):143–200, 1979. doi:10.1080/00018737900101365.

[56] K. H. Hughes and I. Burghardt. Maximum-entropy closure of hydrodynamic moment hierarchies including correlations. *The Journal of Chemical Physics*, **136**(21):214109, 2012. doi:10.1063/1.4720568.

[57] B. Rotenberg, I. Pagonabarraga, and D. Frenkel. Coarse-grained simulations of charge, current and flow in heterogeneous media. *Faraday Discussions*, **144**:223–243, 2010. doi:10.1039/B901553A.

[58] R. Okamoto and A. Onuki. Density functional theory of gas–liquid phase separation in dilute binary mixtures. *Journal of Physics: Condensed Matter*, **28**(24):244012, 2016. doi:10.1088/0953-8984/28/24/244012.

[59] U. M. B. Marconi and S. Melchionna. Multicomponent diffusion in nanosystems. *The Journal of Chemical Physics*, **135**(4):044104, 2011. doi:10.1063/1.3608416.

[60] U. M. B. Marconi and S. Melchionna. Dynamics of fluid mixtures in nanospaces. *The Journal of Chemical Physics*, **134**(6):064118, 2011. doi:10.1063/1.3528221.

[61] U. M. B. Marconi. Non-local kinetic theory of inhomogeneous liquid mixtures. *Molecular Physics*, **109**(7-10):1265–1274, 2011. doi:10.1080/00268976.2011.554902.

[62] D. Camargo, J. A. de la Torre, D. Duque-Zumajo, P. Español, R. Delgado-Buscalioni, and F. Chejne. Nanoscale hydrodynamics near solids. *The Journal of Chemical Physics*, **148**(6):064107, 2018. doi:10.1063/1.5010401.

[63] D. Camargo, J. A. de la Torre, R. Delgado-Buscalioni, F. Chejne, and P. Español. Boundary conditions derived from a microscopic theory of hydrodynamics near solids. *The Journal of Chemical Physics*, **150**(14):144104, 2019. doi:10.1063/1.5088354.

[64] D. Duque-Zumajo, D. Camargo, J. A. de la Torre, F. Chejne, and P. Español. Discrete hydrodynamics near solid planar walls. *Physical Review E*, **99**:052130, 2019. doi:10.1103/PhysRevE.99.052130.

[65] D. Duque-Zumajo, J. A. de la Torre, D. Camargo, and P. Español. Discrete hydrodynamics near solid walls: Non-Markovian effects and the slip boundary condition. *Physical Review E*, **100**:062133, 2019. doi:10.1103/PhysRevE.100.062133.

[66] J. F. Lutsko. Recent Developments in Classical Density Functional Theory. In *Advances in Chemical Physics*, chapter 1, pages 1–92. John Wiley & Sons, 2010. doi:10.1002/9780470564318.ch1.

[67] M. te Vrugt, H. Löwen, and R. Wittkowski. Classical dynamical density functional theory: from fundamentals to applications. *Advances in Physics*, **69**(2):121–247, 2020. doi:10.1080/00018732.2020.1854965.

[68] C. F. Curtiss and R. B. Bird. Multicomponent Diffusion. *Industrial & Engineering Chemistry Research*, **38**(7):2515–2522, 1999. doi:10.1021/ie9901123.

[69] C. F. Curtiss and R. B. Bird. Multicomponent Diffusion. *Industrial & Engineering Chemistry Research*, **40**(7):1791, 2001. doi:10.1021/ie011500j. Erratum.

[70] R. B. Bird and D. J. Klingenberg. Multicomponent diffusion–A brief review. *Advances in Water Resources*, **62**:238–242, 2013. doi:10.1016/j.advwatres.2013.05.010.

[71] P. Rehner, B. Bursik, and J. Gross. Surfactant Modeling Using Classical Density Functional Theory and a Group Contribution PC-SAFT Approach. *Industrial & Engineering Chemistry Research*, **60**(19):7111–7123, 2021. doi:10.1021/acs.iecr.1c00169.

[72] K. R. Rajagopal and L. Tao. *Mechanics of Mixtures*, volume 35 of *Series on Advances in Mathematics for Applied Sciences*. World Scientific, 1995. doi:10.1142/2197.

[73] K. R. Rajagopal. An Introduction to Mixture Theory. In G. P. Galdi, J. Málek, and J. Necas (editors), *Mathematical theory in fluid mechanics*, volume 354 of *Pitman Research Notes in Mathematics Series*, pages 86–113. Longman, 1996.

[74] P. Rehner and J. Gross. Multiobjective Optimization of PCP-SAFT Parameters for Water and Alcohols Using Surface Tension Data. *Journal of Chemical & Engineering Data*, **65**(12):5698–5707, 2020. doi:10.1021/acs.jced.0c00684.

[75] E. Sauer and J. Gross. Prediction of Adsorption Isotherms and Selectivities: Comparison between Classical Density Functional Theory Based on the Perturbed-Chain Statistical Associating Fluid Theory Equation of State and Ideal Adsorbed Solution Theory. *Langmuir*, **35**(36):11690–11701, 2019. doi:10.1021/acs.langmuir.9b02378.

[76] J.-P. Hansen and I. R. McDonald. *Theory of Simple Liquids*. Academic Press, Oxford, 4th edition, 2013. doi:10.1016/C2010-0-66723-X.

[77] S. Kjelstrup, D. Bedeaux, E. Johannessen, and J. Gross. *Non-Equilibrium Thermodynamics for Engineers*. World Scientific Publishing, 2nd edition, 2016. ISBN 9789813200302, 9789813200319. doi:10.1142/10286.

[78] L. Onsager. Reciprocal Relations in Irreversible Processes. I. *Physical Review*, **37**(4):405–426,

1931. doi:10.1103/physrev.37.405.

[79] L. Onsager. Reciprocal Relations in Irreversible Processes. II. *Physical Review*, **38**(12):2265–2279, 1931. doi:10.1103/physrev.38.2265.

[80] O. Lötgering-Lin and J. Gross. Group Contribution Method for Viscosities Based on Entropy Scaling Using the Perturbed-Chain Polar Statistical Associating Fluid Theory. *Industrial & Engineering Chemistry Research*, **54**(32):7942–7952, 2015. doi:10.1021/acs.iecr.5b01698.

[81] O. Lötgering-Lin, M. Fischer, M. Hopp, and J. Gross. Pure Substance and Mixture Viscosities Based on Entropy Scaling and an Analytic Equation of State. *Industrial & Engineering Chemistry Research*, **57**(11):4095–4114, 2018. doi:10.1021/acs.iecr.7b04871.

[82] M. Hopp, J. Mele, and J. Gross. Self-Diffusion Coefficients from Entropy Scaling Using the PCP-SAFT Equation of State. *Industrial & Engineering Chemistry Research*, **57**(38):12942–12950, 2018. doi:10.1021/acs.iecr.8b02406.

[83] M. Hopp, J. Mele, and J. Gross. Erratum to "Self-Diffusion Coefficients from Entropy Scaling Using the PCP-SAFT Equation of State". *Industrial & Engineering Chemistry Research*, **58**(45):20857–20857, 2019. doi:10.1021/acs.iecr.9b05731.

[84] L. S. Darken. Diffusion, Mobility and Their Interrelation through Free Energy in Binary Metallic Systems. *Transactions of the Metallurgical Society of AIME*, **175**:184–201, 1948.

[85] S. Sridhar. A Commentary on "Diffusion, Mobility and Their Interrelation through Free Energy in Binary Metallic Systems", L.S. Darken: Trans. AIME, 1948, vol. 175, p. 184ff. *Metallurgical and Materials Transactions A*, **41**:543–562, 2010. doi:10.1007/s11661-010-0177-7.

[86] Y. Rosenfeld. Relation between the transport coefficients and the internal entropy of simple systems. *Physical Review A*, **15**:2545–2549, 1977. doi:10.1103/PhysRevA.15.2545.

[87] Y. Rosenfeld. Comments on the transport coefficients of dense hard core systems. *Chemical Physics Letters*, **48**(3):467–468, 1977. doi:10.1016/0009-2614(77)85071-9.

[88] Y. Rosenfeld. A quasi-universal scaling law for atomic transport in simple fluids. *Journal of Physics: Condensed Matter*, **11**(28):5415–5427, 1999. doi:10.1088/0953-8984/11/28/303.

[89] J. Zmpitas, A. Bardow, and J. Gross. Prediction of Mutual Diffusion Coefficients based on Stokes-Einstein Equation and the Entropy Scaling Method, ???? Unpublished.

[90] S. Chapman and T. G. Cowling. *The Mathematical Theory of Non-uniform Gases: An Account of the Kinetic Theory of Viscosity, Thermal Conduction and Diffusion in Gases*. Cambridge University Press, Cambridge, 3rd edition, 1990.

[91] J. O. Hirschfelder, C. F. Curtiss, and R. B. Bird. *Molecular theory of gases and liquids*. John Wiley & Sons, New York, 4th edition, 1967.

[92] C. R. Wilke. A Viscosity Equation for Gas Mixtures. *The Journal of Chemical Physics*, **18**(4):517–519, 1950. doi:10.1063/1.1747673.

[93] B. E. Poling, J. M. Prausnitz, and J. P. O'Connell. *The Properties of Gases and Liquids*. McGraw-Hill Professional, New York, 5th edition, 2000.

[94] P. D. Neufeld, A. R. Janzen, and R. A. Aziz. Empirical Equations to Calculate 16 of the Transport Collision Integrals $\Omega^{(l,s)*}$ for the Lennard-Jones (12-6) Potential. *The Journal of Chemical Physics*, **57**(3):1100–1102, 1972. doi:10.1063/1.1678363.

[95] C. R. Wilke and P. Chang. Correlation of diffusion coefficients in dilute solutions. *AIChE Journal*, **1**(2):264–270, 1955. doi:10.1002/aic.690010222.

[96] X. Liu, T. J. Vlugt, and A. Bardow. Predictive Darken Equation for Maxwell-Stefan Diffusivities in Multicomponent Mixtures. *Industrial & Engineering Chemistry Research*, **50**(17):10350–10358, 2011. doi:10.1021/ie201008a.

[97] J. A. Carrillo, S. Kalliadasis, S. P. Perez, and C.-W. Shu. Well-Balanced Finite-Volume Schemes for Hydrodynamic Equations with General Free Energy. *Multiscale Modeling & Simulation*, **18**(1):502–541, 2020. doi:10.1137/18M1230050.

[98] C. Rohde. A local and low-order Navier-Stokes-Korteweg system. In *Nonlinear Partial Differential Equations and Hyperbolic Wave Phenomena*, volume 526 of *Contemporary Mathematics*, pages 315–337. American Mathematical Society, 2010. doi:10.1090/conm/526/10387.

[99] J. Neusser, C. Rohde, and V. Schleper. Relaxation of the Navier–Stokes–Korteweg equations for compressible two-phase flow with phase transition. *International Journal for Numerical Methods in Fluids*, **79**(12):615–639, 2015. doi:10.1002/fld.4065.

[100] A. Chertock, P. Degond, and J. Neusser. An asymptotic-preserving method for a relaxation of the Navier–Stokes–Korteweg equations. *Journal of Computational Physics*, **335**:387–403, 2017. doi:10.1016/j.jcp.2017.01.030.

[101] T. Hitz, J. Keim, C.-D. Munz, and C. Rohde. A parabolic relaxation model for the Navier-Stokes-Korteweg equations. *Journal of Computational Physics*, **421**:109714, 2020. doi:https://doi.org/10.1016/j.jcp.2020.109714.

[102] G. Gassner, F. Lörcher, and C.-D. Munz. A contribution to the construction of diffusion fluxes for finite volume and discontinuous Galerkin schemes. *Journal of Computational Physics*, **224**(2):1049–1063, 2007. doi:10.1016/j.jcp.2006.11.004.

[103] S. Jöns and C.-D. Munz. An Approximate Riemann Solver for Advection–Diffusion Based on the Generalized Riemann Problem. *Communications on Applied Mathematics and Computation*, **2**:515–539, 2020. doi:10.1007/s42967-019-00048-3.

[104] C. Lanczos. *Applied Analysis*. Prentice-Hall Mathematics Series. Prentice-Hall, 1956.

[105] G. D. Byrne and A. C. Hindmarsh. A Polyalgorithm for the Numerical Solution of Ordinary Differential Equations. *ACM Transactions on Mathematical Software*, **1**(1):71–96, 1975. doi:10.1145/355626.355636.

[106] L. F. Shampine and M. W. Reichelt. The MATLAB ODE Suite. *SIAM Journal on Scientific Computing*, **18**(1):1–22, 1997. doi:10.1137/S1064827594276424.

[107] E. Hairer, S. P. Nørsett, and G. Wanner. *Solving Ordinary Differential Equations I: Nonstiff Problems*, volume 8 of *Springer Series in Computational Mathematics*. Springer, 2nd edition, 1992. doi:10.1007/978-3-540-78862-1.

[108] P. Virtanen, R. Gommers, T. E. Oliphant, M. Haberland, T. Reddy, D. Cournapeau, E. Burovski, P. Peterson, W. Weckesser, J. Bright, S. J. van der Walt, M. Brett, J. Wilson, K. J. Millman, N. Mayorov, A. R. J. Nelson, E. Jones, R. Kern, E. Larson, C. J. Carey, İ. Polat, Y. Feng, E. W. Moore, J. VanderPlas, D. Laxalde, J. Perktold, R. Cimrman, I. Henriksen, E. A. Quintero, C. R. Harris, A. M. Archibald, A. H. Ribeiro, F. Pedregosa, P. van Mulbregt, and SciPy 1.0 Contributors. SciPy 1.0: Fundamental Algorithms for Scientific Computing in Python. *Nature Methods*, **17**:261–272, 2020. doi:10.1038/s41592-019-0686-2.

[109] J. A. Carrillo, M. J. Castro, S. Kalliadasis, and S. P. Perez. High-Order Well-Balanced Finite-Volume Schemes for Hydrodynamic Equations With Nonlocal Free Energy. *SIAM Journal on Scientific Computing*, **43**(2):A828–A858, 2021. doi:10.1137/20M1332645.

6 Conclusion & Outlook

In this work, I proposed a hydrodynamic density functional theory (DFT) model for multi-component mixtures that can be derived from a variational principle. To efficiently solve convolution integrals that appear in the hydrodynamic DFT, I gave a derivation on how to efficiently compute the convolution integrals appearing in the PC-SAFT Helmholtz energy functionals in Cartesian, cylindrical, and spherical coordinates using fast Fourier and similar transforms.

Convolution integrals can be computed efficiently in Fourier space using off-the-shelf fast Fourier as well as fast sine and cosine algorithms. In addition, they allow easy exploitation of symmetries, reducing the dimensionality and complexity of many practical problems. In cylindrical coordinates, rotational symmetry can be easily exploited. The resulting convolution integrals are then computed by zero- and first-order Hankel transforms. While previous approaches used logarithmic grids, that are not well suited for hydrodynamic DFT applications, an existing first-order fast Hankel transform algorithm was extended by its inverse transform to overcome this limitation. This new approach uses an equidistant spatial discretization, combining a fast sine and a modification of a fast Abel transform. In spherical coordinates, exploiting spherical symmetry results in the convolution integrals being computed by sine and cosine transforms. Thus, in addition to Cartesian systems, single spherical droplets, radial distribution and van Hove correlation functions, as well as rotationally symmetric pores can be efficiently computed with (dynamic) DFT. This allows, for example, the analysis of size dependence of the interfacial tension of small droplets/bubbles or adsorption isotherms in cylindrical pores or spherical cavities.

Efficient convolution algorithms are crucial for the efficient application of the proposed hydrodynamic DFT model, since the computation of the convolution integrals constitutes the determining factor for the computing time. The proposed hydrodynamic DFT model accounts for viscous forces modeled by a Newtonian shear pressure tensor. For molecular multicomponent diffusion, a Maxwell-Stefan model is applied. A suitable expression for the driving force for diffusion is derived. The driving force includes a term that captures the effect of a pressure gradient or interfacial tension, which contributes substantially to diffusion in the vicinity of interfaces. The expression can be considered an extension of the generalized driving force proposed by Curtiss and Bird [1,2] to inhomogeneous systems. The

use of this driving force is essential because the mechanical equilibrium assumption required in Maxwell-Stefan diffusion is not satisfied with more naïve expressions for the driving force for the intended applications.

The proposed hydrodynamic DFT simplifies to the isothermal Navier-Stokes equation for continuum situations where local Helmholtz energy functionals can be used (which is equivalent to an ordinary thermal equation of state), allowing a bridging of the gap between microscopic and macroscopic length scales. I was able to show that the hydrodynamic DFT model for an isolated system satisfies the first and second law of thermodynamics, even though the model is not formulated in conservative form.

I applied the hydrodynamic DFT model to droplet and bubble coalescence of binary mixtures in one spatial dimension. The transport coefficients (shear viscosity and Maxwell-Stefan diffusion coefficients) are obtained via entropy scaling. Originally developed and parameterized for bulk fluids, I applied the method to inhomogeneous fluids, i.e., the droplet or bubble systems considered. Since the hydrodynamic DFT model is not formulated in conservative form, a well-balanced finite-volume discretization scheme is used that, unlike naïve flux discretizations, does not generate numerical artifacts. The hydrodynamic DFT model combined with the well-balanced finite-volume scheme was proven to be capable of describing droplet and bubble coalescence of pure components and binary mixtures. For the considered systems, *n*-alkane/nitrogen mixtures exhibiting nitrogen enrichment at the vapor-liquid interface, the addition of nitrogen is shown to have a noticeable effect on the coalescence behavior. Furthermore, different behaviors are observed for the coalescence of droplets and bubbles. This is caused by different physical properties in the vapor and liquid phases, which affect the time evolution of the system and thus the driving forces in the component and momentum balance. For the systems considered, droplet coalescence proceeds in two stages: (I) convective and diffusive molecular transport leading to a oscillating coalesced droplet, and (II) slow diffusion of species within a single coalesced droplet. Coalescence of bubbles shows three distinct phases: (I) very rapid convective transport in the vapor phase with minor oscillations, (II) slow diffusive transport, and (III) simultaneous convective and diffusive transport to coalescence.

6.1 Interesting Aspects for Subsequent Investigations

First and foremost, one-dimensional droplets and bubbles are not a good representation for their three-dimensional equivalents. While one-dimensional representations certainly capture the continuous interface and potential for density oscillations of three-dimensional bodies, they are limited by their low dimensionality. Curvature effects and the resulting pressure difference between the droplet or bubble and the environment, as well as oscillations in a

second direction, exist only in higher dimensions. Simulation of two- or three-dimensional systems would enable the analysis of additional phenomena and hence a more accurate representation of reality. Two- or three-dimensional droplets or bubbles allow the analysis of Ostwald ripening, in particular the effect of different components or mixing effects such as the enrichment of one component at the vapor-liquid interface. Furthermore, since in one-dimensional systems the component accumulated at the vapor-liquid interface can only diffuse through the liquid phase (in the case of droplets) or the vapor phase (in the case of bubbles), it is also possible to analyze displacement effects of the component enriched at the interface during coalescence when considering higher-dimensional systems. Consideration of higher-dimensional systems allows not only the observation of coalescence or Ostwald ripening of sessile droplets or bubbles on solid, possibly even heterogeneous, surfaces, but also the determination of dynamic contact angles on these surfaces. Moreover, three-dimensional droplets can then be compared to molecular dynamics simulations of droplets or bubbles, validating the hydrodynamic DFT model or helping to identify model shortcomings for further improvement, including the validity of entropy scaling methods for inhomogeneous fluids.

In addition, some numerical aspects warrant exploration. These include the discretization of the gradient operator that appears in the thermodynamic driving forces of the diffusive fluxes. The current discretization does not conserve discrete stationary states* between two adjoining cells because in addition to the adjacent cells, the next-to-nearest cells are also used to approximate the gradient. The application of numerical time integration algorithms tailored to fluid dynamics problems should also be further investigated, especially when considering higher-dimensional systems. While the fast Fourier transforms applied to compute the convolution integrals of DFT show good scaling behavior for larger systems, they do not lend themselves well to domain decomposition, a multi-node parallelization approach commonly used in computational fluid dynamics. Real-space convolution algorithms are better suited for this purpose. First steps toward real-space convolution based on the discontinuous Galërkin spectral element method yielded promising results in one and two dimensions, but are complex to implement for two- or three-dimensional systems for exact integration of the ansatz functions; approximate integration methods could help with this issue.

The hydrodynamic DFT model was derived for isothermal situations. Although rigorous derivation of a non-isothermal dynamical system usually requires a functional for internal energy and entropy, it would be worthwhile to test whether a thermodynamically consistent extension of the hydrodynamic DFT model could be achieved by simply including an internal energy balance.

*see eq. (5.59)

References

[1] C. F. Curtiss and R. B. Bird. Multicomponent Diffusion. *Industrial & Engineering Chemistry Research*, **38**(7):2515–2522, 1999. doi:10.1021/ie9901123.

[2] C. F. Curtiss and R. B. Bird. Multicomponent Diffusion. *Industrial & Engineering Chemistry Research*, **40**(7):1791, 2001. doi:10.1021/ie011500j. Erratum.

Appendices

A Supporting Information: Guide to Efficient Solution of PC-SAFT Classical Density Functional Theory in Various Coordinate Systems Using Fast Fourier and Similar Transforms

The content of this appendix is a literal quote of the supporting information:

R. Stierle, E. Sauer, J. Eller, M. Theiss, P. Rehner, P. Ackermann, and J. Gross. Supporting Information: Guide to efficient Solution of PC-SAFT classical Density Functional Theory in various Coordinate Systems using fast Fourier and similar Transforms. *Fluid Phase Equilibria*, **504**:112306, 2020. doi:10.1016/j.fluid.2019.112306

Abstract

Classical density functional theory (DFT) is a powerful tool for studying solvation or problems where resolution of interfacial domains or interfacial properties among phases (or thin films) is required. Many interesting problems necessitate multi-dimensional modeling, which calls for robust and efficient algorithmic implementations of the Helmholtz energy functionals. A possible approach for achieving efficient numerical solutions is using the convolution theorem of the Fourier transform. This study is meant to facilitate research and application of DFT methods, by providing a detailed guide on solving DFT problems in multi-dimensional domains. The work covers functionals based on weighted densities, such as the fundamental measure theory (FMT), or a Helmholtz energy functional based on the perturbed-chain statistical associating fluid theory (PC-SAFT) equation of state. Methods for efficiently solving the convolution integrals in Fourier space are presented for Cartesian, cylindrical, and spherical coordinates. For cylindrical and spherical coordinate systems, rotational and spherical symmetry is exploited, respectively. To enable easy implementation, our approach is based on fast Fourier, fast Hankel, fast sine and cosine transforms on equidistant grids, all of which can be applied using off-the-shelf algorithms. Subtle details for implementing algorithms in cylindrical and spherical coordinate systems are emphasized.

A.1 Introduction

Efficient numerical solution of convolution integrals is important for solving classical density functional theory (DFT) or dynamic density functional theory (DDFT) in multidimensional problems. The solution of a DFT model, namely the densities of all species, is obtained iteratively. The computational demand for the iterative solution is the repetitive computation of numerous convolution integrals. Naïve numerical convolution through integration leads to long computation times and complicated integration schemes, especially for multidimensional DFT problems. One approach to address this problem is the utilization of the convolution theorem of the Fourier transform. The $\mathcal{O}(N \log N)$ computational complexity of fast Fourier transform (FFT) algorithms (compared to $\mathcal{O}(N^2)$ for numerical convolution) leads to a significant advantage regarding computational performance. Additionally, working with integral transforms like FFT simplifies multidimensional convolutions, because each dimension can be treated separately which averts multidimensional integration schemes.

Several authors applied integral transforms to convolution integrals appearing in DFT. Knepley *et al.* [1] used the FFT approach for convolutions in a DFT for ionic solutions. A short introduction to usage of FFT for Rosenfeld's fundamental measure theory[2] (FMT) was also given. Frink *et al.* [3,4] proposed Fourier space convolution on a multidimensional Cartesian grid in combination with nonlinear iterative solvers and Sears and Frink[5] proposed using FFT in combination with a matrix-free scheme and compared computational efficiency for one-, two- and three-dimensional systems. Hlushak *et al.* [6] employed the FFT on a two-dimensional Cartesian grid to analyze flexible chain molecules at curved surfaces, whereas Hlushak *et al.* [7], and Hlushak *et al.* [8] studied attractive particles in nanopores. While analyzing rotationally symmetric systems, rotational symmetry was not exploited in the computation of the convolution integrals, leading to unnecessary computational overhead. Oettel *et al.* applied the Fourier convolution approach within the framework of three-dimensional FMT and compared results to those obtained by phase-field models[10] and Monte Carlo simulations[9]. A similar analysis of crystal structures and solid-liquid interfaces using three-dimensional FMT combined with a Helmholtz energy contribution to account for attractive interactions was conducted by Wang *et al.* [11]. Solvation effects in water were studied by Levesque *et al.* [12]; solvation energies of amino acid side chains by Liu *et al.* [13], both by three-dimensional DFT. Zhou *et al.* [14] applied three-dimensional Cartesian DFT to heterogeneous nucleation of Lennard-Jones fluids on solid walls.

For cylindrical systems, rotational symmetry can be exploited to reduce dimensionality of the DFT problem. In one-dimensional cylindrical coordinates, González *et al.* [15] proposed using the Hankel transform for computation of the convolution in Fourier space. The fast Hankel

transform was not employed, however. Malijevský[16] and Mariani *et al.*[17] took advantage of rotational symmetry to formulate the convolution integrals of FMT for cylindrical coordinates in real space. In Fourier space this was done by Boţan *et al.*[18] for the analysis of hard-sphere fluids in annular wedges. In cylindrical coordinates the Fourier transform can not be computed using FFT, but requires a, preferably fast, Hankel transform algorithm for the radial direction. Boţan *et al.*[18] reformulated the DFT problem on a logarithmic grid to apply a fast Hankel transform.

Spherical symmetry can be exploited to efficiently compute spherical DFT systems in one dimension. This was applied by González *et al.*[15] to hard spheres in a spherical cavity, utilizing Fourier space convolution. For FMT in spherical coordinates projection of the weight functions onto one dimension was described by Roth[19].

Convolution in Fourier space by exploiting the FFT or similar algorithms is not the only approach to speed up the computation of the convolution integrals appearing in DFT problems. Yatsyshin *et al.* introduced a Chebyshev pseudo-spectral collocation method in combination with Clenshaw-Curtis quadrature for computation of the convolution integrals in one[20] and two dimensions[21] of a Cartesian grid, extended by Nold *et al.*[22]. Contrary to FFT convolution, equidistant grid spacing is not required, but possible. Problem-specific grid spacing has potential to reduce computational effort. Xu and Cao[23] used a two-dimensional multiscale finite element approach to reduce computational complexity for the convolution integrals.

Computation time, of course, not only depends on the performance of the Helmholtz functional computation and the involved convolution integrals but also depends on the algorithm used to solve the system of nonlinear equations as well. Previous work on numerical algorithms can be found in Frink *et al.*[3,4], Kovalenko *et al.*[24], Frink and Salinger[25,26], Frink *et al.*[27], a comparison of different nonlinear solvers in Mairhofer and Gross[28].

Classical DFT or DDFT are theoretical approaches that carry molecular detail through averaged quantities. DFT approaches are predictive when a suitable Helmholtz energy functional is applied. We aim at applying FFT convolution to a functional consistent with the perturbed-chain statistical associating fluid theory (PC-SAFT) equation of state[29,30]. The PC-SAFT equation of state is formulated in terms of the Helmholtz energy allowing easy generalization to Helmholtz energy functionals. PC-SAFT provides good descriptions of thermodynamic properties in bulk phases for a wide variety of real substances and mixtures, including components of low molecular mass[30], but also complex species like polymers[31] or associating substances[32]. The underlying molecular model regards molecules as hard chains with attractive van der Waals segment-segment interactions or hydrogen-bonding (associating)[32–37] or dipolar and quadrupolar interactions[38–40]. Several approaches combining PC-SAFT and DFT have been proposed. Gross[41] described a DFT for pure substances which was generalized by Klink and

Gross for mixtures and successfully applied to vapor-liquid[42], liquid-liquid interfaces[43]. Klink *et al.*[44] and Lamanna *et al.*[45] applied this PC-SAFT DFT to interfacial transport resistivities. Sauer and Gross[46] suggested a Helmholtz energy functional for the dispersion contribution based on a weighted density approximation suitable for confined systems, predicting physical phenomena like surface tension, contact angles[47] and adsorption isotherms. Similar approaches were taken by Shen *et al.*[48,49], Ye *et al.*[50] and Xu *et al.*[51].

This work provides a practical guide to implementing and solving DFT models that are based on weighted densities. We wish to facilitate the use of DFT approaches in engineering applications. More specifically we demonstrate implementation of the ideal gas, hard-sphere, hard-chain and dispersion contribution of PC-SAFT DFT in Cartesian, cylindrical and spherical coordinate systems. We use the FFT algorithm for Cartesian coordinates and the axial contribution to cylindrical systems, the fast Hankel transform is applied for the radial contribution to cylindrical systems and the fast sine and cosine transform is adopted for systems described in spherical coordinates. In contrast to previous work using cylindrical coordinates[18], we apply the fast Hankel transform of Hansen[52,53], which allows computation of Hankel transforms on equidistant (rather than logarithmic) grids by using a combination of fast Abel[54] and fast sine and cosine transforms. Equidistant grids reduce computational overhead because a smaller number of overall grid points is usually possible, while maintaining the same worst-case grid density as compared to logarithmic grids. A complete presentation of the Helmholtz energy functionals of PC-SAFT DFT is given, including their functional derivatives and a comprehensible introduction to Fourier space convolution. Fourier space convolution is easier to implement than naïve real space convolution, which allows writing robust simulation codes.

A.2 Classical Density Functional Theory Using PC-SAFT Functionals

The starting point for classical DFT is the grand potential functional Ω, which, for a mixture of N_c components is written as

$$\Omega[\{\rho_i(\mathbf{r})\}] = F[\{\rho_i(\mathbf{r})\}] + \sum_{i=1}^{N_\mathrm{c}} \int \rho_i(\mathbf{r}) \left(V_i^{\mathrm{ext}}(\mathbf{r}) - \mu_i\right) \mathrm{d}\mathbf{r} \tag{A.1}$$

with Helmholtz energy functional F, chemical potential μ_i of component i and the external potential V_i^{ext}, acting on component i. Although not made explicit in this notation, the specified variables of Ω are temperature T, volume V, and chemical potentials μ_i of all species. Further, $\rho_i(\mathbf{r})$ describes the density of component i at position $\mathbf{r}$, placing the orientational and conformational degrees of freedom in the de Broglie wavelengths $\Lambda_i(T)$, which will cancel out

in all equations due to isothermal treatment. For DFT with the PC-SAFT[30] chain contribution, the configuration of the chain fluid is considered in an averaged manner only by the position vector $\mathbf{r}$. Therefore, $\rho_i(\mathbf{r})$ denotes the average of density profiles for the individual segments in molecule i. This approximation neglects any density dependence of the internal degrees of freedom, i.e., treating complex fluids as simple ones. Square brackets denote a functional dependence and curly brackets around $\{\rho_i(\mathbf{r})\}$ indicate a vector of all densities within a mixture, $i = 1, \ldots, N_c$.

In equilibrium the grand potential functional is minimal and the value of the grand potential functional reduces to the grand potential $\Omega^0 = \Omega[\{\rho_i^0\}]$. The minimum implies, that for the equilibrium density profile $\{\rho_i^0(\mathbf{r})\}$, the functional derivatives of the grand potential functional Ω with respect to the density profiles $\{\rho_i(\mathbf{r})\}$ vanish according to

$$\left.\frac{\delta\Omega[\{\rho_i\}]}{\delta\rho_j(\mathbf{r})}\right|_{\{\rho_i^0(\mathbf{r})\}} = 0 \tag{A.2}$$

which leads to the main equation of DFT

$$\frac{\delta F[\{\rho_i\}]}{\delta\rho_j(\mathbf{r})} = \mu_j - V_j^{\mathrm{ext}}(\mathbf{r}) \qquad \forall j \tag{A.3}$$

that can be solved for the density profiles $\{\rho_i^0(\mathbf{r})\}$ in the considered volume, provided a model for the Helmholtz energy functional is available.

We consider a state-of-the-art Helmholtz energy functional using PC-SAFT[30], which is based on a division into an ideal gas, hard-sphere, hard-chain, and dispersion contribution according to

$$F[\{\rho_i(\mathbf{r})\}] = F^{\mathrm{ig}}[\{\rho_i(\mathbf{r})\}] + F^{\mathrm{hs}}[\{\rho_i(\mathbf{r})\}] + F^{\mathrm{hc}}[\{\rho_i(\mathbf{r})\}] + F^{\mathrm{disp}}[\{\rho_i(\mathbf{r})\}] \tag{A.4}$$

with model parameters for each component in the mixture i: the hard-sphere radii R_i (or hard-sphere diameters d_i) describing repulsive interactions, the chain lengths m_i, and ε_i, describing the attractive segment-segment interactions. Possible extensions are contributions for association and multipolar interactions[41,46], which are not considered here. The treatment of these terms is entirely analogous to the expressions detailed in this work.

A.2.1 Ideal Gas Contribution

The ideal gas contribution to the Helmholtz energy functional is known exactly,

$$\beta F^{\mathrm{ig}}[\{\rho_i(\mathbf{r})\}] = \sum_{i=1}^{N_\mathrm{c}} \int \rho_i(\mathbf{r}) \Big(\ln\big(\rho_i(\mathbf{r})\Lambda_i^3\big) - 1 \Big) \,\mathrm{d}\mathbf{r} \tag{A.5}$$

where Λ_i denotes the de Broglie wavelength, which contains the translational and internal degrees of freedom of the chain fluid, and $\beta = \frac{1}{k_\mathrm{B} T}$ is the inverse temperature, with Boltzmann constant k_B. This is an approximation for a chain considered as an ideal gas with average treatment of internal degrees of freedom, with corrections therefor introduced in appendix A.2.3. The functional derivative is calculated as

$$\begin{aligned} \frac{\delta \beta F^{\mathrm{ig}}[\{\rho_i\}]}{\delta \rho_j(\mathbf{r})} &= \sum_i^{N_\mathrm{c}} \int \frac{\delta \rho_i(\mathbf{r}')}{\delta \rho_j(\mathbf{r})} \Big(\ln\big(\rho_i(\mathbf{r}')\Lambda_i^3\big) - 1 \Big) \,\mathrm{d}\mathbf{r}' + \sum_i^{N_\mathrm{c}} \int \rho_i(\mathbf{r}') \frac{\delta \ln\big(\rho_i(\mathbf{r}')\Lambda_i^3\big)}{\delta \rho_j(\mathbf{r})} \,\mathrm{d}\mathbf{r}' \\ &= \sum_i^{N_\mathrm{c}} \delta_{ij} \int \delta(\mathbf{r}' - \mathbf{r}) \ln\big(\rho_i(\mathbf{r}')\Lambda_i^3\big) \,\mathrm{d}\mathbf{r}' = \ln\big(\rho_j(\mathbf{r})\Lambda_j^3\big) \end{aligned} \tag{A.6}$$

where we used

$$\frac{\delta \rho_i(\mathbf{r}')}{\delta \rho_j(\mathbf{r})} = \delta_{ij} \delta(\mathbf{r} - \mathbf{r}') \tag{A.7}$$

with δ_{ij} as the Kronecker delta and δ as the Dirac delta function.

A.2.2 Hard-Sphere Contribution – Fundamental Measure Theory

The White-Bear version[19,55,56] of the fundamental measure theory (FMT) is used to calculate the hard-sphere contribution

$$\beta F^{\mathrm{hs}}[\{\rho_i(\mathbf{r})\}] = \int \Phi^{\mathrm{WB}}(\{n_\alpha(\mathbf{r})\}) \,\mathrm{d}\mathbf{r} \tag{A.8}$$

where $\alpha \in \{0, 1, 2, 3, \mathrm{V1}, \mathrm{V2}\}$. The reduced Helmholtz energy density Φ, which is solely a function of the weighted densities $n_\alpha(\mathbf{r})$, is obtained from

$$\begin{aligned} \Phi^{\mathrm{WB}}(\{n_\alpha\}) = -n_0 \ln(1 - n_3) &+ \frac{n_1 n_2 - \mathbf{n}_{\mathrm{V1}} \cdot \mathbf{n}_{\mathrm{V2}}}{1 - n_3} \\ &+ \big((n_2)^3 - 3 n_2 \mathbf{n}_{\mathrm{V2}} \cdot \mathbf{n}_{\mathrm{V2}} \big) \frac{n_3 + (1 - n_3)^2 \ln(1 - n_3)}{36\pi (n_3)^2 (1 - n_3)^2} \end{aligned} \tag{A.9}$$

with the weighted densities $n_\alpha(\mathbf{r})$ calculated via convolution of the density profile ρ_i as

$$n_\alpha(\mathbf{r}) = \sum_{i=1}^{N_c} m_i \int \rho_i(\mathbf{r}')\omega_i^\alpha(\mathbf{r}-\mathbf{r}')\,\mathrm{d}\mathbf{r}' \equiv \sum_{i=1}^{N_c} m_i \rho_i(\mathbf{r}) \otimes \omega_i^\alpha(\mathbf{r}) \tag{A.10}$$

The respective weight functions[2,19,55] ω_i^α are defined as

$$\omega_i^0(\mathbf{r}) = \frac{1}{4\pi R_i^2}\delta(R_i - |\mathbf{r}|) \tag{A.11a}$$

$$\omega_i^1(\mathbf{r}) = \frac{1}{4\pi R_i}\delta(R_i - |\mathbf{r}|) \tag{A.11b}$$

$$\omega_i^2(\mathbf{r}) = \delta(R_i - |\mathbf{r}|) \tag{A.11c}$$

$$\omega_i^3(\mathbf{r}) = \Theta(R_i - |\mathbf{r}|) \tag{A.11d}$$

$$\omega_i^{V1}(\mathbf{r}) = \frac{1}{4\pi R_i}\frac{\mathbf{r}}{|\mathbf{r}|}\delta(R_i - |\mathbf{r}|) \tag{A.11e}$$

$$\omega_i^{V2}(\mathbf{r}) = \frac{\mathbf{r}}{|\mathbf{r}|}\delta(R_i - |\mathbf{r}|) \tag{A.11f}$$

with the hard-sphere radius R_i of component i, the Dirac delta function δ, and the Heaviside step function Θ. We note that, for homogeneous fluids, FMT reduces to the Boublík-Mansoori-Carnahan-Starling-Leland (BMCSL) equation of state[57,58], used as hard-sphere contribution for PC-SAFT.

The PC-SAFT model considers molecules to be composed of chains of spherical segments. A molecule consists of m_i identical spherical segments, commonly referred to as chain length. We note, that in PC-SAFT the chain length is an adjustable parameter characterizing real substances and can take on non-integer values. For chain fluids, m_i has to be considered for the weighted densities in eq. (A.10) of the hard-sphere contribution. Here, $m_i\rho_i$ determines the segment density in contrast to the molecular density ρ_i[46]. Within PC-SAFT, the soft repulsion between molecules of a fluid is modeled by a temperature-dependent effective hard-sphere diameter[30]

$$d_i(T) = 2R_i(T) = \sigma_i[1 - 0.12\exp(-3\beta\varepsilon_i)] \tag{A.12}$$

with PC-SAFT segment size parameter σ_i and energy parameter ε_i defining the van der Waals (dispersive) interaction potential. The functional derivative is calculated as

$$\frac{\delta\beta F^{\mathrm{hs}}[\{\rho_i\}]}{\delta\rho_j(\mathbf{r})} = \int \frac{\delta\Phi}{\delta\rho_j(\mathbf{r})}\,\mathrm{d}\mathbf{r}' = \int \sum_\alpha \frac{\partial\Phi}{\partial n_\alpha(\mathbf{r}')} \cdot \frac{\delta n_\alpha(\mathbf{r}')}{\delta\rho_j(\mathbf{r})}\,\mathrm{d}\mathbf{r}' \tag{A.13}$$

with the functional derivative of the weighted densities according to

$$\begin{aligned}\frac{\delta n_\alpha(\mathbf{r}')}{\delta\rho_j(\mathbf{r})} &= \frac{\delta}{\delta\rho_j(\mathbf{r})}\sum_i^{N_c} m_i \int \rho_i(\mathbf{r}'')\omega_i^\alpha(\mathbf{r}'-\mathbf{r}'')\,\mathrm{d}\mathbf{r}'' \\ &= \sum_i^{N_c} m_i \int \delta_{ij}\delta(\mathbf{r}''-\mathbf{r})\omega_i^\alpha(\mathbf{r}'-\mathbf{r}'')\,\mathrm{d}\mathbf{r}'' = m_j\omega_j^\alpha(\mathbf{r}'-\mathbf{r})\end{aligned} \tag{A.14}$$

Substitution of eq. (A.14) in eq. (A.13) allows the functional derivative to be rewritten as a sum of convolution integrals according to

$$\begin{aligned}\frac{\delta\beta F^{\mathrm{hs}}[\{\rho_i\}]}{\delta\rho_j(\mathbf{r})} &= m_j\sum_\alpha\int\frac{\partial\Phi}{\partial n_\alpha}\omega_j^\alpha(\mathbf{r}'-\mathbf{r})\,\mathrm{d}\mathbf{r}' \\ &= m_j\Bigg(\frac{\partial\Phi}{\partial n_0}\otimes\omega_j^0+\frac{\partial\Phi}{\partial n_1}\otimes\omega_j^1+\frac{\partial\Phi}{\partial n_2}\otimes\omega_j^2+\frac{\partial\Phi}{\partial n_3}\otimes\omega_j^3 \\ &\qquad -\frac{\partial\Phi}{\partial\mathbf{n}_{\mathrm{V1}}}\otimes\omega_j^{\mathrm{V1}}-\frac{\partial\Phi}{\partial\mathbf{n}_{\mathrm{V2}}}\otimes\omega_j^{\mathrm{V2}}\Bigg)\end{aligned} \tag{A.15}$$

The scalar weight functions are even, with

$$\omega_i^\alpha(\mathbf{r}'-\mathbf{r}) = \omega_i^\alpha(\mathbf{r}-\mathbf{r}') \qquad \text{for } \alpha\in\{0,1,2,3\} \tag{A.16}$$

while the vector weight functions are odd functions

$$\boldsymbol{\omega}_i^\alpha(\mathbf{r}'-\mathbf{r}) = -\boldsymbol{\omega}_i^\alpha(\mathbf{r}-\mathbf{r}') \qquad \text{for } \alpha\in\{\mathrm{V1},\mathrm{V2}\} \tag{A.17}$$

leading to the minus signs in eq. (A.15). The partial derivatives $\frac{\partial\Phi^{\mathrm{WB}}}{\partial n_\alpha}$ are derived from eq. (A.9), as

$$\frac{\partial\Phi^{\mathrm{WB}}}{\partial n_0} = -\ln(1-n_3) \tag{A.18a}$$

$$\frac{\partial\Phi^{\mathrm{WB}}}{\partial n_1} = \frac{n_2}{1-n_3} \tag{A.18b}$$

$$\frac{\partial\Phi^{\mathrm{WB}}}{\partial n_2} = \frac{n_1}{1-n_3}+3(n_2^2-\mathbf{n}_{\mathrm{V2}}\cdot\mathbf{n}_{\mathrm{V2}})\frac{n_3+(1-n_3)^2\ln(1-n_3)}{36\pi n_3^2(1-n_3)^2} \tag{A.18c}$$

$$\begin{aligned}\frac{\partial\Phi^{\mathrm{WB}}}{\partial n_3} &= \frac{n_0}{1-n_3}+\frac{n_1n_2-\mathbf{n}_{\mathrm{V1}}\cdot\mathbf{n}_{\mathrm{V2}}}{(1-n_3)^2} \\ &\quad -\frac{n_2^3-3n_2\mathbf{n}_{\mathrm{V2}}\cdot\mathbf{n}_{\mathrm{V2}}}{36\pi}\left(\frac{n_3^2-5n_3+2}{n_3^2(1-n_3)^3}+\frac{2\ln(1-n_3)}{n_3^3}\right)\end{aligned} \tag{A.18d}$$

$$\frac{\partial\Phi^{\mathrm{WB}}}{\partial\mathbf{n}_{\mathrm{V1}}} = -\frac{\mathbf{n}_{\mathrm{V2}}}{1-n_3} \tag{A.18e}$$

$$\frac{\partial \Phi^{\mathrm{WB}}}{\partial \mathbf{n}_{\mathrm{V2}}} = -\frac{\mathbf{n}_{\mathrm{V1}}}{1-n_3} - n_2 \mathbf{n}_{\mathrm{V2}} \frac{n_3 + (1-n_3)^2 \ln(1-n_3)}{6\pi n_3^2 (1-n_3)^2} \tag{A.18f}$$

A.2.3 Hard-Chain Contribution

The PC-SAFT chain contribution to the Helmholtz energy functional is based on Wertheim's thermodynamic perturbation theory[33–36] and has been developed by Tripathi and Chapman[59,60]. Here we follow the description of Sauer and Gross[46]

$$\begin{aligned}\beta F^{\mathrm{hc}}[\{\rho_i(\mathbf{r})\}] = &\sum_{i=1}^{N_c}(m_i-1)\int \rho_i(\mathbf{r})\Big(\ln\left(\rho_i(\mathbf{r})\right)-1\Big)\,\mathrm{d}\mathbf{r} \\ &-\sum_{i=1}^{N_c}(m_i-1)\int \rho_i(\mathbf{r})\Big(\ln\left(y_{ii}^{dd}(\{\bar{\rho}_i^{\mathrm{hc}}(\mathbf{r})\})\lambda_i^{\mathrm{hc}}(\mathbf{r})\right)-1\Big)\,\mathrm{d}\mathbf{r} \\ &+\sum_{i=1}^{N_c}\int \rho_i(\mathbf{r})\,\mathrm{d}\mathbf{r}\Big(m_i \ln\left(\Lambda_{\mathrm{s},i}^3\right)-\ln\left(\Lambda_i^3\right)\Big)\end{aligned} \tag{A.19}$$

with the cavity correlation function at contact distance[60,61] y_{ii}^{dd}, the weighted density in the interpenetration volume of two segments around the position of a molecule $\bar{\rho}_i^{\mathrm{hc}}$, the weighted density at contact-distance around a segment of the chain λ_i^{hc}. The bar ($\bar{}$) above quantities indicates them being, or using, a weighted density. The second term in eq. (A.19) uses the ideal gas of non-bonded segments as a reference state. The first and last term on the right-hand side correct the ideal gas contribution, eq. (A.5), of the chain fluid used in appendix A.2.1, where the whole chain is considered as one ideal gas particle. Because the second term in eq. (A.19) considers the fluid on non-bounded segments as a reference fluid, the ideal gas contribution of the (m_i-1) additional segments has to be added. The last term contains the de Broglie wavelength of an individual segment $\Lambda_{\mathrm{s},i}$ and of the chain Λ_i. This term is irrelevant for all isothermal applications and, therefore, it will be neglected henceforth (for a more detailed description see appendix D in Sauer and Gross[46]).

The weighted densities for the chain contribution are computed as

$$\bar{\rho}_i^{\mathrm{hc}}(\mathbf{r}) = \frac{3}{4\pi d_i^3}\int \rho_i(\mathbf{r}')\Theta(d_i-|\mathbf{r}-\mathbf{r}'|)\,\mathrm{d}\mathbf{r}' \equiv \int \rho_i(\mathbf{r}')\omega_i^{\mathrm{hc},\rho}(\mathbf{r}-\mathbf{r}')\,\mathrm{d}\mathbf{r}' = \rho_i(\mathbf{r})\otimes\omega_i^{\mathrm{hc},\rho}(\mathbf{r}) \tag{A.20}$$

with the weight function $\omega_i^{\mathrm{hc},\rho}(\mathbf{r}) = \frac{3}{4\pi d_i^3}\Theta(d_i-|\mathbf{r}|)$. The average densities at contact-distance around a segment of chain i is defined as

$$\lambda_i^{\mathrm{hc}}(\mathbf{r}) = \frac{1}{4\pi d_i^2}\int \rho_i(\mathbf{r}')\delta(d_i-|\mathbf{r}-\mathbf{r}'|)\,\mathrm{d}\mathbf{r}' \equiv \int \rho_i(\mathbf{r}')\omega_i^{\mathrm{hc},\lambda}(\mathbf{r}-\mathbf{r}')\,\mathrm{d}\mathbf{r}' = \rho_i(\mathbf{r})\otimes\omega_i^{\mathrm{hc},\lambda}(\mathbf{r}) \tag{A.21}$$

with the weight function $\omega_i^{\mathrm{hc},\lambda}(\mathbf{r}) = \frac{1}{4\pi d_i^2}\delta(d_i - |\mathbf{r}|)$. The cavity correlation function y_{ii}^{dd} is calculated based on the Mansoori-Carnahan-Starling-Leland theory, evaluated with weighted densities[60,61], leading to

$$y_{ii}^{dd}(\{\bar{\rho}_i(\mathbf{r})\}) = \frac{1}{1-\bar{\zeta}_3(\mathbf{r})} + \frac{1.5\, d_i \bar{\zeta}_2(\mathbf{r})}{(1-\bar{\zeta}_3(\mathbf{r}))^2} + \frac{0.5\,(d_i \bar{\zeta}_2(\mathbf{r}))^2}{(1-\bar{\zeta}_3(\mathbf{r}))^3} \tag{A.22}$$

with the weighted quantities

$$\bar{\zeta}_2(\mathbf{r}) = \frac{\pi}{6}\sum_{i=1}^{N_c} \bar{\rho}_i^{\mathrm{hc}}(\mathbf{r}) m_i d_i^2 \tag{A.23a}$$

$$\bar{\zeta}_3(\mathbf{r}) = \frac{\pi}{6}\sum_{i=1}^{N_c} \bar{\rho}_i^{\mathrm{hc}}(\mathbf{r}) m_i d_i^3 \tag{A.23b}$$

The functional derivative of the hard-chain contribution, eq. (A.19), is calculated as

$$\begin{aligned}
\frac{\delta \beta F^{\mathrm{hc}}[\{\rho_i\}]}{\delta \rho_j(\mathbf{r})} = &\sum_{i=1}^{N_c}(m_i - 1)\int \frac{\delta \rho_i(\mathbf{r}')}{\delta \rho_j(\mathbf{r})} \ln(\rho_i(\mathbf{r}'))\,\mathrm{d}\mathbf{r}' \\
&- \sum_{i=1}^{N_c}(m_i - 1)\int \frac{\delta \rho_i(\mathbf{r}')}{\delta \rho_j(\mathbf{r})}\Big(\ln\big(y_{ii}^{dd}(\{\bar{\rho}_i^{\mathrm{hc}}(\mathbf{r}')\})\lambda_i^{\mathrm{hc}}(\mathbf{r}')\big) - 1\Big)\,\mathrm{d}\mathbf{r}' \\
&- \sum_{i=1}^{N_c}(m_i - 1)\int \frac{\rho_i(\mathbf{r}')}{y_{ii}^{dd}(\{\bar{\rho}_i^{\mathrm{hc}}(\mathbf{r}')\})} \sum_{k=1}^{N_c} \frac{\partial y_{ii}^{dd}(\{\bar{\rho}_i^{\mathrm{hc}}(\mathbf{r}')\})}{\partial \bar{\rho}_k^{\mathrm{hc}}(\mathbf{r}')} \frac{\delta \bar{\rho}_k^{\mathrm{hc}}(\mathbf{r}')}{\delta \rho_j(\mathbf{r})}\,\mathrm{d}\mathbf{r}' \\
&- \sum_{i=1}^{N_c}(m_i - 1)\int \frac{\rho_i(\mathbf{r}')}{\lambda_i^{\mathrm{hc}}(\mathbf{r}')} \frac{\delta \lambda_i^{\mathrm{hc}}(\mathbf{r}')}{\delta \rho_j(\mathbf{r})}\,\mathrm{d}\mathbf{r}'
\end{aligned} \tag{A.24}$$

The occurring functional derivatives of the weighted densities, eqs. (A.20) and (A.21), are computed as follows: because both weight functions $\omega_i^{\mathrm{hc},\rho}$ and $\omega_i^{\mathrm{hc},\lambda}$ are even functions, the functional derivatives simplify to

$$\begin{aligned}
\frac{\delta \bar{\rho}_k^{\mathrm{hc}}(\mathbf{r}')}{\delta \rho_j(\mathbf{r})} &= \int \frac{\delta \rho_k(\mathbf{r}'')}{\delta \rho_j(\mathbf{r})} \omega_k^{\mathrm{hc},\rho}(\mathbf{r}' - \mathbf{r}'')\,\mathrm{d}\mathbf{r}'' = \int \delta_{jk}\delta(\mathbf{r}'' - \mathbf{r})\omega_k^{\mathrm{hc},\rho}(\mathbf{r}' - \mathbf{r}'')\,\mathrm{d}\mathbf{r}'' \\
&= \delta_{jk}\omega_k^{\mathrm{hc},\rho}(\mathbf{r}' - \mathbf{r}) = \delta_{jk}\omega_k^{\mathrm{hc},\rho}(\mathbf{r} - \mathbf{r}')
\end{aligned} \tag{A.25}$$

$$\begin{aligned}
\frac{\delta \lambda_i^{\mathrm{hc}}(\mathbf{r}')}{\delta \rho_j(\mathbf{r})} &= \int \frac{\delta \rho_i(\mathbf{r}'')}{\delta \rho_j(\mathbf{r})} \omega_i^{\mathrm{hc},\lambda}(\mathbf{r}' - \mathbf{r}'')\,\mathrm{d}\mathbf{r}'' = \int \delta_{ij}\delta(\mathbf{r}'' - \mathbf{r})\omega_i^{\mathrm{hc},\lambda}(\mathbf{r}' - \mathbf{r}'')\,\mathrm{d}\mathbf{r}'' \\
&= \delta_{ij}\omega_i^{\mathrm{hc},\lambda}(\mathbf{r}' - \mathbf{r}) = \delta_{ij}\omega_i^{\mathrm{hc},\lambda}(\mathbf{r} - \mathbf{r}')
\end{aligned} \tag{A.26}$$

Substitution of eq. (A.7) in eq. (A.24) leads to the following simplification

$$\begin{aligned}\frac{\delta\beta F^{\mathrm{hc}}[\{\rho_i\}]}{\delta\rho_j(\mathbf{r})} &= (m_j-1)\ln(\rho_j(\mathbf{r}))-(m_j-1)\left(\ln\left(y_{jj}^{dd}(\{\bar{\rho}_i^{\mathrm{hc}}(\mathbf{r})\})\lambda_j^{\mathrm{hc}}(\mathbf{r})\right)-1\right)\\ &\quad-\sum_{i=1}^{N_c}(m_i-1)\int\frac{\rho_i(\mathbf{r}')}{y_{ii}^{dd}(\{\bar{\rho}_i^{\mathrm{hc}}(\mathbf{r}')\})}\frac{\partial y_{ii}^{dd}(\{\bar{\rho}_i^{\mathrm{hc}}(\mathbf{r}')\})}{\partial\bar{\rho}_j^{\mathrm{hc}}(\mathbf{r}')}\omega_j^{\mathrm{hc},\rho}(\mathbf{r}-\mathbf{r}')\,\mathrm{d}\mathbf{r}'\\ &\quad-(m_j-1)\int\frac{\rho_j(\mathbf{r}')}{\lambda_j^{\mathrm{hc}}(\mathbf{r}')}\omega_j^{\mathrm{hc},\lambda}(\mathbf{r}-\mathbf{r}')\,\mathrm{d}\mathbf{r}'\end{aligned}\tag{A.27}$$

which can be rewritten using the standard notation for convolution integrals, as

$$\begin{aligned}\frac{\delta\beta F^{\mathrm{hc}}[\{\rho_i\}]}{\delta\rho_j(\mathbf{r})} &= (m_j-1)\ln(\rho_j(\mathbf{r}))-(m_j-1)\left(\ln\left(y_{jj}^{dd}(\{\bar{\rho}_i^{\mathrm{hc}}(\mathbf{r})\})\lambda_j^{\mathrm{hc}}(\mathbf{r})\right)-1\right)\\ &\quad-\sum_{i=1}^{N_c}(m_i-1)\left(\frac{\rho_i(\mathbf{r})}{y_{ii}^{dd}(\{\bar{\rho}_i^{\mathrm{hc}}(\mathbf{r})\})}\frac{\partial y_{ii}^{dd}(\{\bar{\rho}_i^{\mathrm{hc}}(\mathbf{r})\})}{\partial\bar{\rho}_j^{\mathrm{hc}}(\mathbf{r})}\right)\otimes\omega_j^{\mathrm{hc},\rho}(\mathbf{r})\\ &\quad-(m_j-1)\left(\frac{\rho_j(\mathbf{r})}{\lambda_j^{\mathrm{hc}}(\mathbf{r})}\right)\otimes\omega_j^{\mathrm{hc},\lambda}(\mathbf{r})\end{aligned}\tag{A.28}$$

with the partial derivative of the cavity correlation function y_{ii}^{dd} obtained from

$$\begin{aligned}\frac{\partial y_{ii}^{dd}(\{\bar{\rho}_i^{\mathrm{hc}}(\mathbf{r})\})}{\partial\bar{\rho}_j^{\mathrm{hc}}(\mathbf{r})} &= \left(\frac{1.5\,d_i}{(1-\bar{\zeta}_3(\mathbf{r}))^2}+\frac{d_i^2\bar{\zeta}_2(\mathbf{r})}{(1-\bar{\zeta}_3(\mathbf{r}))^3}\right)\frac{\pi}{6}m_j d_j^2\\ &\quad+\left(\frac{1}{(1-\bar{\zeta}_3(\mathbf{r}))^2}+\frac{3\,d_i\bar{\zeta}_2(\mathbf{r})}{(1-\bar{\zeta}_3(\mathbf{r}))^3}+\frac{1.5(d_i\bar{\zeta}_2(\mathbf{r}))^2}{(1-\bar{\zeta}_3(\mathbf{r}))^4}\right)\frac{\pi}{6}m_j d_j^3\end{aligned}\tag{A.29}$$

A.2.4 Dispersive Contribution

The dispersive contribution is obtained via the approach proposed by Sauer and Gross[46] which utilizes the PC-SAFT equation of state[30]. In contrast to previously proposed dispersion functionals[41–43], the functional of Sauer and Gross[46] is formulated as a weighted density approximation

$$\beta F^{\mathrm{disp}}[\{\rho_i(\mathbf{r})\}] = \int\bar{\rho}^{\mathrm{disp}}(\mathbf{r})\tilde{a}^{\mathrm{disp}}(\{\bar{\rho}_i^{\mathrm{disp}}(\mathbf{r})\})\,\mathrm{d}\mathbf{r}\tag{A.30}$$

with the reduced, dispersive Helmholtz energy contribution for a bulk fluid

$$\tilde{a}^{\mathrm{disp}}(\{\bar{\rho}_i^{\mathrm{disp}}(\mathbf{r})\}) = -2\pi\bar{\rho}^{\mathrm{disp}}(\mathbf{r})I_1(\bar{\eta},\bar{m})\overline{m^2\varepsilon\sigma^3}-\pi\bar{\rho}^{\mathrm{disp}}(\mathbf{r})\bar{m}C_1(\bar{\eta},\bar{m})I_2(\bar{\eta},\bar{m})\overline{m^2\varepsilon^2\sigma^3}\tag{A.31}$$

with

$$\overline{m^2\varepsilon^{(n)}\sigma^3} = \sum_{k=1}^{N_c}\sum_{l=1}^{N_c} \bar{x}_k(\mathbf{r})\bar{x}_l(\mathbf{r}) m_k m_l \left(\beta\varepsilon_{kl}\right)^{(n)} \sigma_{kl}^3 \tag{A.32}$$

obtained from the PC-SAFT equation of state[30] with the combining rules for unlike segments, obtained from

$$\sigma_{ij} = \frac{\sigma_i + \sigma_j}{2} \tag{A.33a}$$

$$\varepsilon_{ij} = \sqrt{\varepsilon_i \varepsilon_j}(1 - k_{ij}) \tag{A.33b}$$

with the binary interaction parameter k_{ij}, and using the and the weighted density for the dispersion contribution defined as

$$\begin{aligned}\bar{\rho}_i^{\mathrm{disp}}(\mathbf{r}) &= \frac{3}{4\pi\psi^3 d_i^3}\int \rho_i(\mathbf{r}')\Theta\left(\psi d_i - |\mathbf{r}-\mathbf{r}'|\right)\mathrm{d}\mathbf{r}' \\ &\equiv \int \rho_i(\mathbf{r}')\omega_i^{\mathrm{disp}}(\mathbf{r}-\mathbf{r}')\,\mathrm{d}\mathbf{r}' = \rho_i(\mathbf{r}) \otimes \omega_i^{\mathrm{disp}}(\mathbf{r})\end{aligned} \tag{A.34}$$

with $\psi = 1.3862$ as the size parameter for the influence region of the weight function $\omega_i^{\mathrm{disp}}(\mathbf{r}) = \frac{3}{4\pi\psi^3 d_i^3}\Theta(\psi d_i - |\mathbf{r}|)$[46]. The absolute weighted density profile is computed as the sum of all partial weighted densities

$$\bar{\rho}^{\mathrm{disp}}(\mathbf{r}) = \sum_{i=1}^{N_c} \bar{\rho}_i^{\mathrm{disp}}(\mathbf{r}) = \sum_{i=1}^{N_c} \bar{x}_i(\mathbf{r})\bar{\rho}^{\mathrm{disp}}(\mathbf{r}) \tag{A.35}$$

from which one can calculate the mole fraction profile $\bar{x}_i$, the distributed weighted chain length $\bar{m}$, the weighted packing fraction profile $\bar{\eta}$

$$\bar{x}_i(\mathbf{r}) = \frac{\bar{\rho}_i^{\mathrm{disp}}(\mathbf{r})}{\bar{\rho}^{\mathrm{disp}}(\mathbf{r})} \tag{A.36}$$

$$\bar{m}(\mathbf{r}) = \sum_{i=1}^{N_c} \bar{x}_i(\mathbf{r}) m_i \tag{A.37}$$

$$\bar{\eta}(\mathbf{r}) = \frac{\pi}{6}\sum_{i=1}^{N_c} \bar{\rho}_i^{\mathrm{disp}}(\mathbf{r}) m_i d_i^3 \tag{A.38}$$

The power series representation of the correlation integrals are defined as

$$I_1(\bar{\eta},\bar{m}) = \sum_{n=0}^{6} a_n(\bar{m})\bar{\eta}^n \tag{A.39}$$

$$I_2(\bar{\eta},\bar{m}) = \sum_{n=0}^{6} b_n(\bar{m})\bar{\eta}^n \tag{A.40}$$

$$a_n(\bar{m}) = a_{0n} + \frac{\bar{m}-1}{\bar{m}}a_{1n} + \frac{\bar{m}-1}{\bar{m}}\frac{\bar{m}-2}{\bar{m}}a_{2n} \tag{A.41}$$

$$b_n(\bar{m}) = b_{0n} + \frac{\bar{m}-1}{\bar{m}}b_{1n} + \frac{\bar{m}-1}{\bar{m}}\frac{\bar{m}-2}{\bar{m}}b_{2n} \tag{A.42}$$

with model constants a_{0n}, a_{1n}, a_{2n} and b_{0n}, b_{1n}, b_{2n} from Gross and Sadowski[30], as well as the compressibility of the hard-chain reference fluid

$$C_1(\bar{\eta},\bar{m}) = \left(1 + \bar{m}\frac{8\bar{\eta}-2\bar{\eta}^2}{(1-\bar{\eta})^4} + (1-\bar{m})\frac{20\bar{\eta}-27\bar{\eta}^2+12\bar{\eta}^3-2\bar{\eta}^4}{[(1-\bar{\eta})(2-\bar{\eta})]^2}\right)^{-1} \tag{A.43}$$

obtained from PC-SAFT[30].

The functional derivative of eq. (A.30) can be written in terms of the convolution of the residual chemical potential $\beta\mu_j^{\mathrm{disp}}$ with the weigh function ω_j^{disp} as

$$\begin{aligned}\frac{\delta\beta F^{\mathrm{disp}}[\{\rho_i\}]}{\delta\rho_j(\mathbf{r})} &= \int \sum_{i=1}^{N_c} \frac{\delta\left(\bar{\rho}^{\mathrm{disp}}(\mathbf{r}')\tilde{a}^{\mathrm{disp}}(\{\bar{\rho}_i^{\mathrm{disp}}(\mathbf{r}')\})\right)}{\delta\bar{\rho}_i^{\mathrm{disp}}(\mathbf{r}')}\frac{\delta\bar{\rho}_i^{\mathrm{disp}}(\mathbf{r}')}{\delta\rho_j(\mathbf{r})}\,\mathrm{d}\mathbf{r}' \\ &= \int \sum_{i=1}^{N_c} \frac{\partial\left(\bar{\rho}^{\mathrm{disp}}(\mathbf{r}')\tilde{a}^{\mathrm{disp}}(\{\bar{\rho}_i^{\mathrm{disp}}(\mathbf{r}')\})\right)}{\partial\bar{\rho}_i^{\mathrm{disp}}(\mathbf{r}')}\delta_{ij}\omega_i^{\mathrm{disp}}(\mathbf{r}-\mathbf{r}')\,\mathrm{d}\mathbf{r}' \\ &= \beta\mu_j^{\mathrm{disp}}(\{\bar{\rho}_i^{\mathrm{disp}}(\mathbf{r})\}) \otimes \omega_j^{\mathrm{disp}}(\mathbf{r})\end{aligned} \tag{A.44}$$

utilizing eq. (A.7), as well as the functional derivative of the weighted densities

$$\begin{aligned}\frac{\delta\bar{\rho}_i^{\mathrm{disp}}(\mathbf{r}')}{\delta\rho_j(\mathbf{r})} &= \frac{\delta}{\delta\rho_j(\mathbf{r})}\int \rho_i(\mathbf{r}'')\omega_i^{\mathrm{disp}}(\mathbf{r}'-\mathbf{r}'')\,\mathrm{d}\mathbf{r}'' = \int \delta_{ij}\delta(\mathbf{r}''-\mathbf{r})\omega_i^{\mathrm{disp}}(\mathbf{r}'-\mathbf{r}'')\,\mathrm{d}\mathbf{r}'' \\ &= \delta_{ij}\omega_i^{\mathrm{disp}}(\mathbf{r}'-\mathbf{r}) = \delta_{ij}\omega_i^{\mathrm{disp}}(\mathbf{r}-\mathbf{r}')\end{aligned} \tag{A.45}$$

For brief notation, we termed the partial derivative $\frac{\partial\left(\bar{\rho}^{\mathrm{disp}}(\mathbf{r})\tilde{a}^{\mathrm{disp}}(\{\bar{\rho}_i^{\mathrm{disp}}(\mathbf{r})\})\right)}{\partial\bar{\rho}_i^{\mathrm{disp}}(\mathbf{r})}$ as the chemical potential $\beta\mu_i^{\mathrm{disp}}(\{\bar{\rho}_i^{\mathrm{disp}}(\mathbf{r})\})$, which is calculated as follows

$$\begin{aligned}\beta\mu_j^{\mathrm{disp}}(\{\bar{\rho}_i^{\mathrm{disp}}(\mathbf{r})\}) &= \frac{\partial\left(\bar{\rho}^{\mathrm{disp}}(\mathbf{r})\tilde{a}^{\mathrm{disp}}(\{\bar{\rho}_i^{\mathrm{disp}}(\mathbf{r})\})\right)}{\partial\bar{\rho}_j^{\mathrm{disp}}(\mathbf{r})}\\ &= -\pi\sum_{k=1}^{N_c}\sum_{l=1}^{N_c}\left(2\frac{\partial I_1}{\partial\bar{\rho}_j^{\mathrm{disp}}}+\left(\frac{\partial\bar{m}}{\partial\bar{\rho}_j^{\mathrm{disp}}}C_1I_2+\bar{m}\frac{\partial C_1}{\partial\bar{\rho}_j^{\mathrm{disp}}}I_2+\bar{m}C_1\frac{\partial I_2}{\partial\bar{\rho}_j^{\mathrm{disp}}}\right)\beta\varepsilon_{kl}\right)\\ &\qquad\times\left(\bar{\rho}_k^{\mathrm{disp}}(\mathbf{r})\bar{\rho}_l^{\mathrm{disp}}(\mathbf{r})m_km_l\beta\varepsilon_{kl}\sigma_{kl}^3\right)\\ &\quad-2\pi\sum_{k=1}^{N_c}\left(\left(2I_1+\bar{m}C_1I_2\beta\varepsilon_{jk}\right)\bar{\rho}_k^{\mathrm{disp}}(\mathbf{r})m_jm_k\beta\varepsilon_{jk}\sigma_{jk}^3\right)\end{aligned}\tag{A.46}$$

with the derivatives

$$\frac{\partial\bar{\eta}}{\partial\bar{\rho}_j^{\mathrm{disp}}}=\frac{\pi}{6}m_jd_j^3\tag{A.47}$$

$$\frac{\partial\bar{m}}{\partial\bar{\rho}_j^{\mathrm{disp}}}(\mathbf{r})=\frac{m_j-\bar{m}(\mathbf{r})}{\bar{\rho}^{\mathrm{disp}}(\mathbf{r})}\tag{A.48}$$

$$\frac{\partial I_1}{\partial\bar{\rho}_j^{\mathrm{disp}}}=\frac{\partial I_1}{\partial\bar{m}}\frac{\partial\bar{m}}{\partial\bar{\rho}_j^{\mathrm{disp}}}+\frac{\partial I_1}{\partial\bar{\eta}}\frac{\partial\bar{\eta}}{\partial\bar{\rho}_j^{\mathrm{disp}}}\tag{A.49}$$

$$\frac{\partial I_1}{\partial\bar{m}}=\sum_{n=0}^{6}\left(a_{1n}\frac{1}{\bar{m}^2}+a_{2n}\frac{3\bar{m}-4}{\bar{m}^3}\right)\bar{\eta}^n\tag{A.50}$$

$$\frac{\partial I_1}{\partial\bar{\eta}}=\sum_{n=1}^{6}a_n(\bar{m})\,n\,\bar{\eta}^{n-1}\tag{A.51}$$

$$\frac{\partial I_2}{\partial\bar{\rho}_j^{\mathrm{disp}}}=\frac{\partial I_2}{\partial\bar{m}}\frac{\partial\bar{m}}{\partial\bar{\rho}_j^{\mathrm{disp}}}+\frac{\partial I_2}{\partial\bar{\eta}}\frac{\partial\bar{\eta}}{\partial\bar{\rho}_j^{\mathrm{disp}}}\tag{A.52}$$

$$\frac{\partial I_2}{\partial \bar{m}} = \sum_{n=0}^{6} \left(b_{1n} \frac{1}{\bar{m}^2} + b_{2n} \frac{3\bar{m}-4}{\bar{m}^3} \right) \bar{\eta}^n \tag{A.53}$$

$$\frac{\partial I_2}{\partial \bar{\eta}} = \sum_{n=1}^{6} b_n(\bar{m})\, n\, \bar{\eta}^{n-1} \tag{A.54}$$

$$\frac{\partial C_1}{\partial \bar{\rho}_j^{\text{disp}}} = \frac{\partial C_1}{\partial \bar{m}} \frac{\partial \bar{m}}{\partial \bar{\rho}_j^{\text{disp}}} + \frac{\partial C_1}{\partial \bar{\eta}} \frac{\partial \bar{\eta}}{\partial \bar{\rho}_j^{\text{disp}}} \tag{A.55}$$

$$\frac{\partial C_1}{\partial \bar{m}} = -C_1(\bar{m},\bar{\eta})^2 \left(\frac{8\bar{\eta}-2\bar{\eta}^2}{(1-\bar{\eta})^4} - \frac{20\bar{\eta}-27\bar{\eta}^2+12\bar{\eta}^3-2\bar{\eta}^4}{[(1-\bar{\eta})(2-\bar{\eta})]^2} \right) \tag{A.56}$$

$$\frac{\partial C_1}{\partial \bar{\eta}} = -C_1(\bar{m},\bar{\eta})^2 \left(\bar{m} \frac{8+20\bar{\eta}-4\bar{\eta}^2}{(1-\bar{\eta})^5} + (1-\bar{m}) \frac{40-48\bar{\eta}+12\bar{\eta}^2+2\bar{\eta}^3}{[(1-\bar{\eta})(2-\bar{\eta})]^3} \right) \tag{A.57}$$

A.3 Fourier Space Convolutions

The PC-SAFT functionals and functional derivatives can be calculated efficiently in Fourier space, by making use of the convolution theorem of the Fourier transform. In this section, we show how to compute the required Fourier transforms in various coordinate systems using off-the-shelf FFT, fast Hankel, fast sine/cosine transform algorithms.

We show the procedure by considering weighted densities as convolutions of density ρ_i with weight function ω_i. One transforms the density profile ρ_i to Fourier space using a discrete transform scheme and, after multiplication in Fourier space with the analytically transformed weight function, transforms the result back to real space using the inverse discrete transform scheme according to

$$\begin{aligned} \bar{\rho}_i(\mathbf{r}) &= \int \rho_i(\mathbf{r}')\omega_i(\mathbf{r}-\mathbf{r}')\,\mathrm{d}\mathbf{r}' = \rho_i(\mathbf{r}) \otimes \omega_i(\mathbf{r}) \\ &= \mathcal{F}^{-1}\left[\mathcal{F}\left[\rho_i(\mathbf{r})\right]\mathcal{F}\left[\omega_i(\mathbf{r})\right]\right] = \mathcal{F}^{-1}\left[\hat{\rho}_i(\mathbf{k})\hat{\omega}_i(\mathbf{k})\right] \end{aligned} \tag{A.58}$$

with the Fourier space vector $\mathbf{k}$, and introducing the Fourier transform $\mathcal{F}$ and inverse Fourier

transform operator $\mathcal{F}^{-1}$. The circumflex ($\hat{}$) above quantities indicates them being the Fourier transforms of the respective quantity. The analytically transformed weight functions for FMT, eq. (A.59), hard-chain contribution, eq. (A.60) and dispersion contribution, eq. (A.61) are calculated as

$$\hat{\omega}_i^0(\mathbf{k}) = \mathrm{j}_0(2\pi R_i|\mathbf{k}|) \tag{A.59a}$$
$$\hat{\omega}_i^1(\mathbf{k}) = R_i \mathrm{j}_0(2\pi R_i|\mathbf{k}|) \tag{A.59b}$$
$$\hat{\omega}_i^2(\mathbf{k}) = 4\pi R_i^2 \mathrm{j}_0(2\pi R_i|\mathbf{k}|) \tag{A.59c}$$
$$\hat{\omega}_i^3(\mathbf{k}) = \frac{4}{3}\pi R_i^3 \big(\mathrm{j}_0(2\pi R_i|\mathbf{k}|) + \mathrm{j}_2(2\pi R_i|\mathbf{k}|)\big) \tag{A.59d}$$
$$\hat{\omega}_i^{\mathrm{V1}}(\mathbf{k}) = \frac{-\mathrm{i}\,\mathbf{k}}{2R_i}\hat{\omega}_i^3(\mathbf{k}) \tag{A.59e}$$
$$\hat{\omega}_i^{\mathrm{V2}}(\mathbf{k}) = -\mathrm{i}\,2\pi\mathbf{k}\hat{\omega}_i^3(\mathbf{k}) \tag{A.59f}$$

$$\hat{\omega}_i^{\mathrm{hc},\rho}(\mathbf{k}) = \mathrm{j}_0(4\pi R_i|\mathbf{k}|) + \mathrm{j}_2(4\pi R_i|\mathbf{k}|) \tag{A.60a}$$
$$\hat{\omega}_i^{\mathrm{hc},\lambda}(\mathbf{k}) = \mathrm{j}_0(4\pi R_i|\mathbf{k}|) \tag{A.60b}$$

$$\hat{\omega}_i^{\mathrm{disp}}(\mathbf{k}) = \mathrm{j}_0(4\pi\psi R_i|\mathbf{k}|) + \mathrm{j}_2(4\pi\psi R_i|\mathbf{k}|) \tag{A.61}$$

with the spherical Bessel functions of the first kind of order zero and two, defined by

$$\mathrm{j}_0(\xi) = \frac{\sin(\xi)}{\xi} \tag{A.62a}$$
$$\mathrm{j}_2(\xi) = \left(\frac{3}{\xi^2} - 1\right)\frac{\sin(\xi)}{\xi} - \frac{3\cos(\xi)}{\xi^2} \tag{A.62b}$$

In comparison to the sine and cosine representation of the Fourier transformed weight functions used in appendix B.1, eqs. (B.1)–(B.3), a description exploiting spherical Bessel functions allows writing shorter and safer code. Additionally, the limits for $\mathbf{k} \to 0$, eqs. (B.4)–(B.6), do not have to be considered explicitly, because spherical Bessel functions have well defined limits: $\mathrm{j}_0(0) = 1$ and $\mathrm{j}_2(0) = 0$.

A.3.1 Convolution in Cartesian Coordinates

For Cartesian coordinates we substitute $\mathbf{r} = [x, y, z]^\intercal$ and $\mathbf{k} = [k_x, k_y, k_z]^\intercal$. The Fourier transform of the density profiles is computed as

$$\hat{\rho}_i(k_x, k_y, k_z) = \mathcal{F}_x \mathcal{F}_y \mathcal{F}_z \left[\rho_i(x, y, z)\right] \tag{A.63}$$

just as presented in appendix B.2, eq. (B.11).

A.3.1.1 Hard-Sphere Contribution – Fundamental Measure Theory Convolutions in Cartesian Coordinates

For computation of the scalar-valued ($\alpha \in \{0, 1, 2, 3\}$) weighted densities

$$n_\alpha(x, y, z) = \sum_{i=1}^{N_c} m_i \mathcal{F}_x^{-1} \mathcal{F}_y^{-1} \mathcal{F}_z^{-1} \left[\hat{\rho}_i(k_x, k_y, k_z) \hat{\omega}_i^\alpha(k_x, k_y, k_z)\right] \tag{A.64}$$

the inverse Fourier transform for scalar functions, eq. (B.12), is needed. For the vector-valued ($\alpha \in \{\mathrm{V1}, \mathrm{V2}\}$) weighted densities we use the vector-valued weight functions, $\hat{\omega}_i^{\mathrm{V1}}(\mathbf{k}) = \frac{-\mathrm{i}}{2R_i} \mathbf{k} \hat{\omega}_i^3(\mathbf{k})$ and $\hat{\omega}_i^{\mathrm{V2}}(\mathbf{k}) = -\mathrm{i}\, 2\pi \mathbf{k} \hat{\omega}_i^3(\mathbf{k})$. The inverse Fourier transform is obtained as

$$\mathbf{n}_{\mathrm{V1}}(x, y, z) = \sum_{i=1}^{N_c} \frac{m_i}{2R_i} \mathcal{F}^{-1} \left[-\mathrm{i}\, \hat{\rho}_i(\mathbf{k}) \mathbf{k} \hat{\omega}_i^3(\mathbf{k})\right] \tag{A.65a}$$

$$\mathbf{n}_{\mathrm{V2}}(x, y, z) = \sum_{i=1}^{N_c} 2\pi m_i \mathcal{F}^{-1} \left[-\mathrm{i}\, \hat{\rho}_i(\mathbf{k}) \mathbf{k} \hat{\omega}_i^3(\mathbf{k})\right] \tag{A.65b}$$

with

$$\mathcal{F}^{-1} \left[-\mathrm{i}\, \hat{\rho}_i(\mathbf{k}) \mathbf{k} \hat{\omega}_i^3(\mathbf{k})\right] = \begin{pmatrix} \mathcal{F}_x^{-1} \mathcal{F}_y^{-1} \mathcal{F}_z^{-1} \left[-\mathrm{i}\, \hat{\rho}_i(k_x, k_y, k_z)\, k_x\, \hat{\omega}_i^3(k_x, k_y, k_z)\right] \\ \mathcal{F}_x^{-1} \mathcal{F}_y^{-1} \mathcal{F}_z^{-1} \left[-\mathrm{i}\, \hat{\rho}_i(k_x, k_y, k_z)\, k_y\, \hat{\omega}_i^3(k_x, k_y, k_z)\right] \\ \mathcal{F}_x^{-1} \mathcal{F}_y^{-1} \mathcal{F}_z^{-1} \left[-\mathrm{i}\, \hat{\rho}_i(k_x, k_y, k_z)\, k_z\, \hat{\omega}_i^3(k_x, k_y, k_z)\right] \end{pmatrix} \tag{A.66}$$

using the inverse Fourier transform for vector-valued functions from eq. (B.19). The convolution integrals of the White-Bear Helmholtz energy density derivatives $\frac{\partial \Phi}{\partial n_\alpha}$ with the weight functions ω_i^α are computed similarly.

The scalar-valued convolution integrals in eq. (A.15) are obtained using the scalar inverse

Fourier transform from eq. (B.12), leading to

$$\frac{\partial \Phi}{\partial n_\alpha} \otimes \omega_i^\alpha = \mathcal{F}_x^{-1}\mathcal{F}_y^{-1}\mathcal{F}_z^{-1}\left[\frac{\hat{\partial \Phi}}{\partial n_\alpha}(k_x,k_y,k_z)\hat{\omega}_i^\alpha(k_x,k_y,k_z)\right] \tag{A.67}$$

with the scalar Fourier transform of the partial derivative of the Helmholtz energy density, eq. (B.11), computed according to

$$\frac{\hat{\partial \Phi}}{\partial n_\alpha}(k_x,k_y,k_z) = \mathcal{F}_x\mathcal{F}_y\mathcal{F}_z\left[\frac{\partial \Phi}{\partial n_\alpha}(x,y,z)\right] \tag{A.68}$$

The vector-valued convolution integrals in eq. (A.15) can be handled using the inverse Fourier transform of scalar-valued functions, eq. (B.12), leading to

$$\frac{\partial \Phi}{\partial \mathbf{n}_\alpha} \otimes \omega_i^\alpha = \mathcal{F}_x^{-1}\mathcal{F}_y^{-1}\mathcal{F}_z^{-1}\left[\frac{\hat{\partial \Phi}}{\partial \mathbf{n}_\alpha}\Big|_{k_x}\hat{\omega}_i^\alpha|_{k_x} + \frac{\hat{\partial \Phi}}{\partial \mathbf{n}_\alpha}\Big|_{k_y}\hat{\omega}_i^\alpha|_{k_y} + \frac{\hat{\partial \Phi}}{\partial \mathbf{n}_\alpha}\Big|_{k_z}\hat{\omega}_i^\alpha|_{k_z}\right] \tag{A.69}$$

where the dot product in Fourier space is used according to

$$\frac{\hat{\partial \Phi}}{\partial \mathbf{n}_\alpha}\cdot\hat{\omega}_i^\alpha = \begin{pmatrix} \frac{\hat{\partial \Phi}}{\partial \mathbf{n}_\alpha}\big|_{k_x} \\ \frac{\hat{\partial \Phi}}{\partial \mathbf{n}_\alpha}\big|_{k_y} \\ \frac{\hat{\partial \Phi}}{\partial \mathbf{n}_\alpha}\big|_{k_z} \end{pmatrix} \cdot \begin{pmatrix} \hat{\omega}_i^\alpha|_{k_x} \\ \hat{\omega}_i^\alpha|_{k_y} \\ \hat{\omega}_i^\alpha|_{k_z} \end{pmatrix} = \frac{\hat{\partial \Phi}}{\partial \mathbf{n}_\alpha}\Big|_{k_x}\hat{\omega}_i^\alpha|_{k_x} + \frac{\hat{\partial \Phi}}{\partial \mathbf{n}_\alpha}\Big|_{k_y}\hat{\omega}_i^\alpha|_{k_y} + \frac{\hat{\partial \Phi}}{\partial \mathbf{n}_\alpha}\Big|_{k_z}\hat{\omega}_i^\alpha|_{k_z} \tag{A.70}$$

whereby the vector-valued weight functions, eqs. (A.59e) and (A.59f), in Fourier space in each direction are defined as

$$\hat{\omega}_i^{\mathrm{V1}}|_{k_x}(k_x,k_y,k_z) = \frac{-\mathrm{i}}{2R_i}k_x\hat{\omega}_i^3(k_x,k_y,k_z) \tag{A.71a}$$

$$\hat{\omega}_i^{\mathrm{V1}}|_{k_y}(k_x,k_y,k_z) = \frac{-\mathrm{i}}{2R_i}k_y\hat{\omega}_i^3(k_x,k_y,k_z) \tag{A.71b}$$

$$\hat{\omega}_i^{\mathrm{V1}}|_{k_z}(k_x,k_y,k_z) = \frac{-\mathrm{i}}{2R_i}k_z\hat{\omega}_i^3(k_x,k_y,k_z) \tag{A.71c}$$

$$\hat{\omega}_i^{\mathrm{V2}}|_{k_x}(k_x,k_y,k_z) = -\mathrm{i}\,2\pi k_x\hat{\omega}_i^3(k_x,k_y,k_z) \tag{A.72a}$$

$$\hat{\omega}_i^{\mathrm{V2}}|_{k_y}(k_x,k_y,k_z) = -\mathrm{i}\,2\pi k_y\hat{\omega}_i^3(k_x,k_y,k_z) \tag{A.72b}$$

$$\hat{\omega}_i^{\mathrm{V2}}|_{k_z}(k_x,k_y,k_z) = -\mathrm{i}\,2\pi k_z\hat{\omega}_i^3(k_x,k_y,k_z) \tag{A.72c}$$

The vector-valued Fourier transform, eq. (B.16), of the vector-valued derivatives of the reduced

Helmholtz energy yields

$$\frac{\partial \hat{\Phi}}{\partial \mathbf{n}_\alpha}(k_x,k_y,k_z) = \begin{pmatrix} \mathcal{F}_x\mathcal{F}_y\mathcal{F}_z\left[\frac{\partial\Phi}{\partial \mathbf{n}_\alpha}\Big|_x(x,y,z)\right] \\ \mathcal{F}_x\mathcal{F}_y\mathcal{F}_z\left[\frac{\partial\Phi}{\partial \mathbf{n}_\alpha}\Big|_y(x,y,z)\right] \\ \mathcal{F}_x\mathcal{F}_y\mathcal{F}_z\left[\frac{\partial\Phi}{\partial \mathbf{n}_\alpha}\Big|_z(x,y,z)\right] \end{pmatrix} \tag{A.73}$$

A.3.1.2 Hard-Chain Contribution Convolutions in Cartesian Coordinates

For the hard-chain contribution the two weighted densities $\bar{\rho}_i^{\mathrm{hc}}$ and λ_i^{hc} are calculated with the scalar Fourier transform according to

$$\bar{\rho}_i^{\mathrm{hc}}(x,y,z) = \rho_i(x,y,z) \otimes \omega_i^{\mathrm{hc},\rho}(x,y,z) = \mathcal{F}_x^{-1}\mathcal{F}_y^{-1}\mathcal{F}_z^{-1}\left[\hat{\rho}_i(k_x,k_y,k_z)\hat{\omega}_i^{\mathrm{hc},\rho}(k_x,k_y,k_z)\right] \tag{A.74}$$

$$\lambda^{\mathrm{hc}}(x,y,z) = \rho_i(x,y,z) \otimes \omega_i^{\mathrm{hc},\lambda}(x,y,z) = \mathcal{F}_x^{-1}\mathcal{F}_y^{-1}\mathcal{F}_z^{-1}\left[\hat{\rho}_i(k_x,k_y,k_z)\hat{\omega}_i^{\mathrm{hc},\lambda}(k_x,k_y,k_z)\right] \tag{A.75}$$

In similar fashion, the other two convolutions from eq. (A.28) are obtained from

$$\begin{aligned} &\int \frac{\rho_i(\mathbf{r}')}{y_{ii}^{dd}(\{\bar{\rho}_i(\mathbf{r}')\})} \frac{\partial y_{ii}^{dd}(\{\bar{\rho}_i(\mathbf{r}')\})}{\partial \bar{\rho}_j(\mathbf{r}')} \omega_j^{\mathrm{hc},\rho}(\mathbf{r}-\mathbf{r}')\,\mathrm{d}\mathbf{r}' \\ &\qquad = \mathcal{F}_x^{-1}\mathcal{F}_y^{-1}\mathcal{F}_z^{-1}\left[\mathcal{F}_x\mathcal{F}_y\mathcal{F}_z\left[\frac{\rho_i(x,y,z)}{y_{ii}^{dd}(\{\bar{\rho}_i\})}\frac{\partial y_{ii}^{dd}(\{\bar{\rho}_j\})}{\partial \bar{\rho}_j}\right]\hat{\omega}_j^{\mathrm{hc},\rho}(k_x,k_y,k_z)\right] \end{aligned} \tag{A.76}$$

$$\int \frac{\rho_j(\mathbf{r}')}{\lambda_j^{\mathrm{hc}}(\mathbf{r}')}\omega_j^{\mathrm{hc},\lambda}(\mathbf{r}-\mathbf{r}')\,\mathrm{d}\mathbf{r}' = \mathcal{F}_x^{-1}\mathcal{F}_y^{-1}\mathcal{F}_z^{-1}\left[\mathcal{F}_x\mathcal{F}_y\mathcal{F}_z\left[\frac{\rho_j(x,y,z)}{\lambda_j^{\mathrm{hc}}(x,y,z)}\right]\hat{\omega}_j^{\mathrm{hc},\lambda}(k_x,k_y,k_z)\right] \tag{A.77}$$

A.3.1.3 Dispersive Contribution Convolutions in Cartesian Coordinates

The dispersion contribution weighted densities $\bar{\rho}_i^{\mathrm{disp}}$ are computed with the scalar Fourier transform, leading to

$$\bar{\rho}_i^{\mathrm{disp}}(x,y,z) = \rho_i(x,y,z) \otimes \omega_i^{\mathrm{disp}}(x,y,z) = \mathcal{F}_x^{-1}\mathcal{F}_y^{-1}\mathcal{F}_z^{-1}\left[\hat{\rho}_i(k_x,k_y,k_z)\hat{\omega}_i^{\mathrm{disp}}(k_x,k_y,k_z)\right] \tag{A.78}$$

The convolution for the functional derivative, eq. (A.44), is obtained in similar fashion according to

$$\mu_j^{\mathrm{disp}}\left(\bar{\rho}^{\mathrm{disp}}(x,y,z)\right) \otimes \omega_j^{\mathrm{disp}}(x,y,z) = \mathcal{F}_x^{-1}\mathcal{F}_y^{-1}\mathcal{F}_z^{-1}\left[\hat{\mu}_j^{\mathrm{disp}}(k_x,k_y,k_z)\hat{\omega}_j^{\mathrm{disp}}(k_x,k_y,k_z)\right] \tag{A.79}$$

with the Fourier transform of the distributed residual chemical potential of the dispersion contribution computed via

$$\hat{\mu}_j^{\mathrm{disp}}\left(\bar{\rho}^{\mathrm{disp}}(x,y,z)\right)(k_x,k_y,k_z) = \mathcal{F}_x\mathcal{F}_y\mathcal{F}_z\left[\mu_j^{\mathrm{disp}}(x,y,z)\right] \tag{A.80}$$

A.3.2 Convolution in Cylindrical Coordinates

We regard problems in cylindrical coordinates with angular symmetry, leading to two-dimensional problems. The presented formalism follows Boţan *et al.* [18], but instead of separating the external potential to obtain vanishing boundary conditions, we separate the density profile directly. The fast Hankel transform algorithm used for computing the Fourier transform requires the function to vanish for large values of the radial coordinate r. That is why we decompose the density profile into a part that approaches zero at large $r = r_{\max}$ and a part that only depends on the axial coordinate according to

$$\rho_i(r,z) = \rho_i^{\Delta}(r,z) + \rho_i^{\infty}(z) \tag{A.81}$$

The contribution that shifts the density profiles is defined at the r-boundary $\rho_i^{\infty}(z) \equiv \rho_i(r = r_{\max}, z)$. The remaining contribution $\rho_i^{\Delta}(r,z)$ is well-behaved for a treatment with the fast Hankel transform.

The Fourier transform of the density profiles is computed according to eq. (B.29) as presented in appendix B.2

$$\hat{\rho}_i(k_r,k_z) = \mathcal{F}_z\mathcal{H}_0\left[\rho_i^{\Delta}(r,z)\right] + \mathcal{F}_z\left[\rho_i^{\infty}(z)\right]\frac{\delta(k_r)}{2\pi k_r} \tag{A.82}$$

with the Hankel transform of order zero $\mathcal{H}_0$. The solely z-dependent contribution ρ_i^{∞} is transformed via a Fourier transform in z-direction, while the analytical Hankel transform in the constant r-direction yields $\frac{\delta(k_r)}{2\pi k_r}$.

A.3.2.1 Fundamental Measure Theory Convolutions in Cylindrical Coordinates

The scalar-valued ($\alpha \in \{0,1,2,3\}$) weighted densities n_α, are calculated using the inverse Fourier transform for scalar functions, eq. (B.30), leading to

$$n_\alpha(r,z) = \sum_{i=1}^{N_c} m_i\left(\mathcal{F}_z^{-1}\mathcal{H}_0^{-1}\left[\hat{\rho}_i^{\Delta}(k_r,k_z)\hat{\omega}_i^{\alpha}(k_r,k_z)\right] + \mathcal{F}_z^{-1}\left[\hat{\rho}^{\infty}(k_z)\hat{\omega}_i^{\alpha}(k_r=0,k_z)\right]\right) \tag{A.83}$$

For the vector-valued ($\alpha \in \{\mathrm{V1}, \mathrm{V2}\}$) weighted densities we use the vector-valued weight functions, $\hat{\omega}_i^{\mathrm{V1}}(\mathbf{k}) = \frac{-\mathrm{i}}{2R_i}\mathbf{k}\hat{\omega}_i^3(\mathbf{k})$ and $\hat{\omega}_i^{\mathrm{V2}}(\mathbf{k}) = -\mathrm{i}\,2\pi\mathbf{k}\hat{\omega}_i^3(\mathbf{k})$. The inverse Fourier transform is obtained as

$$\mathbf{n}_{\mathrm{V1}}(r,z) = \sum_{i=1}^{N_\mathrm{c}} \frac{m_i}{2R_i}\left(\begin{pmatrix} \mathcal{F}_z^{-1}\mathcal{H}_1^{-1}\left[\hat{\rho}_i^{\Delta}(k_r,k_z)\,k_r\,\hat{\omega}_i^3(k_r,k_z)\right] \\ 0 \\ \mathcal{F}_z^{-1}\mathcal{H}_0^{-1}\left[-\mathrm{i}\,\hat{\rho}_i^{\Delta}(k_r,k_z)\,k_z\,\hat{\omega}_i^3(k_r,k_z)\right] \end{pmatrix} + \begin{pmatrix} 0 \\ 0 \\ \mathcal{F}_z^{-1}\left[-\mathrm{i}\,\hat{\rho}_i^{\infty}(k_z)\,k_z\,\hat{\omega}_i^3(k_r=0,k_z)\right] \end{pmatrix}\right) \tag{A.84}$$

$$\mathbf{n}_{\mathrm{V2}}(r,z) = \sum_{i=1}^{N_\mathrm{c}} 2\pi m_i\left(\begin{pmatrix} \mathcal{F}_z^{-1}\mathcal{H}_1^{-1}\left[\hat{\rho}_i^{\Delta}(k_r,k_z)\,k_r\,\hat{\omega}_i^3(k_r,k_z)\right] \\ 0 \\ \mathcal{F}_z^{-1}\mathcal{H}_0^{-1}\left[-\mathrm{i}\,\hat{\rho}_i^{\Delta}(k_r,k_z)\,k_z\,\hat{\omega}_i^3(k_r,k_z)\right] \end{pmatrix} + \begin{pmatrix} 0 \\ 0 \\ \mathcal{F}_z^{-1}\left[-\mathrm{i}\,\hat{\rho}_i^{\infty}(k_z)\,k_z\,\hat{\omega}_i^3(k_r=0,k_z)\right] \end{pmatrix}\right) \tag{A.85}$$

with the Hankel transform of zeroth and first order, $\mathcal{H}_0$ and $\mathcal{H}_1$, respectively. For this result we made use of the inverse Fourier transform for vector-valued functions, eq. (B.45). The convolution integrals of the White-Bear Helmholtz energy density derivatives $\frac{\partial\Phi}{\partial n_\alpha}$ with the weight functions ω_i^α are computed similarly. The partial derivatives $\frac{\partial\Phi}{\partial n_\alpha}$ at the r-boundary do not approach zero in general. Analogous to eq. (A.81), we therefore shift the profile by splitting the partial derivatives into a r- and z-dependent contribution $\frac{\partial\Phi^\Delta}{\partial n_\alpha}(r,z)$, which approaches zero at the r-boundary, and the z-dependent value at the r-boundary $\frac{\partial\Phi^\infty}{\partial n_\alpha}(z)$ according to

$$\frac{\partial\Phi}{\partial n_\alpha}(r,z) = \frac{\partial\Phi^\Delta}{\partial n_\alpha}(r,z) + \frac{\partial\Phi^\infty}{\partial n_\alpha}(z) \tag{A.86}$$

For the scalar terms one obtains

$$\frac{\partial\Phi}{\partial n_\alpha} \otimes \omega_i^\alpha = \mathcal{F}_z^{-1}\mathcal{H}_0^{-1}\left[\frac{\partial\hat{\Phi}^\Delta}{\partial n_\alpha}(k_r,k_z)\hat{\omega}_i^\alpha(k_r,k_z)\right] + \mathcal{F}_z^{-1}\left[\frac{\partial\hat{\Phi}^\infty}{\partial n_\alpha}(k_z)\hat{\omega}_i^\alpha(k_r=0,k_z)\right] \tag{A.87}$$

using the scalar inverse Fourier transform from eq. (B.30). With the scalar Fourier transform, eq. (B.29), of the partial derivative of the Helmholtz energy density according to

$$\frac{\partial\hat{\Phi}}{\partial n_\alpha}(k_r,k_z)=\mathcal{F}_z\mathcal{H}_0\left[\frac{\partial\Phi^\Delta}{\partial n_\alpha}(r,z)\right]+\mathcal{F}_z\left[\frac{\partial\Phi^\infty}{\partial n_\alpha}(z)\right]\frac{\delta(k_r)}{2\pi k_r} \tag{A.88}$$

For the vector-valued contributions we compute the dot product in Fourier space

$$\frac{\partial\hat{\Phi}}{\partial\mathbf{n}_\alpha}\cdot\hat{\omega}_i^\alpha=\begin{pmatrix}\frac{\partial\hat{\Phi}}{\partial\mathbf{n}_\alpha}\big|_{k_r}\\0\\\frac{\partial\hat{\Phi}}{\partial\mathbf{n}_\alpha}\big|_{k_z}\end{pmatrix}\cdot\begin{pmatrix}\hat{\omega}_i^\alpha|_{k_r}\\0\\\hat{\omega}_i^\alpha|_{k_z}\end{pmatrix}=\frac{\partial\hat{\Phi}}{\partial\mathbf{n}_\alpha}\Big|_{k_r}\hat{\omega}_i^\alpha|_{k_r}+\frac{\partial\hat{\Phi}}{\partial\mathbf{n}_\alpha}\Big|_{k_z}\hat{\omega}_i^\alpha|_{k_z} \tag{A.89}$$

with the weight functions from eqs. (A.59e) and (A.59f)

$$\hat{\omega}_i^{\mathrm{V1}}|_{k_r}(k_r,k_z)=\frac{-\mathrm{i}}{2R_i}k_r\hat{\omega}_i^3(k_r,k_z) \tag{A.90a}$$

$$\hat{\omega}_i^{\mathrm{V1}}|_{k_z}(k_r,k_z)=\frac{-\mathrm{i}}{2R_i}k_z\hat{\omega}_i^3(k_r,k_z) \tag{A.90b}$$

$$\hat{\omega}_i^{\mathrm{V2}}|_{k_r}(k_r,k_z)=-\mathrm{i}\,2\pi k_r\hat{\omega}_i^3(k_r,k_z) \tag{A.91a}$$

$$\hat{\omega}_i^{\mathrm{V2}}|_{k_z}(k_r,k_z)=-\mathrm{i}\,2\pi k_z\hat{\omega}_i^3(k_r,k_z) \tag{A.91b}$$

using the inverse Fourier transform for scalar functions from eq. (B.30). This results in

$$\frac{\partial\Phi}{\partial\mathbf{n}_\alpha}\otimes\omega_i^\alpha=\mathcal{F}_z^{-1}\mathcal{H}_0^{-1}\left[\frac{\partial\hat{\Phi}}{\partial\mathbf{n}_\alpha}\Big|_{k_r}\hat{\omega}_i^\alpha|_{k_r}+\frac{\partial\hat{\Phi}}{\partial\mathbf{n}_\alpha}\Big|_{k_z}\hat{\omega}_i^\alpha|_{k_z}\right] \tag{A.92}$$

with the vector-valued Fourier transform, eq. (B.38), of the vector-valued derivatives

$$\frac{\partial\hat{\Phi}}{\partial\mathbf{n}_\alpha}(k_r,k_z)=\begin{pmatrix}\mathcal{F}_z\mathcal{H}_1\left[-\mathrm{i}\,\frac{\partial\Phi^\Delta}{\partial\mathbf{n}_\alpha}\big|_r(r,z)\right]\\0\\\mathcal{F}_z\mathcal{H}_0\left[\frac{\partial\Phi^\Delta}{\partial\mathbf{n}_\alpha}\big|_z(r,z)\right]\end{pmatrix}+\begin{pmatrix}0\\0\\\mathcal{F}_z\left[\frac{\partial\Phi^\infty}{\partial\mathbf{n}_\alpha}(z)\right]\frac{\delta(k_r)}{2\pi k_r}\end{pmatrix} \tag{A.93}$$

For $\alpha=\mathrm{V1}$, we obtain

$$\begin{aligned}\frac{\partial\Phi}{\partial\mathbf{n}_{\mathrm{V1}}}\otimes\omega_i^{\mathrm{V1}}=\mathcal{F}_z^{-1}\mathcal{H}_0^{-1}\Bigg[&\frac{-\mathrm{i}}{2R_i}\hat{\omega}_i^3(k_r,k_z)\left(k_r\frac{\partial\hat{\Phi}^\Delta}{\partial\mathbf{n}_{\mathrm{V1}}}\Big|_{k_r}(k_r,k_z)+k_z\frac{\partial\hat{\Phi}^\Delta}{\partial\mathbf{n}_{\mathrm{V1}}}\Big|_{k_z}(k_r,k_z)\right)\Bigg]\\&+\mathcal{F}_z^{-1}\left[\frac{-\mathrm{i}}{2R_i}\hat{\omega}_i^3(k_r=0,k_z)k_z\frac{\partial\hat{\Phi}^\infty}{\partial\mathbf{n}_{\mathrm{V1}}}\Big|_{k_z}(k_z)\right]\end{aligned} \tag{A.94}$$

Likewise, for $\alpha = \mathrm{V2}$ this results in

$$\frac{\partial \Phi}{\partial \mathbf{n}_{\mathrm{V2}}} \otimes \omega_i^{\mathrm{V2}} = \mathcal{F}_z^{-1}\mathcal{H}_0^{-1}\left[-\mathrm{i}2\pi\, \hat{\omega}_i^3(k_r,k_z)\left(k_r \frac{\partial \hat{\Phi}^{\Delta}}{\partial \mathbf{n}_{\mathrm{V2}}}\bigg|_{k_r}(k_r,k_z) + k_z \frac{\partial \hat{\Phi}^{\Delta}}{\partial \mathbf{n}_{\mathrm{V2}}}\bigg|_{k_z}(k_r,k_z)\right)\right] + \mathcal{F}_z^{-1}\left[-\mathrm{i}2\pi\, \hat{\omega}_i^3(k_r=0,k_z) k_z \frac{\partial \hat{\Phi}^{\infty}}{\partial \mathbf{n}_{\mathrm{V2}}}\bigg|_{k_z}(k_z)\right] \quad \text{(A.95)}$$

A.3.2.2 Hard-Chain Contribution Convolutions in Cylindrical Coordinates

For the hard-chain contribution the two weighted densities $\bar{\rho}_i^{\mathrm{hc}}$ and λ_i^{hc} are computed with the scalar Fourier transform according to

$$\begin{aligned}\bar{\rho}_i^{\mathrm{hc}}(r,z) &= \rho_i(r,z) \otimes \omega_i^{\mathrm{hc},\rho}(r,z) \\ &= \mathcal{F}_z^{-1}\mathcal{H}_0^{-1}\left[\hat{\rho}_i^{\Delta}(k_r,k_z)\hat{\omega}_i^{\mathrm{hc},\rho}(k_r,k_z)\right] + \mathcal{F}_z^{-1}\left[\hat{\rho}_i^{\infty}(k_z)\hat{\omega}_i^{\mathrm{hc},\rho}(k_r=0,k_z)\right]\end{aligned} \quad \text{(A.96)}$$

as well as

$$\begin{aligned}\lambda^{\mathrm{hc}}(r,z) &= \rho_i(r,z) \otimes \omega_i^{\mathrm{hc},\lambda}(r,z) \\ &= \mathcal{F}_z^{-1}\mathcal{H}_0^{-1}\left[\hat{\rho}_i^{\Delta}(k_r,k_z)\hat{\omega}_i^{\mathrm{hc},\lambda}(k_r,k_z)\right] + \mathcal{F}_z^{-1}\left[\hat{\rho}_i^{\infty}(k_z)\hat{\omega}_i^{\mathrm{hc},\lambda}(k_r=0,k_z)\right]\end{aligned} \quad \text{(A.97)}$$

In similar fashion, the other two convolutions from eq. (A.28) are computed as

$$\begin{aligned}&\int \frac{\rho_i(\mathbf{r}')}{y_{ii}^{dd}(\{\bar{\rho}_i(\mathbf{r}')\})} \frac{\partial y_{ii}^{dd}(\{\bar{\rho}_i(\mathbf{r}')\})}{\partial \bar{\rho}_j(\mathbf{r}')} \omega_j^{\mathrm{hc},\rho}(\mathbf{r}-\mathbf{r}')\,\mathrm{d}\mathbf{r}' \\ &\qquad = \mathcal{F}_z^{-1}\mathcal{H}_0^{-1}\left[\mathcal{F}_z\mathcal{H}_0\left[\left(\frac{\rho_i(r,z)}{y_{ii}^{dd}(\{\bar{\rho}_i\})}\frac{\partial y_{ii}^{dd}(\{\bar{\rho}_j\})}{\partial \bar{\rho}_j}\right)^{\Delta}\right]\hat{\omega}_j^{\mathrm{hc},\rho}(k_r,k_z)\right] \\ &\qquad\quad + \mathcal{F}_z^{-1}\left[\mathcal{F}_z\left[\left(\frac{\rho_i(r,z)}{y_{ii}^{dd}(\{\bar{\rho}_i\})}\frac{\partial y_{ii}^{dd}(\{\bar{\rho}_j\})}{\partial \bar{\rho}_j}\right)^{\infty}\right]\hat{\omega}_j^{\mathrm{hc},\rho}(k_r=0,k_z)\right]\end{aligned} \quad \text{(A.98)}$$

and

$$\int \frac{\rho_j(\mathbf{r}')}{\lambda_j^{\mathrm{hc}}(\mathbf{r}')}\omega_j^{\mathrm{hc},\lambda}(\mathbf{r}-\mathbf{r}')\,\mathrm{d}\mathbf{r}' = \mathcal{F}_z^{-1}\mathcal{H}_0^{-1}\left[\mathcal{F}_z\mathcal{H}_0\left[\left(\frac{\rho_j(r,z)}{\lambda_j^{\mathrm{hc}}(r,z)}\right)^{\Delta}\right]\hat{\omega}_j^{\mathrm{hc},\lambda}(k_r,k_z)\right] + \mathcal{F}_z^{-1}\left[\mathcal{F}_z\left[\left(\frac{\rho_j(z)}{\lambda_j^{\mathrm{hc}}(z)}\right)^{\infty}\right]\hat{\omega}_j^{\mathrm{hc},\lambda}(k_r=0,k_z)\right] \quad \text{(A.99)}$$

A.3.2.3 Dispersive Contribution Convolutions in Cylindrical Coordinates

For the dispersion contribution the weighted densities $\bar{\rho}_i^{\text{disp}}$ are computed with the scalar Fourier transform according to

$$\begin{aligned}\bar{\rho}_i^{\text{disp}}(r,z) &= \rho_i(r,z) \otimes \omega_i^{\text{disp}}(r,z) \\ &= \mathcal{F}_z^{-1}\mathcal{H}_0^{-1}\left[\hat{\rho}_i^{\Delta}(k_r,k_z)\hat{\omega}_i^{\text{disp}}(k_r,k_z)\right] + \mathcal{F}_z^{-1}\left[\hat{\rho}_i^{\infty}(k_z)\hat{\omega}_i^{\text{disp}}(k_r=0,k_z)\right] \end{aligned} \tag{A.100}$$

while the convolution for the functional derivative from eq. (A.44) is computed in similar fashion, as

$$\begin{aligned}\mu_j^{\text{disp}}\left(\bar{\rho}^{\text{disp}}(r,z)\right) \otimes \omega_j^{\text{disp}}(r,z) = \mathcal{F}_z^{-1}\mathcal{H}_0^{-1}\Big[\hat{\mu}_j^{\text{disp},\Delta}(k_r,k_z)\hat{\omega}_j^{\text{disp}}(k_r,k_z)\Big] \\ + \mathcal{F}_z^{-1}\left[\hat{\mu}_j^{\text{disp},\infty}(k_z)\hat{\omega}_j^{\text{disp}}(k_r=0,k_z)\right]\end{aligned} \tag{A.101}$$

with the Fourier transform of the distributed residual chemical potential of the dispersion contribution

$$\hat{\mu}_j^{\text{disp}}\left(\bar{\rho}^{\text{disp}}(r,z)\right)(k_r,k_z) = \mathcal{F}_z\mathcal{H}_0\left[\mu_j^{\text{disp},\Delta}(r,z)\right] + \mathcal{F}_z\left[\mu_j^{\text{disp},\infty}(z)\right]\frac{\delta(k_r)}{2\pi k_r} \tag{A.102}$$

A.3.3 Convolution in Spherical Coordinates

The fast sine/cosine transform algorithms used for computing the Fourier transform in spherical coordinates require the function to vanish for large values of r. If the density profiles $\rho_i(r)$ do not approach zero, we define shifted profiles $\rho_i^{\Delta}(r)$ which do approach zero at large radial distances $r = r_{\max}$ by splitting the density profile

$$\rho_i(r) = \rho_i^{\Delta}(r) + \rho_i^{\infty} \tag{A.103}$$

into a r-dependent contribution $\rho_i^{\Delta}(r)$, vanishing at the boundary, and the constant value at the boundary $\rho_i^{\infty}(r = r_{\max})$. The Fourier transform of the density profiles is computed as presented in appendix B.2 according to eq. (B.53) while the constant boundary value can be computed analytically, leading to

$$\hat{\rho}_i(k_r) = \frac{2}{k_r}\mathcal{SIN}\left[\rho_i^{\Delta}(r)\,r\right] + \rho_i^{\infty}\delta(k_r) \tag{A.104}$$

A.3.3.1 Fundamental Measure Theory Convolutions in Spherical Coordinates

The scalar-valued ($\alpha \in \{0,1,2,3\}$) weighted densities n_α, are then calculated based on the inverse Fourier transform for scalar functions, eq. (B.54), leading to

$$n_\alpha(r) = \sum_{i=1}^{N_c} m_i \left(\frac{2}{r} \mathcal{SIN}\left[\hat{\rho}_i^{\Delta}(k_r) \hat{\omega}_i^{\alpha}(k_r)\, k_r \right] + \rho_i^{\infty}\, \hat{\omega}_i^{\alpha}(k_r = 0) \right) \tag{A.105}$$

For the vector-valued ($\alpha \in \{\mathrm{V1}, \mathrm{V2}\}$) weighted densities we use the vector-valued weight functions, $\hat{\omega}_i^{\mathrm{V1}}(\mathbf{k}) = \frac{-\mathrm{i}}{2R_i}\mathbf{k}\hat{\omega}_i^3(\mathbf{k})$ and $\hat{\omega}_i^{\mathrm{V2}}(\mathbf{k}) = -\mathrm{i}\,2\pi\mathbf{k}\hat{\omega}_i^3(\mathbf{k})$, and transform them back to real space using the inverse Fourier transform for vector-valued functions from eq. (B.72). For the vector-valued weight functions

$$\mathbf{n}_{\mathrm{V1}}(r) = \sum_{i=1}^{N_c} \frac{m_i}{2R_i} \left(\mathbf{e}_r \frac{\mathrm{i}}{\pi r^2} \mathcal{SIN}\left[-\mathrm{i}\, \hat{\rho}_i^{\Delta}(k_r)\, k_r\, \hat{\omega}_i^3(k_r) \right] - \mathbf{e}_r \frac{2\mathrm{i}}{r} \mathcal{COS}\left[-\mathrm{i}\, \hat{\rho}_i^{\Delta}(k_r)\, k_r\, \hat{\omega}_i^3(k_r)\, k_r \right] \right) \tag{A.106}$$

$$\mathbf{n}_{\mathrm{V2}}(r) = \sum_{i=1}^{N_c} 2\pi m_i \left(\mathbf{e}_r \frac{\mathrm{i}}{\pi r^2} \mathcal{SIN}\left[-\mathrm{i}\, \hat{\rho}_i^{\Delta}(k_r)\, k_r\, \hat{\omega}_i^3(k_r) \right] - \mathbf{e}_r \frac{2\mathrm{i}}{r} \mathcal{COS}\left[-\mathrm{i}\, \hat{\rho}_i^{\Delta}(k_r)\, k_r\, \hat{\omega}_i^3(k_r)\, k_r \right] \right) \tag{A.107}$$

the convolution with the constant value from shifting the density profile vanishes due to $\hat{\omega}_i^{\mathrm{V1}}(k_r = 0) = 0 = \hat{\omega}_i^{\mathrm{V2}}(k_r = 0)$. The convolution integrals of the White-Bear Helmholtz energy density derivatives $\frac{\partial \Phi}{\partial n_\alpha}$ with the weight functions ω_i^α are computed similarly. If the partial derivatives $\frac{\partial \Phi}{\partial n_\alpha}$ do not vanish, we shift the profile to zero by splitting the partial derivatives into a r-dependent contribution $\frac{\partial \Phi^{\Delta}}{\partial n_\alpha}(r)$, vanishing at the boundary, and the constant value at the boundary $\frac{\partial \Phi^{\infty}}{\partial n_\alpha}$ according to

$$\frac{\partial \Phi}{\partial n_\alpha}(r) = \frac{\partial \Phi^{\Delta}}{\partial n_\alpha}(r) + \frac{\partial \Phi^{\infty}}{\partial n_\alpha} \tag{A.108}$$

For the scalar terms one obtains

$$\frac{\partial \Phi}{\partial n_\alpha} \otimes \omega_i^\alpha = \frac{2}{r} \mathcal{SIN}\left[\frac{\partial \hat{\Phi}^{\Delta}}{\partial n_\alpha}(k_r) \hat{\omega}_i^\alpha(k_r)\, k_r \right] + \frac{\partial \Phi^{\infty}}{\partial n_\alpha} \hat{\omega}_i^\alpha(k_r = 0) \tag{A.109}$$

using the scalar inverse Fourier transform from eq. (B.54). With the scalar Fourier transform of the partial derivative of the Helmholtz energy density, eq. (B.53), obtained from

$$\frac{\hat{\partial\Phi}}{\partial n_\alpha}(k_r) = \frac{2}{k_r}\mathcal{SIN}\left[\frac{\partial\Phi^\Delta}{\partial n_\alpha}(r)\,r\right] + \frac{\partial\Phi^\infty}{\partial n_\alpha}\delta(k_r) \tag{A.110}$$

For the vector-valued derivatives we compute the dot product

$$\begin{aligned}\frac{\hat{\partial\Phi}}{\partial\mathbf{n}_\alpha}\cdot\hat{\omega}_i^\alpha &= \left.\frac{\partial\hat{\Phi}^\Delta}{\partial\mathbf{n}_\alpha}\right|_{k_r}\mathbf{e}_{k_r}\cdot\hat{\omega}_i^\alpha|_{k_r}\mathbf{e}_{k_r} + \left.\frac{\partial\Phi^\infty}{\partial\mathbf{n}_\alpha}\right|_{k_r}\delta(k_r)\mathbf{e}_{k_r}\cdot\hat{\omega}_i^\alpha|_{k_r}\mathbf{e}_{k_r}\\ &= \left.\frac{\partial\hat{\Phi}^\Delta}{\partial\mathbf{n}_\alpha}\right|_{k_r}\hat{\omega}_i^\alpha|_{k_r} + \left.\frac{\partial\Phi^\infty}{\partial\mathbf{n}_\alpha}\right|_{k_r}\delta(k_r)\hat{\omega}_i^\alpha|_{k_r}\end{aligned} \tag{A.111}$$

in Fourier space, the convolution with the constant value from shifting the density profile vanishes due to $\hat{\omega}_i^{\mathrm{V1}}(k_r=0)=0=\hat{\omega}_i^{\mathrm{V2}}(k_r=0)$. With the weight functions, eqs. (A.59e) and (A.59f), obtained from

$$\hat{\omega}_i^{\mathrm{V1}}|_{k_r}(k_r) = \frac{-\mathrm{i}}{2R_i}k_r\hat{\omega}_i^3(k_r) \tag{A.112}$$

$$\hat{\omega}_i^{\mathrm{V2}}|_{k_r}(k_r) = -\mathrm{i}\,2\pi k_r\hat{\omega}_i^3(k_r) \tag{A.113}$$

In real space, this results in

$$\frac{\partial\Phi}{\partial\mathbf{n}_\alpha}\otimes\omega_i^\alpha = \frac{2}{r}\mathcal{SIN}\left[\left.\frac{\partial\hat{\Phi}^\Delta}{\partial\mathbf{n}_\alpha}\right|_{k_r}\hat{\omega}_i^\alpha|_{k_r}k_r\right] \tag{A.114}$$

with the inverse Fourier transform for scalar functions from eq. (B.54). With the vector-valued Fourier transform of the vector-valued derivatives, eq. (B.63), obtained from

$$\frac{\hat{\partial\Phi}}{\partial\mathbf{n}_\alpha}(k_r) = \mathbf{e}_{k_r}\frac{2\mathrm{i}}{k_r}\mathcal{COS}\left[\left.\frac{\partial\Phi^\Delta}{\partial\mathbf{n}_\alpha}\right|_r(r)\,r\right] - \mathbf{e}_{k_r}\frac{\mathrm{i}}{\pi k_r^2}\mathcal{SIN}\left[\left.\frac{\partial\Phi^\Delta}{\partial\mathbf{n}_\alpha}\right|_r(r)\right] + \mathbf{e}_{k_r}\left.\frac{\partial\Phi^\infty}{\partial\mathbf{n}_\alpha}\right|_{k_r}\delta(k_r) \tag{A.115}$$

For $\alpha=\mathrm{V1}$, we obtain

$$\frac{\partial\Phi}{\partial\mathbf{n}_{\mathrm{V1}}}\otimes\omega_i^{\mathrm{V1}} = \frac{2}{r}\mathcal{SIN}\left[\frac{-\mathrm{i}}{2R_i}k_r\hat{\omega}_i^3(k_r)\left.\frac{\partial\hat{\Phi}^\Delta}{\partial\mathbf{n}_{\mathrm{V1}}}\right|_{k_r}k_r\right] \tag{A.116}$$

Likewise, for $\alpha = \mathrm{V2}$ this results in

$$\frac{\partial \Phi}{\partial \mathbf{n}_{\mathrm{V2}}} \otimes \omega_i^{\mathrm{V2}} = \frac{2}{r} \mathcal{SIN}\left[-\mathrm{i}\, 2\pi k_r \hat{\omega}_i^3(k_r) \frac{\partial \hat{\Phi}^{\Delta}}{\partial \mathbf{n}_{\mathrm{V1}}}\bigg|_{k_r} k_r \right] \tag{A.117}$$

A.3.3.2 Hard-Chain Contribution Convolutions in Spherical Coordinates

The two weighted densities $\bar{\rho}_i^{\mathrm{hc}}$ and λ_i^{hc} for the hard-chain contribution are computed with the scalar Fourier transform according to

$$\bar{\rho}_i^{\mathrm{hc}}(r) = \rho_i(r) \otimes \omega_i^{\mathrm{hc},\rho}(r) = \mathcal{SIN}\left[\hat{\rho}_i^{\Delta}(k_r) \hat{\omega}_i^{\mathrm{hc},\rho}(k_r) \right] + \hat{\rho}_i^{\infty} \hat{\omega}_i^{\mathrm{hc},\rho}(k_r = 0) \tag{A.118}$$

and

$$\lambda^{\mathrm{hc}}(r,z) = \rho_i(r,z) \otimes \omega_i^{\mathrm{hc},\lambda}(r,z) = \mathcal{SIN}\left[\hat{\rho}_i^{\Delta}(k_r) \hat{\omega}_i^{\mathrm{hc},\lambda}(k_r) \right] + \hat{\rho}_i^{\infty} \hat{\omega}_i^{\mathrm{hc},\lambda}(k_r = 0) \tag{A.119}$$

In similar fashion, the other two convolutions from eq. (A.28) are computed via

$$\begin{aligned} \int \frac{\rho_i(\mathbf{r}')}{y_{ii}^{dd}(\{\bar{\rho}_i(\mathbf{r}')\})} \frac{\partial y_{ii}^{dd}(\{\bar{\rho}_i(\mathbf{r}')\})}{\partial \bar{\rho}_j(\mathbf{r}')} \omega_j^{\mathrm{hc},\rho}(\mathbf{r} - \mathbf{r}')\, \mathrm{d}\mathbf{r}' \\ = \mathcal{SIN}\left[\mathcal{SIN}\left[\left(\frac{\rho_i(r)}{y_{ii}^{dd}(\{\bar{\rho}_i\})} \frac{\partial y_{ii}^{dd}(\{\bar{\rho}_j\})}{\partial \bar{\rho}_j} \right)^{\Delta} \right] \hat{\omega}_j^{\mathrm{hc},\rho}(k_r) \right] \\ + \left(\frac{\rho_i(r)}{y_{ii}^{dd}(\{\bar{\rho}_i\})} \frac{\partial y_{ii}^{dd}(\{\bar{\rho}_j\})}{\partial \bar{\rho}_j} \right)^{\infty} \hat{\omega}_j^{\mathrm{hc},\rho}(k_r = 0) \end{aligned} \tag{A.120}$$

and

$$\begin{aligned} \int \frac{\rho_j(\mathbf{r}')}{\lambda_j^{\mathrm{hc}}(\mathbf{r}')} \omega_j^{\mathrm{hc},\lambda}(\mathbf{r} - \mathbf{r}')\, \mathrm{d}\mathbf{r}' = \mathcal{SIN}\left[\mathcal{SIN}\left[\left(\frac{\rho_j(r)}{\lambda_j^{\mathrm{hc}}(r)} \right)^{\Delta} \right] \hat{\omega}_j^{\mathrm{hc},\lambda}(k_r) \right] \\ + \left(\frac{\rho_j(z)}{\lambda_j^{\mathrm{hc}}(z)} \right)^{\infty} \hat{\omega}_j^{\mathrm{hc},\lambda}(k_r = 0) \end{aligned} \tag{A.121}$$

A.3.3.3 Dispersive Contribution Convolutions in Spherical Coordinates

For the dispersion contribution the weighted densities $\bar{\rho}_i^{\mathrm{disp}}$ are computed with the scalar Fourier transform according to

$$\bar{\rho}_i^{\mathrm{disp}}(r) = \rho_i(r) \otimes \omega_i^{\mathrm{disp}}(r) = \mathcal{SIN}\left[\hat{\rho}_i^{\Delta}(k_r) \hat{\omega}_i^{\mathrm{disp}}(k_r) \right] + \hat{\rho}_i^{\infty} \hat{\omega}_i^{\mathrm{disp}}(k_r = 0) \tag{A.122}$$

The convolution for the functional derivative from eq. (A.44) is computed in similar fashion, as

$$\mu_j^{\text{disp}}\left(\bar{\rho}^{\text{disp}}(r)\right) \otimes \omega_j^{\text{disp}}(r) = \mathcal{SIN}\left[\hat{\mu}_j^{\text{disp},\Delta}(k_r)\hat{\omega}_j^{\text{disp}}(k_r)\right] + \hat{\mu}_j^{\text{disp},\infty}\hat{\omega}_j^{\text{disp}}(k_r = 0) \tag{A.123}$$

with the Fourier transform of the distributed residual chemical potential of the dispersion contribution obtained from

$$\hat{\mu}_j^{\text{disp}}\left(\bar{\rho}^{\text{disp}}(r)\right)(k_r) = \mathcal{SIN}\left[\mu_j^{\text{disp},\Delta}(r)\right] + \mu_j^{\text{disp},\infty}\delta(k_r) \tag{A.124}$$

A.4 From Integral Transform to Discretized Representation

In this section, we discuss the transition from continuous integral transforms to discrete representations of the inhomogeneous field variables (e.g., ρ_i). For Cartesian coordinates, the fast Fourier transform is used. For cylindrical coordinates we apply a combination of the fast Fourier and the fast Hankel transform (from a combination of fast Abel and fast Fourier transform, appearing as fast sine and cosine transform). For spherical coordinates the fast sine and cosine transforms are utilized. Because the weight functions from the weighted density approaches ω_i are transformed to Fourier space analytically, we also show the connection of the **r**-grid in real space to the **k**-grid in Fourier space. The fast Fourier, fast sine and fast cosine transforms are taken from *FFTPACK*[62,63], while the fast Abel transform follows Hansen[53] and Hansen and Law[54], described in detail in appendix B.4. Strategies to minimize Gibbs phenomenon are presented in appendix B.6.

A.4.1 Cartesian Grid

For Cartesian coordinates, we use the FFT in each dimension. A schematic grid is visualized in figure A.1. FFT algorithms require real space samples evaluated on an equidistant grid. Even though a physical problem may be non-periodic in the domain of interest $L_{\text{in},z}$, fast Fourier transforms will treat the considered domain as is it was surrounded by infinitely many (i.e., periodic) images of itself. To suppress the unwanted effect of periodic copies of the regarded domain, definition of a buffer region $L_{\text{out},z}$ on each side of the domain is needed. The two outer buffer regions $L_{\text{out},z}$ also serve as constant boundary conditions for the evaluation of the weighted densities at the boundary. Due to the functional nature of the problem a buffer domain is required as boundary condition, in contrast to boundary conditions for functions where information about a single point is sufficient.

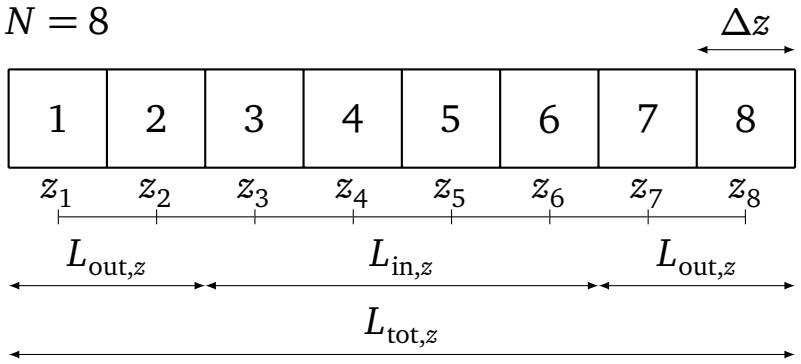

Figure A.1: Schematic equidistant Cartesian grid with $N = 8$ grid points and grid spacing Δz. The partitioned elements represent a discretization used for finite volume methods, while the function to be transformed is evaluated at the center of those elements z_i. The density profiles are computed on the inner domain $L_{\text{in},z}$, while the buffer zones $L_{\text{out},z}$ compensate the periodic continuation of the FFT and serve as boundary conditions.

A.4.1.1 Grid and Boundary Conditions

We thus consider a grid covering three domains, the two outer buffer domains with length $L_{\text{out},z}$, and the inner domain of interest with length $L_{\text{in},z}$, where the density profiles are iterated. To better connect this section to the previous one, we remind that the grand potential functional Ω is a functional of density profiles $\{\rho_i\}$ and a function of the variables $(\{\mu_i\}, T, V)$, whereby the system volume V is defined by the domain length $L_{\text{in},z}$ in z-direction. The choice for the value of the buffer length $L_{\text{out},z}$ is determined by the *influence length* of the weight functions. Here, the dispersion contribution has the largest influence length $2\psi R_i$ in every direction (with ψ from appendix A.2.4). Because two types of convolutions are computed (one for computation of the weighted density profiles and one for the convolution of the reduced Helmholtz energy with the weight functions), the buffer length $L_{\text{out},z}$ has to be at least twice the value of $2\psi R_i$. After each of the two convolutions, a fraction of the buffer domain with length $2\psi R_i$ is tainted due to possible inhomogeneous boundary conditions and periodic continuation of the FFT, which leads to the length of the buffer zone, as

$$L_{\text{out},z} \geq \max_i \{4\psi R_i(T)\} \tag{A.125}$$

A.4.1.2 Discrete Representation for FFT Algorithm

We now explain the **k**-grid in Fourier space for the computation of the weight functions, eqs. (A.59)–(A.61), is computed as follows. The approach is shown for one dimension only. Higher dimensions are the result of multiple consecutive Fourier transforms and can be treated analogously.

The discrete Fourier transform with Fourier variable k as used in FFT algorithms is defined as the following sum

$$\hat{f}_k = \sum_{j=0}^{N-1} f_j \, \mathrm{e}^{-2\pi \mathrm{i} \frac{jk}{N}} \qquad \text{with } k = 0, \ldots, (N-1) \tag{A.126}$$

which transforms a finite series of N equally-spaced samples $z_j = j\,\Delta z$ of a function f_j into a series of equally-spaced samples of the function in Fourier space $\hat{f}_k$. Index j denotes the discrete grid points in real space, while k denotes the grid points in Fourier space.

In comparison, the continuous Fourier transform can be discretized as well with $z_j = j\Delta z$ and $f(z_j) = f_j$. The continuous Fourier transform then leads to a similar equation as the discretization of the Fourier transform, eq. (A.126), namely to

$$\hat{f}(k_z) = \int_{z=-\infty}^{\infty} f(z) \, \mathrm{e}^{-2\pi \mathrm{i} z k_z} \, \mathrm{d}z \approx \sum_{j=0}^{N-1} f_j \, \mathrm{e}^{-2\pi \mathrm{i} j \Delta z k_z} \, \Delta z \tag{A.127}$$

where the result is multiplied with Δz compared to the unscaled version in eq. (A.126). Comparison of the arguments of the exponential functions in eqs. (A.126) and (A.127), $\frac{jk}{N} = j\Delta z k_z$, yields the discretization in Fourier space, as

$$k_z = \frac{k}{N\Delta z} = \frac{k}{L_{\mathrm{tot},z}} \qquad \text{with } k = 0, \ldots, (N-1) \tag{A.128}$$

At first glance, this result differs from the one proposed by Knepley *et al.* [1], because we define $L_{\mathrm{tot},z}$ differently. We evaluate the function to be transformed at the center of the elements in figure A.1 instead of the edges, as done by Knepley *et al.* [1], so that the regarded overall domain for the work of Knepley *et al.* ($\tilde{L}_{\mathrm{tot},z} = L_{\mathrm{tot},z} - \Delta z$) is different to our overall domain length ($L_{\mathrm{tot},z}$) for the same number of grid points N and the same discretization step size Δz. Complex-valued FFT algorithms include negative k-values as well. For an even number of grid points, the k-vector for the computation of the discrete representation of the weight functions, eqs. (A.59)–(A.61), is

$$k_z = \frac{1}{L_{\mathrm{tot},z}} \left[0, 1, \ldots, \left(\frac{N}{2} - 1 \right), \left(-\frac{N}{2} \right), \ldots, -1 \right] \tag{A.129}$$

For real-valued FFT algorithms, the k-vector looks differently

$$k_z = \frac{1}{L_{\mathrm{tot},z}} \left[0, 1, 1, 2, 2, \ldots, \left(\frac{N}{2} \right) \right] \tag{A.130}$$

This yields a k_z-grid in Fourier space which is used for the analytical computation of the weight functions $\hat{\omega}_i$, eqs. (A.59)–(A.61). These weight functions $\hat{\omega}_i$ are then multiplied in Fourier space with the FFT output of the function to be convolved, the result of which is transformed back to real space using the inverse FFT. For higher dimensions, the k-grid becomes a two- or three-dimensional array, while k_x and k_y are constructed equivalently to eq. (A.129) or eq. (A.130) with their respective length scale $L_{\mathrm{tot},x}$ and $L_{\mathrm{tot},y}$. The absolute value of $\mathbf{k}$ is calculated as

$$|\mathbf{k}| = \sqrt{k_x^2 + k_y^2 + k_z^2} \tag{A.131}$$

A.4.2 Cylindrical Grid

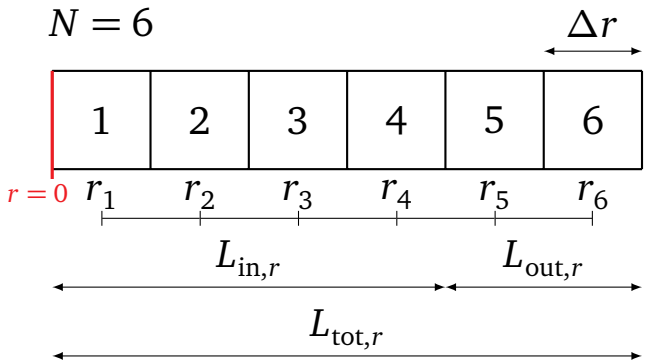

Figure A.2: Schematic equidistant radial grid with $N = 6$ grid points and grid spacing Δr. The partitioned elements represent a discretization used for finite volume methods, while the function to be transformed is evaluated at the center of those elements r_i. The density profiles are computed on the inner domain $L_{\mathrm{in},r}$, while the buffer zone $L_{\mathrm{tot},r}$ serves as boundary condition, where the density profiles ρ_i^{Δ} go to zero.

For cylindrical coordinates, we use the fast Fourier in axial and the fast Hankel transform (as a combination of fast Abel and fast sine and cosine transform) in radial direction. The procedure of the axial direction is equivalent to the approach for Cartesian coordinates as described in the previous section, therefore, only the radial direction is regarded here. A schematic grid is visualized in figure A.2. As opposed to the approach of Boţan *et al.* [18], who computed discrete Hankel transform on a logarithmic grid, we adopt the ideas of Hansen [52,53] and Hansen and Law [54], using a combination of Abel and Fourier transforms, which allows computation of the Hankel transform on equidistant grids.

A.4.2.1 Grid and Boundary Conditions

The radial grid is divided into two domains, the outer domain with length $L_{\mathrm{out},r}$, which is needed as boundary condition for the evaluation of the weighted densities at the boundary, and the inner domain with length $L_{\mathrm{in},r}$, where the density profiles are iterated. Due to even and odd continuation of the fast sine and fast cosine transform, respectively, no boundary domain for $r < 0$ is needed. The size of the outer domain $L_{\mathrm{out},r}$ is determined as described in appendix A.4.1.1. Therefore, the size of the outer domain is determined as

$$L_{\mathrm{out},r} \geq \max_i \{4\psi R_i(T)\} \tag{A.132}$$

A.4.2.2 Discrete Representation for FFT and Fast Hankel Transform Algorithms

The **k**-grid in Fourier space for the computation of the weight functions, eqs. (A.59)–(A.61), is computed as follows. The axial direction is equivalent to the Cartesian grid, eq. (A.128), whereas for the radial component the k-values correspond to twice the domain shown in figure A.2. Instead of the Fourier, the discrete sine and cosine transform are used, which exploit symmetry and, therefore, require only half of the Fourier domain. The length of the whole Fourier domain in radial direction is $(2L_{\mathrm{tot},r})$. This leads to the following k-grid for the radial component

$$k_r = \frac{k}{2N\Delta r} = \frac{k}{2L_{\mathrm{tot},r}} \qquad \text{with } k = 0, \ldots, (N-1) \tag{A.133}$$

This yields a k_r-grid in Fourier space which, together with the k_z-grid, is used for the analytical computation of the weight functions $\hat{\omega}_i$, eqs. (A.59)–(A.61). These weight functions $\hat{\omega}_i$ are then multiplied in Fourier space with the FFT and fast Hankel transform output of the function to be convolved, and this result can be transformed back to real space using the inverse FFT and inverse fast Hankel transform algorithms. For two dimensional problems in cylindrical coordinates, the **k**-grid becomes a two-dimensional array. The absolute value of **k** is calculated as

$$|\mathbf{k}| = \sqrt{k_r^2 + k_z^2} \tag{A.134}$$

In this work, we utilize the projection-slice theorem for the computation of the Hankel transform, where the Hankel transform is replaced by

$$\mathcal{H}_0[f(r)] = \mathcal{F}_r \mathcal{A}[f(r)] \tag{A.135}$$

a combination of Fourier $\mathcal{F}$ and Abel transform $\mathcal{A}$. The algorithm for computation of the fast Hankel transform is based on work of Hansen [52] and described in detail in appendix B.4. The inverse transform is computed from a combination of inverse Abel and inverse Fourier transform, as

$$\mathcal{H}_0^{-1}\left[\hat{f}(k_r)\right] = \mathcal{A}^{-1}\mathcal{F}_r^{-1}\left[\hat{f}(k_r)\right] \tag{A.136}$$

The Abel transform is computed as described in appendix B.4. As a result of rotational symmetry, all density profiles are even with respect to $r = 0$. This allows using the cosine instead of the Fourier transform. Because some calculations require a division by the radius r, we locate the first grid point at $r = \frac{\Delta r}{2}$. For this grid distribution, we require the discrete cosine transform II ($\mathcal{DCT}_{\text{II}}$) which is available in *FFTPACK* as subroutine *COSQ1B*. More details on the discrete cosine transform are presented in appendix B.5. The Fourier transform of scalar functions $f(r,z)$, using the Hankel transform of zeroth order as in eq. (B.29), is computed from

$$\hat{f}(k_r,k_z) = \mathcal{F}_z\,\mathcal{DCT}_{\text{II}}\,\mathcal{A}[f(r,z)] \tag{A.137}$$

with the Abel transform $\mathcal{A}$. The inverse transform uses the discrete cosine transform III ($\mathcal{DCT}_{\text{III}} = \mathcal{DCT}_{\text{II}}^{-1}$) which is available in *FFTPACK* as subroutine *COSQ1F* and can be computed via

$$f(r,z) = \mathcal{A}^{-1}\,\mathcal{DCT}_{\text{III}}\,\mathcal{F}_z^{-1}\left[\hat{f}(k_r,k_z)\right] \tag{A.138}$$

For vector-valued functions, the Hankel transform of first order is computed from the zeroth order Hankel transform with eq. (B.75) from appendix B.3, leading to

$$\hat{f}(k_r,k_z)|_{k_r} = \mathcal{F}_z\mathcal{H}_1\left[f(r,z)|_r\right] = \mathcal{F}_z\left[\frac{1}{2\pi k_r}\mathcal{DCT}_{\text{II}}\mathcal{A}\left[\frac{f(r,z)|_r}{r} + \frac{\partial f(r,z)|_r}{\partial r}\right]\right] \tag{A.139}$$

The application of this equation is limited to the radial contribution in eq. (A.93) where $f(r,z)|_r = -\mathrm{i}\,\frac{\partial\Phi^{\Delta}}{\partial\mathbf{n}_\alpha}\Big|_r(r,z)$ is an odd function in r. This leads to the derivative $\frac{\partial f(r,z)|_r}{\partial r}$ being an even function. Even continuation of the $\mathcal{DCT}_{\text{II}}$ allows neglecting the odd contribution $\frac{f(r,z)|_r}{r}$, which leads to the simpler form

$$\hat{f}(k_r,k_z)|_{k_r} = \mathcal{F}_z\left[\frac{1}{2\pi k_r}\mathcal{DCT}_{\text{II}}\mathcal{A}\left[\frac{\partial f(r,z)|_r}{\partial r}\right]\right] \tag{A.140}$$

The derivative $\frac{\partial f(r,z)}{\partial r}$ can be approximated using central differences with vanishing boundary conditions from

$$\frac{\partial f(z,r^{(n)})}{\partial r} \approx \frac{f(r^{(n+1)},z)-f(r^{(n-1)},z)}{r^{(n+1)}-r^{(n-1)}} \tag{A.141}$$

The inverse transform is computed similarly according to

$$\begin{aligned} f(r,z)|_r &= \mathcal{H}_1^{-1}\mathcal{F}_z^{-1}\left[\hat{f}(k_r,k_z)|_{k_r}\right] = \frac{1}{r}\mathcal{H}_0^{-1}\left[\frac{\mathcal{F}_z^{-1}\left[\hat{f}(k_r,k_z)|_{k_r}\right]}{2\pi k_r} + \frac{\partial \mathcal{F}_z^{-1}\left[\hat{f}(k_r,k_z)|_{k_r}\right]}{\partial k_r}\right] \\ &= \frac{1}{r}\mathcal{A}^{-1}\mathcal{F}_r^{-1}\left[\frac{\mathcal{F}_z^{-1}\left[\hat{f}(k_r,k_z)|_{k_r}\right]}{2\pi k_r} + \frac{\partial \mathcal{F}_z^{-1}\left[\hat{f}(k_r,k_z)|_{k_r}\right]}{\partial k_r}\right] \end{aligned} \tag{A.142}$$

The derivative in the second term of eq. (A.142) can be replaced using the identity

$$\mathcal{F}_r^{-1}\left[\frac{\partial \hat{g}(k_r,z)}{\partial k_r}\mathrm{i}\right] = 2\pi r\mathcal{F}_r^{-1}\left[\hat{g}(k_r,z)\right] \tag{A.143}$$

with $\hat{g}(k_r,z) = \mathcal{F}_z^{-1}\left[\hat{f}(k_r,k_z)|_{k_r}\right]$. This is applied to eqs. (A.84) and (A.85) where $\hat{g}(k_r,z)$ is a real even function in k_r, making $\left(\frac{\partial \hat{g}(k_r,z)}{\partial k_r}\mathrm{i}\right)$ purely imaginary and odd in k_r. The purely imaginary and odd inverse Fourier transform $\mathcal{F}_r^{-1}\left[\frac{\partial \hat{g}(k_r,z)}{\partial k_r}\mathrm{i}\right]$ can, therefore, be replaced by the sine transform $2\pi r\mathcal{DST}_{\mathrm{III}}[\hat{g}(k_r,z)]$. The first term in eq. (A.142) transforms an even function and allows for replacing the Fourier transform $\mathcal{F}_r^{-1}$ with the $\mathcal{DCT}_{\mathrm{III}}$ according to

$$f(r,z)|_r = \frac{1}{r}\mathcal{A}^{-1}\left[\mathcal{DCT}_{\mathrm{III}}\mathcal{F}_z^{-1}\left[\frac{\hat{f}(k_r,k_z)|_{k_r}}{2\pi k_r}\right] + 2\pi r\mathcal{DST}_{\mathrm{III}}\mathcal{F}_z^{-1}\left[\hat{f}(k_r,k_z)|_{k_r}\right]\right] \tag{A.144}$$

Equation (A.140) with eq. (A.141), and eq. (A.144) are our final equations for the forward and inverse transform in radial direction, respectively.

Here we require the discrete sine transform III ($\mathcal{DST}_{\mathrm{III}}$) which is available in *FFTPACK* as subroutine *SINQ1F*. The grid for the $\mathcal{DST}_{\mathrm{III}}$ algorithm has to be shifted in Fourier space. The procedure is described in appendix A.4.3.2 and visualized in figure A.5. More details on the discrete sine and cosine transform are presented in appendix B.5.

A.4.3 Spherical Grid

In spherical coordinates we only consider one-dimensional problems, where angular symmetry exists. We use the fast sine and fast cosine transform. A schematic grid is visualized in figure A.3. Fast sine and cosine transform algorithms require real space samples evaluated on an equidistant grid.

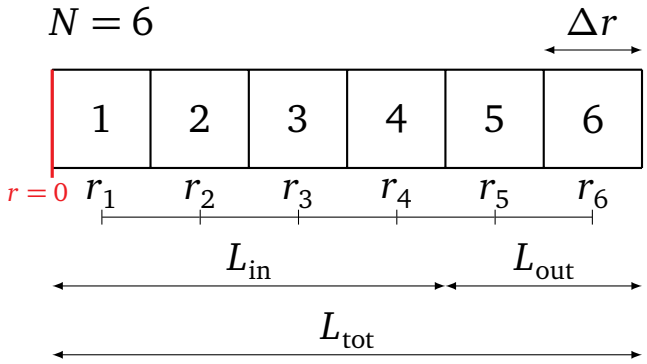

Figure A.3: Schematic equidistant spherical grid with $N = 6$ grid points and grid spacing Δr. The partitioned elements represent a discretization used for finite volume methods, while the function to be transformed is evaluated at the center of those elements r_i. The density profiles are computed on the inner domain L_{in}, while the buffer zone L_{out} compensates for periodic continuation of the fast sine and cosine transform, and serves as boundary condition, where the density profiles ρ_i^{Δ} go to zero.

A.4.3.1 Grid and Boundary Conditions

Similar to cylindrical coordinates, no boundary domain for $r < 0$ is needed, because the used algorithms for the discrete sine and cosine transform assume odd and even continuation, respectively, which can be exploited here due to spherical symmetry requirements. The size of the outer domain L_{out} is determined as described in appendix A.4.1.1. Therefore, the size of the outer domain is determined as

$$L_{\text{out}} \geq \max_i \{4\psi R_i(T)\} \tag{A.145}$$

A.4.3.2 Discrete Representation for Sine and Cosine Transform Algorithms

The **k**-grid in Fourier space for the computation of the weight functions, eqs. (A.59)–(A.61), is computed as follows. The discrete sine and cosine transform are recovered by discretization of the derived Fourier transform in spherical coordinates. There are four relevant variants of the sine and cosine transform, each with a set of different boundary conditions and discretization schemes. Due to the singularity at the origin in spherical coordinates, we locate the first grid point at $r = \frac{\Delta r}{2}$. For this grid distribution, we need the discrete sine transform II ($\mathcal{DST}_{\text{II}}$) according to

$$\hat{f}_{k^*} = \sum_{j=0}^{N-1} f_j \sin\left(\frac{\pi}{N}\left(j + \frac{1}{2}\right)(k^* + 1)\right) \qquad \text{with } k^* = 0, \ldots, (N-1) \tag{A.146}$$

which is available in *FFTPACK* as subroutine *SINQ1B*. More details on the discrete sine transform are presented in appendix B.5. The iteration variable k^* does not represent the true Fourier variable k, which for the $\mathcal{DST}_{\text{II}}$ is obtained from $k = k^* + 1$.

The matching discrete cosine transform is the $\mathcal{DCT}_{\text{II}}$, computed as

$$\hat{f}_k = \sum_{j=0}^{N-1} f_j \cos\left(\frac{\pi}{N}\left(j+\frac{1}{2}\right)k\right) \qquad \text{with } k = 0,\ldots,(N-1) \tag{A.147}$$

which is available in *FFTPACK* as subroutine *COSQ1B*. More details on the discrete cosine transform are presented in appendix B.5. Both transforms transform a finite series of equally-spaced samples $z_j = \frac{1}{N}(j+\frac{1}{2})$ of a function f_j into a series of equal length in Fourier space $\hat{f}_k$. The index j denotes the discrete grid points in real space, while k denotes the grid points in Fourier space.

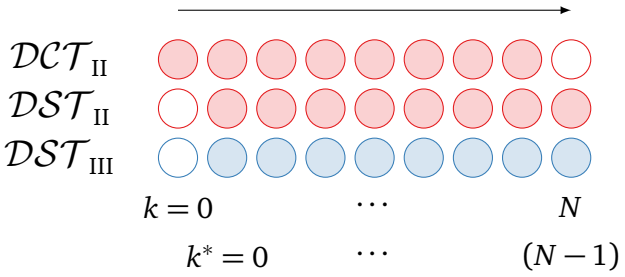

Figure A.4: Shift of indices to match $\mathcal{DST}_{\text{II}}$ and $\mathcal{DCT}_{\text{II}}$ to $\mathcal{DST}_{\text{III}}$. Filled spheres represent the k-grid of the respective forward (red) and inverse (blue) transform.

For both transforms, indices k and k^* run from $0,\ldots,(N-1)$ in Fourier space, but the $\mathcal{DST}_{\text{II}}$ treats the point $k = 0$ implicitly as $\hat{f}_{k=0}^{\mathcal{DST}} = 0$, while the $\mathcal{DCT}_{\text{II}}$ treats the value $\hat{f}_{k=0}^{\mathcal{DCT}}$ explicitly. In contrast, the $\mathcal{DCT}_{\text{II}}$ does not provide a value for $k = N$, while the $\mathcal{DST}_{\text{II}}$ does (as $k^* = N-1$). Because the transformation to Fourier space in eqs. (A.106), (A.107), and (A.115) requires $f(r)$ to be multiplied with r, the argument of the sine and cosine transform are always zero at $r = 0$, which leads to $\hat{f}_{k=0}^{\mathcal{DCT}} = 0$.

For the computation of eq. (A.115) a combination of $\mathcal{DST}_{\text{II}}$ and $\mathcal{DCT}_{\text{II}}$ is needed. Because the inverse transform, eq. (A.114), uses solely the $\mathcal{DST}_{\text{III}}$ the value $\hat{f}_{k=0}^{\mathcal{DCT}} = 0$ can be neglected, but the value for $k = N$ (or $k^* = N-1$) for the $\mathcal{DST}_{\text{III}}$ has to be added: $\hat{f}_{k=N}^{\mathcal{DST}} = 0$. This approach is not exact, but a reasonable approximation as $\hat{f}_{k\to\infty}^{\mathcal{DCT}} \to 0$ for smooth functions and appropriate number of grid points. This procedure is necessary to match the different k-values of the $\mathcal{DST}_{\text{II}}$, $\mathcal{DCT}_{\text{II}}$ and $\mathcal{DST}_{\text{III}}$. The shifting of indices is visualized in figure A.4.

The inverse of the $\mathcal{DST}_{\text{II}}$ and $\mathcal{DCT}_{\text{II}}$ are the $\mathcal{DST}_{\text{III}}$ and $\mathcal{DCT}_{\text{III}}$, respectively. The $\mathcal{DST}_{\text{III}}$ is available from *FFTPACK* as subroutine *SINQ1F* and $\mathcal{DCT}_{\text{III}}$ as subroutine *COSQ1F*. Again, the k-values of the $\mathcal{DST}_{\text{III}}$ and $\mathcal{DCT}_{\text{III}}$ do not match. For computation of eqs. (A.106) and (A.107),

a function in Fourier space as result of a $\mathcal{DST}_{\text{II}}$ is transformed back to real space using the $\mathcal{DST}_{\text{III}}$ and $\mathcal{DCT}_{\text{III}}$. The $\mathcal{DST}_{\text{III}}$ can be performed immediately. For the inverse transform using the $\mathcal{DCT}_{\text{III}}$, the exact value $\hat{f}^{\mathcal{DCT}}_{k=0} = 0$ has to be added. Therefore, $\hat{f}^{\mathcal{DST}}_{k=N}$ is disregarded, which has negligible effect as $\hat{f}^{\mathcal{DCT}}_{k\to\infty} \to 0$ for smooth functions and appropriate number of grid points. The shifting of indices is visualized in figure A.5.

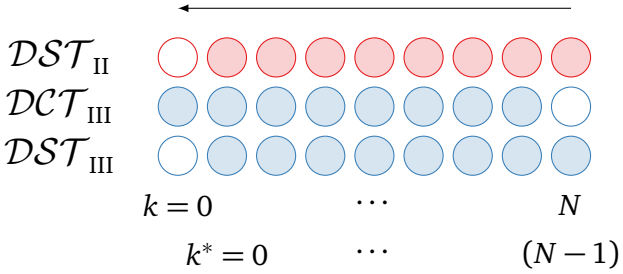

Figure A.5: Shift of indices to match $\mathcal{DST}_{\text{II}}$ and $\mathcal{DCT}_{\text{III}}$ to $\mathcal{DST}_{\text{II}}$. Filled spheres represent the k-grid of the respective forward (red) and inverse (blue) transform.

For computation of the appropriate discrete k-grid, the analytical sine transform can be discretized with $r_j = (j + \frac{1}{2})\Delta z$ and $f(r_j) = f_j$. This leads to a similar equation as the discrete sine transform, eq. (A.146), according to

$$\hat{f}(k_r) = \int_{r=0}^{\infty} f(r) \sin(2\pi r k_r)\, \mathrm{d}r \approx \sum_{j=0}^{N-1} f_j \sin\left(2\pi\left(j + \frac{1}{2}\right)\Delta r k_r\right)\Delta r \tag{A.148}$$

Comparison of the arguments of the sine functions in eqs. (A.147) and (A.148), $\frac{\pi}{N}(j+\frac{1}{2})(k^*+1) = 2\pi(j+\frac{1}{2})\Delta r k_r$, yields the discretization in Fourier space according to

$$k_r = \frac{k^*+1}{2N\Delta z} = \frac{k^*+1}{2L_{\text{tot}}} \qquad \text{with } k^* = 0, \ldots, (N-1) \tag{A.149}$$

In contrast to eq. (A.128), we divide by $(2L_{\text{tot}})$, because the $\mathcal{DST}_{\text{II}}$ assumes odd continuation by considering only half of the domain compared to the corresponding Fourier transform. For N grid points, the k-vector for the computation of the discrete representation of the weight functions, eqs. (A.59)–(A.61), is

$$k_r^{\mathcal{DST}} = \frac{1}{2L_{\text{tot}}}[1, \ldots, N] \tag{A.150}$$

while the same approach leads to a k-vector for the $\mathcal{DCT}_{\text{II}}$ according to

$$k_r^{\mathcal{DCT}} = \frac{1}{2L_{\text{tot}}}[0, \ldots, (N-1)] \tag{A.151}$$

This yields a k_r-grid in Fourier space which is used for the analytical computation of the weight functions $\hat{\omega}_i$, eqs. (A.59)–(A.61). These weight functions $\hat{\omega}_i$ are then multiplied in Fourier space with the $\mathcal{DST}_{\text{II}}$ and $\mathcal{DCT}_{\text{II}}$ output of the function to be convolved, while this result can be directly transformed back to real space using the $\mathcal{DST}_{\text{III}}$ and $\mathcal{DCT}_{\text{III}}$ algorithms.

A.5 Performance Analysis of FFT Convolution

To compare the efficiency of convolution algorithms using fast Fourier or similar transforms (i.e., discrete sine, cosine and Abel transforms), we compare the performance of one-dimensional FFT convolutions, computed via

$$\rho \otimes \omega = \mathcal{F}_z^{-1}\left[\mathcal{F}_z\left[\rho(z)\right]\hat{\omega}(k_z)\right] \tag{A.152}$$

with three real space convolution algorithms. We adapt the notation of the weighted densities defined in eq. (A.10).

The first real space convolution algorithm, hereafter referred to as *naïve* convolution, approximates the convolution integral of a density profile ρ with the weight function ω (each with N discretization points) over the whole discrete domain, where the value for the i-th element of the discrete sequence is computed according to[64]

$$(\rho \otimes \omega)_i = \frac{1}{N}\sum_{k=0}^{N-1} \omega_k \rho_{i-k} \qquad \forall i \tag{A.153}$$

The second real space algorithm, referred to as *compact* convolution, exploits the fact that weight functions are nonzero on a finite domain. As a consequence, the sequence for the weight function is shorter (length $M < N$) than the sequence for the density profile. Therefore, the value for the i-th element is computed as

$$(\rho \otimes \omega)_i = \frac{1}{M}\sum_{k=-\frac{M-1}{2}}^{\frac{M-1}{2}} \omega_k \rho_{i-k} \qquad \forall i \tag{A.154}$$

with the number of discretization points $M \in \{2n+1 | n \in \mathbb{N}^+\}$ for the weight function, which is always an odd number due to the symmetry of the weight function.

The third real space algorithm uses dense *matrix* multiplication

$$\rho \otimes \omega = \boldsymbol{\omega}\boldsymbol{\rho} \tag{A.155}$$

with the convolution matrix $\boldsymbol{\omega}$ and the density profile vector $\boldsymbol{\rho}$.

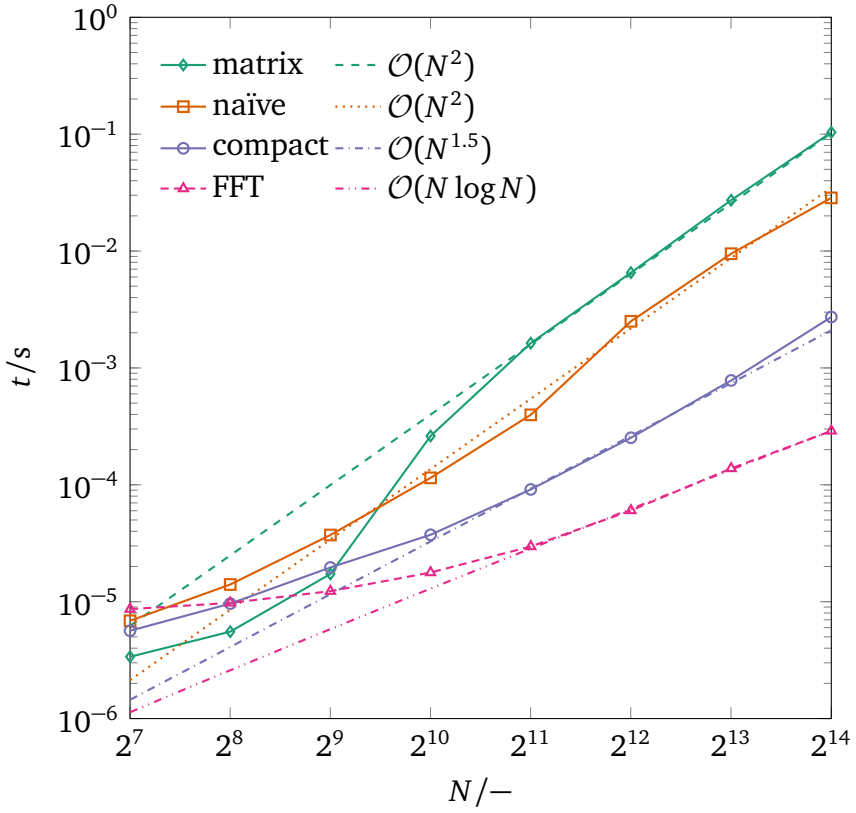

Figure A.6: Comparison of computing time t for one convolution using Fourier space, naïve, compact and matrix multiplication convolution, eqs. (A.152)–(A.155) respectively, for different number of grid points N, including scaling behavior $\mathcal{O}$. Length of the inner domain is $L_{\text{in},z} = 100\,\text{Å}$ and the radius for convolution is $R = 1.8\,\text{Å}$.

Figure A.6 depicts the computing time for one convolution using the four algorithms defined in eqs. (A.152)–(A.155) with respect to the number of spatial discretization points N. Additionally, scaling behavior $\mathcal{O}$ of the used algorithms is presented (non-continuous lines).

For small system sizes N, convolutions with convolution matrices perform best, while computing times for naïve, compact and FFT convolutions are higher (staying in the same order of magnitude). For $N = 2^{14}$, the scaling behavior of the FFT, $\mathcal{O}(N \log N)$, renders the FFT convolution at least one order of magnitude faster than the remaining algorithms. For a large number of discretization points, convolutions using a matrix product, eq. (A.155), take the longest, while naïve convolutions, eq. (A.153), compute faster; both scaling with $\mathcal{O}(N^2)$. Compact convolutions, eq. (A.154), scale better with respect to approximately $\mathcal{O}(N^{1.5})$, making this convolution algorithm for large systems superior to the matrix product and naïve approach. FFT convolutions, eq. (A.152), scale best for large systems (here $N = 2^{14}$) according to $\mathcal{O}(N \log N)$, performing at least one order of magnitude better than the remaining algorithms. Even for typical number of discretization points $N = 2^{10} = 1024$ convolution algo-

rithms exploiting fast Fourier or similar transforms perform best among the four considered numerical convolution approaches.

To summarize, convolution algorithms exploiting fast Fourier or similar transforms perform best for relevant systems among the four considered numerical convolution approaches.

A.6 Conclusion

This work serves as a guide on efficient numerical implementations of classical DFT methods in Cartesian, cylindrical and spherical coordinates using the convolution theorem of the Fourier transform. Applied to Helmholtz energy functionals expressed in terms of weighted densities, this allows for fast and easy DFT calculations using off-the-shelf algorithms: fast Fourier, Hankel, sine and cosine transforms. Especially for two- and three-dimensional problems, using Fourier space convolution simplifies computation of multi-dimensional convolution integrals compared to real space methods.

References

[1] M. G. Knepley, D. A. Karpeev, S. Davidovits, R. S. Eisenberg, and D. Gillespie. An efficient algorithm for classical density functional theory in three dimensions: Ionic solutions. *The Journal of Chemical Physics*, **132**(12):124101, 2010. doi:10.1063/1.3357981.

[2] Y. Rosenfeld. Free-energy model for the inhomogeneous hard-sphere fluid mixture and density-functional theory of freezing. *Physical Review Letters*, **63**:980–983, 1989. doi:10.1103/PhysRevLett.63.980.

[3] L. J. D. Frink, A. G. Salinger, M. P. Sears, J. D. Weinhold, and A. L. Frischknecht. Numerical challenges in the application of density functional theory to biology and nanotechnology. *Journal of Physics: Condensed Matter*, **14**(46):12167, 2002. doi:10.1088/0953-8984/14/46/320.

[4] L. J. D. Frink, M. G. Martin, A. G. Salinger, and M. A. Heroux. High performance computing for the application of molecular theories to biological systems. *Journal of Physics: Conference Series*, **46**(1):304–306, 2006. doi:10.1088/1742-6596/46/1/042.

[5] M. P. Sears and L. J. Frink. A new efficient method for density functional theory calculations of inhomogeneous fluids. *Journal of Computational Physics*, **190**(1):184–200, 2003. doi:10.1016/S0021-9991(03)00270-5.

[6] S. P. Hlushak, W. Rżysko, and S. Sokołowski. Density functional study of flexible chain molecules at curved surfaces. *The Journal of Chemical Physics*, **131**(9):094904, 2009. doi:10.1063/1.3213623.

[7] S. P. Hlushak, C. McCabe, and P. T. Cummings. Fourier space approach to the classical density functional theory for multi-Yukawa and square-well fluids. *The Journal of Chemical Physics*, **137**(10):104104, 2012. doi:10.1063/1.4749381.

[8] S. P. Hlushak, P. T. Cummings, and C. McCabe. Comparison of several classical density functional theories for the adsorption of flexible chain molecules into cylindrical nanopores. *The Journal of Chemical Physics*, **139**(23):234902, 2013. doi:10.1063/1.4843655.

[9] M. Oettel, S. Görig, A. Härtel, H. Löwen, M. Radu, and T. Schilling. Free energies, vacancy concentrations, and density distribution anisotropies in hard-sphere crystals: A combined density functional and simulation study. *Physical Review E*, **82**:051404, 2010. doi:10.1103/PhysRevE.82.051404.

[10] M. Oettel, S. Dorosz, M. Berghoff, B. Nestler, and T. Schilling. Description of hard-sphere crystals and crystal-fluid interfaces: A comparison between density functional approaches and a phase-field crystal model. *Physical Review E*, **86**:021404, 2012. doi:10.1103/PhysRevE.86.021404.

[11] X. Wang, J. Mi, and C. Zhong. Density functional theory for crystal-liquid interfaces of Lennard-Jones fluid. *The Journal of Chemical Physics*, **138**(16):164704, 2013. doi:10.1063/1.4802633.

[12] M. Levesque, R. Vuilleumier, and D. Borgis. Scalar fundamental measure theory for hard spheres

in three dimensions: Application to hydrophobic solvation. *The Journal of Chemical Physics*, **137**(3):034115, 2012. doi:10.1063/1.4734009.

[13] Y. Liu, S. Zhao, and J. Wu. A Site Density Functional Theory for Water: Application to Solvation of Amino Acid Side Chains. *Journal of Chemical Theory and Computation*, **9**(4):1896–1908, 2013. doi:10.1021/ct3010936.

[14] D. Zhou, J. Mi, and C. Zhong. Three-Dimensional Density Functional Study of Heterogeneous Nucleation of Droplets on Solid Surfaces. *The Journal of Physical Chemistry B*, **116**(48):14100–14106, 2012. doi:10.1021/jp307820w.

[15] A. González, J. A. White, F. L. Román, and S. Velasco. Density functional theory of fluids in nanopores: Analysis of the fundamental measures theory in extreme dimensional-crossover situations. *The Journal of Chemical Physics*, **125**(6):064703, 2006. doi:10.1063/1.2227389.

[16] A. Malijevský. Fundamental measure theory in cylindrical geometry. *The Journal of Chemical Physics*, **126**(13):134710, 2007. doi:10.1063/1.2713106.

[17] N. J. Mariani, C. Mocciaro, M. A. Campesi, and G. F. Barreto. On the computation of fundamental measure theory in pores with cylindrical symmetry. *The Journal of Chemical Physics*, **132**(20):204104, 2010. doi:10.1063/1.3425873.

[18] V. Boţan, F. Pesth, T. Schilling, and M. Oettel. Hard-sphere fluids in annular wedges: Density distributions and depletion potentials. *Physical Review E*, **79**:061402, 2009. doi:10.1103/PhysRevE.79.061402.

[19] R. Roth. Fundamental measure theory for hard-sphere mixtures: a review. *Journal of Physics: Condensed Matter*, **22**(6):063102, 2010. doi:10.1088/0953-8984/22/6/063102.

[20] P. Yatsyshin, N. Savva, and S. Kalliadasis. Spectral methods for the equations of classical density-functional theory: Relaxation dynamics of microscopic films. *The Journal of Chemical Physics*, **136**(12):124113, 2012. doi:10.1063/1.3697471.

[21] P. Yatsyshin, N. Savva, and S. Kalliadasis. Wetting of prototypical one- and two-dimensional systems: Thermodynamics and density functional theory. *The Journal of Chemical Physics*, **142**(3):034708, 2015. doi:10.1063/1.4905605.

[22] A. Nold, B. D. Goddard, P. Yatsyshin, N. Savva, and S. Kalliadasis. Pseudospectral methods for density functional theory in bounded and unbounded domains. *Journal of Computational Physics*, **334**:639–664, 2017. doi:10.1016/j.jcp.2016.12.023.

[23] X. Xu and D. Cao. Multiscaled density-functional theory for helical polymers. *The Journal of Chemical Physics*, **131**(5):054901, 2009. doi:10.1063/1.3197004.

[24] A. Kovalenko, S. Ten-no, and F. Hirata. Solution of three-dimensional reference interaction site model and hypernetted chain equations for simple point charge water by modified method of direct inversion in iterative subspace. *Journal of Computational Chemistry*, **20**(9):928–936, 1999.

doi:10.1002/(SICI)1096-987X(19990715)20:9<928::AID-JCC4>3.0.CO;2-X.

[25] L. J. D. Frink and A. G. Salinger. Two- and Three-Dimensional Nonlocal Density Functional Theory for Inhomogeneous Fluids. *Journal of Computational Physics*, **159**(2):407–424, 2000. doi:10.1006/jcph.2000.6454.

[26] L. J. D. Frink and A. G. Salinger. Two- and Three-Dimensional Nonlocal Density Functional Theory for Inhomogeneous Fluids. *Journal of Computational Physics*, **159**(2):425–439, 2000. doi:10.1006/jcph.2000.6455.

[27] L. J. D. Frink, A. L. Frischknecht, M. A. Heroux, M. L. Parks, and A. G. Salinger. Toward Quantitative Coarse-Grained Models of Lipids with Fluids Density Functional Theory. *Journal of Chemical Theory and Computation*, **8**(4):1393–1408, 2012. doi:10.1021/ct200707b.

[28] J. Mairhofer and J. Gross. Numerical aspects of classical density functional theory for one-dimensional vapor-liquid interfaces. *Fluid Phase Equilibria*, **444**:1–12, 2017. doi:10.1016/j.fluid.2017.03.023.

[29] J. Gross and G. Sadowski. Application of perturbation theory to a hard-chain reference fluid: an equation of state for square-well chains. *Fluid Phase Equilibria*, **168**(2):183–199, 2000. doi:10.1016/S0378-3812(00)00302-2.

[30] J. Gross and G. Sadowski. Perturbed-Chain SAFT: An Equation of State Based on a Perturbation Theory for Chain Molecules. *Industrial & Engineering Chemistry Research*, **40**(4):1244–1260, 2001. doi:10.1021/ie0003887.

[31] J. Gross and G. Sadowski. Modeling Polymer Systems Using the Perturbed-Chain Statistical Associating Fluid Theory Equation of State. *Industrial & Engineering Chemistry Research*, **41**(5):1084–1093, 2002. doi:10.1021/ie010449g.

[32] J. Gross and G. Sadowski. Application of the Perturbed-Chain SAFT Equation of State to Associating Systems. *Industrial & Engineering Chemistry Research*, **41**(22):5510–5515, 2002. doi:10.1021/ie010954d.

[33] M. S. Wertheim. Fluids with highly directional attractive forces. I. Statistical thermodynamics. *Journal of Statistical Physics*, **35**(1):19–34, 1984. doi:10.1007/BF01017362.

[34] M. S. Wertheim. Fluids with highly directional attractive forces. II. Thermodynamic perturbation theory and integral equations. *Journal of Statistical Physics*, **35**(1):35–47, 1984. doi:10.1007/BF01017363.

[35] M. S. Wertheim. Fluids with highly directional attractive forces. III. Multiple attraction sites. *Journal of Statistical Physics*, **42**(3):459–476, 1986. doi:10.1007/BF01127721.

[36] M. S. Wertheim. Fluids with highly directional attractive forces. IV. Equilibrium polymerization. *Journal of Statistical Physics*, **42**(3):477–492, 1986. doi:10.1007/BF01127722.

[37] W. G. Chapman, G. Jackson, and K. E. Gubbins. Phase equilibria of associating fluids. *Molecular*

Physics, **65**(5):1057–1079, 1988. doi:10.1080/00268978800101601.

[38] J. Gross. An equation-of-state contribution for polar components: Quadrupolar molecules. *AIChE Journal*, **51**(9):2556–2568, 2005. doi:10.1002/aic.10502.

[39] J. Gross and J. Vrabec. An equation-of-state contribution for polar components: Dipolar molecules. *AIChE Journal*, **52**(3):1194–1204, 2006. doi:10.1002/aic.10683.

[40] J. Vrabec and J. Gross. Vapor–Liquid Equilibria Simulation and an Equation of State Contribution for Dipole–Quadrupole Interactions. *The Journal of Physical Chemistry B*, **112**(1):51–60, 2008. doi:10.1021/jp072619u.

[41] J. Gross. A density functional theory for vapor-liquid interfaces using the PCP-SAFT equation of state. *The Journal of Chemical Physics*, **131**(20):204705, 2009. doi:10.1063/1.3263124.

[42] C. Klink and J. Gross. A Density Functional Theory for Vapor–Liquid Interfaces of Mixtures Using the Perturbed-Chain Polar Statistical Associating Fluid Theory Equation of State. *Industrial & Engineering Chemistry Research*, **53**(14):6169–6178, 2014. doi:10.1021/ie4029895.

[43] C. Klink, B. Planková, and J. Gross. Density Functional Theory for Liquid–Liquid Interfaces of Mixtures Using the Perturbed-Chain Polar Statistical Associating Fluid Theory Equation of State. *Industrial & Engineering Chemistry Research*, **54**(16):4633–4642, 2015. doi:10.1021/acs.iecr.5b00445.

[44] C. Klink, C. Waibel, and J. Gross. Analysis of Interfacial Transport Resistivities of Pure Components and Mixtures Based on Density Functional Theory. *Industrial & Engineering Chemistry Research*, **54**(45):11483–11492, 2015. doi:10.1021/acs.iecr.5b03270.

[45] G. Lamanna, C. Steinhausen, B. Weigand, A. Preusche, B. Bork, A. Dreizler, R. Stierle, and J. Gross. On the importance of non-equilibrium models for describing the coupling of heat and mass transfer at high pressure. *International Communications in Heat and Mass Transfer*, **98**:49–58, 2018. doi:10.1016/j.icheatmasstransfer.2018.07.012.

[46] E. Sauer and J. Gross. Classical Density Functional Theory for Liquid–Fluid Interfaces and Confined Systems: A Functional for the Perturbed-Chain Polar Statistical Associating Fluid Theory Equation of State. *Industrial & Engineering Chemistry Research*, **56**(14):4119–4135, 2017. doi:10.1021/acs.iecr.6b04551.

[47] E. Sauer, A. Terzis, M. Theiss, B. Weigand, and J. Gross. Prediction of Contact Angles and Density Profiles of Sessile Droplets Using Classical Density Functional Theory Based on the PCP-SAFT Equation of State. *Langmuir*, **34**(42):12519–12531, 2018. doi:10.1021/acs.langmuir.8b01985.

[48] G. Shen, X. Ji, and X. Lu. A hybrid perturbed-chain SAFT density functional theory for representing fluid behavior in nanopores. *The Journal of Chemical Physics*, **138**(22):224706, 2013. doi:10.1063/1.4808160.

[49] G. Shen, X. Ji, S. Öberg, and X. Lu. A hybrid perturbed-chain SAFT density functional the-

ory for representing fluid behavior in nanopores: Mixtures. *The Journal of Chemical Physics*, **139**(19):194705, 2013. doi:10.1063/1.4825078.

[50] Z. Ye, J. Cai, H. Liu, and Y. Hu. Density and chain conformation profiles of square-well chains confined in a slit by density-functional theory. *The Journal of Chemical Physics*, **123**(19):194902, 2005. doi:10.1063/1.2117009.

[51] X. Xu, D. E. Cristancho, S. Costeux, and Z.-G. Wang. Density-functional theory for polymer-carbon dioxide mixtures: A perturbed-chain SAFT approach. *The Journal of Chemical Physics*, **137**(5):054902, 2012. doi:10.1063/1.4742346.

[52] E. W. Hansen. Fast Hankel transform algorithm. *IEEE Transactions on Acoustics, Speech, and Signal Processing*, **33**(3):666–671, 1985. doi:10.1109/TASSP.1985.1164579.

[53] E. W. Hansen. Correction to "Fast Hankel transform algorithm". *IEEE Transactions on Acoustics, Speech, and Signal Processing*, **34**(3):623–624, 1986. doi:10.1109/TASSP.1986.1164860.

[54] E. W. Hansen and P.-L. Law. Recursive methods for computing the Abel transform and its inverse. *J. Opt. Soc. Am. A*, **2**(4):510–520, 1985. doi:10.1364/JOSAA.2.000510.

[55] R. Roth, R. Evans, A. Lang, and G. Kahl. Fundamental measure theory for hard-sphere mixtures revisited: the White Bear version. *Journal of Physics: Condensed Matter*, **14**(46):12063, 2002. doi:10.1088/0953-8984/14/46/313.

[56] Y.-X. Yu and J. Wu. Structures of hard-sphere fluids from a modified fundamental-measure theory. *The Journal of Chemical Physics*, **117**(22):10156–10164, 2002. doi:10.1063/1.1520530.

[57] T. Boublík. Hard-Sphere Equation of State. *The Journal of Chemical Physics*, **53**(1):471–472, 1970. doi:10.1063/1.1673824.

[58] G. A. Mansoori, N. F. Carnahan, K. E. Starling, and T. W. L. Jr. Equilibrium Thermodynamic Properties of the Mixture of Hard Spheres. *The Journal of Chemical Physics*, **54**(4):1523–1525, 1971. doi:10.1063/1.1675048.

[59] S. Tripathi and W. G. Chapman. Microstructure and Thermodynamics of Inhomogeneous Polymer Blends and Solutions. *Physical Review Letters*, **94**:087801, 2005. doi:10.1103/PhysRevLett.94.087801.

[60] S. Tripathi and W. G. Chapman. Microstructure of inhomogeneous polyatomic mixtures from a density functional formalism for atomic mixtures. *The Journal of Chemical Physics*, **122**(9):094506, 2005. doi:10.1063/1.1853371.

[61] E. Kierlik and M. L. Rosinberg. A perturbation density functional theory for polyatomic fluids. II. Flexible molecules. *The Journal of Chemical Physics*, **99**(5):3950–3965, 1993. doi:10.1063/1.466142.

[62] P. N. Swarztrauber. Vectorizing the FFTs. In G. Rodrigue (editor), *Parallel Computations*, pages 51–83. Academic Press, New York, 1982. doi:10.1016/B978-0-12-592101-5.50007-5.

[63] P. N. Swarztrauber. FFT algorithms for vector computers. *Parallel Computing*, **1**(1):45–63, 1984. doi:10.1016/S0167-8191(84)90413-7.

[64] T. Butz. *Fourier Transformation for Pedestrians*. Springer, 2006. doi:10.1007/978-3-319-16985-9.

B Supporting Information Appendices: Guide to Efficient Solution of PC-SAFT Classical Density Functional Theory in Various Coordinate Systems Using Fast Fourier and Similar Transforms

The content of this appendix is a literal quote of the appendix of the supporting information:

R. Stierle, E. Sauer, J. Eller, M. Theiss, P. Rehner, P. Ackermann, and J. Gross. Supporting Information: Guide to efficient Solution of PC-SAFT classical Density Functional Theory in various Coordinate Systems using fast Fourier and similar Transforms. *Fluid Phase Equilibria*, **504**:112306, 2020. doi:10.1016/j.fluid.2019.112306

B.1 Fourier Transform of Weight Functions

The analytically transformed weight functions for FMT, eq. (B.1), hard-chain contribution, eq. (B.2), and dispersion contribution, eq. (B.3), using a functional representation including sine and cosine, are calculated as

$$\hat{\omega}_i^0(\mathbf{k}) = \frac{\sin(2\pi R_i|\mathbf{k}|)}{2\pi R_i|\mathbf{k}|} \tag{B.1a}$$

$$\hat{\omega}_i^1(\mathbf{k}) = \frac{\sin(2\pi R_i|\mathbf{k}|)}{2\pi|\mathbf{k}|} \tag{B.1b}$$

$$\hat{\omega}_i^2(\mathbf{k}) = \frac{2R_i\sin(2\pi R_i|\mathbf{k}|)}{|\mathbf{k}|} \tag{B.1c}$$

$$\hat{\omega}_i^3(\mathbf{k}) = \frac{1}{2\pi^2|\mathbf{k}|^3}\big(\sin(2\pi R_i|\mathbf{k}|) - 2\pi R_i|\mathbf{k}|\cos(2\pi R_i|\mathbf{k}|)\big) \tag{B.1d}$$

$$\hat{\omega}_i^{V1}(\mathbf{k}) = \frac{-\mathrm{i}\,\mathbf{k}}{2R_i}\hat{\omega}_i^3(\mathbf{k}) \tag{B.1e}$$

$$\hat{\omega}_i^{V2}(\mathbf{k}) = -\mathrm{i}\,2\pi\mathbf{k}\hat{\omega}_i^3(\mathbf{k}) \tag{B.1f}$$

$$\hat{\omega}_i^{\mathrm{hc},\rho}(\mathbf{k}) = \frac{3}{64\pi^3 R_i^3 |\mathbf{k}|^3}\Big(\sin(4\pi R_i|\mathbf{k}|) - 4\pi R_i|\mathbf{k}|\cos(4\pi R_i|\mathbf{k}|)\Big) \tag{B.2a}$$

$$\hat{\omega}_i^{\mathrm{hc},\lambda}(\mathbf{k}) = \frac{\sin(4\pi R_i|\mathbf{k}|)}{4\pi R_i|\mathbf{k}|} \tag{B.2b}$$

$$\hat{\omega}_i^{\mathrm{disp}}(\mathbf{k}) = \frac{3}{64\pi^3 \psi^3 R_i^3 |\mathbf{k}|^3}\Big(\sin(4\pi\psi R_i|\mathbf{k}|) - 4\pi\psi R_i|\mathbf{k}|\cos(4\pi\psi R_i|\mathbf{k}|)\Big) \tag{B.3}$$

For $\mathbf{k} \to 0$, the limits can be calculated according to

$$\lim_{\mathbf{k}\to 0} \hat{\omega}_i^0(\mathbf{k}) = 1 \tag{B.4a}$$

$$\lim_{\mathbf{k}\to 0} \hat{\omega}_i^1(\mathbf{k}) = R_i \tag{B.4b}$$

$$\lim_{\mathbf{k}\to 0} \hat{\omega}_i^2(\mathbf{k}) = 4\pi R_i^2 \tag{B.4c}$$

$$\lim_{\mathbf{k}\to 0} \hat{\omega}_i^3(\mathbf{k}) = \frac{4}{3}\pi R_i^3 \tag{B.4d}$$

$$\lim_{\mathbf{k}\to 0} \hat{\omega}_i^{\mathrm{V1}}(\mathbf{k}) = 0 \tag{B.4e}$$

$$\lim_{\mathbf{k}\to 0} \hat{\omega}_i^{\mathrm{V2}}(\mathbf{k}) = 0 \tag{B.4f}$$

$$\lim_{\mathbf{k}\to 0} \hat{\omega}_i^{\mathrm{hc},\rho}(\mathbf{k}) = 1 \tag{B.5a}$$

$$\lim_{\mathbf{k}\to 0} \hat{\omega}_i^{\mathrm{hc},\lambda}(\mathbf{k}) = 1 \tag{B.5b}$$

$$\lim_{\mathbf{k}\to 0} \hat{\omega}_i^{\mathrm{disp}}(\mathbf{k}) = 1 \tag{B.6}$$

B.2 Fourier Transform for Calculation of Convolution Integrals

All convolution integrals occurring throughout this work are convolutions of either a functional derivative of the Helmholtz energy, or a density, with a suitable weight function ω. These convolution integrals can be calculated efficiently using fast Fourier transform algorithms. In this appendix, the Fourier transform $\mathcal{F}$ and its inverse $\mathcal{F}^{-1}$ in different coordinate systems are derived in pedagogical detail.

In Cartesian coordinates the standard fast Fourier transform can be used for all directions (for 1-D, 2-D and 3-D systems). For cylindrical coordinates, rotational symmetry (2-D) can be exploited, such that one can use the standard fast Fourier transform for the axial direction and the fast Hankel transform (of order 0 and 1 for scalar and vector weighted functions, respectively) for the radial direction. In cylindrical coordinates (1-D), only fast Hankel transforms are used. For spherically symmetric systems (1-D), fast sine/cosine transforms are used for the calculation of the Fourier and the inverse Fourier transform.

In the following, we lay out the details of how to compute the Fourier and inverse Fourier transform for Cartesian (1-D, 2-D & 3-D), cylindrical (2-D), cylindrical and spherical (1-D) coordinates. Detailed derivations are presented to show consistency of the approach and facilitate own implementations of DFT methods. The Fourier and inverse Fourier transform are defined as

$$\hat{\mathfrak{f}}(\mathbf{k}) = \int \mathfrak{f}(\mathbf{r}) \mathrm{e}^{-2\pi \mathrm{i}\,\mathbf{r}\cdot\mathbf{k}}\,\mathrm{d}\mathbf{r} \tag{B.7a}$$

$$\mathfrak{f}(\mathbf{r}) = \int \hat{\mathfrak{f}}(\mathbf{k}) \mathrm{e}^{2\pi \mathrm{i}\,\mathbf{r}\cdot\mathbf{k}}\,\mathrm{d}\mathbf{k} \tag{B.7b}$$

with $\mathfrak{f}$ as the function to be transformed, the imaginary unit i, and the position vector in real and Fourier space $\mathbf{r}$ and $\mathbf{k}$, respectively. Here, $\mathbf{r}\cdot\mathbf{k}$ stands for the dot product of two vectors, and the circumflex ($\hat{}$) indicates the function being considered in Fourier space. By exploiting symmetry in the appropriate coordinate system, the Fourier transform from eq. (B.7a) can be used for the derivation of the appropriate integral transform. In the following, integral transforms for Cartesian, cylindrical and spherical coordinates are calculated for scalar and vector-valued functions $\mathfrak{f} = \{f, \mathbf{f}\}$, respectively.

B.2.1 Cartesian Coordinates

The Fourier transform is formulated in Cartesian coordinates, therefore, the Cartesian vectors are used for the dot product of $\mathbf{r}$ and $\mathbf{k}$, leading to

$$\mathbf{r}\cdot\mathbf{k} = \begin{pmatrix} x \\ y \\ z \end{pmatrix} \cdot \begin{pmatrix} k_x \\ k_y \\ k_z \end{pmatrix} = x k_x + y k_y + z k_z \tag{B.8}$$

and the volume integral in eq. (B.7a) simplifies to a triple integral with volume element $\mathrm{d}\mathbf{r} = \mathrm{d}x\,\mathrm{d}y\,\mathrm{d}z$, leading to

$$\begin{aligned}\hat{\mathfrak{f}}(k_x,k_y,k_z) &= \int_{z=-\infty}^{\infty}\int_{y=-\infty}^{\infty}\int_{x=-\infty}^{\infty} \mathfrak{f}(x,y,z)\mathrm{e}^{-2\pi\mathrm{i}xk_x}\,\mathrm{d}x\mathrm{e}^{-2\pi\mathrm{i}yk_y}\,\mathrm{d}y\,\mathrm{e}^{-2\pi\mathrm{i}zk_z}\,\mathrm{d}z \\ &= \mathcal{F}_x\mathcal{F}_y\mathcal{F}_z\left[\mathfrak{f}(x,y,z)\right] \end{aligned} \tag{B.9}$$

The inverse Fourier transform is computed similarly according to

$$\begin{aligned}\mathfrak{f}(x,y,z) &= \int_{k_z=-\infty}^{\infty}\int_{k_y=-\infty}^{\infty}\int_{k_x=-\infty}^{\infty} \hat{\mathfrak{f}}(k_x,k_y,k_z)\mathrm{e}^{2\pi\mathrm{i}xk_x}\,\mathrm{d}k_x\mathrm{e}^{2\pi\mathrm{i}yk_y}\,\mathrm{d}k_y\,\mathrm{e}^{2\pi\mathrm{i}zk_z}\,\mathrm{d}k_z \\ &= \mathcal{F}_x^{-1}\mathcal{F}_y^{-1}\mathcal{F}_z^{-1}\left[\hat{\mathfrak{f}}(k_x,k_y,k_z)\right] \end{aligned} \tag{B.10}$$

B.2.1.1 Fourier Transform of Scalar Quantities

The x-, y- and z-direction of the Fourier transform can be separated according to

$$\hat{f}(k_x,k_y,k_z) = \mathcal{F}_x\mathcal{F}_y\mathcal{F}_z\left[f(x,y,z)\right] \tag{B.11}$$

yielding a Fourier transform in each direction.

B.2.1.2 Inverse Fourier Transform of Scalar Quantities

The inverse transform can be treated analogously, leading to

$$f(x,y,z) = \mathcal{F}_x^{-1}\mathcal{F}_y^{-1}\mathcal{F}_z^{-1}\left[\hat{f}(k_x,k_y,k_z)\right] \tag{B.12}$$

B.2.1.3 Fourier Transform of Vector Quantities

The Fourier transform of vector quantities is performed by splitting the vector into its different contributions depending on the underlying coordinate system. For the case of Cartesian unit vectors

$$\mathbf{e}_x = \begin{pmatrix}1\\0\\0\end{pmatrix}, \mathbf{e}_y = \begin{pmatrix}0\\1\\0\end{pmatrix}, \mathbf{e}_z = \begin{pmatrix}0\\0\\1\end{pmatrix} \tag{B.13}$$

the vector-valued function $\mathbf{f}$ can be represented according to

$$\mathbf{f}(x,y,z) = \begin{pmatrix} f_x \\ f_y \\ f_z \end{pmatrix} = f_x \mathbf{e}_x + f_y \mathbf{e}_y + f_z \mathbf{e}_z \tag{B.14}$$

Although this detailed treatment may not be necessary here, we include it nonetheless, as it will help to understand the forthcoming treatment in cylindrical and spherical coordinates. The Fourier transform of $\mathbf{f}$ is calculated via

$$\hat{\mathbf{f}}(k_x,k_y,k_z) = \int_{z=-\infty}^{\infty} \int_{y=-\infty}^{\infty} \int_{x=-\infty}^{\infty} \begin{pmatrix} f_x(x,y,z) \\ f_y(x,y,z) \\ f_z(x,y,z) \end{pmatrix} \mathrm{e}^{-2\pi \mathrm{i} x k_x} \,\mathrm{d}x \, \mathrm{e}^{-2\pi \mathrm{i} y k_y} \,\mathrm{d}y \, \mathrm{e}^{-2\pi \mathrm{i} z k_z} \,\mathrm{d}z \tag{B.15}$$

or element-wise, as

$$\hat{\mathbf{f}}(k_x,k_y,k_z) = \begin{pmatrix} \hat{f}_{k_x}(k_x,k_y,k_z) \\ \hat{f}_{k_y}(k_x,k_y,k_z) \\ \hat{f}_{k_z}(k_x,k_y,k_z) \end{pmatrix} = \begin{pmatrix} \mathcal{F}_x \mathcal{F}_y \mathcal{F}_z \left[f_x(x,y,z) \right] \\ \mathcal{F}_x \mathcal{F}_y \mathcal{F}_z \left[f_y(x,y,z) \right] \\ \mathcal{F}_x \mathcal{F}_y \mathcal{F}_z \left[f_z(x,y,z) \right] \end{pmatrix} \tag{B.16}$$

Each of the elements of the vector-valued function can be transformed to Fourier space individually and, just as for scalar-valued functions, can be transformed for every direction separately.

B.2.1.4 Inverse Fourier Transform of Vector Quantities

Treatment of the inverse transform of a vector quantity is analogous to the treatment laid out in the previous section, i.e., with the Cartesian unit vectors in Fourier space

$$\mathbf{e}_{k_x} = \begin{pmatrix} 1 \\ 0 \\ 0 \end{pmatrix}, \mathbf{e}_{k_y} = \begin{pmatrix} 0 \\ 1 \\ 0 \end{pmatrix}, \mathbf{e}_{k_z} = \begin{pmatrix} 0 \\ 0 \\ 1 \end{pmatrix} \tag{B.17}$$

the vector-valued function $\hat{\mathbf{f}}$ can be represented according to

$$\hat{\mathbf{f}}(k_x,k_y,k_z) = \begin{pmatrix} \hat{f}_{k_x} \\ \hat{f}_{k_y} \\ \hat{f}_{k_z} \end{pmatrix} = \hat{f}_{k_x} \mathbf{e}_{k_x} + \hat{f}_{k_y} \mathbf{e}_{k_y} + \hat{f}_{k_z} \mathbf{e}_{k_z} \tag{B.18}$$

The inverse Fourier transform of $\hat{\mathbf{f}}$ is calculated as

$$\begin{aligned}\mathbf{f}(x,y,z) &= \int_{k_z=-\infty}^{\infty}\int_{k_y=-\infty}^{\infty}\int_{k_x=-\infty}^{\infty}\begin{pmatrix}\hat{f}_{k_x}(k_x,k_y,k_z)\\ \hat{f}_{k_y}(k_x,k_y,k_z)\\ \hat{f}_{k_z}(k_x,k_y,k_z)\end{pmatrix} \mathrm{e}^{2\pi \mathrm{i} x k_x}\,\mathrm{d}k_x\,\mathrm{e}^{2\pi \mathrm{i} y k_y}\,\mathrm{d}k_y\,\mathrm{e}^{2\pi \mathrm{i} z k_z}\,\mathrm{d}k_z \\ &= \begin{pmatrix}f_x(x,y,z)\\ f_y(x,y,z)\\ f_z(,y,z)\end{pmatrix} = \begin{pmatrix}\mathcal{F}_x^{-1}\mathcal{F}_y^{-1}\mathcal{F}_z^{-1}\left[\hat{f}_{k_x}(k_x,k_y,k_z)\right]\\ \mathcal{F}_x^{-1}\mathcal{F}_y^{-1}\mathcal{F}_z^{-1}\left[\hat{f}_{k_y}(k_x,k_y,k_z)\right]\\ \mathcal{F}_x^{-1}\mathcal{F}_y^{-1}\mathcal{F}_z^{-1}\left[\hat{f}_{k_z}(k_x,k_y,k_z)\right]\end{pmatrix}\end{aligned} \tag{B.19}$$

Each of the elements of the vector-valued function can be transformed to Fourier space individually and, just as for scalar-valued functions, can be transformed for every direction consecutively.

B.2.1.5 Treatment of 1-D & 2-D Cartesian Coordinates

Fourier transform of 1-D or 2-D Cartesian coordinates can be understood as a subset of the 3-D Fourier transform. The dot product in eq. (B.8) for one dimension in x-direction is $\mathbf{r}\cdot\mathbf{k} = xk_x$. This simplifies the Fourier, eq. (B.9), and inverse Fourier transform, eq. (B.10), to $\hat{\mathfrak{f}}(k_x) = \mathcal{F}_x[\mathfrak{f}(x)]$ and $\mathfrak{f}(x) = \mathcal{F}_x^{-1}\left[\hat{\mathfrak{f}}(k_x)\right]$, respectively. The Fourier and its inverse transform of a scalar quantity result in

$$\hat{f}(k_x) = \mathcal{F}_x[f(x)] \tag{B.20a}$$

$$f(x) = \mathcal{F}_x^{-1}\left[\hat{f}(k_x)\right] \tag{B.20b}$$

For a vector quantity, the Fourier and its inverse transform yield

$$\hat{\mathbf{f}}(k_x) = \mathcal{F}_x[f_x(x)] \tag{B.21a}$$

$$\mathbf{f}(x) = \mathcal{F}_x^{-1}\left[\hat{f}_{k_x}(k_x)\right] \tag{B.21b}$$

2-D Cartesian coordinates are the consequence of disregarding one dimension from the general 3-D case.

B.2.2 Cylindrical Coordinates

In cylindrical coordinates, the dot product $\mathbf{r}\cdot\mathbf{k}$ is calculated as

$$\mathbf{r}\cdot\mathbf{k} = \begin{pmatrix} r\cos\varphi \\ r\sin\varphi \\ z \end{pmatrix} \cdot \begin{pmatrix} k_r\cos k_\varphi \\ k_r\sin k_\varphi \\ k_z \end{pmatrix} \tag{B.22}$$

with the radial coordinate r and k_r in the polar plane, the azimuthal angle φ and k_φ, and the axial direction z and k_z, in real and Fourier space, respectively. The identity $\cos\varphi\cos k_\varphi + \sin\varphi\sin k_\varphi = \cos(\varphi - k_\varphi) = \cos(k_\varphi - \varphi)$ simplifies eq. (B.22) to

$$\mathbf{r}\cdot\mathbf{k} = r k_r\cos\varphi + z k_z \tag{B.23}$$

where we chose a $\mathbf{k}$-vector parallel to the k_x-axis in Fourier space which implies $k_\varphi = 0$. With the volume element $\mathrm{d}\mathbf{r} = r\,\mathrm{d}\varphi\,\mathrm{d}r\,\mathrm{d}z$, and the result of eq. (B.23), the Fourier transform from eq. (B.7a) can be written as

$$\hat{\mathfrak{f}}(k_r,k_z) = \int_{z=-\infty}^{\infty}\int_{r=0}^{\infty} \mathfrak{f}(r,z) \int_{\varphi=0}^{2\pi} \mathrm{e}^{-2\pi\mathrm{i}\,r k_r\cos\varphi}\,\mathrm{d}\varphi\; r\;\mathrm{d}r\,\mathrm{e}^{-2\pi\mathrm{i}\,z k_z}\,\mathrm{d}z \tag{B.24}$$

The inverse Fourier transform can be computed analogously, leading to

$$\mathfrak{f}(r,z) = \int_{k_z=-\infty}^{\infty}\int_{k_r=0}^{\infty} \hat{\mathfrak{f}}(k_r,k_z) \int_{k_\varphi=0}^{2\pi} \mathrm{e}^{2\pi\mathrm{i}\,r k_r\cos k_\varphi}\,\mathrm{d}k_\varphi\; k_r\;\mathrm{d}k_r\,\mathrm{e}^{2\pi\mathrm{i}\,z k_z}\,\mathrm{d}k_z \tag{B.25}$$

B.2.2.1 Cylindrical Fourier Transform of Scalar Quantities

We consider cases of rotational symmetry, where the integral in eq. (B.24) simplifies through integration. With the definition of the Bessel function of first kind and zeroth order

$$\mathrm{J}_0(\xi) = \frac{1}{2\pi}\int_{\varphi=0}^{2\pi} \mathrm{e}^{\mathrm{i}\,\xi\cos\varphi}\,\mathrm{d}\varphi \tag{B.26}$$

with dummy variable ξ and the identity $\mathrm{J}_0(-\xi) = \mathrm{J}_0(\xi)$, the Fourier transform from eq. (B.24) simplifies to

$$\hat{f}(k_r, k_z) = \int_{z=-\infty}^{\infty} 2\pi \int_{r=0}^{\infty} f(r,z) r \mathrm{J}_0(2\pi r k_r)\,\mathrm{d}r\, \mathrm{e}^{-2\pi \mathrm{i} z k_z}\,\mathrm{d}z \tag{B.27}$$

The integration over the r-coordinate can be performed using the Hankel transform $\mathcal{H}$, which for order ν is defined as

$$\mathcal{H}_\nu[f(r)] = 2\pi \int_0^{\infty} f(r) r \mathrm{J}_\nu(2\pi r k_r)\,\mathrm{d}r \tag{B.28}$$

with the Bessel function of first kind and ν-th order J_ν. Performing the integration over z using the Fourier transform $\mathcal{F}_z$, the Fourier transform of $f(r,z)$ follows as

$$\hat{f}(k_r, k_z) = \mathcal{F}_z \mathcal{H}_0[f(r,z)] \tag{B.29}$$

B.2.2.2 Cylindrical Inverse Fourier Transform of Scalar Quantities

Because the Bessel function of first kind and zeroth order is even $\mathrm{J}_0(\xi) = \mathrm{J}_0(-\xi)$, the inverse Fourier transform $\hat{f}(k_r, k_z)$ can be computed analogous to the previous section as

$$f(r,z) = \mathcal{F}_z^{-1} \mathcal{H}_0^{-1}\left[\hat{f}(k_r, k_z)\right] \tag{B.30}$$

with the inverse Hankel transform $\mathcal{H}_\nu^{-1}$ of order ν of the k_r-coordinate as

$$\mathcal{H}_\nu^{-1}\left[\hat{f}(k_r)\right] = 2\pi \int_0^{\infty} \hat{f}(k_r) k_r \mathrm{J}_\nu(2\pi r k_r)\,\mathrm{d}k_r \tag{B.31}$$

and the inverse Fourier transform $\mathcal{F}_z^{-1}$ of the k_z-coordinate.

B.2.2.3 Cylindrical Fourier Transform of Vector Quantities

Analogous to appendix B.2.1.3, the Fourier transform of vector quantities in cylindrical coordinates is performed by splitting the vector into its different contributions: radial f_r,

azimuthal f_φ and axial f_z, with their respective unit vectors according to

$$\mathbf{e}_r = \begin{pmatrix} \cos\varphi \\ \sin\varphi \\ 0 \end{pmatrix}, \mathbf{e}_\varphi = \begin{pmatrix} -\sin\varphi \\ \cos\varphi \\ 0 \end{pmatrix}, \mathbf{e}_z = \begin{pmatrix} 0 \\ 0 \\ 1 \end{pmatrix} \tag{B.32}$$

these unit vectors are defined in a Cartesian frame of reference, which allows the Fourier transforms to be treated analogously to the above regarded case in Cartesian coordinates. The vector quantity can then be decomposed into three parts, as

$$\mathbf{f}(r,\varphi,z) = f_r\mathbf{e}_r + f_\varphi\mathbf{e}_\varphi + f_z\mathbf{e}_z \tag{B.33}$$

However, due to rotational symmetry $\mathbf{f}$ is only a function of the radius r and the axial coordinate z, whereas the azimuthal contribution equals zero, $f_\varphi = 0$, leading to

$$\mathbf{f}(r,\varphi,z) = f_r \begin{pmatrix} \cos\varphi \\ \sin\varphi \\ 0 \end{pmatrix} + f_z \begin{pmatrix} 0 \\ 0 \\ 1 \end{pmatrix} \tag{B.34}$$

The Fourier transform of $\mathbf{f}$ is then calculated as

$$\hat{\mathbf{f}}(k_r,k_z) = \int_{z=-\infty}^{\infty}\int_{r=0}^{\infty}\int_{\varphi=0}^{2\pi} \begin{pmatrix} f_r(r,z)\cos\varphi \\ f_r(r,z)\sin\varphi \\ f_z(r,z) \end{pmatrix} \mathrm{e}^{-2\pi\mathrm{i}\,r k_r\cos\varphi}\,\mathrm{d}\varphi\; r\;\mathrm{d}r\,\mathrm{e}^{-2\pi\mathrm{i}zk_z}\,\mathrm{d}z \tag{B.35}$$

With the definition of Bessel's first integral of order ν for Bessel functions of first kind

$$\mathrm{J}_\nu(\xi) = \frac{1}{2\pi\mathrm{i}^{\,\nu}}\int_{\varphi=0}^{2\pi} \mathrm{e}^{\mathrm{i}\,\xi\cos\varphi}\cos(\nu\varphi)\,\mathrm{d}\varphi \tag{B.36}$$

eq. (B.35) simplifies to

$$\hat{\mathbf{f}}(k_r,k_z) = \int_{z=-\infty}^{\infty} 2\pi \int_{r=0}^{\infty} \begin{pmatrix} -\mathrm{i}\,f_r(r,z)\mathrm{J}_1(2\pi r k_r) \\ 0 \\ f_z(r,z)\mathrm{J}_0(2\pi r k_r) \end{pmatrix} r\;\mathrm{d}r\,\mathrm{e}^{-2\pi\mathrm{i}zk_z}\,\mathrm{d}z \tag{B.37}$$

after utilization of $\mathrm{J}_0(-\xi) = \mathrm{J}_0(\xi)$ and $\mathrm{J}_1(-\xi) = -\mathrm{J}_1(\xi)$. Finally, the Hankel transform, eq. (B.28), and the Fourier transform can be exploited, leading to

$$\hat{\mathbf{f}}(k_r, k_z) = \int_{z=-\infty}^{\infty} \begin{pmatrix} \mathcal{H}_1[-\mathrm{i} f_r(r,z)] \\ 0 \\ \mathcal{H}_0[f_z(r,z)] \end{pmatrix} \mathrm{e}^{-2\pi \mathrm{i} z k_z} \,\mathrm{d}z = \begin{pmatrix} \mathcal{F}_z \mathcal{H}_1[-\mathrm{i} f_r(r,z)] \\ 0 \\ \mathcal{F}_z \mathcal{H}_0[f_z(r,z)] \end{pmatrix} \tag{B.38}$$

B.2.2.4 Cylindrical Inverse Fourier Transform of Vector Quantities

Treatment of the inverse transform of a vector quantity is analogous to the treatment laid out in the previous section, i.e., with the unit vectors in cylindrical coordinates in Fourier space

$$\mathbf{e}_{k_r} = \begin{pmatrix} \cos k_\varphi \\ \sin k_\varphi \\ 0 \end{pmatrix}, \mathbf{e}_{k_\varphi} = \begin{pmatrix} -\sin k_\varphi \\ \cos k_\varphi \\ 0 \end{pmatrix}, \mathbf{e}_{k_z} = \begin{pmatrix} 0 \\ 0 \\ 1 \end{pmatrix} \tag{B.39}$$

the vector-valued function $\hat{\mathbf{f}}$ can be represented according to

$$\hat{\mathbf{f}}(k_r, k_\varphi, k_z) = \hat{f}_{k_r} \mathbf{e}_{k_r} + \hat{f}_{k_\varphi} \mathbf{e}_{k_\varphi} + \hat{f}_{k_z} \mathbf{e}_{k_z} \tag{B.40}$$

Due to rotational symmetry $\hat{\mathbf{f}}$ is only a function of the radius k_r and the axial coordinate k_z (the azimuthal contribution equals zero, $\hat{f}_{k_\varphi} = 0$), this leads to

$$\hat{\mathbf{f}}(k_r, k_\varphi, k_z) = \hat{f}_{k_r} \begin{pmatrix} \cos k_\varphi \\ \sin k_\varphi \\ 0 \end{pmatrix} + \hat{f}_{k_z} \begin{pmatrix} 0 \\ 0 \\ 1 \end{pmatrix} \tag{B.41}$$

Applying the inverse Fourier transform yields

$$\mathbf{f}(r,z) = \int_{k_z=-\infty}^{\infty} \int_{k_r=0}^{\infty} \int_{k_\varphi=0}^{2\pi} \begin{pmatrix} \hat{f}_{k_r}(k_r, k_z) \cos k_\varphi \\ \hat{f}_{k_r}(k_r, k_z) \sin k_\varphi \\ \hat{f}_{k_z}(k_r, k_z) \end{pmatrix} \mathrm{e}^{2\pi \mathrm{i} r k_r \cos k_\varphi} \,\mathrm{d}k_\varphi \, k_r \, \mathrm{d}k_r \mathrm{e}^{2\pi \mathrm{i} z k_z} \,\mathrm{d}k_z \tag{B.42}$$

With the definition of Bessel's first integral of order ν for Bessel functions of first kind and zeroth J_0 and first order J_1

$$\mathrm{J}_\nu(\xi) = \frac{1}{2\pi \mathrm{i}^\nu} \int_{k_\varphi=0}^{2\pi} \mathrm{e}^{\mathrm{i}\xi \cos(k_\varphi)} \cos(\nu k_\varphi) \,\mathrm{d}k_\varphi \tag{B.43}$$

eq. (B.42) simplifies to

$$\mathbf{f}(r,z) = \int_{k_z=-\infty}^{\infty} 2\pi \int_{k_r=0}^{\infty} \begin{pmatrix} \mathrm{i}\hat{f}_{k_r}(k_r,k_z)\mathrm{J}_1(2\pi r k_r) \\ 0 \\ \hat{f}_{k_z}(k_r,k_z)\mathrm{J}_0(2\pi r k_r) \end{pmatrix} k_r \,\mathrm{d}k_r \,\mathrm{e}^{2\pi \mathrm{i} z k_z} \,\mathrm{d}k_z \tag{B.44}$$

Finally, the Hankel transform, eq. (B.28), and the inverse Fourier transform can be exploited, leading to

$$\mathbf{f}(r,z) = \int_{k_z=-\infty}^{\infty} \begin{pmatrix} \mathcal{H}_1^{-1}\left[\mathrm{i}\hat{f}_{k_r}(k_r,k_z)\right] \\ 0 \\ \mathcal{H}_0^{-1}\left[\hat{f}_{k_z}(k_r,k_z)\right] \end{pmatrix} \mathrm{e}^{2\pi \mathrm{i} z k_z} \,\mathrm{d}k_z = \begin{pmatrix} \mathcal{F}_z^{-1}\mathcal{H}_1^{-1}\left[\mathrm{i}\hat{f}_{k_r}(k_r,k_z)\right] \\ 0 \\ \mathcal{F}_z^{-1}\mathcal{H}_0^{-1}\left[\hat{f}_{k_z}(k_r,k_z)\right] \end{pmatrix} \tag{B.45}$$

Note the different sign in the radial component compared to eq. (B.38), this is due to J_1 being an odd function.

B.2.2.5 Treatment of 1-D Cylindrical Coordinates

Fourier transform of one dimension in cylindrical coordinates can be understood as a subset of the two dimensional Fourier transform in cylindrical coordinates. The dot product in eq. (B.23) simplifies for one dimension to $\mathbf{r}\cdot\mathbf{k} = r k_r \cos\varphi$. This simplifies the Fourier, eq. (B.24), and inverse Fourier transform, eq. (B.25). The Fourier and its inverse transform of a scalar quantity result in

$$\hat{f}(k_r) = \mathcal{H}_0\left[f(r)\right] \tag{B.46a}$$
$$f(r) = \mathcal{H}_0^{-1}\left[\hat{f}(k_r)\right] \tag{B.46b}$$

For a vector quantity, the Fourier and its inverse transform yield

$$\hat{\mathbf{f}}(k_r) = \mathcal{H}_1\left[-\mathrm{i} f_r(r)\right] \tag{B.47a}$$
$$\mathbf{f}(r) = \mathcal{H}_1^{-1}\left[\mathrm{i}\hat{f}_{k_r}(k_r)\right] \tag{B.47b}$$

B.2.3 Spherical Coordinates

For spherical coordinates, $\mathbf{r}\cdot\mathbf{k}$ can be written as

$$\mathbf{r}\cdot\mathbf{k} = \begin{pmatrix} r\cos\varphi\sin\vartheta \\ r\sin\varphi\sin\vartheta \\ r\cos\vartheta \end{pmatrix} \cdot \begin{pmatrix} k_r\cos k_\varphi \sin k_\vartheta \\ k_r \sin k_\varphi \sin k_\vartheta \\ k_r \cos k_\vartheta \end{pmatrix} \tag{B.48}$$

with radial coordinate r and k_r, azimuthal angle φ and k_φ, and polar angle ϑ and k_ϑ, in real and Fourier space, respectively. We limit consideration to cases of rotational symmetry. Spherical symmetry can be exploited utilizing the identity $\cos\vartheta\cos k_\vartheta + \sin\vartheta\sin k_\vartheta = \cos(\vartheta - k_\vartheta) = \cos(k_\vartheta - \vartheta)$ and choosing a $\mathbf{k}$-vector parallel to the k_z-axis in Fourier space with $\mathbf{k} = (0,0,k)^\intercal$ which implies $k_\vartheta = 0$. This simplifies the dot product $\mathbf{r}\cdot\mathbf{k}$ in eq. (B.48) to

$$\mathbf{r}\cdot\mathbf{k} = r k_r \cos\vartheta \tag{B.49}$$

With the volume element $\mathrm{d}\mathbf{r} = r^2\sin\vartheta\,\mathrm{d}\varphi\,\mathrm{d}\vartheta\,\mathrm{d}r$, and the result of eq. (B.49), the Fourier transform, eq. (B.7a), is calculated according to

$$\hat{\mathfrak{f}}(k_r) = \int_{r=0}^{\infty}\int_{\vartheta=0}^{\pi}\int_{\varphi=0}^{2\pi} \mathfrak{f}(r)\mathrm{e}^{-2\pi\mathrm{i}rk_r\cos\vartheta} r^2\sin\vartheta\,\mathrm{d}\varphi\,\mathrm{d}\vartheta\,\mathrm{d}r \tag{B.50}$$

The inverse Fourier transform can be computed analogously, as

$$\mathfrak{f}(r) = \int_{k_r=0}^{\infty}\int_{k_\vartheta=0}^{\pi}\int_{k_\varphi=0}^{2\pi} \hat{\mathfrak{f}}(k_r)\mathrm{e}^{2\pi\mathrm{i}rk_r\cos k_\vartheta} k_r^2\sin k_\vartheta\,\mathrm{d}k_\varphi\,\mathrm{d}k_\vartheta\,\mathrm{d}k_r \tag{B.51}$$

B.2.3.1 Spherical Fourier Transform of Scalar Quantities

Due to spherical symmetry, the integral in eq. (B.50) simplifies through integration. Integration over φ yields $\int_0^{2\pi}\mathrm{d}\varphi = 2\pi$. Via substitution we can integrate over ϑ with $u = \cos\vartheta$ and $\mathrm{d}u = -\sin\vartheta\,\mathrm{d}\vartheta$, leading to

$$\hat{f}(k_r) = -2\pi\int_{r=0}^{\infty}\int_{u=1}^{-1} f(r)\mathrm{e}^{-2\pi\mathrm{i}rk_r u} r^2\,\mathrm{d}u\,\mathrm{d}r = \int_{r=0}^{\infty} f(r)\frac{\mathrm{e}^{2\pi\mathrm{i}rk_r} - \mathrm{e}^{-2\pi\mathrm{i}rk_r}}{\mathrm{i}rk_r} r^2\,\mathrm{d}r \tag{B.52}$$

Using Euler's formula yields

$$\hat{f}(k_r) = \frac{2}{k_r} \int_{r=0}^{\infty} f(r) r \sin(2\pi r k_r)\, \mathrm{d}r \equiv \frac{2}{k_r} \mathcal{SIN}[f(r)r] \tag{B.53}$$

with the definition of the sine transform $\mathcal{SIN}$. The Fourier transform for spherically symmetric systems simplifies to the sine transform.

B.2.3.2 Spherical Inverse Fourier Transform of Scalar Quantities

Treatment of the inverse transform, eq. (B.51), is analogous to the treatment laid out in the previous section, i.e.,

$$f(r) = \frac{2}{r} \int_{k_r=0}^{\infty} \hat{f}(k_r) k_r \sin(2\pi r k_r)\, \mathrm{d}k_r \equiv \frac{2}{r} \mathcal{SIN}\left[\hat{f}(k_r) k_r\right] \tag{B.54}$$

with the self-inverse sine transform $\mathcal{SIN}$.

B.2.3.3 Spherical Fourier Transform of Vector Quantities

Analogous to appendix B.2.1.3 and B.2.2.3, the Fourier transform of vector quantities in spherical coordinates is performed by separating the vector into different contributions: radial f_r, polar f_ϑ, and azimuthal f_φ, with their respective unit vectors according to

$$\mathbf{e}_r = \begin{pmatrix} \cos\varphi \sin\vartheta \\ \sin\varphi \sin\vartheta \\ \cos\vartheta \end{pmatrix}, \mathbf{e}_\vartheta = \begin{pmatrix} \cos\varphi \cos\vartheta \\ \sin\varphi \cos\vartheta \\ -\sin\vartheta \end{pmatrix}, \mathbf{e}_\varphi = \begin{pmatrix} -\sin\varphi \\ \cos\varphi \\ 0 \end{pmatrix} \tag{B.55}$$

$$\mathbf{f}(r, \vartheta, \varphi) = f_r \mathbf{e}_r + f_\vartheta \mathbf{e}_\vartheta + f_\varphi \mathbf{e}_\varphi \tag{B.56}$$

However, due to spherical symmetry $\mathbf{f}$ is only a function of the radius $r = |\mathbf{r}|$. Therefore, both other contributions equal zero, $f_\vartheta = 0 = f_\varphi$, leading to

$$\mathbf{f}(r, \vartheta, \varphi) = f_r \begin{pmatrix} \cos\varphi \sin\vartheta \\ \sin\varphi \sin\vartheta \\ \cos\vartheta \end{pmatrix} \tag{B.57}$$

The Fourier transform of $\mathbf{f}$ then yields

$$\hat{\mathbf{f}}(k_r) = \int_{r=0}^{\infty}\int_{\vartheta=0}^{\pi}\int_{\varphi=0}^{2\pi} \begin{pmatrix} f_r(r)\cos\varphi\sin\vartheta \\ f_r(r)\sin\varphi\sin\vartheta \\ f_r(r)\cos\vartheta \end{pmatrix} \mathrm{e}^{-2\pi\mathrm{i}rk_r\cos\vartheta} r^2\sin\vartheta\,\mathrm{d}\varphi\,\mathrm{d}\vartheta\,\mathrm{d}r \tag{B.58}$$

Performing the integration over φ leads to vanishing contributions for the first and second vector entry due to $\int_{\varphi=0}^{2\pi}\cos(\varphi)\,\mathrm{d}\varphi = 0$ and $\int_{\varphi=0}^{2\pi}\sin(\varphi)\,\mathrm{d}\varphi = 0$. As a result, we only regard the z-direction, leading to

$$\hat{\mathbf{f}}(k_r) = \int_{r=0}^{\infty}\int_{\vartheta=0}^{\pi} f_r(r) \begin{pmatrix} 0 \\ 0 \\ 2\pi\cos\vartheta \end{pmatrix} \mathrm{e}^{-2\pi\mathrm{i}rk_r\cos\vartheta} r^2\sin\vartheta\,\mathrm{d}\vartheta\,\mathrm{d}r \tag{B.59}$$

With $(0,0,2\pi\cos(\vartheta))^\intercal = 2\pi\cos(\vartheta)\mathbf{e}_z$, eq. (B.59) yields

$$\hat{\mathbf{f}}(k_r) = \mathbf{e}_z \int_{r=0}^{\infty}\int_{\vartheta=0}^{\pi} f_r(r) 2\pi\cos\vartheta\,\mathrm{e}^{-2\pi\mathrm{i}rk_r\cos\vartheta} r^2\sin\vartheta\,\mathrm{d}\vartheta\,\mathrm{d}r \tag{B.60}$$

Integration over ϑ is carried out using the substitution $u = \cos\vartheta$ and $\mathrm{d}u = -\sin\vartheta\,\mathrm{d}\vartheta$ followed by partial integration, leading to

$$\begin{aligned} \hat{\mathbf{f}}(k_r) &= -\mathbf{e}_z \int_{r=0}^{\infty}\int_{u=1}^{-1} f_r(r) 2\pi u\mathrm{e}^{-2\pi\mathrm{i}rk_r u} r^2\,\mathrm{d}u\,\mathrm{d}r \\ &= -\mathbf{e}_z \int_{r=0}^{\infty} f_r(r)\left(\frac{\mathrm{e}^{2\pi\mathrm{i}rk_r} + \mathrm{e}^{-2\pi\mathrm{i}rk_r}}{\mathrm{i}rk_r} + \frac{\mathrm{e}^{-2\pi\mathrm{i}rk_r} - \mathrm{e}^{2\pi\mathrm{i}rk_r}}{2\pi(\mathrm{i}rk_r)^2}\right) r^2\,\mathrm{d}r \end{aligned} \tag{B.61}$$

Using Euler's formula gives

$$\hat{\mathbf{f}}(k_r) = \mathbf{e}_z \frac{2\mathrm{i}}{k_r} \int_{r=0}^{\infty} f_r(r) r\cos(2\pi rk_r)\,\mathrm{d}r - \mathbf{e}_z \frac{\mathrm{i}}{\pi k_r^2} \int_{r=0}^{\infty} f_r(r)\sin(2\pi rk_r)\,\mathrm{d}r \tag{B.62}$$

Due to alignment of vector $\mathbf{k}$ in Fourier space with $\mathbf{e}_z$, implying $\mathbf{e}_z = \mathbf{e}_{k_r}$ we obtain a combination of sine ($\mathcal{SIN}$) and cosine transform ($\mathcal{COS}$) according to

$$\hat{\mathbf{f}}(k_r) = \mathbf{e}_{k_r} \frac{2\mathrm{i}}{k_r} \mathcal{COS}[f_r(r)r] - \mathbf{e}_{k_r} \frac{\mathrm{i}}{\pi k_r^2} \mathcal{SIN}[f_r(r)] \tag{B.63}$$

B.2.3.4 Spherical Inverse Fourier Transform of Vector Quantities

Treatment of the inverse transform of a vector quantity is similar to the treatment in the previous section, i.e., with the unit vectors in spherical coordinates in Fourier space

$$\mathbf{e}_{k_r} = \begin{pmatrix} \cos k_\varphi \sin k_\vartheta \\ \sin k_\varphi \sin k_\vartheta \\ \cos k_\vartheta \end{pmatrix}, \mathbf{e}_{k_\vartheta} = \begin{pmatrix} \cos k_\varphi \cos k_\vartheta \\ \sin k_\varphi \cos k_\vartheta \\ -\sin k_\vartheta \end{pmatrix}, \mathbf{e}_{k_\varphi} = \begin{pmatrix} -\sin k_\varphi \\ \cos k_\varphi \\ 0 \end{pmatrix} \tag{B.64}$$

the vector-valued function $\hat{\mathbf{f}}$ can be represented according to

$$\hat{\mathbf{f}}(k_r, k_\vartheta, k_\varphi) = f_{k_r}\mathbf{e}_{k_r} + f_{k_\vartheta}\mathbf{e}_{k_\vartheta} + f_{k_\varphi}\mathbf{e}_{k_\varphi} \tag{B.65}$$

Due to spherical symmetry $\hat{\mathbf{f}}$ is only a function of the radius $k_r = |\mathbf{k}|$. Therefore, all other contributions besides the radial one equal zero, leading to

$$\hat{\mathbf{f}}(k_r, k_\vartheta, k_\varphi) = f_{k_r} \begin{pmatrix} \cos k_\varphi \sin k_\vartheta \\ \sin k_\varphi \sin k_\vartheta \\ \cos k_\vartheta \end{pmatrix} \tag{B.66}$$

Applying the inverse Fourier transform yields

$$\mathbf{f}(r) = \int_{k_r=0}^{\infty} \int_{k_\vartheta=0}^{\pi} \int_{k_\varphi=0}^{2\pi} \begin{pmatrix} \hat{f}_{k_r}(k_r) \cos k_\varphi \sin k_\vartheta \\ \hat{f}_{k_r}(k_r) \sin k_\varphi \sin k_\vartheta \\ \hat{f}_{k_r}(k_r) \cos k_\vartheta \end{pmatrix} \mathrm{e}^{2\pi \mathrm{i} r k_r \cos k_\vartheta} k_r^2 \sin k_\vartheta \, \mathrm{d}k_\varphi \, \mathrm{d}k_\vartheta \, \mathrm{d}k_r \tag{B.67}$$

Performing the integration over k_φ leads to vanishing contributions for the first and second vector entry due to $\int_{k_\varphi=0}^{2\pi} \cos k_\varphi \, \mathrm{d}k_\varphi = 0$ and $\int_{k_\varphi=0}^{2\pi} \sin k_\varphi \, \mathrm{d}k_\varphi = 0$. As a result, we only regard the z-direction, leading to

$$\mathbf{f}(r) = \int_{k_r=0}^{\infty} \int_{k_\vartheta=0}^{\pi} \hat{f}_{k_r}(k_r) \begin{pmatrix} 0 \\ 0 \\ 2\pi \cos k_\vartheta \end{pmatrix} \mathrm{e}^{2\pi \mathrm{i} r k_r \cos k_\vartheta} k_r^2 \sin k_\vartheta \, \mathrm{d}k_\vartheta \, \mathrm{d}k_r \tag{B.68}$$

With $(0, 0, 2\pi \cos k_\vartheta)^\mathsf{T} = 2\pi \cos k_\vartheta \mathbf{e}_{k_z}$, eq. (B.68) yields

$$\mathbf{f}(r) = \mathbf{e}_{k_z} \int_{k_r=0}^{\infty} \int_{k_\vartheta=0}^{\pi} \hat{f}_{k_r}(k_r) 2\pi \cos k_\vartheta \mathrm{e}^{2\pi \mathrm{i} r k_r \cos k_\vartheta} k_r^2 \sin k_\vartheta \, \mathrm{d}k_\vartheta \, \mathrm{d}k_r \tag{B.69}$$

Integration over k_ϑ is carried out using the substitution $u = \cos k_\vartheta$ and $\mathrm{d}u = -\sin k_\vartheta \,\mathrm{d}\vartheta$ followed by partial integration, leading to

$$\begin{aligned}\mathbf{f}(r) &= -\mathbf{e}_{k_z} \int_{k_r=0}^{\infty} \int_{u=1}^{-1} \hat{f}_{k_r}(k_r) 2\pi u \mathrm{e}^{2\pi \mathrm{i} r k_r u} k_r^2 \,\mathrm{d}u \,\mathrm{d}k_r \\ &= \mathbf{e}_{k_z} \int_{k_r=0}^{\infty} \hat{f}_{k_r}(k_r) \left(\frac{\mathrm{e}^{-2\pi \mathrm{i} r k_r} + \mathrm{e}^{2\pi \mathrm{i} r k_r}}{\mathrm{i} r k_r} + \frac{\mathrm{e}^{-2\pi \mathrm{i} r k_r} - \mathrm{e}^{2\pi \mathrm{i} r k_r}}{2\pi (\mathrm{i} r k_r)^2} \right) k_r^2 \,\mathrm{d}k_r \end{aligned} \tag{B.70}$$

Using Euler's formula yields

$$\mathbf{f}(r) = \mathbf{e}_{k_z} \frac{\mathrm{i}}{\pi r^2} \int_{k_r=0}^{\infty} \hat{f}_{k_r}(k_r) \sin(2\pi r k_r) \,\mathrm{d}k_r - \mathbf{e}_{k_z} \frac{2\mathrm{i}}{r} \int_{k_r=0}^{\infty} \hat{f}_{k_r}(k_r) k_r \cos(2\pi r k_r) \,\mathrm{d}k_r \tag{B.71}$$

Due to alignment of the vector $\mathbf{r}$ in Fourier space with $\mathbf{e}_{k_z}$, implying $\mathbf{e}_r = \mathbf{e}_{k_z}$ we obtain a combination of sine and cosine transform according to

$$\mathbf{f}(r) = \mathbf{e}_r \frac{\mathrm{i}}{\pi r^2} \mathcal{SIN}\left[\hat{f}_{k_r}(k_r)\right] - \mathbf{e}_r \frac{2\mathrm{i}}{r} \mathcal{COS}\left[\hat{f}_{k_r}(k_r) k_r\right] \tag{B.72}$$

Note that the forward Fourier transform, eq. (B.63), differs slightly from the inverse transform, eq. (B.72).

B.3 Computation of First-Order Hankel Transform with Algorithm for Zeroth Order

In the following, we derive a way to compute the Hankel transform of first order with algorithms solving the Hankel transform of zeroth order. The Hankel transform of first order is defined as

$$\mathcal{H}_1[f(r)] = 2\pi \int_{r=0}^{\infty} f(r) \mathrm{J}_1(2\pi r k_r) r \,\mathrm{d}r \tag{B.73}$$

with the Bessel function of first kind and first order J_1. Exploiting $\mathrm{J}_1(r) = -\mathrm{J}_0'(r)$, with the derivative with respect to r of the Bessel function of first kind and zeroth order J_0', and the

coordinate transform $r = \frac{x}{2\pi k_r} \rightarrow \mathrm{d}r = \frac{\mathrm{d}x}{2\pi k_r}$, leads to

$$\mathcal{H}_1[f(r)] = -\frac{1}{2\pi k_r^2} \int_{x=0}^{\infty} f\left(\frac{x}{2\pi k_r}\right) \mathrm{J}_0'(x) x \,\mathrm{d}x \tag{B.74}$$

Integration by parts with vanishing integration bounds $\left[f\left(\frac{x}{2\pi k_r}\right)\mathrm{J}_0(x)x\right]_0^{\infty} = 0$ leaves us with

$$\begin{aligned}\mathcal{H}_1[f(r)] &= \frac{1}{2\pi k_r^2} \int_{x=0}^{\infty} \left(\frac{x}{2\pi k_r} f'\left(\frac{x}{2\pi k_r}\right) + f\left(\frac{x}{2\pi k_r}\right)\right) \mathrm{J}_0(x)\,\mathrm{d}x \\ &= \frac{1}{k_r} \int_{r=0}^{\infty} \left(\frac{f(r)}{r} + f'(r)\right) \mathrm{J}_0(2\pi r k_r) r \,\mathrm{d}r = \frac{1}{2\pi k_r} \mathcal{H}_0\left[\frac{f(r)}{r} + f'(r)\right]\end{aligned} \tag{B.75}$$

where the prime ($'$) denotes the derivative with respect to r. Instead of computing the discrete Hankel transform on a logarithmic grid as was done by Boţan *et al.* [1] or Hamilton [2], we follow the approach of Hansen [3–5] and compute the Hankel transform on an equidistant grid by a combination of the fast Abel and fast Fourier transform. The algorithm used for the fast Abel transform is described below.

B.4 Computation of the Abel and Inverse Abel Transform

The algorithm for the Abel transform is taken from Hansen [3,5] and Hansen and Law [4]. The recursive scheme computes the Abel and inverse Abel transform on an equidistant grid with N grid points, using the parameters given in table B.1. We define the grid in radial direction as depicted in figure A.2.

The algorithm described in eq. (B.76) computes the forward and inverse Abel transform using a low order state-space model (dimension $K = 9$). The input of the linear system is the

first-order hold approximation of the discrete function f_n to be transformed, leading to

$$\mathbf{x}_{n-1} = \Phi_n \mathbf{x}_n + B_{0,n} f_n + B_{1,n} f_{n-1} \tag{B.76a}$$
$$F_n = C\mathbf{x}_n \tag{B.76b}$$
$$\mathbf{x}_N = 0 \tag{B.76c}$$
$$\Phi_n = \operatorname{diag}\left\{\left(\frac{r_n}{r_{n-1}}\right)^{\lambda_1}, \ldots, \left(\frac{r_n}{r_{n-1}}\right)^{\lambda_K}\right\} \tag{B.76d}$$
$$C = [1, \ldots, 1] \tag{B.76e}$$
$$B_{0,n} = \left[h_1\beta_{0,n}(\lambda_1), \ldots, h_K\beta_{0,n}(\lambda_K)\right]^\intercal \tag{B.76f}$$
$$B_{1,n} = \left[h_1\beta_{1,n}(\lambda_1), \ldots, h_K\beta_{1,n}(\lambda_K)\right]^\intercal \tag{B.76g}$$

with the grid point index n, the grid dependent states of the state-space model $\mathbf{x}_n$, the grid dependent state transition matrix Φ_n, the grid dependent input vectors $B_{0,n}$ and $B_{1,n}$, the discrete (inverse) Abel transform F_n, the output vector of the state-space representation of the linear system C, the radial grid points r_n, as well as the model parameters from Hansen[3,4], λ_k and h_k (see table B.1). The recursion is started at the outermost grid point r_N with $\mathbf{x}_N = 0$ and is continued inwards toward the center of the radial grid. This method cannot be used if $r_{n-1} = 0$. For the forward transform one uses $\beta^{\mathrm{f}}_{0,n}$ and $\beta^{\mathrm{f}}_{1,n}$, obtained from

$$\beta^{\mathrm{f}}_{0,n}(\lambda_k) = \frac{2r_{n-1}}{r_n - r_{n-1}} \frac{r_{n-1} + \left(r_n(\lambda_k+1) - r_{n-1}(\lambda_k+2)\right)\left(\frac{r_n}{r_{n-1}}\right)^{\lambda_k+1}}{(\lambda_k+1)(\lambda_k+2)} \tag{B.77a}$$
$$\beta^{\mathrm{f}}_{1,n}(\lambda_k) = \frac{2r_{n-1}}{r_n - r_{n-1}} \frac{\left(r_{n-1}(\lambda_k+1) - r_n(\lambda_k+2)\right) + r_n\left(\frac{r_n}{r_{n-1}}\right)^{\lambda_k+1}}{(\lambda_k+1)(\lambda_k+2)} \tag{B.77b}$$

For the inverse transform one uses $\beta^{\mathrm{b}}_{0,n}$ and $\beta^{\mathrm{b}}_{1,n}$ according to

$$\beta^{\mathrm{b}}_{0,n}(\lambda_k) = \begin{cases} -\frac{1}{\pi(r_n - r_{n-1})} \ln\left(\frac{r_n}{r_{n-1}}\right) & \lambda_k = 0 \\ \frac{1}{\pi\lambda_k(r_n - r_{n-1})}\left(1 - \left(\frac{r_n}{r_{n-1}}\right)^{\lambda_k}\right) & \lambda_k \neq 0 \end{cases} \tag{B.78a}$$
$$\beta^{\mathrm{b}}_{1,n}(\lambda_k) = -\beta^{\mathrm{b}}_{0,n}(\lambda_k) \tag{B.78b}$$

Table B.1: Parameters for Abel transform[3].

k	h_k/π	λ_k
1	0.318	0
2	0.19	-2.1
3	0.35	-6.2
4	0.82	-22.4
5	1.8	-92.5
6	3.9	-414.5
7	8.3	-1889.4
8	19.6	-8990.9
9	48.3	-47391.1

B.5 Discrete Sine- & Cosine Transforms

In this work, in appendix A.4.2.2 and A.4.3.2 we used the discrete versions of the sine and cosine transforms. Both transforms transform between a finite series of equally-spaced samples $j = 0, \ldots, (N-1)$ of a function f_j in real space, and a series of equal length and equally-spaced samples $k = 0, \ldots, (N-1)$ in Fourier space $\hat{f}_k$. The index j denotes the discrete grid points in real space, while k denotes the grid points in Fourier space.

The discrete sine transforms $\mathcal{DST}_{\text{II}}$ and $\mathcal{DST}_{\text{III}}$ of the function f are defined by

$$\hat{f}_{k^*}^{\mathcal{DST}_{\text{II}}} = \sum_{j=0}^{N-1} f_j \sin\left(\frac{\pi}{N}\left(j+\frac{1}{2}\right)(k^*+1)\right) \qquad \text{with } k^* = 0, \ldots, (N-1) \tag{B.79a}$$

$$f_j^{\mathcal{DST}_{\text{III}}} = \frac{(-1)^j}{2}\hat{f}_{N-1} + \sum_{k^*=0}^{N-2} \hat{f}_{k^*} \sin\left(\frac{\pi}{N}(k^*+1)\left(j+\frac{1}{2}\right)\right) \quad \text{with } j = 0, \ldots, (N-1) \tag{B.79b}$$

with the number of discrete grid points N, where the iteration variable k^* does not represent the true Fourier variable k, which for the discrete sine transforms is obtained from $k = k^* + 1$.

The $\mathcal{DST}_{\text{II}}$ assumes the function f_j to be odd around $j = (-\frac{1}{2})$ and $j = (N - \frac{1}{2})$ (equivalent to $r = 0$ and $r = L_{\text{tot}}$ in figure A.3). However, the $\mathcal{DST}_{\text{III}}$ implies the function $\hat{f}_{k^*}$ to be odd around $k^* = (-1)$ and even around $k^* = (N-1)$ (equivalent to $k = 0$ and $k = N$, respectively). Both discrete sine transforms are scaled with the factor $\eta = \frac{1}{\sqrt{2N}}$, allowing usage of the two transforms as direct inverses of each other: $\mathcal{DST}_{\text{II}}^{-1} = \mathcal{DST}_{\text{III}}$.

The discrete cosine transforms $\mathcal{DCT}_{\text{II}}$ and $\mathcal{DCT}_{\text{III}}$ are defined by

$$\hat{f}_k^{\mathcal{DCT}_{\text{II}}} = \sum_{j=0}^{N-1} f_j \cos\left(\frac{\pi}{N}\left(j+\frac{1}{2}\right)k\right) \qquad \text{with } k = 0,\ldots,(N-1) \tag{B.80a}$$

$$f_j^{\mathcal{DCT}_{\text{III}}} = \frac{1}{2}\hat{f}_0 + \sum_{k=1}^{N-1} \hat{f}_k \cos\left(\frac{\pi}{N}k\left(j+\frac{1}{2}\right)\right) \qquad \text{with } j = 0,\ldots,(N-1) \tag{B.80b}$$

The $\mathcal{DCT}_{\text{II}}$ assumes the function f_j to be even around $j = (-\frac{1}{2})$ and $j = (N-\frac{1}{2})$ (equivalent to $r = 0$ and $r = L_{\text{tot}}$ in figure A.3). However, the $\mathcal{DCT}_{\text{III}}$ implies the function $\hat{f}_k$ to be even around $k = 0$ and odd around $k = N$. Both discrete cosine transforms are scaled with the factor $\eta = \frac{1}{\sqrt{2N}}$, allowing usage of the two transforms as direct inverses of each other: $\mathcal{DCT}_{\text{II}}^{-1} = \mathcal{DCT}_{\text{III}}$.

B.6 Reducing Gibbs Phenomenon via the Lanczos σ-Factor

Fourier transform algorithms applied to very sharp density profiles or non-periodic boundary conditions, as used for Cartesian coordinates in appendix A.4.1.1, can cause ringing artifacts at profile discontinuities (Gibbs phenomenon). These artifacts can be reduced by multiplication of the Fourier space representation of the function with the Lanczos σ-factor[6]

$$\sigma(k) = \operatorname{sinc}\frac{k}{M} = \frac{\sin \pi\frac{k}{M}}{\pi\frac{k}{M}} \tag{B.81}$$

with the Fourier variable k, and where M denotes the number of k-values in the dimension of interest ($k = 0,\ldots,M-1$). For the FFT with an even number of grid points we get $M = \frac{N}{2}+1$, with N as the number of grid points (see eqs. (A.129) and (A.130)). For fast sine & cosine transforms $M = (N+1)$ and $M = N$ hold, respectively (see eqs. (A.150) and (A.151)).

The procedure can easily be implemented by multiplying the weight functions with the σ-factor. For multidimensional Fourier transforms, the σ-factor has to be multiplied for every dimension separately. For example, for 3-D Cartesian, 2-D cylindrical and 1-D spherical coordinates the Lanczos σ-factor is computed as

$$\hat{\omega}_i^{\sigma}(\mathbf{k}) = \hat{\omega}_i(k_x,k_y,k_z)\sigma_x(k_x)\sigma_y(k_y)\sigma_z(k_z) \tag{B.82a}$$

$$\hat{\omega}_i^{\sigma}(\mathbf{k}) = \hat{\omega}_i(k_z,k_r)\sigma_z(k_z)\sigma_r(k_r) \tag{B.82b}$$

$$\hat{\omega}_i^{\sigma}(\mathbf{k}) = \hat{\omega}_i(k_r)\sigma_r(k_r) \tag{B.82c}$$

For increased smoothing, the weight function can be multiplied with the σ-factor multiple

times.

For Cartesian coordinates, robustness of the FFT can further be increased by enforcing periodic boundary conditions via an additional domain, with respect to the ones displayed in figure A.1, using a smooth transition function (for example the hyperbolic tangent). The sine and cosine transform inherently possess this property. Enforcing periodic boundary conditions is only relevant if no Lanczos σ-factor is used.

B.7 Comparison of Convolution Results in Different Coordinate Systems

Computation of the convolution integrals discussed in appendix A.3 depends on the underlying coordinate system. Figure B.1 presents results of three convolutions of density profile ρ with different weight functions from FMT[7], obtaining weighted densities n_0, n_3 and n_{V1}, for Cartesian, cylindrical and spherical coordinates. The remaining weighted densities (n_1, n_2 and n_{V1}) differ from the considered ones only by a constant, and are thus not shown here.

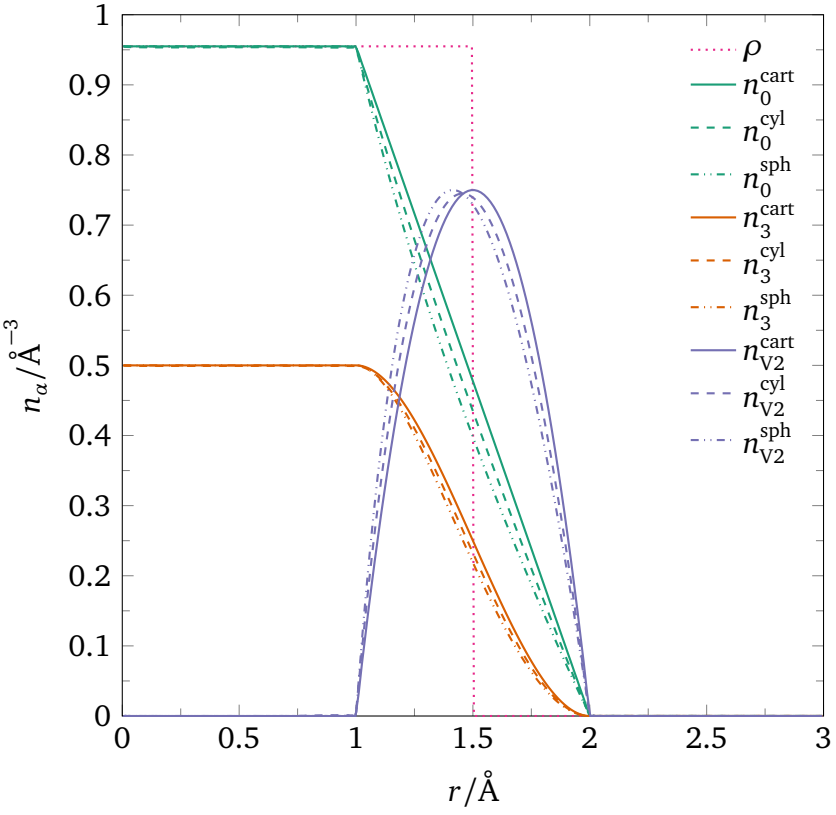

Figure B.1: Comparison of one-dimensional convolutions in Cartesian, cylindrical and spherical coordinates presenting weighted densities n_0, n_3 and n_{V2} for a hard-sphere fluid with radius $R = 0.5\,\text{Å}$ modeled with FMT[7]. The density profile is given as a Heaviside step function $\rho(r) = \frac{3}{\pi}\Theta(1.5\,\text{Å} - r)\,\text{Å}^{-3}$.

For $r \to \infty$ the convolution results are not dependent on the underlying coordinate system. Only for small systems, such as the system depicted here, deviations occur. The weighted densities in the region from 0–1 Å and 2–3 Å are equivalent for the three coordinate systems, while differences are revealed between 1–2 Å in the influence length $R = 0.5$ Å of the weight function around the density jump at $r = 1.5$ Å. Between 1 Å and 2 Å, the scalar-valued weighted densities are smaller for cylindrical, and smallest for spherical coordinates, compared to Cartesian coordinates. The maximum of the vector-valued weighted densities lies directly on the density step for Cartesian coordinates, while for cylindrical and spherical coordinate systems the maximum is shifted towards smaller radii.

References

[1] V. Boţan, F. Pesth, T. Schilling, and M. Oettel. Hard-sphere fluids in annular wedges: Density distributions and depletion potentials. *Physical Review E*, **79**:061402, 2009. doi:10.1103/PhysRevE.79.061402.

[2] A. J. S. Hamilton. Uncorrelated modes of the non-linear power spectrum. *Monthly Notices of the Royal Astronomical Society*, **312**(2):257–284, 2000. doi:10.1046/j.1365-8711.2000.03071.x.

[3] E. W. Hansen. Fast Hankel transform algorithm. *IEEE Transactions on Acoustics, Speech, and Signal Processing*, **33**(3):666–671, 1985. doi:10.1109/TASSP.1985.1164579.

[4] E. W. Hansen and P.-L. Law. Recursive methods for computing the Abel transform and its inverse. *J. Opt. Soc. Am. A*, **2**(4):510–520, 1985. doi:10.1364/JOSAA.2.000510.

[5] E. W. Hansen. Correction to "Fast Hankel transform algorithm". *IEEE Transactions on Acoustics, Speech, and Signal Processing*, **34**(3):623–624, 1986. doi:10.1109/TASSP.1986.1164860.

[6] C. Lanczos. *Applied Analysis*. Prentice-Hall Mathematics Series. Prentice-Hall, 1956.

[7] R. Roth, R. Evans, A. Lang, and G. Kahl. Fundamental measure theory for hard-sphere mixtures revisited: the White Bear version. *Journal of Physics: Condensed Matter*, **14**(46):12063, 2002. doi:10.1088/0953-8984/14/46/313.

C Appendix: A Fast Inverse Hankel Transform of First Order for Computing Vector-Valued Weight Functions Appearing in Fundamental Measure Theory in Cylindrical Coordinates

The content of this appendix is a literal quote of the appendix of:

R. Stierle and J. Gross. A fast inverse Hankel Transform of first Order for Computing vector-valued weight Functions appearing in Fundamental Measure Theory in cylindrical Coordinates. *Fluid Phase Equilibria*, **511**:112500, 2020. doi:10.1016/j.fluid.2020.112500

C.1 Computation of Hankel Transform of Order 1 from Hankel Transform of Order 0

In [section 3.4.2.2][†], we proposed computation of the Hankel transform of first order $\mathcal{H}_1$ from the zeroth order Hankel transform, as

$$\mathcal{H}_1[f(r)] = \frac{1}{2\pi k_r}\mathcal{H}_0\left[\frac{f(r)}{r} + f'(r)\right] \tag{C.1}$$

while its inverse $\mathcal{H}_1^{-1}$ is computed according to

$$\mathcal{H}_1^{-1}\left[\hat{f}(k_r)\right] = \frac{1}{r}\mathcal{H}_0^{-1}\left[\frac{\hat{f}(k_r)}{2\pi k_r} + \hat{f}'(k_r)\right] \tag{C.2}$$

[†]The text in the original publication reads: [our earlier work[1] section 4.2.2].

References

[1] R. Stierle, E. Sauer, J. Eller, M. Theiss, P. Rehner, P. Ackermann, and J. Gross. Guide to efficient solution of PC-SAFT classical Density Functional Theory in various Coordinate Systems using fast Fourier and similar Transforms. *Fluid Phase Equilibria*, **504**:112306, 2020. doi:10.1016/j.fluid.2019.112306.

D Appendix: Hydrodynamic Density Functional Theory for Mixtures from a Variational Principle and Its Application to Droplet Coalescence

The content of this appendix is a literal quote of the appendix of:

R. Stierle and J. Gross. Hydrodynamic Density Functional Theory for Mixtures from a Variational Principle and Its Application to Droplet Coalescence. *The Journal of Chemical Physics*, **155**(13):134101, 2021. doi:10.1063/5.0060088

D.1 Notation

For the derivation in section 5.2.2, we use the following notation. The velocity gradient is defined as

$$\nabla \mathbf{v} \equiv \begin{pmatrix} \frac{\partial v_1}{\partial r_1} & \cdots & \frac{\partial v_d}{\partial r_1} \\ \vdots & \ddots & \vdots \\ \frac{\partial v_1}{\partial r_d} & \cdots & \frac{\partial v_d}{\partial r_d} \end{pmatrix} = \begin{pmatrix} \nabla v_1 & \cdots & \nabla v_d \end{pmatrix} \tag{D.1}$$

with the velocity and spatial coordinate components, v_i and r_i, respectively. Left-hand side multiplication of a vector with a matrix is defined by

$$\mathbf{v} \cdot \mathbf{T} = \begin{pmatrix} \sum_i v_i T_{i1} \\ \vdots \\ \sum_i v_i T_{id} \end{pmatrix} \tag{D.2}$$

with matrix elements T_{ij}. The divergence of a matrix is defined as

$$\nabla \cdot \mathbf{T} \equiv \begin{pmatrix} \sum_i \frac{\partial T_{i1}}{\partial r_i} \\ \vdots \\ \sum_i \frac{\partial T_{id}}{\partial r_i} \end{pmatrix} \tag{D.3}$$

while the double dot product is defined by

$$\mathbf{A} : \mathbf{B} \equiv \sum_i \sum_j A_{ij} B_{ij} \tag{D.4}$$

D.2 Divergence Theorem and No-Flux Boundary Condition

The divergence theorem for a closed, bounded set $\Omega \subset \mathbb{R}^d$ with a piecewise smooth boundary $\partial\Omega$ for a scalar b and a vector $\mathbf{v}$ can be stated as

$$\int_{\partial\Omega} (b\mathbf{v}) \cdot \hat{\mathbf{n}} \, \mathrm{d}A = \int_{\Omega} \nabla \cdot (b\mathbf{v}) \, \mathrm{d}\mathbf{r} = \int_{\Omega} b(\nabla \cdot \mathbf{v}) \, \mathrm{d}\mathbf{r} + \int_{\Omega} (\nabla b) \cdot \mathbf{v} \, \mathrm{d}\mathbf{r} \tag{D.5}$$

with the outward unit normal vector $\hat{\mathbf{n}}$ of the boundary.

For the transport problem in this work, $\Omega \subset \mathbb{R}^d$ represents our computational domain with the surface/boundary $A = \partial\Omega$, $\mathbf{v}$ is the barycentric velocity, and b is the transported property. If we assume that there is no transport of b across the boundary, the product $b\mathbf{v} \cdot \hat{\mathbf{n}} = 0$ vanishes, leading to

$$\int_{\partial\Omega} (b\mathbf{v}) \cdot \hat{\mathbf{n}} \, \mathrm{d}A = 0 = \int_{\Omega} \nabla \cdot (b\mathbf{v}) \, \mathrm{d}\mathbf{r} \tag{D.6}$$

which in combination with eq. (D.5) results in

$$\int_{\Omega} b(\nabla \cdot \mathbf{v}) \, \mathrm{d}\mathbf{r} = -\int_{\Omega} (\nabla b) \cdot \mathbf{v} \, \mathrm{d}\mathbf{r} \tag{D.7}$$

D.3 Maxwell-Stefan Diffusion Formulation

Maxwell-Stefan diffusion[1–3] for multicomponent mixtures as described in eq. (5.32) can be expressed for isothermal systems as

$$\begin{pmatrix} -\rho_1 \nabla\beta\mu_1^{\text{diff}} \\ \vdots \\ -\rho_{N_\text{c}-1} \nabla\beta\mu_{N_\text{c}-1}^{\text{diff}} \end{pmatrix} = \mathbf{B} \begin{pmatrix} \mathbf{j}_1^{\text{diff}} \\ \vdots \\ \mathbf{j}_{N_\text{c}-1}^{\text{diff}} \end{pmatrix} \tag{D.8}$$

with the generalized driving forces[1–3], for hydrodynamic DFT defined by

$$\rho_i \nabla\beta\mu_i^{\text{diff}} \equiv \rho_i \nabla\left(\frac{\delta\beta F}{\delta\rho_i} + \beta V_i^{\text{ext}}\right) - w_i \sum_{j=1}^{N_\text{c}} \rho_j \nabla\left(\frac{\delta\beta F}{\delta\rho_j} + \beta V_j^{\text{ext}}\right) \tag{D.9}$$

with the mass fraction $w_i \equiv \frac{\check{m}_i \rho_i}{\check{m}\rho}$. The structure of eq. (D.9) is equal to the structure of the *generalized driving force*[1–3], which reads for isothermal cases

$$\rho \mathbf{d}_i \equiv \rho_i \nabla\beta\mu_i - w_i \sum_{j=1}^{N_\text{c}} \rho_j \nabla\beta\mu_j \tag{D.10}$$

The matrix $\mathbf{B}$ is defined as[4]

$$B_{ij} = \begin{cases} x_i \left(\frac{\check{m}_i}{\check{m}_{N_\text{c}}} \frac{1}{\mathcal{D}_{iN_\text{c}}} - \frac{1}{\mathcal{D}_{ij}}\right) & \text{for } j \neq i \\ \frac{\check{m}_i}{\check{m}_{N_\text{c}}} \frac{x_i}{\mathcal{D}_{iN_\text{c}}} + \sum_{k\neq i}^{N_\text{c}} \frac{x_k}{\mathcal{D}_{ik}} & \text{for } j = i \end{cases} \tag{D.11}$$

with the molar fractions x_i, the Maxwell-Stefan diffusion coefficients $\mathcal{D}_{ij}$, and the molecular mass $\check{m}_i$ for component indices i and j, where we already exploited the relation for the diffusive molecular flux of the N_c-th component (vanishing sum of all diffusive molecular fluxes) for the barycentric reference velocity[5]

$$\check{m}_{N_\text{c}} \mathbf{j}_{N_\text{c}}^{\text{diff}} = -\sum_{i=1}^{N_\text{c}-1} \check{m}_i \mathbf{j}_i^{\text{diff}} \tag{D.12}$$

The molecular fluxes can be calculated by inverting the matrix $\mathbf{B}$, which leads to

$$\begin{pmatrix} \mathbf{j}_1^{\text{diff}} \\ \vdots \\ \mathbf{j}_{N_\text{c}-1}^{\text{diff}} \end{pmatrix} = -\mathbf{B}^{-1} \begin{pmatrix} \rho_1 \nabla\beta\mu_1^{\text{diff}} \\ \vdots \\ \rho_{N_\text{c}-1} \nabla\beta\mu_{N_\text{c}-1}^{\text{diff}} \end{pmatrix} \tag{D.13}$$

D.4 Time Derivatives of Helmholtz Energy Functionals

The time derivative of functionals of the Helmholtz energy and the external potential over a stationary domain used in eq. (5.41) is calculated via

$$\begin{aligned}\frac{\partial}{\partial t}\left(F[\{\rho_i\}]+\int\sum_{i=1}^{N_c}\rho_i V_i^{\text{ext}}\,\mathrm{d}\mathbf{r}\right)&=\int\sum_{i=1}^{N_c}\frac{\delta F[\{\rho_i\}]}{\delta\rho_i(\mathbf{r})}\frac{\partial\rho_i(\mathbf{r})}{\partial t}\,\mathrm{d}\mathbf{r}'+\int\sum_{i=1}^{N_c}\frac{\partial\rho_i(\mathbf{r})}{\partial t}V_i^{\text{ext}}(\mathbf{r})\,\mathrm{d}\mathbf{r}\\&=\int\sum_{i=1}^{N_c}\frac{\delta\big(\rho(\mathbf{r}')a(\{\bar\rho_i(\mathbf{r}')\})\big)}{\delta\rho_i(\mathbf{r})}\frac{\partial\rho_i(\mathbf{r})}{\partial t}\,\mathrm{d}\mathbf{r}'+\int\sum_{i=1}^{N_c}\frac{\partial\rho_i(\mathbf{r})}{\partial t}V_i^{\text{ext}}(\mathbf{r})\,\mathrm{d}\mathbf{r}\end{aligned}\tag{D.14}$$

[...] by using the functional derivative of the weighted density, defined by

$$\frac{\delta F[\{\rho_i\}]}{\delta\rho_i(\mathbf{r})}=\int\frac{\delta\big(\rho(\mathbf{r}')a(\{\bar\rho_i(\mathbf{r}')\})\big)}{\delta\rho_i(\mathbf{r})}\,\mathrm{d}\mathbf{r}'\tag{D.15}$$

eq. (D.14) simplifies to

$$\int\sum_{i=1}^{N_c}\left(\frac{\delta F[\{\rho_i\}]}{\delta\rho_i(\mathbf{r})}+V_i^{\text{ext}}(\mathbf{r})\right)\frac{\partial\rho_i(\mathbf{r})}{\partial t}\,\mathrm{d}\mathbf{r}\tag{D.16}$$

which corresponds to eq. (5.41). Here, we explicitly considered the integration variables for clarity. Since the integration domain is stationary, Reynolds theorem simplifies to differentiation under the integral sign.

For local Helmholtz energy functionals (e.g., local density approximations and density/squared gradient theories) the equality of eqs. (D.14) and (D.16) applies not only to the integral but also to the local form.

D.5 Wave Speed of the Non-diffusive Hydrodynamic Density Functional Theory Model

The Jacobian matrix $\tilde{\mathbf{J}}\equiv\nabla_{\tilde{\mathbf{U}}}\tilde{\mathbf{F}}^{\text{conv}}$ of the purely convective one-dimensional hydrodynamic DFT model ($\mathbf{F}^{\text{diff}}=0$ and $\mathbf{S}=0$) of a binary mixture with

$$\tilde{\mathbf{U}}=\begin{pmatrix}\check{m}_1\rho_1\\\check{m}_2\rho_2\\\check{m}\rho\mathbf{v}\end{pmatrix}\qquad\text{and}\qquad\tilde{\mathbf{F}}^{\text{conv}}(\tilde{\mathbf{U}})=\begin{pmatrix}\check{m}_1\rho_1\mathbf{v}\\\check{m}_2\rho_2\mathbf{v}\\\check{m}\rho\mathbf{v}\mathbf{v}^{\intercal}+p^{\text{ig}}(\rho)\mathbb{I}\end{pmatrix}\tag{D.17}$$

considering the component and momentum balances (the continuity equation is linearly dependent on the two component balances) in contrast to the corresponding variant in eq. (5.64) is

$$\tilde{\mathbf{J}} = \begin{pmatrix} w_2 v & -w_1 v & w_1 \\ -w_2 v & w_1 v & w_2 \\ \frac{k_B T}{\check{m}_1} - v^2 & \frac{k_B T}{\check{m}_2} - v^2 & 2v \end{pmatrix} \tag{D.18}$$

with the velocity component v and the mass fractions $w_i \equiv \frac{\check{m}_i \rho_i}{\check{m}\rho}$ with $w_1 + w_2 = 1$. The eigenvalues of the Jacobian matrix, which represent the wave propagation speeds in the hydrodynamic DFT model, can be calculated to be

$$\lambda_1 = v \qquad \text{and} \qquad \lambda_{2/3} = v \pm c_s^{ig} \tag{D.19}$$

with the isothermal speed of sound of the ideal gas contribution $c_s^{ig} = \sqrt{\frac{1}{\check{m}} \left(\frac{\partial p^{ig}}{\partial \rho} \right)_T} = \sqrt{\frac{k_B T}{\check{m}}}$ and the eigenvectors

$$\boldsymbol{\lambda}_1 = \begin{pmatrix} -\check{m}_1 \\ \check{m}_2 \\ (\check{m}_2 - \check{m}_1) v \end{pmatrix} \qquad \text{and} \qquad \boldsymbol{\lambda}_{2/3} = \begin{pmatrix} w_1 \\ w_2 \\ v \pm c_s^{ig} \end{pmatrix} \tag{D.20}$$

D.6 Mathematical Cell-Wise Entropy Identity

Based on the local version of the kinetic energy balance, eq. (5.37), we can derive a local mathematical entropy balance for the hydrodynamic DFT model for mixtures outlined in section 5.4.1 considering the ideal gas pressure, as

$$\frac{\partial \varrho}{\partial t} + \nabla \cdot \mathbf{G} = -\sum_{i=1}^{N_c} \left(\rho_i \mathbf{v} + \mathbf{j}_i^{diff} \right) \cdot \nabla \left(\frac{\delta F^{res}}{\delta \rho_i} + V_i^{ext} \right) - T \sum_{i=1}^{N_c} \mathbf{j}_i^{diff} \cdot \left(-\frac{1}{T} \nabla \mu_i^{diff} \right) - T \boldsymbol{\tau} : \left(-\frac{1}{T} \nabla \mathbf{v} \right) \tag{D.21}$$

with the mathematical entropy ϱ and mathematical entropy flux $\mathbf{G}$ defined by

$$\varrho = \frac{\check{m}}{2} \rho |\mathbf{v}|^2 + \rho a^{ig} \tag{D.22a}$$

$$\mathbf{G} = \frac{\check{m}}{2} \rho |\mathbf{v}|^2 \mathbf{v} + \sum_{i=1}^{N_c} \left(\rho_i \mathbf{v} + \mathbf{j}_i^{diff} \right) \frac{\partial (\rho a^{ig})}{\partial \rho_i} + \boldsymbol{\tau} \cdot \mathbf{v} \tag{D.22b}$$

analogous to the cell-wise mathematical entropy balance for pure fluids described by Carrillo *et al.* [6]. The non-diffusive ($\boldsymbol{\tau} = 0$ and $\mathbf{j}_i^{diff} = 0$) hydrodynamic DFT model satisfies the condition

$$\nabla_{\tilde{\mathbf{U}}}\mathbf{G}(\tilde{\mathbf{U}}) = \nabla_{\tilde{\mathbf{U}}}\varrho(\tilde{\mathbf{U}})\tilde{\mathbf{J}}(\tilde{\mathbf{U}}) \tag{D.23}$$

with the Jacobian matrix for the non-diffusive hydrodynamic DFT model $\tilde{\mathbf{J}}$, eq. (D.18), which in combination with a strictly convex* mathematical entropy ϱ shows that the non-diffusive hydrodynamic DFT model is also purely hyperbolic[7] even for mixtures, motivating the application of the well-balanced scheme developed by Carrillo *et al.*[6] for the convective fluxes in the mixture.

Integrating eq. (D.21) over the entire spatial domain and assuming no transport across the domain boundary (cf. appendix D.2) lead directly to the global dissipation relation, eq. (5.50), where the local and non-local contributions to the Helmholtz energy functional can be treated in the same way.

Guarantees for the finite-volume scheme as proven by Carrillo *et al.*[6] are probably not possible with the applied discretization scheme described in appendix D.7.

D.7 Approximating Gradients via Lifting

To maintain the order of the discretization scheme, we employ the so-called lifting[8] to approximate the gradients $\left\{\{-\nabla\mu_i\},-\nabla\mathbf{v}\right\}$ that occur in the thermodynamic driving forces for molecular and momentum transport (cf. section 5.2.4.1). Therefore, the second-order partial differential equations in eq. (5.64) are replaced by a system of coupled first-order partial differential algebraic equations, as

$$\frac{\partial\mathbf{U}}{\partial t} + \nabla\cdot\mathbf{F}^{\mathrm{conv}} + \nabla\cdot\begin{pmatrix}0\\ \mathbf{j}_i^{\mathrm{diff}}\\ \boldsymbol{\tau}\end{pmatrix} = \mathbf{S}(\mathbf{r},\mathbf{U}) \tag{D.24a}$$

$$\mathbf{j}_i^{\mathrm{diff}} = -\sum_{j=1}^{N_c-1}(\mathbf{B}^{-1})_{ij}\,\rho_j\nabla\beta\mu_j^{\mathrm{diff}} \qquad \forall i \tag{D.24b}$$

$$\boldsymbol{\tau} = -\zeta\,(\nabla\cdot\mathbf{v})\,\mathbb{I} - \eta\left(\nabla\mathbf{v} + (\nabla\mathbf{v})^{\intercal} - \frac{2}{3}\,(\nabla\cdot\mathbf{v})\,\mathbb{I}\right) \tag{D.24c}$$

where we treat the diffusive molecular flux $\mathbf{j}_i^{\mathrm{diff}}$ and the viscous pressure tensor $\boldsymbol{\tau}$ as additional variables. To obtain the integral mean value for our finite-volume scheme, we integrate eqs. (D.24b) and (D.24c) over finite-volume element Ω_k. For simplicity, we consider here only

*The Helmholtz energy density $\beta\rho a^{\mathrm{ig}} = \sum_i^{N_c}\rho_i\,(\ln(\rho_i)-1)$ of the ideal gas contribution is strictly convex since its Hessian matrix is positive definite.

two-dimensional elements Ω_k, and the extension to three dimensions can be done analogously.

For the chemical potential (defined in eq. (5.58)) gradient, application of the gradient theorem leads to

$$\int_{\Omega_k} \nabla \mu_i \, \mathrm{d}\mathbf{r} = \int_{\partial\Omega_k} \hat{\mathbf{n}} \mu_i \, \mathrm{d}A \tag{D.25}$$

with outward unit normal vector $\hat{\mathbf{n}}$ of the boundary $\partial\Omega_k$ of the finite-volume cell. Performing the integration for cell k, this leads to

$$\nabla(\mu_i)_k = \begin{pmatrix} \frac{(\mu_i)_{k+\frac{1}{2},x} - (\mu_i)_{k-\frac{1}{2},x}}{\Delta x} \\ \frac{(\mu_i)_{k+\frac{1}{2},y} - (\mu_i)_{k-\frac{1}{2},y}}{\Delta y} \end{pmatrix} \tag{D.26}$$

Since the values at the boundaries $k \pm \frac{1}{2}$ are not uniquely defined, we apply an approximate Riemann solver

$$\mathfrak{F}(\mathbf{U}^-_{k+\frac{1}{2}}, \mathbf{U}^+_{k+\frac{1}{2}}) = \frac{1}{2}\left(\mathbf{U}^-_{k+\frac{1}{2}} + \mathbf{U}^+_{k+\frac{1}{2}}\right) \tag{D.27}$$

using the central flux corresponding to the sum of chemical and external potential used in eq. (5.66b). Combining eqs. (D.26) and (D.27) leads to

$$\nabla(\mu_i)_k = \begin{pmatrix} \frac{(\mu_i)_{k+1,x} - (\mu_i)_{k-1,x}}{2\Delta x} \\ \frac{(\mu_i)_{k+1,y} - (\mu_i)_{k-1,y}}{2\Delta y} \end{pmatrix} \tag{D.28}$$

which is equivalent to a central difference scheme.

For the velocity gradient $\nabla\mathbf{v}$, the gradient theorem in eq. (D.25) leads to

$$\int_{\Omega_k} \nabla \mathbf{v} \, \mathrm{d}\mathbf{r} = \int_{\partial\Omega_k} \hat{\mathbf{n}} \mathbf{v}^\intercal \, \mathrm{d}A \tag{D.29}$$

Performing the integration for cell k leads to

$$(\nabla\mathbf{v})_k = \begin{pmatrix} \frac{(v_x)_{k+\frac{1}{2},x} - (v_x)_{k-\frac{1}{2},x}}{\Delta x} & \frac{(v_y)_{k+\frac{1}{2},x} - (v_y)_{k-\frac{1}{2},x}}{\Delta x} \\ \frac{(v_x)_{k+\frac{1}{2},y} - (v_x)_{k-\frac{1}{2},y}}{\Delta y} & \frac{(v_y)_{k+\frac{1}{2},y} - (v_y)_{k-\frac{1}{2},y}}{\Delta y} \end{pmatrix} \tag{D.30}$$

By applying the Riemann solver, eq. (D.27), and defining the velocities at the cell face from

eq. (5.67), we get

$$(\nabla \mathbf{v})_k = \begin{pmatrix} \frac{(v_x)_{k+1,x} - (v_x)_{k-1,x}}{2\Delta x} & \frac{(v_y)_{k+1,x} - (v_y)_{k-1,x}}{2\Delta x} \\ \frac{(v_x)_{k+1,y} - (v_x)_{k-1,y}}{2\Delta y} & \frac{(v_y)_{k+1,y} - (v_y)_{k-1,y}}{2\Delta y} \end{pmatrix} \tag{D.31}$$

which, similar to eq. (D.28), corresponds to a central difference scheme. Equivalently, the transpose of the velocity gradient $(\nabla \mathbf{v})_k^\intercal$ can be obtained, while for the approximation of $\nabla \cdot \mathbf{v}$ the divergence theorem is used instead of the gradient theorem, which finally leads to

$$(\nabla \cdot \mathbf{v})_k = \frac{(v_x)_{k+1,x} - (v_x)_{k-1,x}}{2\Delta x} + \frac{(v_y)_{k+1,y} - (v_y)_{k-1,y}}{2\Delta y} \tag{D.32}$$

D.8 Atomic Unit System

Table D.1: Atomic units used in this work. For the sake of clarity, the unit for a molecule # is explicitly considered here.

number density	ρ	$\#\,\text{Å}^{-3}$
molecular mass	$\check{m}$	$\text{u}\,\#^{-1}$
velocity	$\mathbf{v}/c_\text{s}^\text{ig}$	$\text{Å}\,\text{ps}^{-1}$
time	t	ps
pressure	p	$\text{u}\,\text{Å}^{-1}\,\text{ps}^{-2}$
viscosity	ζ/η	$\text{u}\,\text{Å}^{-1}\,\text{ps}^{-1}$
functional derivative	$\frac{\delta F}{\delta \rho_i}$	$\text{u}\,\text{Å}^{2}\,\#^{-1}\,\text{ps}^{-2}$
functional derivative	$\frac{\delta \beta F}{\delta \rho_i}$	–

Due to the molecular nature of the considered length and time scales, the atomic units from table D.1 are used in this work. The values of the used physical constants is presented in

Table D.2: Values of the physical constants used. For the sake of clarity, the unit for a molecule # is explicitly considered here.

Boltzmann constant	k_B	$1.380\,649 \cdot 10^{-23}$	$\text{J}\,\#^{-1}\,\text{K}^{-1}$
Avogadro constant	N_A	$6.022\,140\,76 \cdot 10^{23}$	$\#\,\text{mol}^{-1}$
ideal gas constant	$\mathbb{R}$	$8.314\,462\,618\,153\,24$	$\text{J}\,\text{mol}^{-1}\,\text{K}^{-1}$

table D.2. For example, the ideal gas law in atomic units is defined as

$$p^\text{ig} = \rho k_\text{B} T \frac{\left(\frac{N_\text{A}}{\#\,\text{mol}^{-1}}\right)}{10} \tag{D.33}$$

The squared isothermal speed of sound in atomic units of the ideal gas contribution using

eq. (D.33) is defined by

$$\left(c_\mathrm{s}^\mathrm{ig}\right)^2 = \frac{1}{\check{m}}\left(\frac{\partial p^\mathrm{ig}}{\partial \rho}\right)_T = \frac{k_\mathrm{B}T}{\check{m}}\left(\frac{N_\mathrm{A}}{10\ \#\,\mathrm{mol}^{-1}}\right) \tag{D.34}$$

using the Avogadro constant N_A. The unit of the Avogadro constant needs to be removed because the factor $\left(\frac{N_\mathrm{A}}{10\ \#\,\mathrm{mol}^{-1}}\right)$ is just a result from converting 'kg' to the atomic mass unit 'u': $1\,\mathrm{kg} = 6.022\,140\,76 \cdot 10^{26}\,\mathrm{u}$. The isothermal speed of sound of the ideal gas contribution only varies in this work with composition through the mean molecular mass of the mixture $\check{m} = \sum_i^{N_\mathrm{c}} x_i \check{m}_i$.

More conversions are shown in table D.3.

Table D.3: Conversions of physical properties to atomic units.

viscosity	$1\,\mathrm{Pa\,s}$	$\frac{N_\mathrm{A}}{\#\,\mathrm{mol}^{-1}} 1 \cdot 10^{-19}\,\mathrm{u\,Å^{-1}\,ps^{-1}}$
diffusion coefficient	$1\,\mathrm{m^2\,s^{-1}}$	$1 \cdot 10^{8}\,\mathrm{Å^2\,ps^{-1}}$
atomic mass unit	$1\,\mathrm{kg}$	$6.022\,140\,76 \cdot 10^{26}\,\mathrm{u}$

References

[1] C. F. Curtiss and R. B. Bird. Multicomponent Diffusion. *Industrial & Engineering Chemistry Research*, **38**(7):2515–2522, 1999. doi:10.1021/ie9901123.

[2] C. F. Curtiss and R. B. Bird. Multicomponent Diffusion. *Industrial & Engineering Chemistry Research*, **40**(7):1791, 2001. doi:10.1021/ie011500j. Erratum.

[3] R. B. Bird and D. J. Klingenberg. Multicomponent diffusion–A brief review. *Advances in Water Resources*, **62**:238–242, 2013. doi:10.1016/j.advwatres.2013.05.010.

[4] D. Bothe. On the Maxwell-Stefan Approach to Multicomponent Diffusion. In J. Escher, P. Guidotti, M. Hieber, P. Mucha, J. W. Prüss, Y. Shibata, G. Simonett, C. Walker, and W. Zajaczkowski (editors), *Parabolic Problems: The Herbert Amann Festschrift*, pages 81–93. Springer, Basel, 2011. doi:10.1007/978-3-0348-0075-4_5.

[5] S. Kjelstrup, D. Bedeaux, E. Johannessen, and J. Gross. *Non-Equilibrium Thermodynamics for Engineers*. World Scientific Publishing, 2nd edition, 2016. ISBN 9789813200302, 9789813200319. doi:10.1142/10286.

[6] J. A. Carrillo, S. Kalliadasis, S. P. Perez, and C.-W. Shu. Well-Balanced Finite-Volume Schemes for Hydrodynamic Equations with General Free Energy. *Multiscale Modeling & Simulation*, **18**(1):502–541, 2020. doi:10.1137/18M1230050.

[7] F. Bouchut. *Nonlinear stability of finite Volume Methods for hyperbolic conservation laws: And Well-Balanced schemes for sources*. Frontiers in Mathematics. Birkhäuser, Basel, 2004. doi:10.1007/b93802.

[8] D. N. Arnold, F. Brezzi, B. Cockburn, and L. D. Marini. Unified Analysis of Discontinuous Galerkin Methods for Elliptic Problems. *SIAM Journal on Numerical Analysis*, **39**(5):1749–1779, 2002. doi:10.1137/S0036142901384162.